

Macropores in Si: fundamental study and prospective applications

Dissertation
zur Erlangung des akademischen Grades
Doktor der Ingenieurwissenschaften
(Dr.-Ing.)
der Technischen Fakultät
Christian-Albrechts-Universität zu Kiel

vorgelegt von
Eugen Foca

Kiel 2007

Reviewers:

1st - Prof. Dr. Helmut Föll

2nd - Prof. Dr. Ion M. Tiginyanu

To my parents

Contents

1	Introduction	1
1.1	Goals of the work	3
1.2	Structure of the thesis	4
2	Theoretical aspects of the semiconductor-liquid interface	7
2.1	The semiconductor-electrolyte contact	7
2.1.1	Energetic bands model for materials	7
2.1.2	Doping of semiconductors	8
2.1.3	Electrolyte solutions	10
2.1.4	Semiconductor-metal junction	12
2.1.5	Semiconductor-electrolyte junction	13
2.2	Si-HF contact	15
2.3	The calculation of the dissolution valence	19
2.4	Current Burst Model for the oscillation regime	20
2.4.1	General remarks	24
2.4.2	Implementation of the CBM in a Monte Carlo simulation tool	26
2.4.3	Basic results and interpretation of simulations with the CBM	34
2.4.4	Calculation of secondary quantities	39
2.5	Pore formation in Si	41
2.6	Pore formation in the Current Burst Model	45
3	Photonic Crystals and application using porous materials	47
3.1	Fundamentals of Photonic Crystals	47
3.1.1	Maxwell equations and the periodic dielectric media	47
3.1.2	Light propagation in PC	50
3.1.3	The scalability of the Maxwell equations	52
3.2	Porous Si as host material for gas sensor application	54

4	Experimental setups and analytical methods used in the work	57
4.1	Electrochemical etching and plating	57
4.1.1	Etching of macroporous n-Si	57
4.1.2	Electroplating of metals	58
4.2	Analytical tools	59
4.2.1	FFT impedance spectroscopy	59
4.2.2	Scanning Electron Microscope	63
4.2.3	Atomic Force Microscope	63
4.3	Photonic Crystals measurements	63
4.3.1	Microwave measurements	63
5	Modeling electrochemical phenomena at the Si electrode	67
5.1	Current oscillations	67
5.1.1	General results and representations	67
5.2	Damped current oscillations	71
5.2.1	Potential dependence of prime quantities	73
5.3	Current oscillations induced by extrinsic synchronization	75
5.4	Forced current oscillations	77
5.5	Potential oscillations	78
5.5.1	General remarks	78
5.6	Results of simulations	82
5.7	Interpretation and more detailed simulations	87
5.8	Discussion	91
5.8.1	Merits and limits of the current-burst model	91
5.8.2	Possible extensions of the CBM and future work	94
6	Experimental work on porous Si for photonic applications	97
6.1	Etching of special structures	97
6.1.1	Introduction	97
6.1.2	Adiabatic taper	98
6.1.3	Anti reflection layer	99
6.2	FFT impedance spectroscopy for the control of pore growth	100
6.2.1	Introduction	100
6.2.2	Voltage impedance	101
6.2.3	Experimental Results and Discussion to the Voltage Impedance	109
6.2.4	Photo Impedance	121
6.2.5	Results and Discussion of the Photo Impedance	123

6.3	The role of alcohols in the electrolytes for pore etching	128
6.3.1	Introduction	128
6.3.2	Experimental results	128
6.3.3	Discussion	133
6.4	Inhibition of pore wall roughness	135
6.4.1	Introduction	135
6.4.2	Experimental results	136
6.4.3	Discussion	141
6.5	Composite materials for PC applications	145
6.5.1	Introduction	145
6.5.2	Experimental results	147
6.5.3	Discussion	152
6.6	Conclusions	156
7	Experimental work on optical elements based on Photonic Crystals	159
7.1	Calculation methods	159
7.2	Concave lenses	161
7.2.1	Square lattice lens	162
7.2.2	Triangular lattice lens	173
7.2.3	Discussion	180
7.3	Derivate of the concave lens	188
7.3.1	Refractive index and lattice constant gradient lenses	188
7.3.2	Holographic lenses	190
7.4	Negative index materials with inhomogeneous rods	202
7.4.1	Results of simulations	204
7.4.2	Experimental results	207
7.4.3	Discussion	212
7.5	Conclusions	215
8	Summary and Outlook	219
	Bibliography	223
	Partial publications	235
	Curriculum Vitae	239
	Acknowledgments	241

1 Introduction

In the first quarter of the previous century Lord Rutherford, a great physicist, used to say: "In science there is only physics. The rest is stamp collecting." [1]. This credo might sound somewhat ridiculous at present but expresses the real state of the art of science in those years: each field of science experienced a vertiginous development. However, the interaction between scientists with different backgrounds remained only marginal. Rutherford was a brilliant scientist, and by 1953 acknowledged biology as a science too. That was the time when the X-ray diffraction was successfully applied for the investigation of the structure of the DNA molecule. The age of scientific interactions started as "an emerging era" as L. Laughlin called it in his book "A different Universe".

Indeed, since the middle of the last century we are witnessing a real metamorphosis in the scientific community. Biology merged to some extent with engineering to the new research field bio-engineering; solid state physics and parts of chemistry and engineering combined to nano-science and nano-technology; nano-technology combined with mechanical engineering generated nano-tribology; organic chemistry and semiconductor engineering may soon replace the generic transistor based on crystalline semiconductors; materials science and archeology brought forth archeometallurgy, and so on and so forth.

This work is, to some extent, multidisciplinary. It covers such areas as: simulations and modeling of fundamental electrochemical processes at the Si-HF interface, in particular the oscillatory behavior of the Si electrode; investigation of the pore growth phenomenology in n-Si; development of novel optical elements based on Photonic Crystals (PCs) as well as concepts for new generation of metamaterials, i.e. Negative Index Materials (NIM). The connections between these partially quite disparate fields are not obvious, but will be outlined below.

With respect to Si electrochemistry, one of its most remarkable features, which never has been fully understood, are the self-induced potential or current oscillations. These "electrode oscillations" are easily observed in the external circuit for parts of the electropolishing regime and thus are not usually associated with pore growth. "Oscillating electrodes" were noted about 150 years ago by Faraday [2] and are rather common in electrochemistry. Oscillations were found in such systems as, e.g., Ni and Fe electrodes in H₂SO₄ solution [3, 4, 5, 6], Cu in HCl [7, 8, 9], iron in chloride solutions [10], to name just a few. Several theoretical models

were formulated that tried to explain oscillating electrodes and chemical oscillations in general [11, 12, 13].

Pore etching in III-V semiconductors may be accompanied by strong potential oscillations [14], and more recently similar observations have been made during Si pore etching [15] and Ge pore etching [16]. This may be seen as an indication that pore etching and self-induced current/potential oscillations are somehow connected, a viewpoint that has been advanced by some of the authors before [17]. Be that as it may, the self-induced current or potential oscillations of Si electrodes in usually aqueous HF electrolytes are interesting enough in their own right, and this work attempts to demonstrate that many features of these oscillations can be quantitatively understood on the base of the so-called current burst model (CBM) [18] introduced before.

The electrochemical pore formation in Si is an old topic [19] with many potential applications and much progress was made toward the development of production technologies [20] and many product prototypes were advanced (see [21] and references therein). Nevertheless, despite all of this work, no product based on porous Si can be found on the market at present. Among the main reasons for this is the still not fully understood mechanism behind pore formation, or more generally, the many open questions in the field of electrochemistry of semiconductors. As an example, many envisioned applications demand precise control of the pore quality (e.g. diameter variations, pore wall roughness) and the present understanding of pore formation mechanisms, although rather advanced in some respects, is not good enough to ensure the full control of the etching process as it would be needed. A lot of questions still challenge the scientists; to mention only a few:

1. What determines the precise pore diameter during the macropore growth in n-Si with backside illumination?
2. How are the mechanisms of macropore growth influenced by nominally uncritical changes in the electrolyte composition?
3. What exactly happens at the pore tip during pore formation? Are there any interactions between the growing pores? If yes (see e.g. [14]) - what are the mechanisms and how do they relate to the external etching parameters?
4. Is there any possibility to access pore etching parameters in-situ? If yes, can that be used for the implementation of an automatic etching process, i.e. a process where etching parameters are constantly readjusted in real-time for obtaining the target structures?

With respect to Photonic Crystals (PCs), one similarity to Si electrochemistry is striking: While the theoretical knowledge base expands continuously since the invention of PC's around

1995, and by now a very advanced level of understanding has been reached [22], there are still no commercial applications really based on (at least two-dimension) PCs on the market. Possible applications, however, are many, e.g., PC based optical fibers [23], IR gas sensors [24], special cavities for lasers [25], and so on. However, all of these possible products still reside in research institutes and R&D departments of some companies. Despite of a very good theoretical grasp of PCs, the imperfect fabrication tools retain applications. PCs often need a very high fabrication precision and being complex by nature this involves a very accurate lattice constant, components geometrical shapes and sizes. Unfortunately the actual fabrication technologies are not mature enough for ensuring the targeted high optical quality of the produced PC devices. Since electrochemically etched macropores in Si are a major method for producing PCs, the connection between PC research and pore formation as mentioned before now becomes obvious.

The starting point of this thesis was the invention by Wehrspohn et al. [24] of a new generation of spectroscopic gas sensors based on PCs. This innovation was triggered by the industry with the intention to replace the common gas spectroscopic sensors, which usually have a volume measured in m^3 , by miniaturized variants. In the case mentioned the intended miniaturization would amount to a factor of 10^9 ! The PC forming the sensing device was intended to be made from macroporous n-Si, produced by the "classic" backside illumination (bsi) etching technique [26]. Part of this work was dedicated to the attempt to realize the structures needed in a production-near environment.

The connection between PCs and semiconductor electrochemistry as outlined above serves as an illustrate of the inner coherence of the topics of this work, but does not yet do justice to the full scope of the work presented here. This will be made clear in the next paragraph.

1.1 Goals of the work

This work focuses on four main topics:

1. Extension and further development of the Current Burst Model (CBM);
2. Deeper understanding and investigation of the macropore formation in Si;
3. Elaboration of techniques for the fabrication of composite materials;
4. Proof of principle of novel optical "negative index" components based on PCs.

The first goal was pursued in the context of an existing simulation tool for current oscillations that could reproduce the experimentally found current oscillations (at constant voltage)

within some parameter space. Here the earlier work [18] will be extended not only to larger sample areas, but also for the first time to several new topics like potential oscillations under galvanostatic conditions, induced current oscillations, and driven oscillations.

The second goal of the thesis focussed on experiments for pore etching employing different chemistries, a better definition of the exact etching parameters in a large parameter space, and finally on the development of methods for obtaining *in-situ* information about the pore properties. The results, combined with the input obtained from the CBM, establish a base for an *in-situ* controlled etching process. Part of this work, done in collaboration with other research groups, was to find the conditions for making a PC based spectroscopic gas sensor with porous Si - hence the acute necessity of such a study.

The third goal - fabrication of composite materials - was not directly connected to the previous task. However, many applications based on porous Si call for "something" inside the pores, and in this part of the work the goal was to develop methods and techniques for the fabrication of the resulting composite material. While any combination of materials can be considered as a composite material, in this case the main target was the electroplating of metals in porous templates. Parallel to understanding the electrodeposition process itself, specific topics were formulated as, e.g., electroplating of metals in very deep macropores, in different porous semiconductors, and also into quite different pore morphologies.

Besides working out the electrochemical approaches for the fabrication of the PCs (etching and, more visionary, electroplating), another main goal of the thesis was to test potential "negative index" optical devices based on PCs first in the microwave range of the spectrum. The results can serve as a proof of principle for optical components like lenses, beam splitters, filters, polarizers, antennas, etc. There is a big advantage of doing this first in the microwave regime: The needed structures are rather large and thus easy to fabricate. Due to the linearity of the Maxwell equations, they can serve as model system, which can be scaled down to higher frequencies while fully preserving the functionality.

All four topics form a logical chain: develop a theoretical background for understanding the phenomenology of the semiconductor-liquid interface; use it for controlling the pore formation in semiconductors; investigate methods for the fabrication of composite materials; use porous materials and technologies for fabricating different metamaterials and implement novel devices and components based on PCs.

1.2 Structure of the thesis

The second chapter gives a theoretical description of the semiconductor-liquid interface. It contains and recounts and defines the basic knowledge and the parameters needed, such as

the theoretical background of semiconductors, semiconductor - electrolyte junctions or the CBM, but also some specifics like the dissolution valence. A short section is dedicated to the phenomenology of the macropore formation in Si with the main focus on n-Si.

The third chapter is dedicated to the topic of Photonic Crystals (PCs) and those applications that are based on porous materials (e.g. PCs as spectroscopic gas sensors). It gives basic definitions regarding the concept of the PCs and considers the light propagation inside a PC. The case of PCs with an index of refraction < 1 or even negative is treated in some detail since this is the class extensively studied in this work. Topics like the "homogenization" of a PC and ascribing a refractive index to these strongly dispersive materials are brought in focus.

The fourth chapter describes the experimental set-ups used in this work. It concerns itself with producing the porous structures as well as with the analytical tools used for the investigation of the porous materials. Special attention is paid to FFT Impedance Spectroscopy, which is used for the characterization of the porosification process. The experimental conditions for the microwave experiments are outlined, too.

The fifth chapter describes the experimental work concerning the modeling of the Si-HF interface by means of the Current Burst Model. It is mainly dedicated to the simulation of the oscillatory behavior of the electrode. It treats different types of the current oscillations: damped, stable, sustained, enforced, etc. The huge amount of secondary data generated by the CBM is analyzed in conjunction with the simulated oscillations. The same is done for potential oscillations.

The sixth chapter is dedicated to the experimental results on porous semiconductors intended for optical applications. The topics treated include: in-situ control of the pore formation in n-Si, etching of special structures, pore formation in different chemical milieu and production of macropores in Si with very smooth pore walls. This chapter also includes a study on the electroplating of metals in porous semiconductors and covers such topics as filling very deep macropores or filling special pore geometries in GaAs.

The seventh chapter reports results obtained with optical components based on PCs with unusual index of refraction, i.e. $n_{eff} < 1$. The negative index metamaterials used were based on uniform rods and on rods with a profile in the dielectric constant. Components tested with a microwave radiation source included focusing lenses, beam splitters, and filters. An algorithm for the optimization of the tested structures is proposed and experimentally tested. The eighth chapter summarizes the results and gives an outlook.

2 Theoretical aspects of the semiconductor-liquid interface

2.1 The semiconductor-electrolyte contact

2.1.1 Energetic bands model for materials

All materials in nature, from their electrical conductivity point of view, can be cataloged in three main groups:

- metals - ρ^1 is in the order of $\mu\Omega cm$;
- semiconductors - ρ is in the order of Ωcm ;
- insulators - non conductive at all.

There are different theories developed for modeling the behavior of materials. For instance, the free electron gas model is able to explain very well such features of the materials as heat capacity, thermal conductivity, etc. However this model fails to explain the distinction between the above mentioned class of materials. In order to better understand the origins of these different class of materials the so called energy bands model is introduced. This is, actually, an enlarged form of the free gas model. The important question that it addresses is: how does the electrons in each material react to the applied electric field.

In order to answer this question one starts with considering that the electrons are arranged in energy bands instead of considering discrete energy levels. These energy bands are separated by regions for which the wavelike electron orbitals do not exist - *energy gaps*.

In Fig. 2.1 the three classes of materials viewed in the framework of the energy bands model are shown. For the case of the insulators the energy gap is immense and hence precludes the transition of the electrons from the valence band into the conduction band. This is the reason why the insulators are not conductive. The semiconductors have a band gap as well, however much smaller than the insulators. As a result if sufficient energy is provided the electrons

¹By ρ is meant the specific resistivity of the materials.

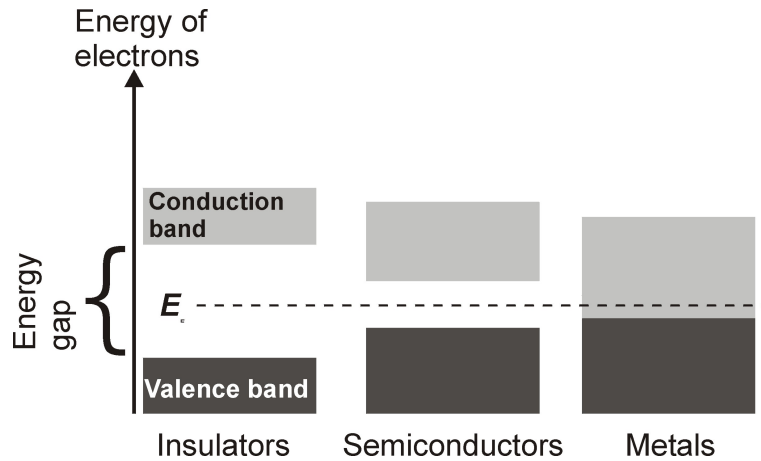


Figure 2.1: *The energy band model which explains the distinction between the three classes of materials: metals, semiconductors and insulators.*

might be excited from the valence band into the conduction band and the material becomes conductive. This excitation energy can have different routes, e.g. thermal, photo excitations. For the last class of materials - metals - the conduction band overlaps with the valence band, i.e. the Fermi level is situated in the conduction band, and no energy gap is available. This ensures a very high electrical conductivity for the metals.

For the intrinsic semiconductors at $T = 0\text{K}$ no electrons will be found in the conduction band and hence they are fully insulating. More generally, the distribution of the electrons is described by the Fermi-Dirac statistic:

$$f(E, T) = \frac{1}{1 + e^{\left(\frac{E - E_F}{kT}\right)}} \quad (2.1)$$

where k is the Boltzmann constant. From this equation can be seen that at $T = 0\text{K}$ the last occupied energy state is at the Fermi level E_F which for the intrinsic semiconductors is placed at $\frac{1}{2}E_g$ where the E_g is the width of the energy gap. The Fermi-Dirac distribution shows that as the temperature increases the probability that an electron occupies an energy state higher than E_F is different than zero - the material becomes (semi)conductive.

2.1.2 Doping of semiconductors

In a semiconductor when an electron is excited from the valence band into the conduction band a hole is left in the valence band. A hole has a positive charge equivalent to that of the electron. It is however described by an effective mass m_{eff} different than that of the electron which might become even negative. The holes together with the electrons determine

the conductivity of a semiconductor which is, in its general form, defined as:

$$\sigma = q^- n_0 \mu_e + q^+ p_0 \mu_h \quad (2.2)$$

where the n_0 and p_0 are the concentrations of the electrons and holes with the mobilities μ_e and μ_h respectively.

Via doping of the semiconductors one can obtain semiconducting substrates where the concentration of electrons (holes) differs from the concentration of holes (electrons). If the concentration of electrons is higher, the semiconductor substrate is called of n-type and electrons are considered the majority carriers while the holes are the minority ones. Vice versa, when the concentration of holes dominates that of electrons, the semiconductor is called p-type and the holes are considered as majority carriers while the electrons are the minority ones.

For the case of an intrinsic semiconductor the material is considered to be pure; at least with negligibly small amount of impurities. In this case each Si atom shares its 4 valence electrons with the neighbors thus forming covalent bonds. When a n-type semiconductor has to be formed the pure Si crystal is doped with a special atom containing 5 valence electrons, called a *Donor* atom. Once it is stabilized in the Si lattice it forms, similarly to a Si atom, four covalent bonds by sharing 4 of its 5 electrons with its Si neighbors. As a result per each donor atom a free electron is "donated" to the lattice. It is common to use P as donor atom for realizing n-Si while B as acceptor for making p-Si. Substituting for a Si atom with one that has only 3 valence electrons triggers the "acceptance" of an additional electron for forming the 4 covalent bonds which create a hole in the lattice. The doping atom is then called *Acceptor* and B is widely used as such.

It is interesting to see how the Fermi level does change as a function of the dopant concentration. In order to preserve the electrical neutrality the concentration of the electrons in a doped semiconductor must equal the total amount of the positive charges, including holes and ionized donors: $n = N_D^+ + p$ where n is the electron density in the conduction band and p is the holes density in the valence band and N_D^+ is the concentration of the ionized donors which is given by:

$$N_D^+ = N_D \left(1 - \frac{1}{1 + \frac{1}{g} \exp\left(\frac{E_D - E_F}{kT}\right)} \right) \quad (2.3)$$

The variable g is called the ground state degeneracy of the donor impurity level and equals 2. A similar expression can be deduced when the acceptors are added to the semiconductor:

$$N_D^- = \frac{N_A}{1 + g \exp\left(\frac{E_A - E_F}{kT}\right)} \quad (2.4)$$

In this case the number g will equal 4. After including these two into the electrical neutrality equation one obtains:

$$N_C \exp\left(-\frac{E_C - E_F}{kT}\right) = N_D \frac{1}{1 + 2 \exp\left(\frac{E_F - E_D}{kT}\right)} + N_V \exp\left(\frac{E_V - E_F}{kT}\right) \quad (2.5)$$

In this equation the N_V is the density of the available states in the valence band and E_V and E_C are the limits of the valence and the conduction bands respectively. For specific N_C , N_D , N_V , E_C , E_D , E_V , and T the Fermi level can be calculated. Similarly the Fermi level for the p-Si can be calculated if considered the electrical neutrality equation.

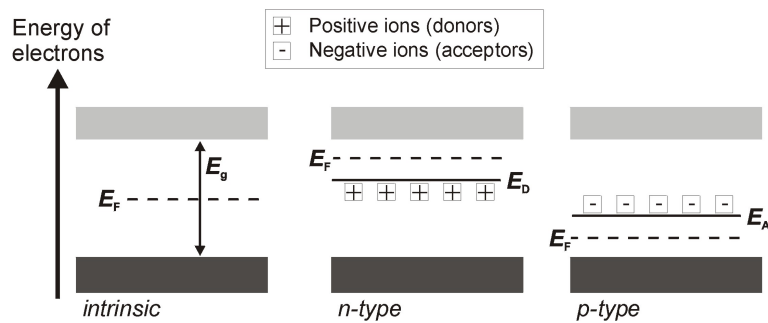


Figure 2.2: The position of the Fermi level for the intrinsic, n-type and p-type semiconductors.

Figure 2.2 shows schematically the position of the Fermi level for different types of doping. It is now obvious why for the n-type semiconductor the conductivity is ensured by the electrons by contrast to the p-type where the free particles are holes.

2.1.3 Electrolyte solutions

According to their generic definition the electrolytes are chemical compounds that dissociate into electrically charged ions when dissolved in a solvent. These solutions can be acids, bases or salts. Although somewhat uncommon, gaseous electrolytes do exist as well.

According to the band model, the charge transfer from the electrode into the electrolyte takes place from an energy level of the solid or surface states into the energy levels located in the orbitals of the ions in the electrolyte. This makes the main difference (from the electronic conductivity point of view) between the solid and the solutions where the energy bands are strongly localized.

The charge transfer from the electrode into the solution occurs via two main reactions: reduction or oxidation. The first involves the transfer of an electron from the electrode into an orbital of the solution ion. The second type of the reactions implies the inverse process, i.e. the transfer of the electron from an ions orbital into the electrode. It is commonly accepted

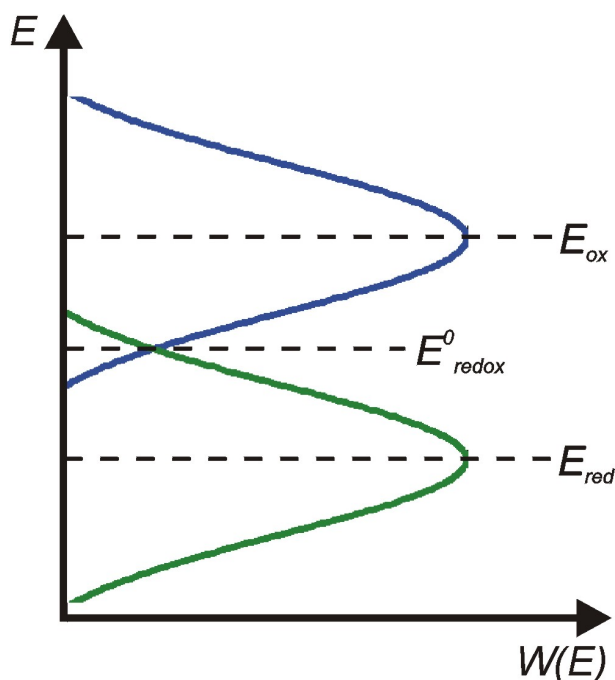


Figure 2.3: *The distribution of the ions/molecules energy levels in a solution.*

to call the flow of electrons from the electrode into the solution *reduction current* and the inverse process, the flow of electrons from the solution into the electrode - *oxidation current*. The ions that donate electrons into the electrode are called the *reducing species* and the ions which accept electrons from the electrode are called *oxidizing species*. A pair consisting of both species is called a *redox couple*.

The energy states of the ions or molecules in the solution are localized. Their distribution, however, is strongly influenced by the solvent molecules that create a solvent shell surrounding each ion or molecule. Taking into account the very high entropy existing in liquid electrolytes, the solvent molecules will strongly fluctuate which leads to continuous changes of the energy levels for the ions or molecules. In this case they can be only statistically defined as shown in Fig. 2.3.

The energy levels corresponding to the oxidizing and reducing species are indicated as E_{ox} and E_{red} . The redox potential E_{redox}^0 is considered to be a sort of the Fermi level of the electrolytic solutions.

When brought in contact with the electrode, after the equilibrium is established, the Fermi level of the electrode must equalize the redox potential of the solution: $E_F = E_{redox}$. For an equal concentration of the reducing ($[E_{red}]$) and oxidizing ($[E_{ox}]$) species the redox potential

is defined as:

$$E_{redox} = E_{redox}^0 - kT \ln \left(\frac{[E_{ox}]}{[E_{red}]} \right) \quad (2.6)$$

One has to mention here that this equation is valid only in equilibrium. For Eq. 2.6 it can be shown that the E_{redox}^0 is always $1/2(E_{ox} + E_{red})$ independent of the equilibrium state of the solution.

2.1.4 Semiconductor-metal junction

When a semiconductor is brought in contact with a metal a Schottky barrier or an ohmic contact can form. Due to the similarity between this contact type and the semiconductor-electrolyte junction, here some important details on this subject will be given.

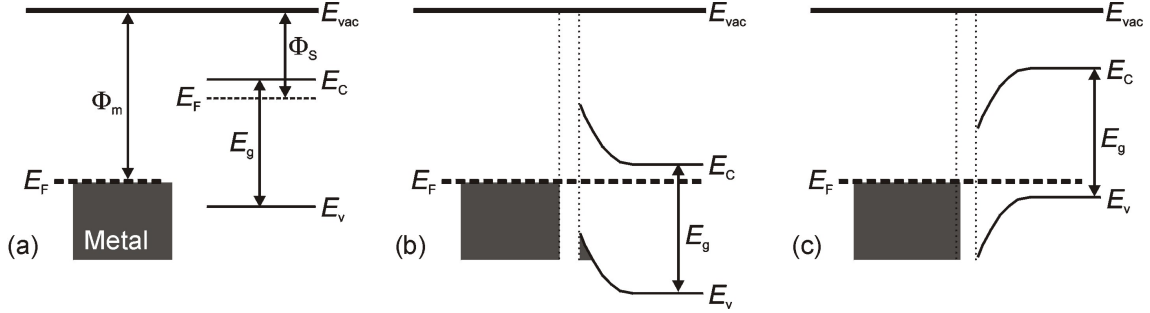


Figure 2.4: *The formation of the Schottky barrier. A metal and a n-type semiconductor before contact (a), n-type semiconductor brought in contact with the metal (b), p-type semiconductor brought in contact with the metal.*

Before bringing a metal in contact with a semiconductor, the bands in either of the materials look similar as in Fig. 2.4a where a metal and a n-type semiconductor are represented. After both types of materials are contacted a barrier will form across the metal-semiconductor junction which is called the Schottky barrier. It is caused by the difference in the working functions for the electrons in the metals (Φ_m) and for that in the semiconductors (Φ_s). If for a n-type semiconductor $\Phi_s < \Phi_m$, then an electron flows from the semiconductor conduction band into the metals states once the junction is established. The barrier form looks similar as in Fig. 2.4b. For the p-type semiconductors the processes run opposite leading to the bending of the bands as indicated in Fig. 2.4c. The height of the Schottky barrier is the difference between the conduction band minimum at the junction and the Fermi level for the n-type semiconductors and the difference between the Fermi level and the valence band maximum at the junction for the p-type semiconductors. Between the bent bands of the semiconductor and the metal an extra region exists called *Interface Specific Region* (ISR). This is a sort of

the transition region from the metal to the semiconductor which determines the magnitude of the Schottky barrier height. The barrier height is in the order of 0.4 - 0.8 eV depending on the type of the metal and doping concentration of the semiconductor.

The electrons moving from the semiconductor into the metal leave the ionized positive donors close to the surface which leads to the formation of a *Space Charge Region* (SCR) and the corresponding embedded electric field. Under the action of this field a net zero current through the junction will result. When the junction is polarized in forward the barrier height is lowered and a current can flow. If polarizing the barrier in the reverse direction a stronger increase in the barrier takes place which completely precludes the majority carriers current flow leading to a large resistance.

2.1.5 Semiconductor-electrolyte junction

Immersing a semiconductor in an electrolyte is similar as contacting with a metal due to the very high concentration of charges in the electrolyte. The interface between the semiconductor and the electrolyte becomes charged. The charging of the interface might be caused either by the majority carriers, leading to accumulation, or by the ionized donors (eventually acceptors), leading to depletion and finally minority carriers can prevail at the interface which leads to inversion.

For a semiconductor under depletion condition the SCR can extend up to several hundreds of nm depending on the doping level and the applied potential across the junction. The width d of the SCR is given by:

$$d = \frac{1}{e} \sqrt{\frac{2\epsilon\epsilon_0 (\Delta E_F + eU_{ex})}{N_D}} \quad (2.7)$$

In the case of the accumulation and inversion the thickness of the charge is much smaller since it is built up by free charge carriers; it is called *Debye layer*.

In the electrolyte the charged ions will rearrange according to the state of the electrode. A schematical picture of the charges distribution at the electrode surface is shown in Fig. 2.5.

In the solution two types of layers are formed. First, in the immediate proximity of the electrode an *Inner Helmholtz Plane* (IHP) which consists mainly of solvent molecules (water for aqueous electrolytes) and (mainly) opposite to the electrode state charged ions surrounded by the solvent molecules. These ions/molecules are specifically adsorbed at the electrode surface. This layer is also called the *inner* or *compact layer*. It is succeeded by the *Outer Helmholtz Plane* (OHP) which consists of fully solvated ions. For relatively low concentrated solutions, i.e. below 0.1 M a Gouy-Chapman layer will be also formed. If the electrolyte is

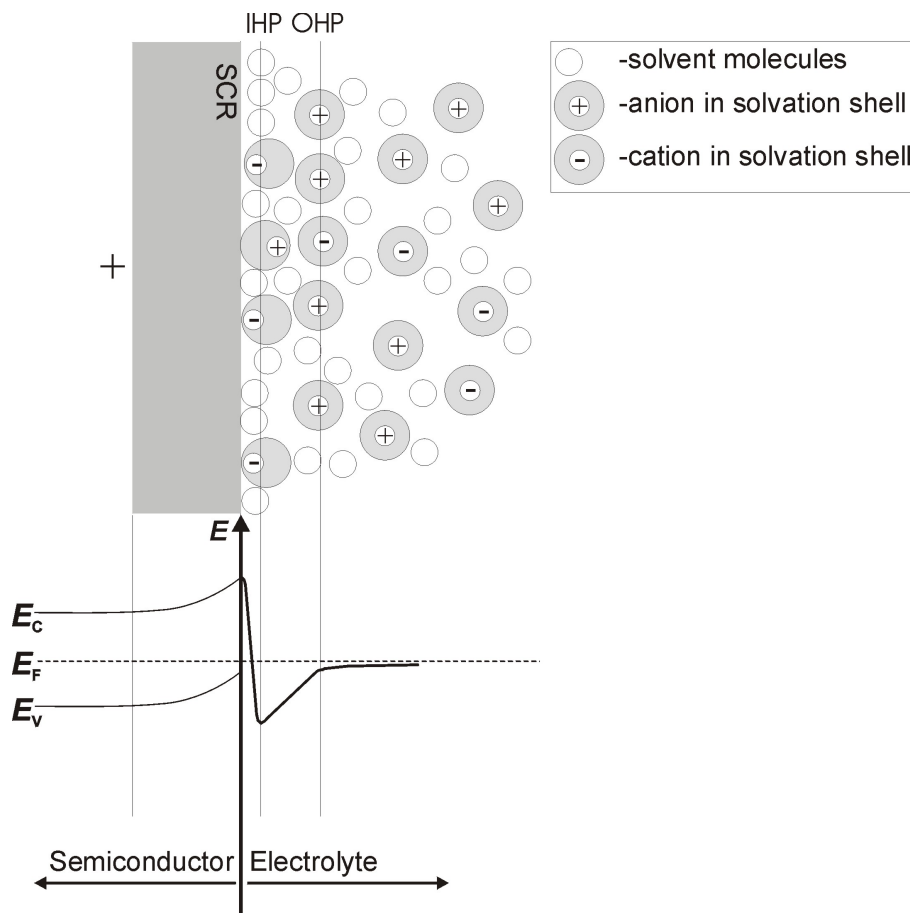


Figure 2.5: Schematic representation of the ions and solvent molecules distribution at the electrode surface together with the distribution of the potential across the junction.

highly concentrated, the two Helmholtz layers can shield the electric field fully. The typical thickness for the two Helmholtz layers is in the range of one nm while the Gouy-Chapman layer extends up to several tenths of nm.

If high enough, the potential dropped in the Helmholtz layer and the SCR in the semiconductor will drive charges across the interface via some electrochemical reactions. Subsequently the double layer structure will strongly affect the rates of the electrode reactions. The factors that affect the electrode reaction rate and currents can be summarized as follows [27]:

1. Mass transfer, i.e. an ion has to move from the electrolyte bulk toward the electrode surface where it will be further reduced or oxidized;
2. Charges transfer toward the surface from the electrode side;
3. Chemical reactions that involve the electron transfer process. They can be divided into homogeneous processes such as protonation or dimerization or heterogeneous such as catalytic decomposition;
4. Other surface reaction can also be considered, e.g. adsorption, desorption.

If none of the points from above limit the charge transfer through the interface, the current will be described by the Butler-Volmer kinetics.

The nature of the semiconductor and the electrolyte will determine the type of the I-V characteristic of the electrode. When the charge transfer is limited by the charge transport from the semiconductor the formed contact is of the Schottky type as described in the previous section. For the case of an n-type electrode in the dark, if it is anodized, the junction will be polarized in reverse and no current will flow unless a junction breakdown occurs generating a large number of holes. If the semiconductor is illuminated the current will increase proportional to the illumination intensity. The situation is similar for the p-type considering the exchanged role of the electrode during the anodization.

A Schottky contact models well the semiconductor-electrolyte interface if the charge transfer is limited by the electrode. As soon as the charge transfer is diffusion limited or rate determined the Schottky contact does not describe well the contact. In this case it is more accurate to use the concept of a metal-insulator-semiconductor.

2.2 Si-HF contact

The I-V curves describing the p-Si and n-Si in contact with HF are shown in Fig. 2.6a and -b, respectively. In the cathodic regime the Si electrode in contact with the electrolyte, p-Si as

well as n-Si, behave as noble metals and only hydrogen evolution can take place. Eventually, in a plating solution the reduction of metals ions at the electrode surface can take place, i.e. electroplating. For the p-Si under the illumination a cathodic current can flow depending on the illumination intensity.

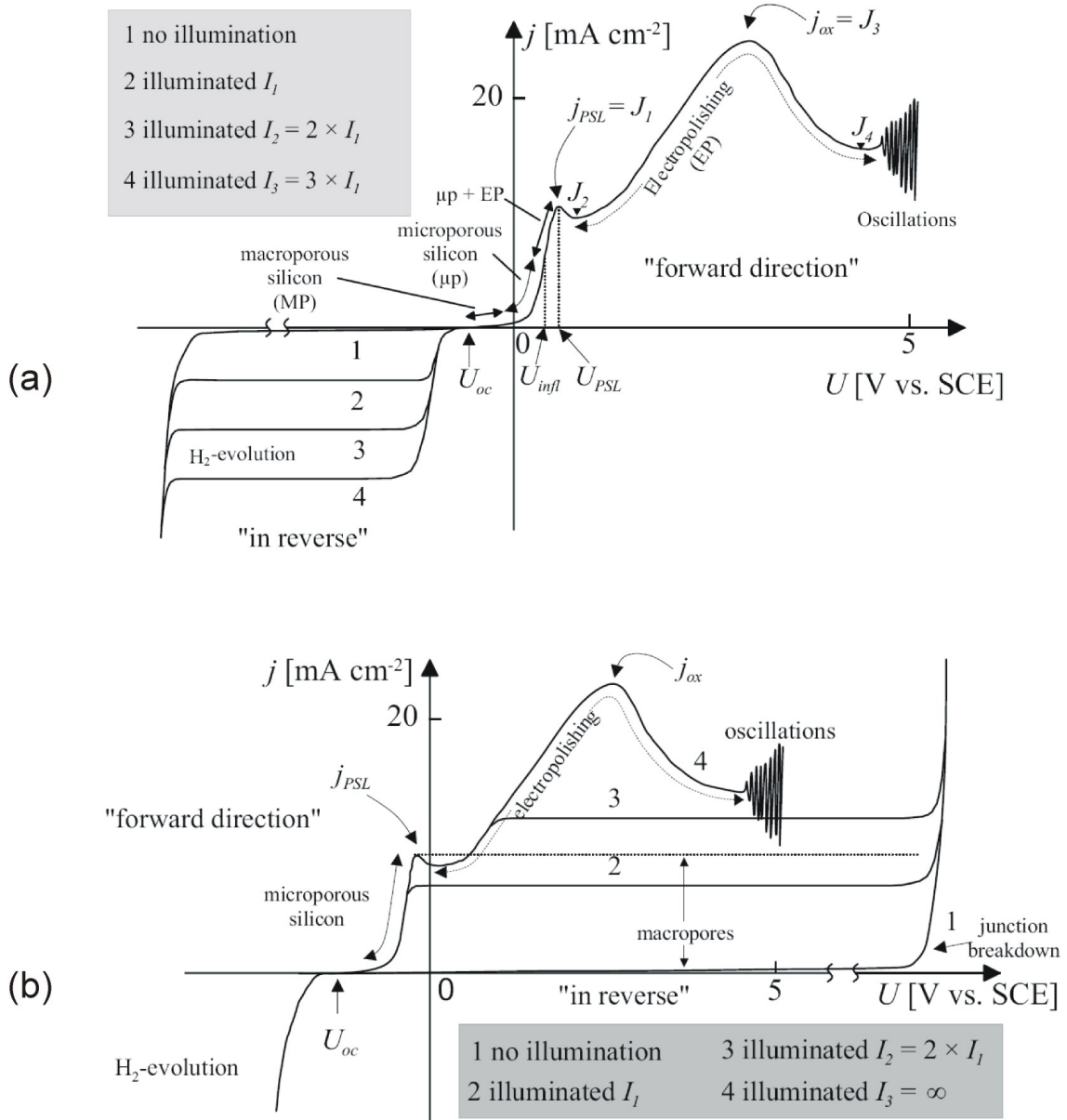


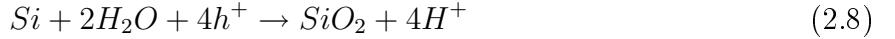
Figure 2.6: The IV curves of the p-type (a) and n-type (b) Si in contact with the HF. Reproduced from [28].

For the anodic regime the dissolution of Si will take place. In the dark, a high current will flow for the p-Si and almost no current flows for the n-Si. Under the illumination no changes will occur for the p-Si and a current can be driven for the n-Si. Under very strong illumination, such that inversion takes place, the n-Si will have a I-V curve similar to the p-Si

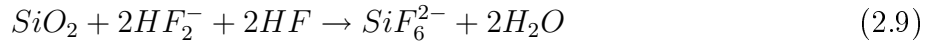
for the anodization regime.

The first current maximum following the open circuit potential U_{OC} is called J_{PSL} . For the potentials in this range, i.e. $U_{OC} < U_{etch} < U_{PSL}$, porous Si will form; for n-type provided that the sample is illuminated. For the p-Si, depending on the magnitude of the current, different types of pores geometries will form, these issues are further discussed in the following sections. For potentials higher than U_{PSL} the region of the "wet" oxide follows. In this range the Si electrode is electropolished. However for voltages below U at J_{ox} the electrode area is rather split into regions where oxide is produced and ulteriorly dissolved and areas where Si is directly dissolved. Only for potentials higher than the $U \equiv J_{ox}$ a closed oxide layer is found on the surface. For a constant current (voltage), voltage (current) oscillations will be encountered for p-Si. The electrochemistry of n-Si is somewhat poorer in this range. Macropores will form for potentials in the saturation regime of the I-V curve under illumination. For considerably high potentials the breakdown of the junction takes place.

By now two main mechanisms for the Si dissolution are accepted: divalent and tetravalent dissolution. Under anodic potentials the Si surface will be covered by an oxide film which in the absence of HF remains on the surface and passivates it. The oxidation of Si will take place under the consumption of 4 holes according to [20]:



If the electrode contains HF the produced oxide will be dissolved purely chemically:



SiF_6^{2-} is only the end product that forms in the electrolyte, directly on the surface an intermediate first forms: SiF_3OH [29]. The tetravalent dissolution mechanism can be summarized in the following picture Fig. 2.7.

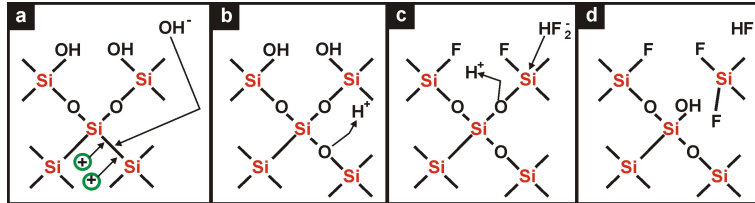
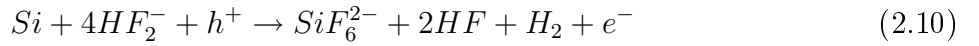


Figure 2.7: The scheme for the tetravalent dissolution.

At considerably high voltages the hydroxyl group OH^- will diffuse to the dangling bonds of the Si atom in the lattice and establishes a Si-O-Si bridge under the consumption of two holes. This is shown in Fig. 2.7a and -b. Having high enough voltage the OH^- group diffuses

even through an existing SiO₂ layer and produces oxide at the Si|SiO₂ interface. More on this issue can be found in Section 2.4. The formed SiO₂ further supports a nucleophilic attack by the fluorine involving the following possible species HF, (HF)₂ or HF₂⁻, Fig. 2.7c and -d. Note that pure HF does not dissolve SiO₂; some traces of water are always needed. This is an indication that the HF molecule must dissociate in order to dissolve SiO₂ [20]. Four charges will be consumed in the dissolution of a Si atom by following this scheme and no hydrogen evolution occurs.

The divalent dissolution takes place via the following electrochemical reaction:



It involves a direct attack on the Si-H terminated surface [30]. After a Si-F bond is formed it becomes very stable and cannot be reverted into a Si-H bond. Furthermore the Si-F bond is much stronger (6 eV) compared to the Si-H bond (3.5eV). After the Si-F bond is established it strongly polarizes the backbonds of the Si atom and weakens them. In a next step they are attacked by the HF or H₂O and the Si atom is completely removed from the lattice. Fig. 2.8 summarizes this scheme.

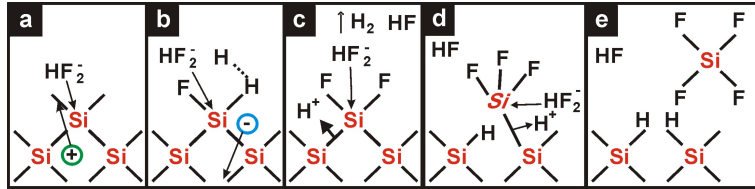


Figure 2.8: *The scheme for the divalent dissolution.*

More general the divalent dissolution is initiated by a hole that approaches the surface and allows for the nucleophilic attack of a Si-H bond, shown in Fig. 2.8a. Since the electrode is in the depletion state without applying any potential the holes will be available only for potentials higher than the OCP otherwise the surface remains hydrogen terminated. In the next step an electron injection takes place, Fig. 2.8b which is energetically more favorable than the consumption of a hole. This is done while attacking a backbond. The dissolution advances further by breaking the other two backbonds via the interaction with HF or H₂O, Fig. 2.8c and -d. The remaining Si atoms are finally passivated by hydrogen, Fig. 2.8e and the process starts again.

2.3 The calculation of the dissolution valence

As already mentioned in the previous section the dissolution valence n is defined as the total number of charges, flowing into external electrical circuit, per dissolution of a Si atom. Mathematically it is described as:

$$n = \frac{n_e + n_h}{n_{Si}} \quad (2.11)$$

where the n_e , n_h and n_{Si} are the number of electrons, holes and Si atoms respectively. Since the evolution of the etching current in time is always known it can be directly translated into the number of exchanged holes and electrons. The most straightforward method used for determining the amount of the dissolved Si atoms is to examine the change in the sample weight before and after the etching, i.e. use gravimetry. While the measuring procedure itself requires only a very precise apparatus applying it for porous Si imposes additional demands. First, in the case of very deep pores, the liquid has to be evacuated from the porous structure otherwise leading to aberrant estimation of the weight loss. Complete removal of the liquids is usually hampered by the catacomb like nature of the structures. In this case a possible solution is to heat the sample enough so that the liquid evaporates. Here one strikes with the second problem and namely, even at room temperatures (but considerably accelerated at higher temperatures) the pore walls oxidize. Considering the huge surface area of the porous substrates (it might reach magnitudes as high as a few hundreds of m^2) the formed oxide will obviously affect the weight loss measurement. The direct consequence of these two problems is that the dissolution valence is often overestimated.

Despite the above mentioned issues the dissolution valence during the anodization of Si could be quite precisely measured [20]. Taking into account that Si has the valence of 4 one would expect that this matches the dissolution valence as well. Indeed it was found that for the anhydrous HF mixed with organic electrolytes $n = 4$ [31]. Also a tetravalent dissolution is found during the electropolishing of Si in HF. In aqueous electrolytes, however, especially in the pore formation regime n decreases below 3 and can have magnitudes even smaller than 2. The reason for that are the peculiar dissolution reaction pathways for the low potentials during the pore formation.

Not only the dissolution valence shows different values in the pore formation regime, it also strongly depends on the substrate and etching parameters, e.g. doping type, doping level, electrolyte type and pH, etc. The strongest variation of n on the doping level is found for the p-Si at the transition from micropores formation to mesopores where the valence changes from values close to 2 toward 3 respectively. For n-Si substrates the major changes are encountered when the electrode is illuminated compared to etching in the dark. For instance the n-Si in the

dark exhibits a dissolution valence close to 3 while decreasing to about 2 when illuminated. This can be easily understood in the framework of the Lehmann model [20]. In the dark only mesopores will be formed. If illuminated the macropores will form in n-Si. According to the mentioned model during the macropores formation, J_{PSL} will flow at the pore tip. As already mentioned earlier the J_{PSL} also presents a change point for the n dependence on etching current which indicates that for $J > J_{PSL}$ the dissolution becomes rather tetravalent. Taking into account that the dissolution valence at the pore walls is 2 and being close to 3 at the pore tips an average dissolution valence leads to values around 2.6 which was also confirmed experimentally by many authors [32]. By contrast at the tips of the macropores in p-Si the dissolution valence is found to be close to 2 [33]. This difference between the two pore categories will become relevant when analyzing the effect of alcohols on the pore formation.

2.4 Current Burst Model for the oscillation regime

Turner reported current oscillations at the Si electrode in the Si/HF system for the first time in 1958 [34]. His main interpretation was that above a certain potential and below a certain value of the electrolyte concentration, the HF concentration at the anode surface is too small to allow the divalent direct dissolution of silicon. Turner was aware that an "electropolishing film" is formed during oscillations, and considered this film to be SiO_2 . While Turner was essentially correct in his interpretation, the mere presence of a (always uninterrupted) SiO_2 film during dissolution is not sufficient to produce oscillations. Nevertheless, it is now generally accepted that almost exclusively tetravalent dissolution takes place in the oscillation regime; *i.e.* dissolution essentially proceeds by current-driven SiO_2 formation and purely chemical SiO_2 dissolution.

In 1988 Gerischer and Lübcke [35] related oscillations of the current density under a constant potential to the periodic growth and dissolution of a SiO_2 layer at the Si/HF interface. They postulated the existence of a "suboxide" SiO_{2-x} between the SiO_2 and Si. As the oxide becomes thicker, the composition of the total oxide layer is closer to SiO_2 . The oxide was supposed to grow by field-assisted oxygen ion diffusion through the oxide towards the SiO_2 - SiO_{2-x} /Si interface. In essence they proposed a nonlinear relation between oxide formation and its dissolution as the cause for the oscillating current density.

Again, this point of view is reasonable, and some non-linear behavior could lead to oscillating solutions of a system of reaction equations. However, there are three basic problems with this approach and other models proposed later, that are worthwhile to be outlined at this point in order to facilitate a critical discussion:

1. Even if some oscillating reaction driven by the local current does take place locally, it is

rather unlikely that all area increments on the electrode will stay in phase without some synchronizing mechanism. Small local variations in, e.g., electrolyte flow, temperature, potential or current density will destroy any initial phase coherence. Given only some oscillating reaction in the form of "micro oscillators" (a term coined later by Chazalviel et al. [36]), at best a damped oscillation could be observed ending in a constant (if somewhat noisy) current resulting from the superposition of many micro oscillators with random phases. Any detailed model therefore must include some mechanism that keeps the oscillations in phase on at least a substantial part of the sample surface.

2. Even if there are nonlinearly coupled reaction equations (in particular if some autocatalytic mechanism is involved), not all of them will produce oscillations, or oscillations as observed with a Si electrode. The well-known Belousov-Zhabotinsky reaction [37] by now has many brethren showing beautiful chemical oscillations; but this kind of chemical oscillation is still more of a curiosity and not a paradigm for electrode oscillations. Moreover, differential equations for the reaction kinetics are not always well suited to describe stochastic phenomena as, e.g., current flow through fluctuating pores in an oxide.
3. Postulating some kind of oscillating balance between oxide formation and dissolution, while not wrong, does little to explain what is really happening. In other words: Qualitative models might be very helpful in approaching the oscillation phenomena, but will by necessity fall short of providing an in-depth understanding of the mechanism involved.

With this remarks in mind, the many models proposed after Gerischer and Lübckes paper [35], can be put in a better perspective.

Föll in 1991 invoked electron tunneling and electronic oxide breakdown under large electrical fields as an essential factor for the Si electrode oscillations [38]. The model could produce local oscillations, but lacks a synchronization mechanism and is purely qualitative. However, it introduced for the first time the particular stochastic component of local oxide breakdown, occurring with a certain probability that is determined by the local field strength, as the reason for local current oscillations or micro oscillators.

Eddowes in 1990 proposed the idea that the second current peak in the *Voltammogram* of the Si/HF system marks the point where an oxide of different stoichiometry (or state) is formed during electropolishing [39]. Smith and Collins enlarged on that idea, postulating a "hard" oxide for high potentials, and a "soft" oxide for low potentials, respectively [40]. Their speculation is based on the fact that the potential at the Si/SiO₂ interface changes as a function of the oxide type that is exposed to the HF at any instance in time. Assuming that the "hard" oxide dissolves less quickly than the "soft" oxide, scenarios can be constructed that

lead to current oscillations. Again, there is some merit in this proposal, but as before it lacks a synchronization mechanism and is purely qualitative.

A big step forward was made in 1992 by Chazalviel and Ozanam [36, 41, 42]. They studied current oscillations under constant potential conditions, but also with superimposed sinusoidal excitation and sharp steps [43]. By contrast to many researchers in the field who reported long-lasting oscillations, they claim that "natural" oscillations are always damped on relatively short time scales. Stable oscillations were only obtained via external excitations of the system, e.g. by a sinusoidal modulation of the applied potential, which lead them to consider the Si/HF system as a kind of resonant system reacting to external stimuli rather than a self-oscillating system. The authors are among the first who proposed the existence of micro oscillators on the electrode, which they considered to be organized in small self-oscillating areas or domains of constant oxide thickness, randomly distributed on the electrode, and suggested that macroscopic oscillations will be detected in the external circuit if these domains (or at least a majority of them), will synchronize. Ozanam et al. then made an attempt for a quantitative description of these oscillating domains together with relevant experimental results in 1993 [44] and arrived at a typical domain size of about 100 nm. Realizing that oscillations are organized in domains and will not be "visible" if the domain size is much smaller than the sample size was a major insight. However, the model did not explain the physical reasons for oscillations or for the synchronization.

Lewerenz and Aggour [45] proposed a model in 1993 that explains the oscillations on the basis of fluctuating pores in the oxide that essentially conduct the local current. Their paper also tries to explain the observed frequency dependence of oscillations on the pH of the solution and the applied potential. Their model seems to be the first one that includes the large volume change from Si to SiO₂ upon reaction, and a postulated interaction of the resulting stress and strain in the SiO₂ film with the dissolution process. Lewerenz and Aggour then invoked stress-induced point defect generation as the cause for pore formation and preferential local dissolution of the oxide as the cause of the oscillations. Oscillation parameters like frequency, amplitude, shape and their dependence on external parameters like potential, pH, HF concentration or temperature, are, in principle, functions of the number of point defects and pores, their spatial distribution, radii and dissolution rate. In other words, specific oxide properties depend sensitively on electrochemical parameters, and these oxide properties are the cause for the oscillations. Later, Grzanna et al. [46, 47] presented a sophisticated mathematical analysis based on variants of this model, which quantitatively reproduced many observed features. They included the necessary synchronization feature, but as a kind of free parameter with no direct physical justification. In the newest version of this model [48], two kinds of oxide are invoked and (compressive) stress-induced formation of microcracks plays a major

role.

In 1996 Lehmann conducted major experimental work that also looked at potential oscillations under galvanostatic conditions (a feature not much investigated before). He tried to explain his results by enlarging on the ideas of Eddowes [39] that predicted the existence of two kinds of the oxide, but also introduces the notion of "flat" and "rough" oxide [49]. The main argumentation line in this work is based on the supposition that the oxide dissolution rate is not constant in time. The transition from flat (dense) oxide obtained close to the Si/SiO₂ to rough (less-dense) oxide, induces also a change in the ionic permeability and the etch rate. On a pure Si surface the oxide grows homogeneously as long as its dissolution rate is smaller than the formation rate and this homogeneous oxide growth also leads to the synchronization of the oscillations. Reaching a certain thickness, the oxide will undergo a transition from dense to less dense or flat to rough, and this causes a strong drop in the potential and fast dissolution of the less-dense oxide forming a porous layer of SiO₂. After the less-dense layer is etched away, the dense part of the oxide is exposed to the electrolyte and the process starts again. The model is completely qualitative and therefore has little predictive power. Nevertheless, the notion of rough and flat oxides has some merit for modeling, and the experimental results pose a big challenge for quantitative models.

In contradiction to other authors, Parkhutik and Matveeva find long lasting potential oscillations at the Si electrodes, however in electrolytes with drastically reduced SiO₂ dissolution rates [50]. They ascribe these sustained oscillations essentially to mechanical changes in the oxide layer. The SiO₂ grows until a certain thickness limit is reached when it will de-attach from the substrate by some lift-off, causing a strong drop in the potential. Beneath the detached oxide a new oxide layer forms and the process continues. The authors claim that X-ray investigations showed a perfect accordance between the number of oscillations and the lifted-off layers. While this mechanism is possible and might be observed under special conditions, it is not the general cause of Si electrode oscillations and moreover purely qualitative. Some related work [51] studied the nature of chaotic and ordered oscillations and invoked porous oxide formation as part of the oscillating mechanism, but remained qualitative and did not offer new insights.

All of these models strive to explain all of the observed oscillatory behavior of the Si electrode in a HF based electrolyte. However, most models are essentially restricted to current oscillations. While it may appear that a model that "explains" current oscillations will automatically also explain potential oscillations, this is not really the case - potential oscillations need more ingredients than just a working current oscillation model. Moreover, there are many blatant or subtle contradictions between the models proposed, e.g., some authors insist that only damped oscillations exist, while others claim that they have found stable oscillations

for reasonably long times. While most models are purely qualitative, even most of the more quantitative models remain at a theoretical level without reproducing measured results, the only exceptions are found in [46, 47] and the related papers.

The general lack of detailed microscopic (actually nanoscopic) mechanisms that produce micro oscillators and some degree of synchronization in most models more or less automatically preclude the generalization of these models to other aspects of semiconductor electrochemistry, most noteworthy current oscillations in space otherwise known as self-ordered pore arrays [52]. There is a deep connection between the formation of self-ordered pore arrays (cf. e.g., the papers on pore single crystals in InP [53] or GaP [54]) as an expression of synchronized current oscillations in space, or "noisy" arrangements of pores with a strongly prevalent spatial frequency (= average distance), and the same phenomena in time as discussed here. Obviously, "current or potential in time oscillation" models with at least a clear option of generalization to "current or potential in space oscillation" would be of interest.

In 1998 the "current burst model" (CBM) was cursorily published [18]; it is the base of the work on the CBM simulations. The CBM was the first fully quantitative model that predicted many features of experimentally observed current oscillations [55] in a "bottom-up" way by simulating electrode reactions with a Monte-Carlo approach on a nm scale.

2.4.1 General remarks

In order to emphasize the quintessence of the current burst model (CBM) we will begin with the (by now mostly accepted) "axiom" or fundamental assumption that the current through a Si electrode is neither homogeneous in space, nor in time. Considering that Si dissolution in general involves at least three reactions (current-driven direct dissolution and oxide formation; purely chemical oxide dissolution), which in a strict sense cannot take place at exactly the same place at exactly the same time, this is a logical necessity. Of course, on slightly larger space and time scales the reactions involved could average to a smooth behavior describable by differential equations, but here we will argue that at least in the oscillatory regime of the current (I) - potential (V) characteristics this is not the case. The postulated inhomogeneity in space and time follows rather directly from the following set of assumptions, which constitute the essentials for the application of the current burst model to electrode oscillations in time:

1. The electrode is completely covered with a (thin) oxide having some (non-uniform) thickness distribution at all times.
2. Charge transfer from the Si to the electrolyte is localized in space and time; a single localized charge transfer process is called a current burst (CB). Its initiation or nucleation occurs with a certain probability $W(E(r))$ at some point (or better pixel with a typical

dimension of $(1.5 \times 1.5) \text{ nm}^2$) at the position r as a function of the local field strength $E(r)$. The probability $W(E)$ increases for increasing field strength or decreasing local oxide thickness $s(r)$. Note that the vector properties of E and r are of no consequence in this context and we will drop the bold font in what follows.

3. The total charge transferred in a CB produces only oxide in the form of an "oxide bump". The lateral extension of this oxide bump is assumed to be comparable to its thickness. In the simplest approximation the total oxide produced is contained in a sphere.
4. Local current flows only during the "on" phase of a CB, and the local oxide thickness increases accordingly. The local field strength thus decreases, and current flow will stop with a certain probability $R(E(r))$; *i.e.* the CB is turned "off". The field strength required for turning a CB off is generally lower than for turning it on; meaning that there is a certain hysteresis in the process. Local current flow in a CB thus lasts for a certain average time t_{CB} defined by the parameters of the system, and in particular by the two probability functions $W(E)$ and $R(E)$.
5. The locally produced oxide dissolves continuously in the HF, the field strength increases, and the process cycle starts again. The oxide dissolution will take place for some average time t_{dis} , after which a new CB and thus a new local cycle will start. The sum of both times defines the time constant or lifetime $\tau_{CB} = t_{CB} + t_{dis}$ of a CB (which is, of course, a property only meaningful as an average quantity for many CBs). It is important to note that the CBM thus introduces intrinsic time constants into the otherwise static electrochemical system Si/HF.

It is clear that within these assumptions any current flowing through oxides lacking perfect thickness uniformity will be automatically localized in space, *i.e.* will only be initiated in regions where the oxide thickness happens to be small enough. Since the oxide thickness in any given pixel is fluctuating - it decreases because the oxide dissolves in HF and increases because of anodic oxidation during current flow - the current in a given pixel will be "on" or "off" in some characteristic yet stochastic pattern in time, and therefore will also be localized in time.

Individual CBs may and will differ in their size, duration, total charge transferred, etc., but for what follows it will be sufficient to consider just averages, *i.e.* treat all CBs as identical. The sum of all individual CBs active at any given time then defines the total current flowing through the electrode at this instant.

If current bursts just happen at a purely random fashion, *i.e.* an individual current burst is not correlated at all to other CBs, the density of CBs in space and time will average to constant

values, and on a macroscopic scale a constant current leading to electropolishing is observed. However, as will be shown in what follows, if there are some interactions between individual next-neighbor CBs correlations may result that lead to oscillations of the CB density in time, in space, or in both. The macroscopic counterparts of these correlations are current oscillations in time, pores (= current oscillations in space), or both. Interactions between neighboring CBs may happen in two extremes: interaction in space, *i.e.* the probability for nucleating a CB at r is influenced somehow by what is going on in the neighborhood, or interaction in time, *i.e.* the probability for nucleating a CB at r at the time t is influenced somehow by what has happened at r before. In what follows we will enlarge on this, but it is helpful to keep in mind that the CB model intrinsically predicts oscillations and pore formation if there are interaction mechanisms leading to correlations between CBs. This is not to say, however, that *all* oscillatory phenomena and *all* pores are *only* due to CBs interactions.

The focus of the work is on the oscillations in time, and for that it is enough to have some interaction between neighboring CBs [52]. The necessary mechanism for this interaction is an intrinsic part of the CBM, already contained in the set of assumptions given before, and easy to conceive as will be shown below.

2.4.2 Implementation of the CBM in a Monte Carlo simulation tool

It remains to cast the current burst model into a form accessible for calculations. The mathematical tool chosen is a Monte Carlo simulation, and in the rest of this section the basic formalism necessary to implement the algorithms will be introduced and discussed to some extent.

First, we consider only very low HF concentrations and p-type Si for the sake of simplicity. In this case the oxide layer always covering the electrode has a thickness s that is smaller than about 10 nm at all times (avoiding possible effects due to mechanical stress), but still large enough at all times to avoid noticeable electron tunneling effects (not producing oxide). Any external potential or anodization potential U_{an} to the electrode (corresponding to the potential measured in actual experiments between the sense electrode and the reference electrode) then will drop across this SiO₂ layer (and to some extent in the adjacent electrolyte). The basic assumptions of the CBM as implemented in a Monte Carlo program then can be formulated as follows: the electric field strength $E(r_p)$ across the oxide film at a pixel with an area $A_p = (1.5 \times 1.5) \text{ nm}^2$ at $r_p =$ pixel number or coordinate is given by

$$E(r_p) = \frac{U_{an}}{s(r_p)} \quad (2.12)$$

An "ionic" breakdown event will occur in that pixel with a certain probability $W(r_p)$, forming a "channel" through the oxide layer and driving oxygen ions towards the Si/SiO₂ interface where they will be consumed in the chemical reaction that results in SiO₂. While it may appear a bit simplistic to calculate the electric field strength via Eq. 2.12, considering that the oxide thickness is not constant, this approach is nevertheless justified in retrospect because the system tends to behave rather homogeneously, *i.e.* the oxide roughness is sufficiently small on a scale comparable to its thickness.

The probability function $W(r_p)$, and $R(r_p)$ for the reverse effect, are the only critical inputs into the CBM. They are derived as follows: below a certain critical minimum thickness of the oxide s_{min} (or above a certain critical field strength E_{max}) the probability for starting a CB is 1. For field strengths below E_{max} , $W(E)$ decreases to zero within some interval ΔE_{max} as shown in Fig. 2.9. For $R(E)$ similar considerations apply, with a minimum field strength E_{min} necessary to stop a CB with probability 1. The use of probability functions

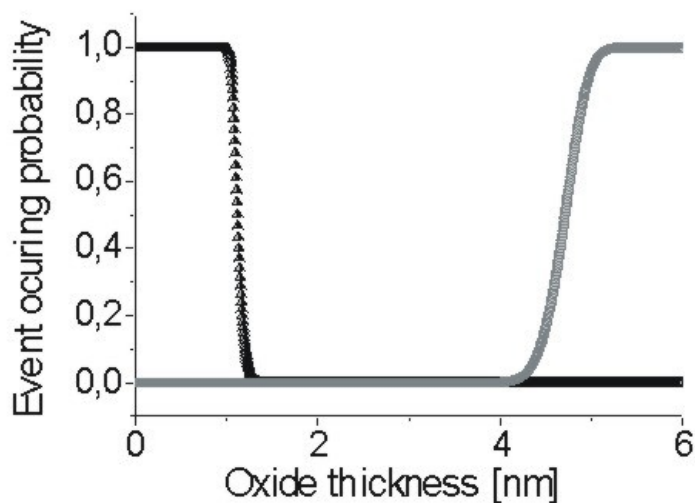


Figure 2.9: Graphical representation of two examples for the probability functions for turning a current burst on (triangles) or off (squares), respectively.

is necessary because electrical breakdown events always have a stochastic character for many possible reasons. The most important one is that the critical field strengths for breakdown events of any kind are always tied to the local oxide "quality", a parameter hard to define structurally, but nevertheless existent and of prime importance, e.g. in microelectronics.

The probabilities $W(E)$ and $R(E)$ for the nucleation or closing of a CB, respectively, are

defined as follows:

$$W(E) = \begin{cases} \exp - \left(\frac{E_{max}-E}{\Delta E_{max}} \right)^2 & \text{for } E \leq E_{max} \\ 1 & \text{for } E > E_{max} \end{cases} \quad (2.13)$$

$$R(E) = \begin{cases} \exp - \left(\frac{E-E_{min}}{\Delta E_{min}} \right)^2 & \text{for } E \geq E_{min} \\ 1 & \text{for } E < E_{min} \end{cases} \quad (2.14)$$

The task thus is to find reasonable values for E_{max} and E_{min} together with reasonable values of the ΔE 's. Since breakdown of "electronic" SiO₂ is a very well known effect, occurring at field strengths around roughly 10 MV/cm in "good" thermal oxides, this gives a first order-of-magnitude for the critical field strength values. Moreover, since it is quite likely that the ionic breakdown postulated here is a consequence of an electronic breakdown damaging the oxide and inducing ionic breakdown, this value even suggests itself. While the kind of ionic breakdown suggested here might be a novelty, it is not a really new, because it is well known (and has been recently demonstrated again [56]) that current flow does occur through oxide layers with finite thicknesses.

The four constants E_{max} , ΔE_{max} , E_{min} , ΔE_{min} in the probability function are the main parameters of the CBM, they simply reflect the uniformity and quality of the oxide. A representative graph of the probability functions as used for most of the simulations (vs. oxide thickness s instead of E) is shown in Fig. 2.9

For an ideal oxide the graphs should be step functions; and it is of course possible to run the simulations for this case, too. However, oscillations in certain cases are not possible if the probability functions are too "hard"; and the slope at $W(E) = 1/2$ must be seen as an important system parameter. Formally, at least three numbers (for symmetric probability functions) are needed, which refer indirectly to oxide properties.

Numerous authors claim the existence of two types of oxide: oxide and "suboxide", soft and hard oxide, flat and rough oxide, etc. At this point we may take that as an indication that one number is deemed not to be sufficient for describing all oxide properties, and that the approach taken here is sound. For our model we chose $E_{max} = 3.5 \times 10^7$ V/cm and $E_{min} = 5 \times 10^7$ V/cm for all simulations if not stated otherwise. These values resulted from a comparison of many simulations to experiments [18] and are in the general range known from electrical breakdown of thin oxide films [57]. The ΔE values defining the slope are variables, but generally are found between 0.1 and 0.2 V/nm depending on the system (or oscillation type) to be modelled.

It is worthwhile to point out that this part of the CBM is fully compatible with a well-known and powerful tool in, e.g., fracture mechanics, known as weakest-link theory or simply

as Weibull statistics [58].

After the CB nucleation, the local oxide thickness will increase in the pixel where the nucleation took place, but also in neighbouring pixels. The growing oxide bump has some lateral extension either due to oxygen diffusion in the Si-SiO₂ interface, to some lateral movements of the breakdown channel (akin to the "dancing" of microflashes below an electrode), or to both. The total amount of oxide produced is directly given by the total amount of charge transferred in a CB on average - and vice versa. Assuming a spherical geometry of the oxide bump, which suggests itself because it follows the equipotential lines and thus constant field strength lines of the system as shown in Fig. 2.10, the average amount of charge Q_{CB} transferred in a CB is given, and so is the average current $I_{CB} = Q_{CB}/\tau_{CB}$ and current density $j_{CB} = Q_{CB}/A_p\tau_{CB}$ (referred to the area A_p of one pixel) of a CB with respect to the average cycle time $\tau_{CB} = t_{CB} + t_{dis}$.

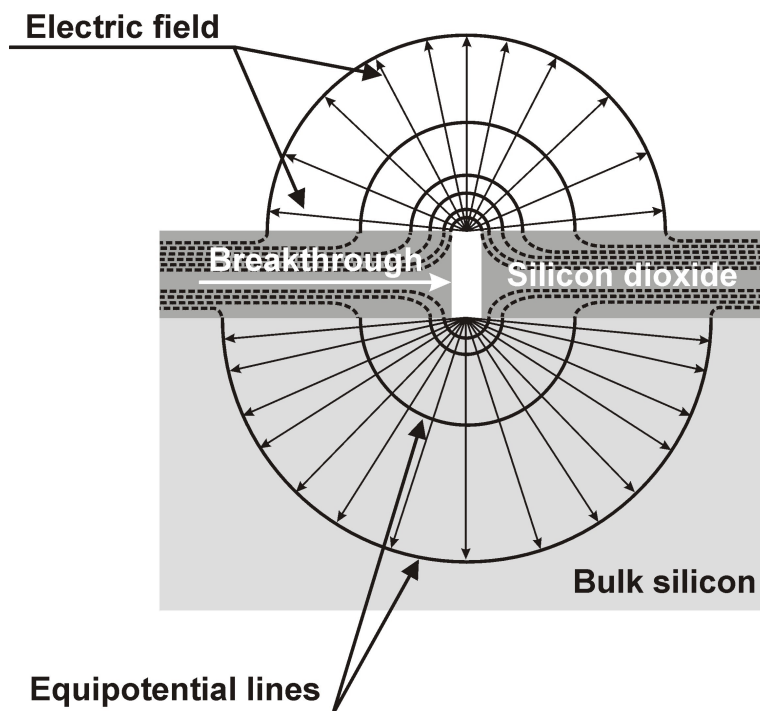


Figure 2.10: Schematic drawing of the electrical field lines and the equipotential planes around a current burst imagined as an ion-conducting channel in the oxide layer.

However, for the Monte Carlo simulation only the current density j_a for the active phase of the CB is needed, and that value is not easily obtained, since τ_{CB} in our case of low HF concentration is dominated by the time t_{dis} it takes to dissolve the oxide again. This is a direct consequence of the CBM: since the current density in a CB is by definition far larger than the macroscopic current density, and since the over-all oxide production from the macroscopic current density must be equal to the over-all oxide dissolution in all cases where the average

oxide thickness stays constant, the oxide dissolution time or "off" time t_{dis} of a CB must exceed the oxide production time or "on" time τ_{CB} by far. Computing τ_{CB} and then j_a from the known total cycle time, while possible in principle, therefore will not give good values, and an independent way of arriving at j_a is needed. In [18] a value for the current $I_a = 0.1$ fA and not for the current density of a CB has been introduced, based on independent experimental observation and since this value gave good results, it will be used throughout. While I_a or j_a is in principle determined by known system parameters, it must be seen as approximation in the CBM and therefore to some extent as a fit parameter.

After some oxide has been grown in the active phase of a CB, it will dissolve purely chemically with an effective dissolution rate α that depends on the "trivial" parameters HF concentration, pH, temperature, roughness of the oxide surface, and "oxide quality". It is thus impossible to find one precise value of α for the system under investigation, but in a sufficiently close approximation α is known well enough. Here we take a value of 0.04 nm/s for the conditions specified. Note that the effective dissolution rate depends on the oxide roughness, rough oxides dissolve faster than smooth ones for the same nominal dissolution rate α . This effect is implemented in the program: by interpolating the effective area between three node points or pixels with different oxide thicknesses, a net or effective dissolution rate automatically results. This effective dissolution rate thus depends on the oxide roughness; it is generally larger than the nominal rate, and it oscillates parallel to the oxide roughness oscillations.

Whatever the precise shape of the oxide bump will be, and however long it takes to produce it, the electric field during its growth decreases at most until the lower limit $E_{min} = U_{an}/s_{max}$ defined above has been reached and the CB has been turned off with a probability of 1.

By now quantitative relationships for a "micro-oscillator" or CB have been defined, the first needed ingredient for any oscillation model. It was claimed already that the second necessary ingredient, a synchronization mechanism, is an intrinsic part of the CBM and thus needs not to be added to the CBM. There is, however, a third ingredient that has not been discussed so far but is also present: de-synchronization or negative feed-back, *i.e.* a mechanism that tends to destroy correlations between CBs. While this may appear counterintuitive, it is known from general considerations of pattern formation including oscillations that a de-synchronization mechanism is often needed if self-organized structures with a certain complexity are to evolve from stochastic processes [59]. Only the interplay of synchronization and de-synchronization (also called positive and negative feedback) tends to produce complex patterns; synchronization alone would either produce fully expressed oscillations or none at all. As will be shown, de-synchronization is also an intrinsic feature of the CBM that only needs to be noticed, but then must be implemented in the Monte Carlo program.

We will now discuss the mechanisms of synchronization and de-synchronization in more

detail, because they apply not only to the simulation of oscillations, but also to more general simulations of stochastic processes on Si electrodes.

A synchronization mechanism is any interaction that leads to some synchronization of the "on" or "off" state of (neighbouring) CBs. It expresses itself by strengthening the oscillations produced in the model; de-synchronization, contrariwise, is the term used for effects that tend to damp those oscillations. Obviously, local current oscillations with random "on" times (and "off" times then t_{CB} seconds later), or *random phases* in more conventional albeit not strictly precise terms, will not lead to macroscopic oscillations, but to a constant current. The term "oscillation" in this context does not imply a well-defined sinusoidal time dependence of the current but more generally any (stochastic) current (or potential) variation where an average frequency, amplitude and phase can be defined in a meaningful way. CBs in some defined area will give exactly that behaviour; a CB thus is nothing but a local current oscillator.

Macroscopic oscillations thus demand some degree of synchronization, *i.e.* a not too small fraction of the CBs present in a given time interval must be "in-phase" or at least phase correlated to some extent, *i.e.* starting and stopping within a not too large time interval. Again, no "perfect" synchronization is needed, and whatever synchronization there is must not necessarily occur on the whole sample surface in order to produce macroscopic oscillations. It is entirely possible that some degree of synchronization only occurs in areas of finite size, which are called domains. The average size of such domains introduces an intrinsic length scale l_{Do} into the system, and strong macroscopic oscillations will only be observed if l_{Do} is in the order of the specimen size. At this point the definition of a domain agrees with those given before, in particular by Ozanam et al. [44], since areas with constant oxide thickness within the CBM are more or less "automatically" also areas with phase-correlated currents. Note, however, that the older concepts of domains need to be enlarged upon later on.

One might distinguish two basically different synchronization mechanisms: indirect (static) synchronization resulting from fixed system conditions, and direct (dynamic) synchronization, resulting from the processes themselves by some form of interaction. The most trivial example for indirect synchronization is a perfectly homogeneous system: if all conditions everywhere on the sample are exactly the same at the beginning of the experiment, exactly the same will happen everywhere at any instance in time. What one CB does, is what all do. Just having local oscillators then would produce oscillations. However, if the underlying micro-oscillators have a stochastic component (e.g. the probability functions $W(E)$ and $R(E)$ for CBs), those oscillations would be damped with a time constant intrinsic to the stochastics of the micro-oscillators. Moreover, in real experiments local conditions like e.g. electrolyte flow are never exactly the same; this also tends to destroy any initial static synchronization. We will therefore not consider static synchronization anymore. In order to exclude the transient

effects of static synchronization, all Monte-Carlo runs are started with a random distribution of the oxide thickness (which is not the same as random phases of CBs at the starting point, however).

Dynamic synchronization is far more powerful, and already contained in the CBM, as outlined before. It results in an easily understandable fashion from the overlap of oxide bumps of neighbouring CBs as illustrated in Fig. 2.11a.

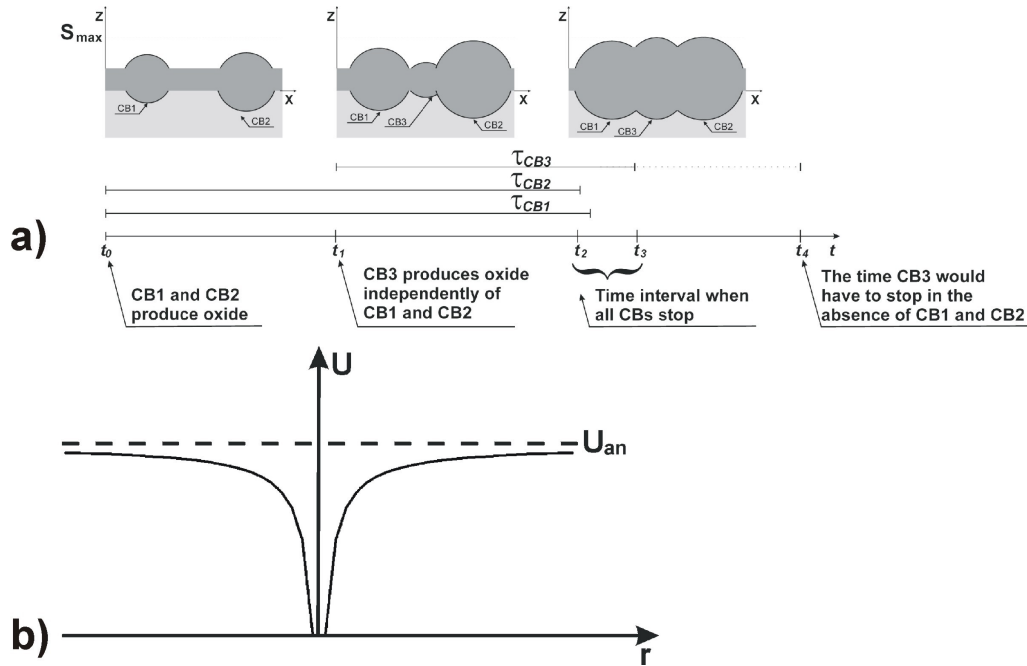


Figure 2.11: Schematic representation of the synchronization (a) and desynchronization (b) mechanisms contained in the CBM. In a) it can be seen that the "switching-off" time of current burst CB3 is correlated to those of CB1 and CB2. b) shows schematically the voltage losses around an active CB, decreasing the nucleation probability of new CBs in the neighbourhood.

The highly schematic picture shows what happens if a CB forms between the oxide bumps of its neighbours-to-be. Even if the time for its nucleation is independent from that of its neighbours, it will clearly switch off earlier than it would have done without the oxide bumps of the neighbours, since it does not have to produce as much oxide for this as an isolated CB. In formal language, its switching-off time is now correlated to what is going on in its neighbourhood. If this correlation is strong enough, stable oscillations will result [52].

Note that while the oxide grows essentially into the depth of the Si in the form of a semi-sphere, the concomitant volume expansion by a factor of two automatically produces a spherical shape and at the same time a certain roughness of the interface and the oxide surface. While the purely chemical oxide dissolution will smooth the oxide *surface*, the Si - SiO₂ *interface* retains its roughness in the quiescent phase of the oscillations, and the CBM, if correct,

must automatically produce the correct (= measured) roughness values without any further adjustments. It is not necessary to incorporate this interaction into the Monte Carlo model - it will evolve by itself since everything needed is already in place. In this context it is important to realize that this correlation *per se* does not depend on the exact shape of the oxide bump; we thus chose the simplest shape, a sphere.

It is not clear at this point that this next neighbour interaction is sufficient to produce large-scale synchronization, but as has been shown before and will be shown here, it will be a sufficient condition if the CB density is large enough to overcome some percolation threshold. It is also important to note here that within the CBM a "non-oscillating" electrode doesn't imply the absence of CBs but rather the absence of synchronization between the CBs. Contrariwise, an oscillating electrode of some kind does not imply that its properties can be explained by some CBM since there are many oscillating electrochemical systems where it is quite likely that other mechanisms are the decisive factors, e.g. mechanical stress [50] or gas evolution; cf. also the excellent review [59] for a general view at oscillations.

As stated before, the CBM also contains an intrinsic de-synchronization mechanism. However, contrary to the synchronization mechanisms, de-synchronization must be coded into the algorithm. The de-synchronisation mechanism is based on the fact that the current density around an active CB is very large and localized, and this will lead to a decrease in the anodization potential across the oxide layer; a simple model for this, employing (nearly) hemispherical symmetry, is illustrated Fig. 2.11b. The current density $j(r)$ in the electrolyte "on top" of an active CB then decreases $\propto r^{-2}$ and the electric field lines in cross-section will show a cylindrical geometry as schematically shown in Fig. 2.10. This determines the form of the newly growing oxide as outlined before and favours the spherical shape of the bumps. The potential decrease in the vicinity of an active CB leads to a decrease in the electric field strength in its neighbourhood (it may be even zero), which in turn decreases the life time t_{CB} of already existing CBs and decreases the probability for the nucleation of a new CB. This effect tends to destroy correlations (CBs tend to be "loners") and thus leads to de-synchronisation.

For a quantitative evaluation we consider that the current I_a flowing during the active phase of a CB through any equipotential surface at distance r from the CB is by definition $I_a = I_{CB} \times t_{dis}/t_{CB} = j_a \times A_p/\pi d^2$. With:

$$j_a(r) = \sigma \times E(r) \tag{2.15}$$

and σ = conductivity of the electrolyte, one can define the potential loss on the sample surface

at a distance r from an active CB as:

$$U = \int_0^r E(r)dr = \int_0^r \frac{I_{CB}}{\sigma\pi r^2} = -\frac{I_{CB}}{\sigma\pi r} \quad (2.16)$$

The potential loss ΔU_{an} in the electrolyte is thus approximately given by the relation:

$$\Delta U_{an} = -\frac{B}{r} \quad (2.17)$$

with $B = I_{CB}/\sigma\pi$ being some experimental constant that can be in principle determined. However, as in the case of the current density in the active phase of a CB, B is to some extent an adjustable parameter. In our case we found that a value for B of $0.2 \text{ V} \times \text{nm}$ (corresponding to the approximate electrolyte conductivity σ of about $5 \times 10^{-4} \text{ Scm}^{-1}$) was best suited for the qualitative and quantitative reproduction of the experimental results. In principle, effects like the Nernst potential, caused by strong concentration gradients of the oxidative species due to a high current through the open channel of the CB, should also be considered, but are neglected for the time being.

Of course, the simple $1/r$ dependence of the potential loss ΔU_{an} leads to arbitrarily large potential losses for $r \rightarrow 0$, which make no sense as soon as $|\Delta U_{an}| > U_{an}$. This problem is remedied by setting $\Delta U_{an} = -U_{an}$ in all pixels where the calculated ΔU_{an} is larger than the actual potential U_{an} , *i.e.* zero field strength conditions are assumed. Nevertheless, in potential loss maps, the calculated ΔU_{an} is displayed because it gives a better representation of the system dynamics and in particular because it is a direct measure of the number of active CBs. In a physical interpretation, areas with $\Delta U_{an} > U_{an}$ in potential loss maps denote diffusion limitation of the current - the potential needed to drive the actual current is larger than the potential available. In other words, the cluster of CBs that would drive ΔU_{an} into unphysical values cannot draw a total current equal to the sum of the standard CB current.

With the data and relations given at this point, almost all ingredients for a Monte Carlo program capable of simulating current flow through a Si electrode held at constant potential in the oscillation regime have been described in sufficient detail to emulate the results given in the next paragraphs. Only for galvanostatic experiments a somewhat more sophisticated approach is needed (e.g. how to keep the potential constant or how to deal with charging / discharging the oxide capacitor), which will be described later.

2.4.3 Basic results and interpretation of simulations with the CBM

The software allows for *in-situ* maps (*i.e.* while the program runs) of the morphology of the SiO_2/HF and SiO_2/Si interface, as well as for calculations of the local oxide thickness, potential

losses and other parameters. This information is displayed (and stored in the memory of the PC) in the form of maps accompanied by histograms as illustrated in Fig. 2.12a. With a certain periodicity (usually every 20 ms) the content of these maps is updated (the "time frame" for an individual calculation is 5 ms); from all the data the dynamics of the system can be retraced and displayed as a "movie". This is quite instructive. The cycle time used for updating the content of the maps, and hence the information about the state of the system, can be decreased if necessary, but this will result in longer simulation times, and a compromise between the information quantity and quality must always be found. The results of one simulation run with one set of input parameters provide the following primary and secondary entities, usually plotted as colour coded maps with histograms for full quantization:

- Macroscopic current density $j_{an}(t)$ (or potential $U_{an}(t)$) in all modes (from strong stable oscillations to constant values) as a function of the major conditions like constant (or modulated) potential or current, HF concentration and temperature.
- Oxide thickness maps as a function of time. From this, secondary oxide characteristics can be obtained, e.g.
 - Capacity of the SiO₂ layer (with Helmholtz layer and SCR capacity usually neglected).
 - Roughness of the oxide thickness as a function of time.
 - Roughness of the of the SiO₂ surface as a function of time.
 - Roughness of the Si - SiO₂ interface as a function of time.
 - Correction factors for converting globally measured capacitances (proportional to $1/ \langle s \rangle$) to the real capacitance (proportional to $\langle 1/s \rangle$).
 - Autocorrelation functions with regard to the oxide thickness, which in turn allows to extract certain correlation lengths l and sizes of correlated areas F
- Special maps indicating e.g. the potential losses on the electrode surface. Those maps allow to obtain the number of active CBs because potential drops are additive.
- Capacitive currents or potential drops in global series resistors as a function of time.
- Additional parameters as a function of time, e.g. the number of CBs nucleated or extinguished in a given time interval.

From a sequence of simulation runs with systematically varied parameters (e.g. potential, current, temperature, electrolyte concentration, serial resistance), the following information can be quantitatively deduced as a function of the variable chosen:

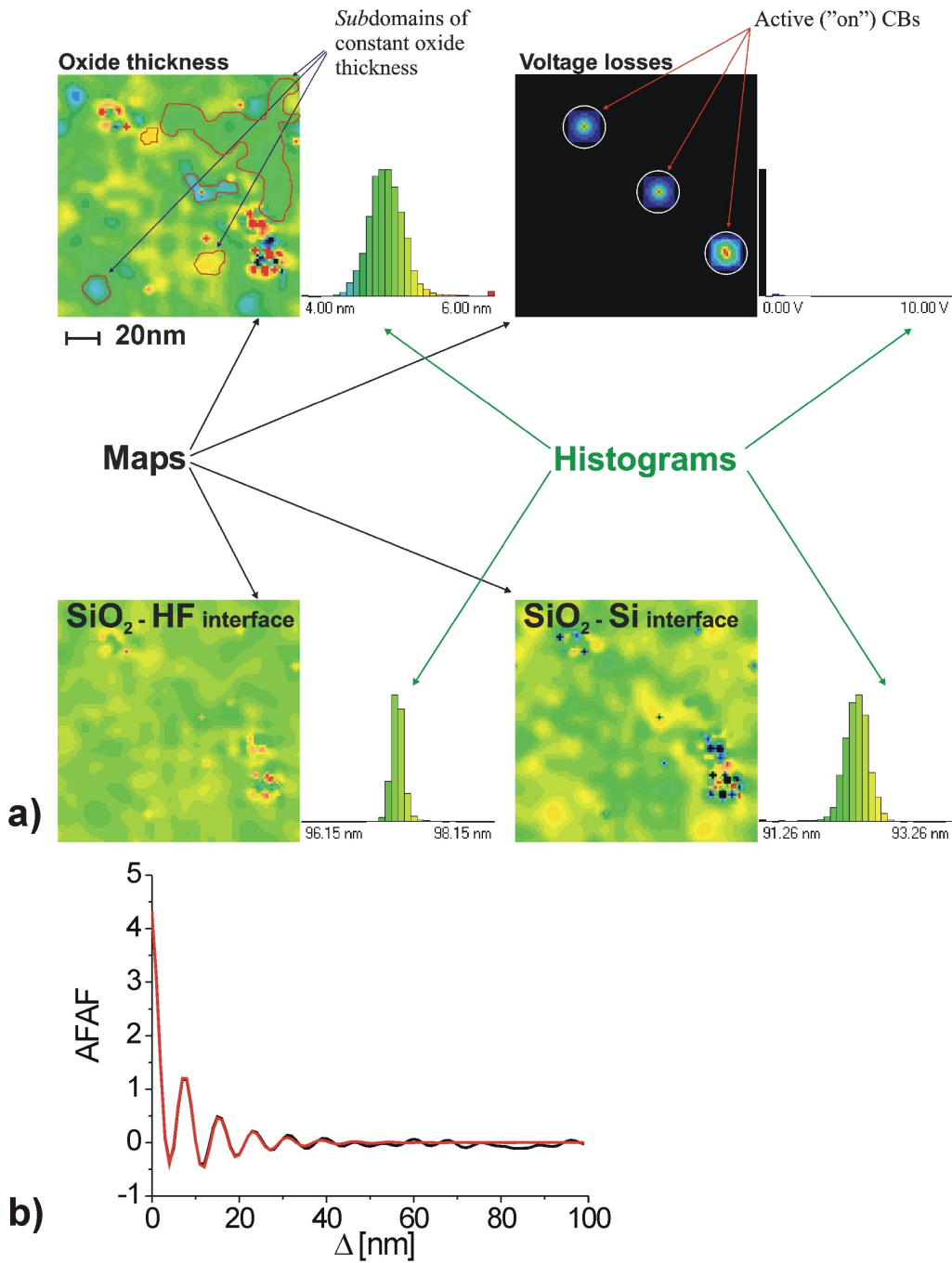


Figure 2.12: Examples of maps generated for one time frame in a simulation run (a). On the oxide thickness map some "smooth" subdomains are schematically indicated. The mottled areas can also be considered to be subdomains. The voltage loss map in this case shows directly the location of active CBs as indicated. For each calculated oxide thickness map the average free autocorrelation function (AFAF) is calculated (black curve) and subsequently fitted (red curve) (b).

- General shape (e.g. *sin*, *saw tooth*, etc.), amplitude and frequency of oscillations.
- Decay constant of damped oscillations.
- General *IV* characteristics for the range of the potential where the basic limitations still apply (e.g. closed oxide).
- Correlation lengths.
- Mean oxide thickness, capacitance, and roughness.

Figure 2.12a illustrates the possibilities of the model with respect to maps. It shows four (especially "simple") representative maps generated at the minimum of strong stable current oscillations (similar to the ones shown in e.g. Fig. 5.1). By definition, pretty much the whole area of the sample then must be one domain, *i.e.* all of the current flowing locally has (about) the same phase. However, looking at the picture, it is clear that the postulated domain has an internal structure with respect to the oxide thickness, the interfaces and the potential losses, and that the current flowing is strongly localized in the three active areas shown in the potential loss map.

At this point it is necessary to make clear what is meant by "phase" with respect to CBs and as applied to the phase of the current or better the (oscillating) resistance regulating the current flow in a domain, since current flow in the CBM model is inherently inhomogeneous in time and space. For this, the total time or "lifetime" τ_{CB} of a CB defines the phase scale: a phase of 360° then corresponds to τ_{CB} , and most of this time the CB is "off", as pointed out before. This definition allows to assign phases to electrode areas where temporarily no current is flowing and thus provides a link to the old (and somewhat naïve) picture of domains, where a domain was defined as an area where the (spatially uniform) current has (about) the same phase and magnitude everywhere. Note also, that this definition correlates the oxide thickness to the phase, albeit in a somewhat indirect way. Moreover, defining phases relative to CBs, makes immediately clear that there must be a considerable spread of CB phases in a domain because otherwise the macroscopic current resulting from synchronized CBs would consist of sharp pulses with the frequency $1/\tau_{CB}$. The half-width of a current peak in $j_{an}(t)$ is therefore a direct measure of the strength of the synchronization. In what follows, phases are always defined as CB phases.

In principle, this definition would allow to generate maps of the local current magnitude and phase by a Hilbert transformation of the temporal-spatial resistance distribution; and those maps would show the domains more directly than the maps provided so far. However, since t_{CB} is an average property and thus not well defined for a single CB, this is not a trivial task and the necessary routines have not yet been implemented.

For lack of a better term, and to facilitate the description of the results of a simulation run, the structures visible within the sample-size domain in Fig. 2.12 will be called subdomains; as it will turn out, there are characteristic features associated with these subdomains outlined in the picture. We will now address the question of what exactly constitutes a domain and how domains develop in time. This has not been discussed in detail in any previous publication, and we will now give a detailed description of what constitutes a domain based on our results:

1. Domains may be multiply connected and frazzled-looking with no obvious boundaries in the maps provided. The boundary, as e.g. in the case of magnetic domains, is a continuous transition from one phase to another one or to random phases.
2. Actual current flow within one domain is spatially rather inhomogeneous and concentrated in "active" areas (visible especially well in the potential loss maps). However, with the phase definition from above, the (CB) phase within a domain is still about the same.
3. While the current in a domain does oscillate in time, the necessary changes of the size and location of the active (and by default passive) areas produce rather non-uniform sub-structures = sub-domains within the domain.
4. Other parameters, like the oxide thickness, show pronounced structures within a domain, too.
5. While there is a meaningful linear size obtainable from the maps (the correlation length of synchronization), it is not necessarily coupled to the domain area size.

The domains described in this way can do everything the simple "classic" domains can do, but avoid many conceptual difficulties that would arise with the more naïve picture. The domains defined here thus are closer to reality, but not as easily visualized as "classical" domains.

Looking at the subdomains in Fig. 2.12 one realizes that they consist mostly of areas where current flow is (and recently was) concentrated ("active" subdomains), and areas where oxide dissolution dominates ("passive" subdomains). The first kind, by the very nature of CBs, produces rough structures (varicoloured or mottled areas); the latter results in quite smooth parts (unicolour). Besides quite different appearances, all subdomains have about the same phase (as defined above) and wander around within the large domain, producing well-defined average properties of the large domain at all times.

In other words, the internal structure of a domain that determines how a domain changes its phase with time is far better visible than the domain itself - and far more interesting!

Some features of subdomains can be assessed by routines described later, most prominently the size of subdomains as expressed in correlation lengths. In Fig. 2.12 some such correlation lengths are indicated, they will be discussed in detail in Sec. 5.5

2.4.4 Calculation of secondary quantities

The most important quantity that is calculated in the simulation program at each time instance is the local oxide thickness. This value can be used to calculate secondary measurable quantities of the system and to observe their dynamics. Supposing that $D(s)$ is the fraction of the surface covered with an oxide of thickness s , the mean oxide thickness $\langle s \rangle$ then is

$$\langle s \rangle = \int s D(s) ds \quad (2.18)$$

and the integration runs always over the whole area. Another important electrode parameter is the roughness Y of the oxide, which has been (indirectly) determined in some experiments by measuring the capacitance $C(t)$ of the system based on in-situ ellipsometry [60, 61] (and references therein). Y is calculated according to

$$Y = \int |s - \langle s \rangle| D(s) ds \quad (2.19)$$

The capacitance C of the oxide layer; easily measured, is practically completely given by the oxide thickness (distribution) and the mean dielectric constant of the oxide via

$$C = \epsilon \epsilon_0 \int \frac{1}{s} D(s) ds = \epsilon \epsilon_0 \left\langle \frac{1}{s} \right\rangle \quad (2.20)$$

with ϵ = dielectric constant of the oxide and ϵ_0 = electric susceptibility of vacuum. Of course, the roughness of the oxide - electrolyte interface and the roughness of the oxide - Si interface can be calculated, too. The latter is quite similar to the total oxide roughness given above. While the roughness of the Si - SiO₂ interface is not (yet) measurable, some quite revealing in-situ measurements of the SiO₂ surface have been made; however on a scale considerably coarser than the one given here [60].

Some quantitative comparisons of experimental findings and results of CBM have been made before [62], the agreements were not only rather perfect but showed that the interpretation of capacitance measurements in terms of a "two oxide" model given in [49] were based on equating the proper average $\langle 1/s \rangle$ with $1/\langle s \rangle$, which is not correct for the roughness actually observed or calculated with the CBM.

The various maps generated by the CBM contain far more information than can be captured

by calculating averages over map parameters. A first attempt has been made to extract some quantitative information about the spatial structure of mapped quantities, in particular for the oxide thickness maps, by using autocorrelation methods. The so-called "average free autocorrelation function" (*AFAF*) was calculated for all oxide maps obtained. The *AFAF* is defined as:

$$AFAF(\Delta) = \frac{1}{L} \int_0^L [s(x) - \langle s \rangle] [s(x + \Delta) - \langle s \rangle] dx \quad (2.21)$$

where Δ is a spatial displacement between two points on the electrode, L is the lateral size of the simulated electrode (*i.e.* 300 nm in our case), $\langle s \rangle$ is the average value of the function $s(x)$, *i.e.* the mean oxide thickness, and x is a space coordinate (*i.e.* on the oxide map in our case).

For this class of problems, *i.e.* for the determination of correlation lengths for some patterns, it is common to use the standard autocorrelation function (*ACF*). However, in our case the average oxide thickness changes between time frames, and these changes are comparable to the thickness changes in the subdomains. The *ACF* is therefore not the best tool for this purpose. It is advantageous to resort to the average free autocorrelation function (*AFAF*) as defined in eq. 2.21. The *AFAF* essentially measures the average magnitude of the correlation of two points separated in space by a distance ; *i.e.* the probability of finding the same oxide thickness at this distance. From the data obtained correlation lengths can be extracted that provide information about the dynamical behaviour of subdomains over time, *i.e.* the changes in areas primarily growing or dissolving oxides.

The *AFAF* is "easily" calculated, *i.e.* it does not take much processing time. But since it is still a function and not a number, it is still not sufficient for plotting relevant parameters as a function of time. In order to do this, the calculated *AFAF*s need to be fitted with a suitable function that contains correlation lengths as desired parameters. The best fitting function for this purpose is defined as

$$f(x) = A(t) \cos [k(t)x - \varphi(t)] \exp\left(-\frac{x}{\Psi(t)}\right) + B(t) \exp\left(-\frac{x}{\chi(t)}\right) + O(t) \quad (2.22)$$

where $A(t)$, $B(t)$, $k(t)$, $\varphi(t)$, $\Psi(t)$, $\chi(t)$, $O(t)$ are the fitting parameters. The first term in the sum contains a cosine function, which, being periodic in space and time, attempts to describe the oxide roughness found in the active subdomains producing growing oxide. The correlation length, *i.e.* the average size of these subdomains is given by $\Psi(t)$. The second term describes the "smooth" subdomains where oxide dissolution takes place; its correlation length is given by $\chi(t)$.

The correlation lengths $\Psi(t)$ and $\chi(t)$ thus give the average length over which subdomains extend. The parameters $A(t)$, $B(t)$ have a more complex nature. While they include the surface

fractions of growing and dissolving subdomains, respectively, they might also include a measure for the oscillation amplitude. However it is rather difficult to quantify these parameters separately, which in turn makes it difficult to give a full interpretation of $A(t)$ and $B(t)$. Later in the text, these parameters will be referred to as "surface fractions" only, but are not used in any depth for the interpretation of the results. The parameter $k(t)$ contains information about the roughness in the growing subdomain. The parameters $\varphi(t)$, $O(t)$, which describe a certain phase lag and an offset, seem to have no particular significance but are simply needed for a better fit.

While it is legitimate to have some doubts about the usefulness of describing a "picture" by 7 fit parameters, the procedure does make some sense; note that for one simulation run some of the information contained in several thousand maps can now be condensed into the time behaviour of these 7 parameters. The snapshots of the oxide thickness shown in Fig. 5.1, and some of the following pictures together with the analysis based on the *AFAF* should be sufficient to prove the merit of the approach presented here.

2.5 Pore formation in Si

Under special anodization conditions the Si substrate brought in contact with HF becomes porous. Depending on the etching conditions there are three pore categories classified according to their diameter d : micropores ($d < 5$ nm), mesopores ($5 < d < 50$ nm) and macropores ($d > 50$ nm). This section focuses mainly on the discussion of the macropore formation in n-Si since these are the types of the pores investigated in this thesis. For the sake of completeness a short introduction into the phenomenology formation of other pore types will be given as well.

Macropores n-Si attracted much attention especially after the discovery by Lehmann and Föll of the etching technique allowing to obtain ordered arrays of pores [26]. This triggered a lot of potential applications ranging from the basic PC [63] up to more sophisticated optical devices as filters [64], biosensors [65], etc. The etching of ordered macropores is possible in n-Si on photo lithographically prestructured wafers where locations on the wafer surface will be defined as nucleation points. Generating the minority carriers via the *Back Side Illumination* (BSI) their concentration can be precisely controlled and hence the amount of dissolved Si.

There are several models claiming to understand the mechanism of macropore formation in n-Si [66, 67]. Many of experiments can be found that contradict a big part of them [32, 68]. Perhaps the most viable remain the models proposed by Lehmann [20] and Zhang [69]. The quintessence of their models is shown in Fig.2.13.

As already discussed in the Section 2.1.5 at the semiconductor electrolyte junction a region

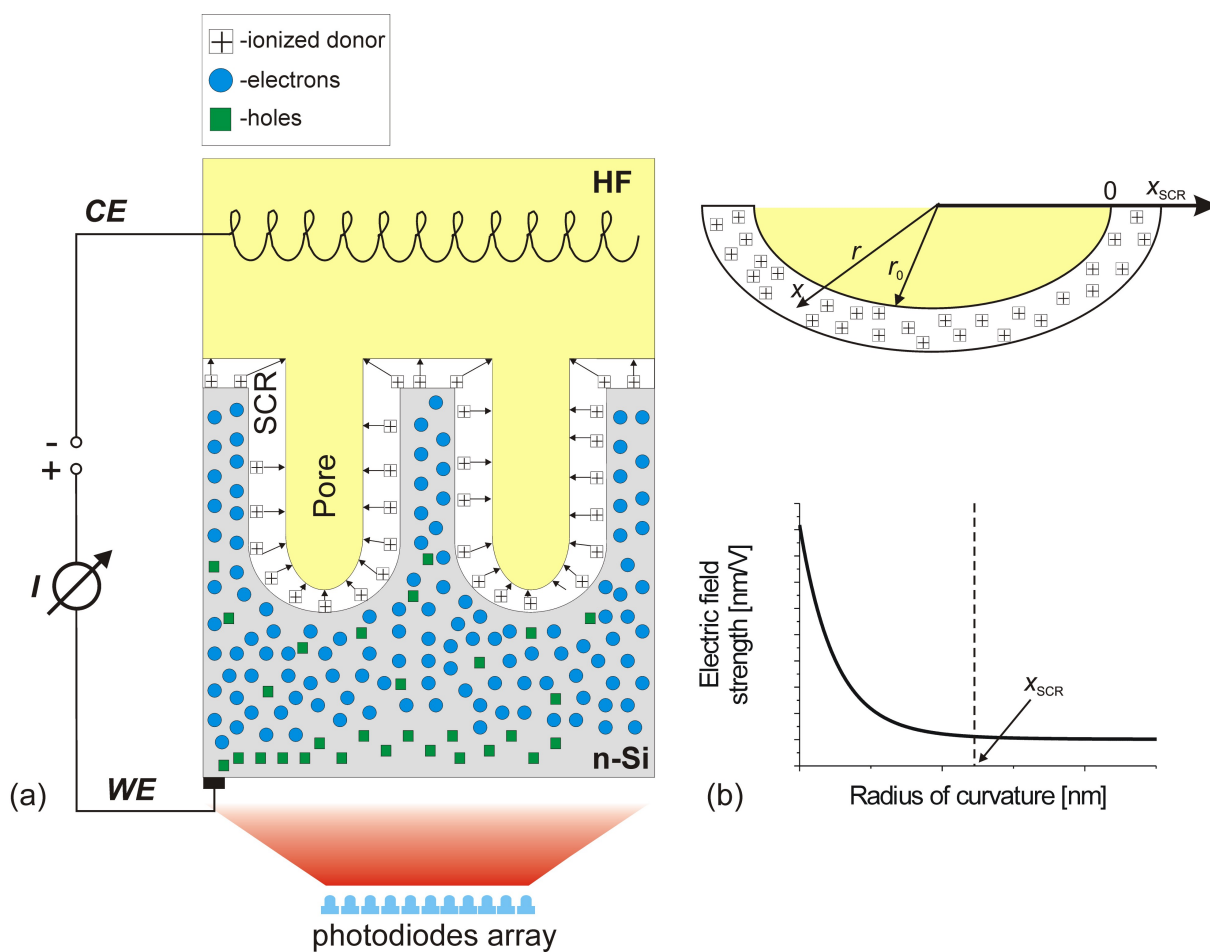


Figure 2.13: The macropore growth mechanism in the framework of the Lehmann model (a). The electric field strength at the pore tip as a function of the curvature radius (b).

depleted of majority charge carriers for the n-Si will form, i.e. the SCR. For the porous electrode the SCR looks as depicted in Fig.2.13a. When anodized the junction is under the reverse condition, resembling the Schottky diode, and can drive large currents if breakdown occurs or if minority carriers are injected into the junction.

The idea of etching ordered macropores in n-Si, advanced by Lehmann and Föll [26] in 1990, consists in generating the necessary minority carriers, i.e. holes, necessary for the dissolution by illuminating the electrode from the back side. The holes will diffuse or under the applied electric field will drift toward the pore tips. When entering the SCR of the pore the electric field accelerates them toward the Si-HF interface where they are consumed in the dissolution reaction. As a consequence the pore will advance into the depth. A necessary condition is that the life time of the holes is large enough. It is usually considered that the diffusion length of the holes has to be in the range of the wafer thickness. Particularly about the n-Si (will become more obvious when compared to the p-Si) the wall thickness can be as large as 10 x SCR [68].

If having holes with a diffusion length comparable to the wafer thickness a natural question arises: why do the pore growth only into the depth and not laterally? The reason for this is the passivation of the Si atoms at the pores walls by the hydrogen, i.e. a Si-H bond is formed for the surface atoms. A passivated atom is then difficult to be removed from the lattice. Jäger et al. found that the macropore walls, in n-Si, represent facets of the (111) planes [70]². The Si atoms on the (111) planes have only one dangling bond as compared to the Si atoms on the (100) planes which have two of them. This leads to the different kinetic on these two planes [20]:

- the etching is slower on the (111) plane as compared to the (100);
- the passivation is better (i.e. more atoms per square unit) on the (111) as compared to the (100)

A freshly emerged pore wall, formed as a result of an advancing tip, will hence be passivated by the H atoms and ulteriorly remain protected against further etching. When thinking in terms of thermodynamics it is obvious that also some etching is taking place too. This being the reason why the pore will grow laterally too, i.e. enlarge their diameter, however if the etching process well controlled macropores as deep as 500 μm can be obtained.

The state of the pore tip during the etching is peculiar and merits special attention. The etching bias, for the macropore growth in n-Si, becomes decoupled from the etching current. The aim of the applied voltage is to drive the holes at the pore tip and to ensure that the

²it is only due to the "very small" resolution of the SEM that usually (110)-like planes are seen as pore walls

electrochemical reactions take place. The voltage that is commonly used during the stable pore growth is able to drive giant currents, if holes available, even allows for electropolishing. Since the amount of holes is precisely controlled by the BSI usually allows for current densities in the range of mA/cm², the applied voltage is always high enough in order to ensure that at the pore tip the condition close to the electropolishing (assuming that the current flows exclusively at the pore tip). According to the Lehmann model [20] under the optimal pore growth conditions the current flowing at the pore tip is J_{PSL} . Increasing further the hole concentration will not increase the etching speed, but will drive the reactions at the tip to be of higher valence or leads to the enlargement of the pore diameter. Increasing the voltage more than the optimum will eventually cause an accumulation at the tip and as a direct consequence, the holes will penetrate the pore walls destroying the passivation of the walls.

Assuming the right illumination intensity and the correct applied voltage it is obvious that if the holes would be equally distributed along the pore no passivation would withstand etching up to such a degree that hundred micrometers deep pores can be etched (this corresponds to tens of etching hours). Obviously there exist a mechanism that preferentially consumes holes at the pore tip and not at the pore wall. Such a mechanism was proposed by Zhang [69] which resides on the following: due to a very small curvature radius of the pore tip compared to the pore wall the electric field strength built in the SCR is by orders of magnitudes higher at the tip compared to the SCR on the walls. It follows directly from solving Poisson equation for a curved surface as in Fig.2.13b:

$$\frac{1}{r^2} \frac{d}{dr} [r^2 E(r)] = \frac{\rho(r)}{4\pi\epsilon\epsilon_0} \quad (2.23)$$

where ϵ_0 is the permittivity of vacuum, ϵ is the dielectric constant of the material, $E(r)$ is the electric field strength in the SCR, $\rho(r)$ is the charge density in the space charge layer, equal to $-qN_D$ for $r_0 < r < r_{SCR}$, N_D is the ionized donor density, q is the elementary electric charge, r_0 is the radius of the curvature of the interface, $r_{SCR} - r_0$ is the width of the space charge region. Using the right boundary conditions found in [69] the dependence of the electric field strength upon the applied potential and the curvature radius can be represented as:

$$E(x + r_0) = \frac{qN_D}{12\pi\epsilon\epsilon_0} \left[- (x + r_0)^2 + \frac{2(x_{SCR} + r_0)^3}{(x + r_0)^2} \right] \quad (2.24)$$

The corresponding plot of the electric field strength as a function of the radius of the curvature is shown also in Fig.2.13b. From this graph one can see that for a wall where the curvature tends to ∞ the electric field strength is by far smaller as at the pore tip. At this point one has to mention however that due to the very small radius of the curvature at the tip, the

SCR width will become drastically smaller. This increases even more the field strength which leads to the formation of additional surface states where the electrons can tunnel. Thus hole generation is also favored at the tip (these holes are now "different" from the photo generated ones) which for the macropore formation might not necessarily be a benefit.

Macropores in p-Si will follow almost the same mechanism as n-Si with the exception that the holes are the majority carriers. One might consider that p-Si under forward condition would lead to the accumulation and not the formation of the SCR. In this case reappears the question of what favors the dissolution at the pore tip compared to the pore wall if no SCR is built. However for moderately doped samples, a SCR will still form and it will be broad enough so that selectivity between the pore tip and the pore wall is provided similar to the n-Si. Obviously, the pore walls thickness in p-Si, especially for very deep macropores, will be $2 \times \text{SCR}$. One has to mention that macropores in substrates with a doping level exceeding 10^{18}cm^{-3} could not be obtained.

As already mentioned, when the applied voltages are high enough at any inhomogeneity in the substrate which has a small radius of curvature, the electron tunneling might be initiated, which lead to the etching of the substrate. This phenomena is especially pronounced when the radius of the curvature of such an initiation pit is smaller than the SCR of the substrate. The pore will advance into the depth and such pores have usually very small diameters, the size scale being determined by the SCR. This category of pores are called mesopores. For mesopores in p-Si the dissolution valence is close to 3 while for the case of n-Si it depends on the etching current and doping and ranges from 2 for 10^{15}cm^{-3} to 3 for 10^{18}cm^{-3} .

2.6 Pore formation in the Current Burst Model

While these models offer quite a good explanation why the pore advances in the depth and its dissolution becomes limited laterally under correct etching conditions they still do not explain what exactly happens at the pore tip and what are the size and time scales that define the etching speed as well as the geometrical form and the diameter of the macropores. These questions can be answered in the framework of the CBM which in the previous section was introduced for explaining the oscillatory behavior of the Si electrode. The only ingredient needed to be added here is the nucleation of a CB on a H terminated surface (i.e. passivated) relaxing the condition that a closed oxide layer has to be always present. This automatically implies that in the passive phase of the CB the SiO_2 can be completely removed until an oxide free surface emerges. On a clean surface, before being passivated, the CB nucleation will take place very fast.

Basically the H-passivation defines, additionally to the interaction in space of the CBs, the

interaction in time during the pore formation. The time constant linking the both interactions is the oxide dissolution rate:

- if the oxide is dissolved quick enough there will be enough time for a new CB nucleation before the H-passivation of the surface otherwise it has to be overcome;
- if the oxide is dissolved slowly enough it favors the overlapping of the oxide bumps and hence their interaction in space.

The time for the oxide dissolution is very long compared to the other chemical time constants, it might take even seconds. Such long time will lead to the formation of large oxide domains which might reach even micrometers, i.e. scale comparable to the area of the macro-pore tip. When the electrode is strongly oscillating the domain size can go up to centimeters, i.e. building a domain over the whole electrode surface.

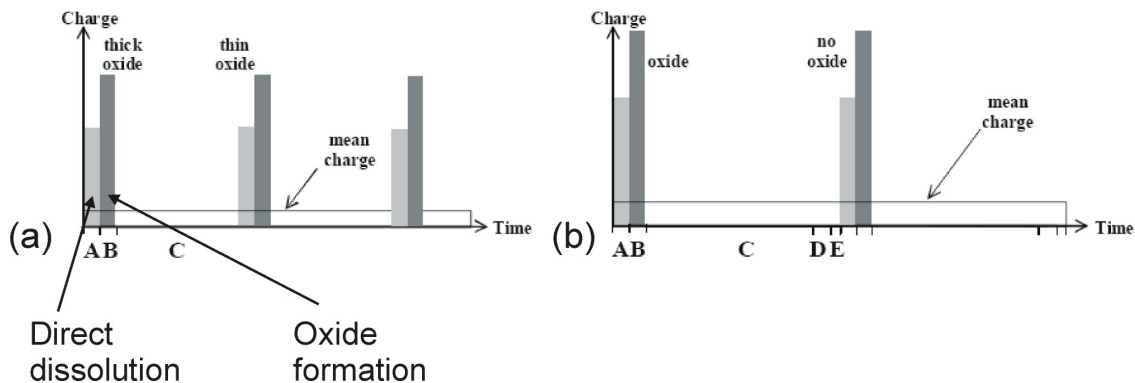


Figure 2.14: The electrochemical processes during the oscillation regime (a) and pore formation (b) in the CBM model [71].

Recalling the main processes from the CBM and adding the H-passivation during the pore formation; the time scale of these processes is shown in Fig.2.14. In the first phase, Fig.2.14a, oxide formation and further growth takes place (B) and it stops growing when most of the CBs switch to their passive phase (A) and only dissolution takes place (C) and then the process starts again. By contrast, during the pores formation, Fig.2.14b, the CBs nucleate on a free surface with the direct dissolution (A) which can be followed by the oxide production (B). After the oxide is completely dissolved during (C) the passivation of the free surface starts (D). After overcoming the passivation (E) a new CB will start.

In this work the pore growth mechanism will be regarded as a mixture of the Lehmann model and the CBM for the pores formation [71]. As it will be shown in the experimental part the CBM has more substance in order to explain the experimental findings with regard to the pore growth phenomena.

3 Photonic Crystals and application using porous materials

3.1 Fundamentals of Photonic Crystals

The materials allowing the full control of the light propagation as well as make possible its localization are, the so called, *Photonic Crystals* (PC). Similar to the electronic materials, the periodic arrangement of the dielectric constant inside such materials can lead to forbidden states for the photons inside the PC known as the *Photonic Band Gap* (PBG). The electromagnetic (EM) waves with frequencies lying in the PBG cannot propagate inside the PC. Additionally, having a source of EM waves surrounded by a PC for which the source's frequency lies in the PBG a full localization of the radiation can be achieved. The physics leading to PBGs and its calculation goes beyond the scope of this thesis and hence will not be further treated.

Photonic Crystals are artificial materials representing compounds of two dielectrics, with different dielectric constants, arranged periodically in 1, 2 or 3 dimensions. Hence the systematization of the PCs: 1D, 2D and 3D. Among the materials used for composing PCs dielectrics are mostly used however this is not limited to. For most application the strongest requirements are weakly absorbing materials as well as a high contrast in the refractive index has to be ensured. In what follows the interaction phenomenology of the EM field with PC will be briefly discussed.

3.1.1 Maxwell equations and the periodic dielectric media

The interaction of the EM field with the PCs is described by the Maxwell equations. For the interaction with homogeneous media the Maxwell equations have the following form:

$$\begin{aligned}\nabla \cdot \epsilon \mathbf{E} = \rho \quad \nabla \times \mathbf{E} + \mu \frac{\partial \mathbf{H}}{\partial t} &= 0 \\ \nabla \cdot \mu \mathbf{H} = 0 \quad \nabla \times \mathbf{H} - \frac{\partial \mathbf{E}}{\partial t} &= \mathbf{J}\end{aligned}\tag{3.1}$$

where the \mathbf{E} and \mathbf{H} are the macroscopic electric and magnetic field with \mathbf{D} and \mathbf{B} being the corresponding electric displacement and magnetic induction. The ρ and \mathbf{J} are the charges and currents respectively.

It was mentioned above that the PCs are basically composed of dielectrics¹. This condition simplifies the Eq. 3.2 by allowing to consider $\rho = \mathbf{J} = 0$. Additionally one can relate the \mathbf{D} to \mathbf{E} and \mathbf{B} to \mathbf{H} as follows:

$$\mathbf{D} = \epsilon_0 \epsilon \mathbf{E} \tag{3.2}$$

$$\mathbf{B} = \mu_0 \mu \mathbf{H}$$

where ϵ_0 is the electric permittivity and μ_0 is the magnetic permeability of vacuum and ϵ and μ are the dielectric constant and magnetic permeability of the media in which the EM waves propagate. The part with the magnetic field in Eq. 3.3 simplifies even more since dealing here with magnetically non active materials, i.e. $\mu = 1$. In order to keep the theory simple it is further considered that the involved materials show a linear behavior.

The \mathbf{E} and \mathbf{H} are both complicated functions that vary sinusoidally in time. In this case a harmonic mode can be considered as a certain field pattern multiplied with a complex exponential, which as it will immediately be shown will simplify the mathematics:

$$\mathbf{H}(\mathbf{r}, t) = \mathbf{H}(\mathbf{r}) e^{i\omega t} \tag{3.3}$$

$$\mathbf{E}(\mathbf{r}, t) = \mathbf{E}(\mathbf{r}) e^{i\omega t}$$

Considering a frequency ω one can find now the exact profile of the mode by inserting Eq. 3.4 in Eq. 3.2. In this case the divergences of the electric and magnetic field can be neglected since delivering 0 and only the other two are of interest. They have now the form:

$$\nabla \times \mathbf{E} + \frac{i\omega}{c} \mathbf{H}(\mathbf{r}) = 0 \tag{3.4}$$

$$\nabla \times \mathbf{H}(\mathbf{r}) - \frac{i\omega}{c} \epsilon(\mathbf{r}) \mathbf{E}(\mathbf{r}) = 0$$

Note that not a constant dielectric constant is involved, but variable in space, i.e. $\epsilon(\mathbf{r})$. If the second equation is divided by $\epsilon(\mathbf{r})$ and then take the curl one obtains the so called *Master*

¹Tentatives to have PCs based on metals or electrically active materials were advanced in the literature too [72]. Such PCs however are not treated here as are PCs based on magnetically active materials.

Equation. The result is presented in $\mathbf{H}(\mathbf{r})$ after eliminating $\mathbf{E}(\mathbf{r})$ and has the following form:

$$\nabla \times \left(\frac{1}{\epsilon(\mathbf{r})} \nabla \times \mathbf{H}(\mathbf{r}) \right) = \left(\frac{\omega}{c} \right)^2 \mathbf{H}(\mathbf{r}) \quad (3.5)$$

Assuming that a variation in space of the $\epsilon(\mathbf{r})$ is known, solving the master equation (Eq. 3.5) allows to find the pattern in space of the $\mathbf{H}(\mathbf{r})$. This can be further translated into the variation of the $\mathbf{E}(\mathbf{r})$ by using the second equation in Eq. 3.5.

Due to the fact that the PC represents a periodic arrangement of dielectric materials the solution of the master equation, Eq. 3.5 has the form of Bloch modes defined as:

$$\mathbf{H}_{\mathbf{k}}(\mathbf{r}) = e^{i\mathbf{k}\mathbf{r}} u_{\mathbf{k}}^{\mathbf{H}}(\mathbf{r}) \quad (3.6)$$

where \mathbf{k} is considered to be the wavevector and $u_{\mathbf{k}}^{\mathbf{H}}(\mathbf{r})$ is a function carrying the periodicity of the PC:

$$u_{\mathbf{k}}^{\mathbf{H}}(\mathbf{r} + \mathbf{R}) = u_{\mathbf{k}}^{\mathbf{H}}(\mathbf{r}) \quad (3.7)$$

where \mathbf{R} is a translation vector in real space lattice which is defined as: $\mathbf{R} = x\mathbf{a}_1 + y\mathbf{a}_2 + z\mathbf{a}_3$ where $\mathbf{a}_1, \mathbf{a}_2$ and \mathbf{a}_3 are the lattice vectors of the PC and x, y and z are integers.

Now the $\mathbf{H}(\mathbf{r})$ can be substituted in the master equation Eq.3.5 and the corresponding modes can be calculated.

For doing this, one takes advantage of the periodic nature of $u_{\mathbf{k}}^{\mathbf{H}}(\mathbf{r})$ and decomposes it into its Fourier components² switching to the reciprocal lattice with the vector $\mathbf{G} = x\mathbf{b}_1 + y\mathbf{b}_2 + z\mathbf{b}_3$ where x, y and z are already the known scalars and $\mathbf{b}_1, \mathbf{b}_2$ and \mathbf{b}_3 are the elementary vectors in the reciprocal lattice.

Not shown here, but finally the Bloch modes will be expressed as a combination of the transmitted plane waves and diffracted waves with the reciprocal vector \mathbf{G} [73]:

$$u_{\mathbf{k}}^{\mathbf{H}}(\mathbf{r}) = \sum_{\mathbf{G}} c_{\mathbf{G}} e^{i(\mathbf{k} + \mathbf{G})\mathbf{r}} \quad (3.8)$$

where $c_{\mathbf{G}}$ is a Fourier coefficient.

The equation 3.8 shows that for the case of PCs with strong modulation in $\epsilon(\mathbf{r})$ the excited waves inside the crystal is a mixture of many diffracted components with different \mathbf{G} . Within the PC no wave propagation angle is defined and the situation is rather "chaotic". Compared to the geometrical optics a qualitative description of the wave propagation is rather impossible. A direct consequence of this is that a PC cannot be ascribed a refractive index as do have the homogeneous materials in the geometrical optics. Nevertheless, as it will be shown later, this

²The same will be done with the periodic function of the dielectric constant $\epsilon(\mathbf{r})$

is possible here as well by employing some non straightforward procedures.

3.1.2 Light propagation in PC

As already mentioned in the previous section, the radiation propagates inside the PC in form of a complicated series of Bloch waves. This makes it rather impossible to predict the trajectory of a wave as known from the geometrical optics as well as makes it impossible directly to ascribe the PC an index of refraction. The index of refraction is however a crucial parameter for the optical design and developing a theoretical approach that would ascribe a PC an index of refraction would be of very great help. It is quite obvious at this point that independent on the methodology of doing so, the estimated index of refraction, if existing, has to be treated as an effective quantity n_{eff} . The PC described by such an effective parameter will be consequently treated as an effectively optical homogeneous material.

For long wavelengths, i.e. $\lambda \gg a$ where λ is the radiation wavelength and a is the PC lattice constant, the issue of ascribing the PC a n_{eff} is relatively straightforward. In crystal optics the refractive index is a result of homogenization of the atomic structure. The PCs formulate a similar problem, i.e. homogenization of a periodic composite with macroscopic inhomogeneities. A very elegant solution for this problem is presented by Halevi et al. [74]. They claim that a PC can be homogenized in the long range wavelengths by weighting the n_{eff} as follows:

$$n_{eff}^{\lambda \gg a} = fn_1 + (1 - f)n_2 \quad (3.9)$$

where n_1 is the refractive index of the first constituent which is present in a fraction f in the PC and n_2 is the refractive index of the second component presented in the fraction $(1 - f)$ respectively. This theory delivered quite reasonable result and taking into account that the PBS of the PC in the long wavelength range shows always a linear behavior it seems quite reasonable what the authors propose. Under these circumstances it can be traced even a path for the rays inside the PC by applying the Snell law. One must point out that despite the fact that a n_{eff} could be ascribed its nature is very anisotropic and the magnitude of n_{eff} will strongly change as a function of the wave vector orientation.

More interestingly, from the point of view of the light propagation in a PC, is the case when the λ is comparable to a . Calculating a n_{eff} with the Eq. 3.9 is inappropriate and approach is needed. Notomi [73] proposed to solve this problem by analyzing the *Equifrequency Surface* (EFS) plots of the PBS.

Figure 3.1a shows the case when the light travels from air into a homogeneous medium, i.e. a dielectric material. A perfect circle has to be treated as a PB of a homogeneous dielectric

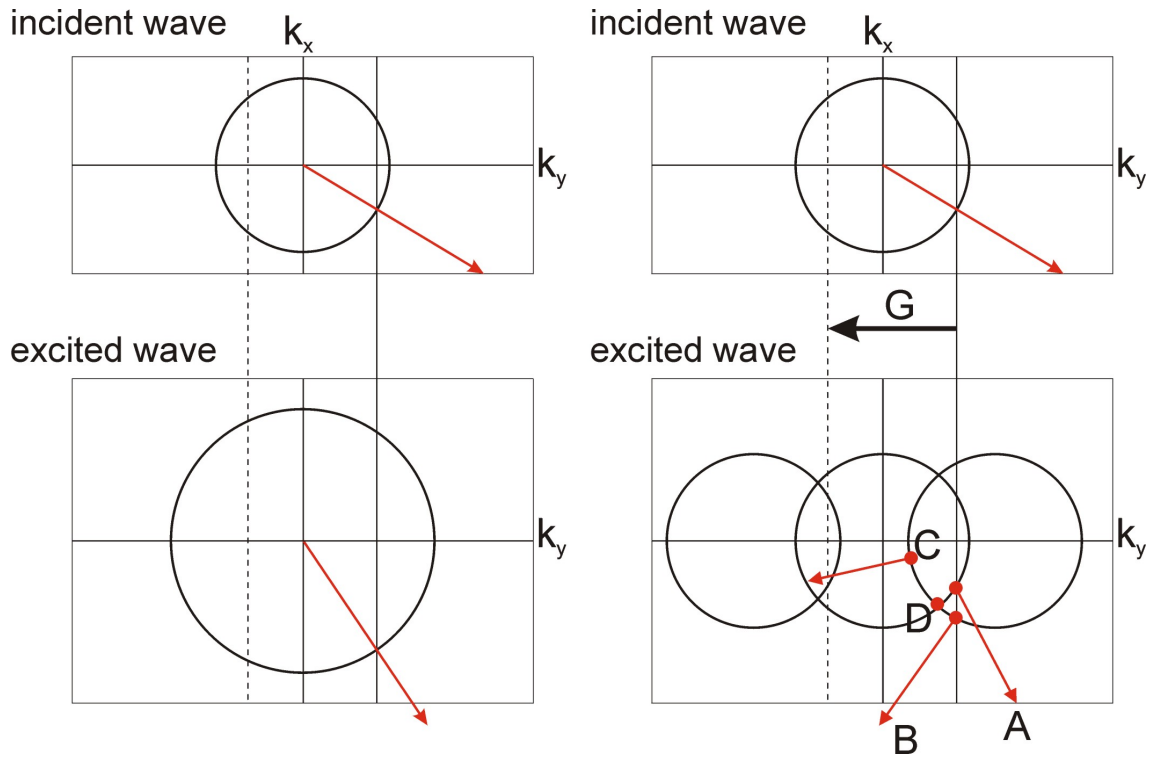


Figure 3.1: The EFS plot for the propagation of light from air to a homogeneous material (a) or through a diffraction grating (b).

with $\omega = ck/n$. In this case, in order to ensure the conservation of the tangential components of the wave vector, the light has to propagate in the direction pointed by the \mathbf{k} vector [75].

When having a diffraction grating, which is the case for PCs, the situation changes (see Fig.3.1b). In this case more EFS plots have to be drawn along the diffraction line. The conservation of the wave vector is a condition here as well which leads to the fact that several beams can be excited at the grating. The point A corresponds to the transmitted wave, point B to the diffracted wave. Under certain conditions even the point C can be excited, however having a \mathbf{k} that is very close to the origin leading to very small values for n_{eff} . Since the light propagation is not along \mathbf{k} , n_{eff} cannot be used in order to trace the trajectory of the wave. Particularly the point D is interesting which is called a singularity by Notomi [73]. At this point another interesting phenomena occurs, namely that the propagation direction remains undefined since it switches from one circle to another. This switch is very sensitive to the incidence angle.

What is discussed above, although it cannot be directly applied to the phenomenology of the wave propagation in PCs will help a lot to for a better understanding. For this consider a PC with a strong modulation in the refractive index. A very illustrative a picture from the paper of Notomi [73] will be shown here, see Fig. 3.2.

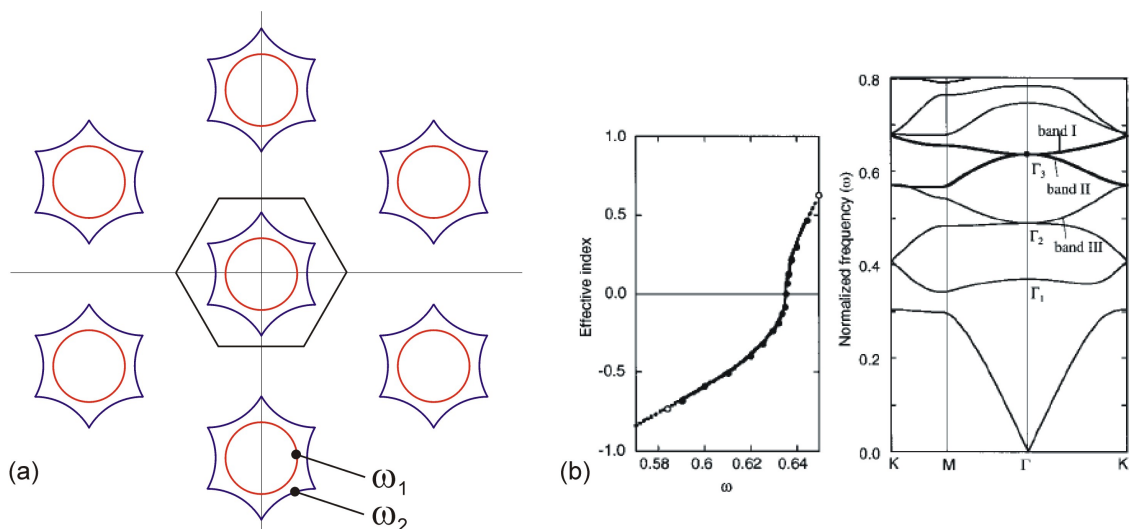


Figure 3.2: *The EFS of a PC based on porous GaAs, the pores representing air cylinders placed perpendicularly to the material's surface (a). Effective index calculated from the EFS together with the PBS of similar PC (b), but of the inverse composition as in (a); reproduced from the Ref. [73].*

Equation 3.8 analytically sums up the total number of the Bloch modes existing in a PC. As already mentioned, due to their chaotic character, the EFS cannot be plotted as easily as was the case for the pure diffraction problem. The EFS plots in this case have other forms that only under specific conditions will resemble a circle. In order to show this, a triangular lattice PC based on porous GaAs, i.e. air cylinders perpendicular to the sample surface, is considered. The EFS of such a crystal will become round only in the vicinity of the band gap, otherwise having shapes as indicated in Fig. 3.2a with a blue line, i.e. ω_1 is closer to the band gap as ω_2 . If the EFS is round, from the shape of the EFS one can calculate the propagation direction, i.e. $\mathbf{v}_g = \nabla_{\mathbf{k}}\omega$ and since it should follow Snell's law n_{eff} can be calculated. An example for the GaAs PC (but inversed as composition) is shown in Fig. 3.2b. It shows that close to the band opening the n_{eff} can be calculated and that all its values are less than 1. The sign of n_{eff} can be positive as well as negative and is determined by the sign of $\nabla_{\mathbf{k}}\omega$.

For the rest of the frequencies (for which the EFS do have a star-shape) n_{eff} is not defined meaning that there cannot be traced the ray trajectory inside the PC. While intuitively excluded from any application design, this region might exhibit interesting functionality. In this work it is only partially treated in the experimental part.

3.1.3 The scalability of the Maxwell equations

In this section will be discussed a very important feature of the Maxwell equation - the scalability. It is important since most of the optical applications involving PCs are targeting

the IR and visible range of the spectrum. This however involve the use of very small feature sizes of the PCs (i.e. small sizes of individual components in a PC). While there exist a plenty of PCs fabrication methods many of them a very costly and it is very often counterproductive to invest resources in producing a PC and only later check if the PC application fulfills its scopes. By making use of the scalability of the Maxwell equations, the EM field evolution in time and space remain unchanged for all frequencies of the spectrum provided that the correct dimensions for the PCs components are chosen. Reducing or increasing the frequency, in order to achieve equal performance, the size of the PC features have to be enlarged or reduced accordingly. This extremely lightens the experimentalists activity since the concepts of eventual PC applications can be first tested in the e.g. microwave regime of the spectrum and if exhibiting the expected functionality ulteriorly scaled to the desired frequency window. The advantage of measuring at e.g. microwaves is indeed the ease of PCs fabrication (it is in the range of mm to cm) and small costs (actually not always) of the constituent materials.

In order to show how the scalability is ensured one recalls the master equation from the previous section, Eq. 3.5. Suppose now instead of a dielectric constant profile $\epsilon(\mathbf{r})$ the PC is scaled with a scaling constant s so will be also the dielectric constant profile, i.e. $\epsilon^{scaled}(\mathbf{r}) = \epsilon(\frac{\mathbf{r}}{s})$. Plugging this in the master equation and considering $\mathbf{r}^{scaled} = s\mathbf{r}$, $\nabla^{scaled} = \frac{\nabla}{s}$ one obtains the following:

$$s\nabla^{scaled} \times \left(\frac{1}{\epsilon(\mathbf{r}^{scaled}/s)} s\nabla^{scaled} \times \mathbf{H}(\mathbf{r}^{scaled}/s) \right) = \left(\frac{\omega}{c} \right)^2 \mathbf{H}(\mathbf{r}^{scaled}/s) \quad (3.10)$$

One can see that $\epsilon(\mathbf{r}^{scaled}/s) = \epsilon^{scaled}(\mathbf{r}^{scaled})$. Dividing both parts by s one obtains the following:

$$\nabla^{scaled} \times \left(\frac{1}{\epsilon^{scaled}(\mathbf{r}^{scaled})} \nabla^{scaled} \times \mathbf{H}(\mathbf{r}^{scaled}/s) \right) = \left(\frac{\omega}{c} \right)^2 \mathbf{H}(\mathbf{r}^{scaled}/s) \quad (3.11)$$

What can be read now from the Eq.3.11 is that $\mathbf{H}^{scaled}(\mathbf{r}^{scaled}) = \mathbf{H}(\mathbf{r}^{scaled}/s)$ and the frequency $\omega^{scaled} = \omega/s$. Now it is obvious that if the frequency is scaled with a factor s the old mode and the frequency will scale with the same factor s . The solution of the problem at any scale is than determined by the solution at other scale.

By following the same argumentation line it can be easily shown that as there exist no fundamental length scale also there is no fundamental value of the dielectric constant [76]. This means that if one considers that the modified dielectric constant follows the law e.g. $\epsilon^{modified}(\mathbf{r}) = \epsilon(\mathbf{r})/s^2$ it can be shown that the modes of the PC remain unchanged with the exception of the frequency which scales by a factor of s : $\omega^{modified} = s\omega$.

In this work it is made use of the scaling law as well. The results presented in Chapter 7 are all obtained at frequencies ranging in the kHz range, i.e. microwaves. The EM field

patterns which are obtained remain unchanged, qualitatively as well as quantitatively, for higher frequencies if, as already discussed, the structural parameters are scaled accordingly. Hence the structures proposed in this work represent a model system which can be scaled to frequencies in the IR or even visible range of the spectrum.

3.2 Porous Si as host material for gas sensor application

Spectroscopic gas sensors make use of the distinct absorption lines of gases, i.e. the gases absorb radiation at certain wavelengths, c.f. Fig. 3.3a. The conventional spectroscopic gas sensor are built in the following way. A big chamber is filled with the gas under investigation. A

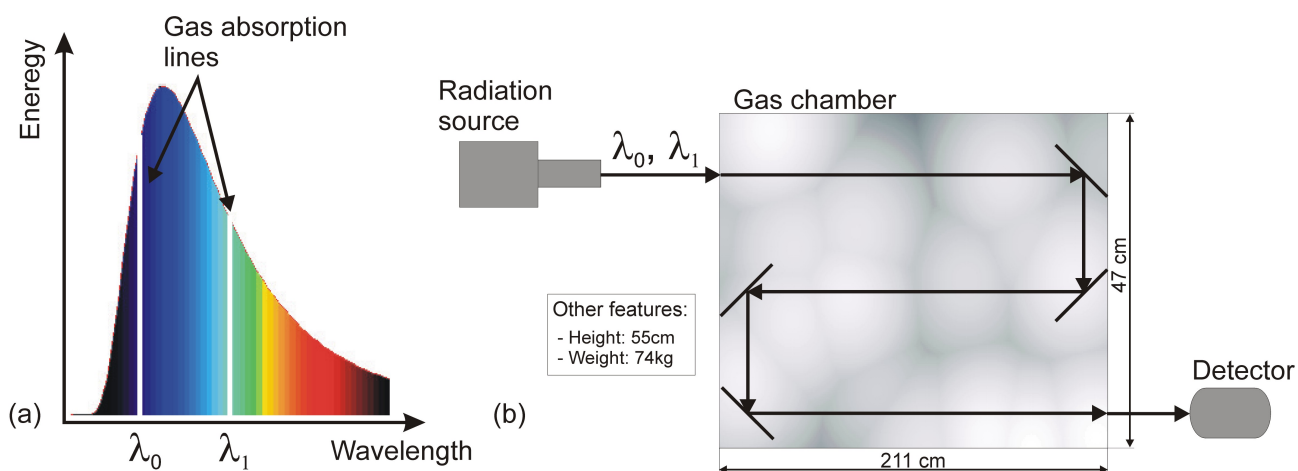


Figure 3.3: Working principle of the spectroscopic gas sensors. Schematics of the black body radiation and absorption lines at specific wavelengths of a certain gas (a). The scheme of a conventional spectroscopic gas sensor (b).

source, radiating with wavelengths matching the gas absorption lines is used. The radiation is reflected several times inside the gas filled chamber so that enough interaction is ensured. After the ray escapes the chamber a calibrated detector is used which by measuring the decrease in the signal intensity analyzes which is the concentration of gas present in the chamber.

The gas absorption will follow the so called Lambert-Beer law:

$$I(l, c) = I_0 e^{-\alpha(\lambda)[c]l} \quad (3.12)$$

where l is the interaction length, $[c]$ is the gas concentration, I_0 is the radiation intensity, $\alpha(\lambda)$ is the absorption coefficient of the gas. Measuring $I(l)$ and knowing the $\alpha(\lambda)$ and I_0 , from this equation the gas concentration $[c]$ can be calculated.

A strong requirement for their good functionality is that the volume of the gas under the investigation is large enough in order to ensure enough absorption. This leads to very large

volumes of the nowadays used sensors, i.e. as shown in Fig. 3.3b it is in the order of 0.5m^3 . While for some special application this is not an issue, there exist different other fields of application where smaller sizes would be desirable. Smaller sizes, however, lead to small gas volumes for the detection and hence often to malfunction of the sensors based on this principle.

One of the approaches to overcome this problem was proposed by Wherspohn et al. [24] which compensates the smaller volume of gas by allowing more time of the photons to interact with the gas molecules. This can be ensured if the radiation speed inside the chamber is drastically reduced. Differently formulated, the goal is to reduce the group velocity v_g of the radiation inside the gas chamber. Quite obviously the first major change that has to be undertaken is to have a new type of chamber.

An elegant solution for this problem is using PCs as host materials. Figure 3.4 shows a PC based on macroporous Si and the corresponding PBS. The slope of the bands defines v_g according to the following formula:

$$v_g = \frac{d\omega}{d\mathbf{k}} \quad (3.13)$$

where ω is the frequency of the radiation and \mathbf{k} is the wave vector inside the PC. One can see that if the bands become flat $v_g \rightarrow 0$ and this is what one is looking for. The PC has now to be designed such that the bands are flat at the wavelengths matching the gas absorption line, i.e. for those wavelength v_g inside the PC will be drastically reduced, see Fig. 3.4a. The design implies to select an appropriate diameter of the pores and lattice constant. Since the PBS is very sensitive on the feature size of the PC this calls for etching pores in n-Si where the characteristics of the pores must be precisely controlled and their distribution predefined by the photo lithography.

The principle of the spectroscopic gas sensor based on macroporous Si is schematically shown in Fig. 3.4b. Very deep macropores can be etched and the structure must be opened from the backside to form a membrane. The pores will act as pipes where the gas is pumped through. Further, using the right polarization and coupling angle of light can be ensured that the modes inside the PC are merely distributed in the pores and not in the Si matrix. This ensures the needed interaction between the radiation and the gas.

The porous structures presented in this work are designed as PCs for spectroscopic sensors for ethanol. The targeted detection wavelength is $\lambda = 3.4\mu\text{m}$ and $\lambda = 9.55\mu\text{m}$. Most of the structures were adapted for the second wavelength. The pores structure have to be round and arranged in a triangular lattice, the lattice constant $a = 4.2\mu\text{m}$; the radius of the pores $r/a = 0.39$.

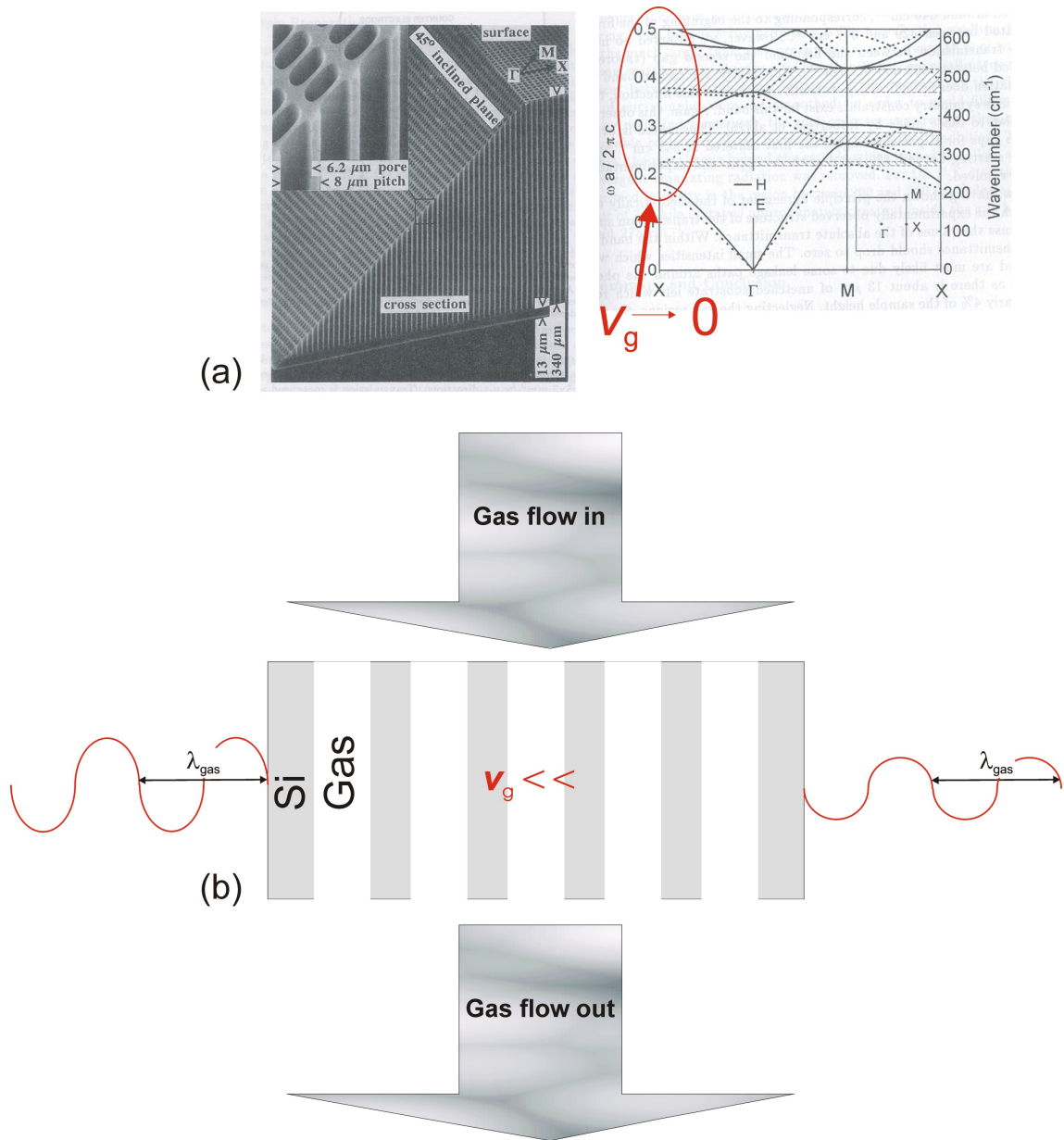


Figure 3.4: Photonic Crystal based on macroporous Si and its PBS [77] (a). With red are marked the frequencies where the $v_g \rightarrow 0$. The principle of the spectroscopic gas sensor with porous Si (b).

4 Experimental setups and analytical methods used in the work

4.1 Electrochemical etching and plating

4.1.1 Etching of macroporous n-Si

Wafers of n-Si with low doping levels corresponding to a resistivity of $5 \Omega\text{cm}$ were used for etching macropores. The substrate orientation is (100). Holes necessary for the growth of macropores in n-type Si are supplied by the standard BSI technique [38, 26]. The samples were pre-structured by standard photolithography before etching; the nucleation pattern produced was a triangular lattice with a lattice constant of $a = 4.2 \mu\text{m}$. The steps of the wafers processing are shown in Fig.4.1.

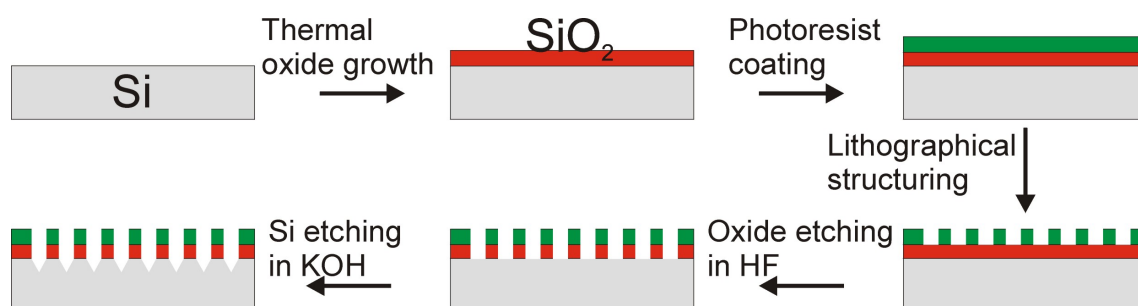


Figure 4.1: *Processing steps of the n-Si wafer prior to the electrochemical etching.*

For the experiments done in aqueous electrolyte 49wt% HF was dissolved in deionized water. The concentration of the electrolyte was calculated in weight percents. For more details see [20]. As standard electrolyte volume was taken 300 ml and the HF amount was calculated according to this volume. For the electrolytes containing alcohols, the HF concentration was calculated based on a solvent composition 1:1.5 H₂O:Alcohol. For the viscous electrolyte the solvent consisted of 100 ml of H₂O and 200 ml of H₂O mixed with 0.5 g of Carboxymethyl-cellulose Sodium Salt. Further the HF concentration was calculated as for the pure water. Ohmic contact with the backside of the sample was possible due to a highly doped n⁺ layer

on the backside of the Si wafer.

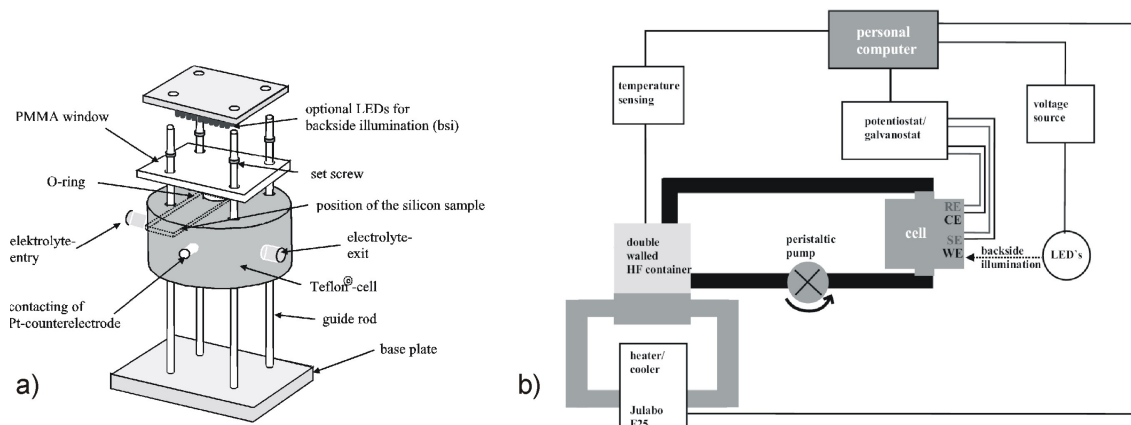


Figure 4.2: The schematics of the etching cell (a) and the construction of the etching setup (b).

The etching cell was built out of teflon, see Fig. 4.2a. It had 4 Pt electrodes: Working (WE), Counter (CE), Sense (SE), and Reference (RE). The WE and SE were connected directly on the sample, however not short circuited. The RE was placed in electrolyte and as close as possible to the sample surface. While the potential was applied between the WE and CE, the SE and RE were used to measure the potential drop on the Si-electrolyte junction, i.e. compensating for the potential losses in the electrolyte and ohmic losses.

All experiments were performed at a constant temperature controlled with an accuracy of typically $\pm 0.1^\circ\text{C}$. A continuous electrolyte flow through the cell was maintained by means of a peristaltic pump, see Fig. 4.2b, ensuring a homogeneous flow of ions or molecules toward and away from the reactive interface.

4.1.2 Electroplating of metals

For the electrodeposition experiments a cell similar with the one for the Si etching was used. A Cu pseudo-reference electrode and a Cu counter electrode were employed. The copper bath electrolyte consisted of $0.1 \text{ mol/L CuSO}_4 + 1.8 \text{ mmol/L H}_2\text{SO}_4$. During the entire electrodeposition process the electrolyte was bubbled by N_2 gas, constantly removing oxygen from the solution. The resistivity of the electrolyte was calculated according to the formula and the data provided in [78]; it is calculated to be about $35 \Omega\text{cm}$. However, the real value is ca. $110 \Omega\text{cm}$ [79], somewhat bigger due to the interaction between anions and cations at high concentration. Before starting the electroplating procedure, the porous Si samples were washed carefully (supersonically) first with 10 % (w/w) HF-ethanol solution, then with ethanol. Drying with N_2 was followed by a dip into a Piranha solution (98 % H_2SO_4 : 30 %

H₂O₂, 1:1 volume) for 10 min [20, 69, 80]. Afterwards, the samples were dried in a vacuum oven at a temperature of 100° C for at least 3 hours. Note that this procedure tends to produce an oxide somewhat thicker and denser than the normal native oxide obtained in air.

Next, the porous sample were immersed into the copper bath electrolyte, and the bath is supersonically agitated in order to fill the pores with electrolyte. Prior to specimen immersion, oxygen dissolved in the electrolyte was removed by vigorous N₂ gas bubbling for at least 15 min.

4.2 Analytical tools

4.2.1 FFT impedance spectroscopy

Fast Fourier Transformed - Impedance Spectroscopy (FFT-IS) - although a standard analytical tool for electrochemists is only sporadically used in other fields of materials science since addressing some very specific problems. Since in chapter 6.2 results are discussed obtained by FFT-IS it is important to discuss the principles of function.

The impedance spectroscopy is a very powerful tool for investigation of the electrical and electrochemical properties of different materials. Assume a potentiostatic (or galvanostatic) experiment where a voltage U (or current density J) is applied. Superimposing a time periodic perturbation signal with the frequency ω on the applied voltage (or current density), i.e. $U + \Delta U \sin \omega t$ a corresponding answer in the current density (or voltage), i.e. $J + \Delta J \sin(\omega t + \varphi)$, can be measured¹. The phase shift is noted with φ . The impedance of the system can be calculated by:

$$Z = \frac{U_{etch} \cdot e^{i\omega t}}{J_{etch} \cdot e^{i\omega t + \varphi}} \quad (4.1)$$

where ω is the perturbation frequency and φ is the phase shift of the J .

The IS involves the calculation of the impedance according to the Eq.4.1 for a series of frequencies which, for a standard spectrograph, will be applied sequentially one after another. The measurements are represented in the form of the *Nyquist plot* which plots the ImZ on the ordinate axes and the ReZ on the abscissa axes each point on the graph corresponding to the frequency ω used for the formation of the perturbation signal.

Making IS enforces three main conditions:

1. **Linearity** The system must have a linear dependence on U as a function of J , i.e. it has to be described by a set of linear differential equations. This ensures that the

¹Throughout the rest of this Section only the perturbation in the voltage and answer in the current will be mentioned. Everything stated can be applied for the inverse experiment just as well.

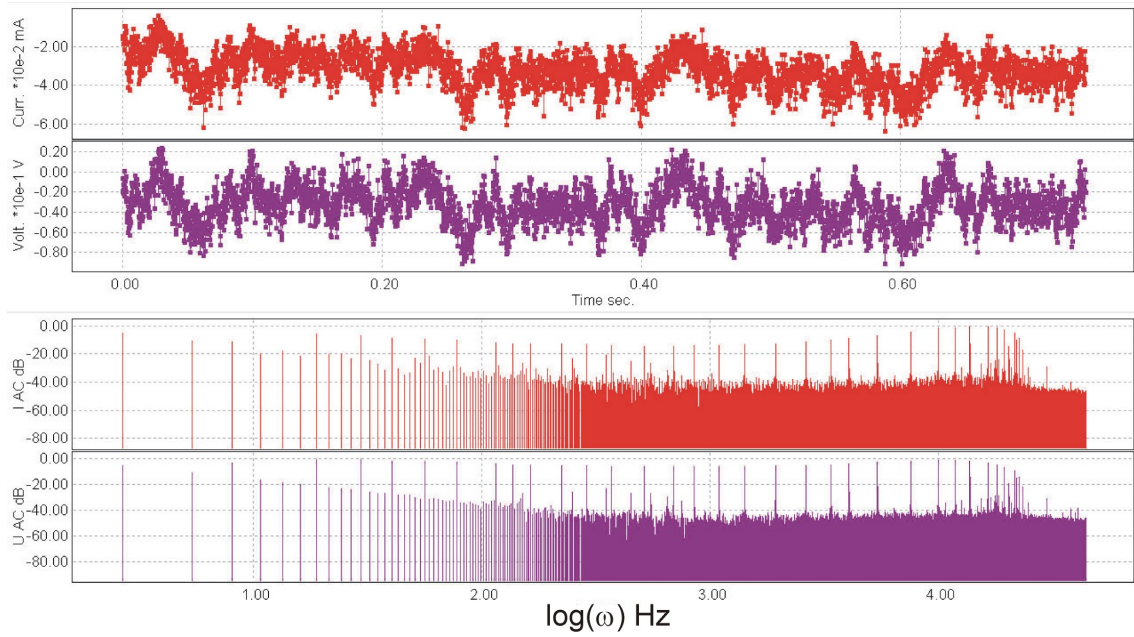


Figure 4.3: The perturbation (blue curve) and the answer (red curve) signals are shown. The two graphs below show the Fourier-transformed signals.

frequency used for the perturbation signal is exactly the one the answer will contain. If the linearity is not ensured the answer signal can be composed of additional frequencies which will make the data interpretation impossible. In order to ensure the linearity the amplitude of the perturbation signal must be kept as small as possible thus ensuring that even in the non-linear regimes of the $U(J)$ the impedance can be measured.

2. **Causality** Applying a perturbation on the voltage the answer in the current has to be caused by the corresponding change in the voltage. It has to be excluded that the current changes as a result of some external factors. As mentioned for the previous condition, the amplitude of the perturbation signal has to be small, however high enough in order to ensure that the change in the system is due to the perturbation.
3. **Stability** The system has to remain unchanged while the perturbation signal is applied. The only processes allowed are those following the perturbation signal. More generally, after the perturbation ends the system has to return in its initial state.

The nowadays powerful computers allow considerable improvement of the generic IS. One can make use of the Fast Fourier Transformation (FFT) which allows to form a perturbation signal that contains concomitantly several frequencies. The method is then called FFT-IS. If the linearity of the system is ensured the answer will contain the same frequencies which can be separated by FFT. The advantage of this approach over the older one is that the impedance

analysis is performed much faster. It lasts the time inherent to the smallest frequency which is considerably faster as waiting the whole frequencies to be consecutively applied. This method is especially preferred for the dynamic systems, e.g. it is the best, if not the single, choice for investigating electrodes porosification.

This concept was used for the current work as well. The perturbation signal was composed out of 30 frequencies ranging from 5 Hz to 20 kHz. The perturbation signal amplitude was always kept sufficiently small to be below the thermal voltage $V = kT/e$ hence ensuring the linear behavior of the system. An example of a perturbation signal is shown in Fig.4.3. The upper two curves show the perturbation signal (blue curve) and the corresponding answer in the current (red). Qualitatively both curves look similar. The other two curves show the FFT of the perturbation and answer signals which shows the power in dB as a function of the $\log(\omega)$. The separate bulks show the employed frequencies².

Analysis of measured impedance spectra is not a trivial task and usually undergoes a complex process. Figure 4.4 shows a very general work flow of how the data is analyzed. Usually it starts with defining a theoretical model which describes how the system behaves under the periodic modulation of the voltage. In this case the mathematical aspect of the physical model will be derived from general concepts of the physics and chemistry containing diffusion equations, reactions kinetics, etc. This will formulate the corresponding equations in terms of concrete system's parameters, i.e. diffusion coefficients of species, degree of electrode porosification, corrosion speed, etc. After the analytical part of the theory is established the measured impedance is fitted and the system's parameters are obtained.

In the present work the FFT-IS is done during the macropore growth in n-Si with BSI. The etching current is a function of the BSI intensity as well as the applied voltage. That is why the impedance performed potentiostatically, further on called *voltage impedance*, and in the illumination, called *photo impedance*. The voltage impedance implied a perturbation in the voltage while the photo impedance a perturbation in the BSI intensity. In both cases the answer in the current was measured. An impedance measurement, for each type, lasted 1 s. During the entire experiment run: 1 s is done impedance in the voltage followed by 1 s pause which continued with 1 s photo impedance followed by 1 s pause and the cycle started again. During a 300 min experiment 6000 data sets for each type of the impedance are acquired. After fitting the data, the system's parameters were expressed as a function of time.

²Due to technical issues most of the frequencies are condensed at the end of the spectrum. That is why if counting the separate bulks the number 30 does not come out.

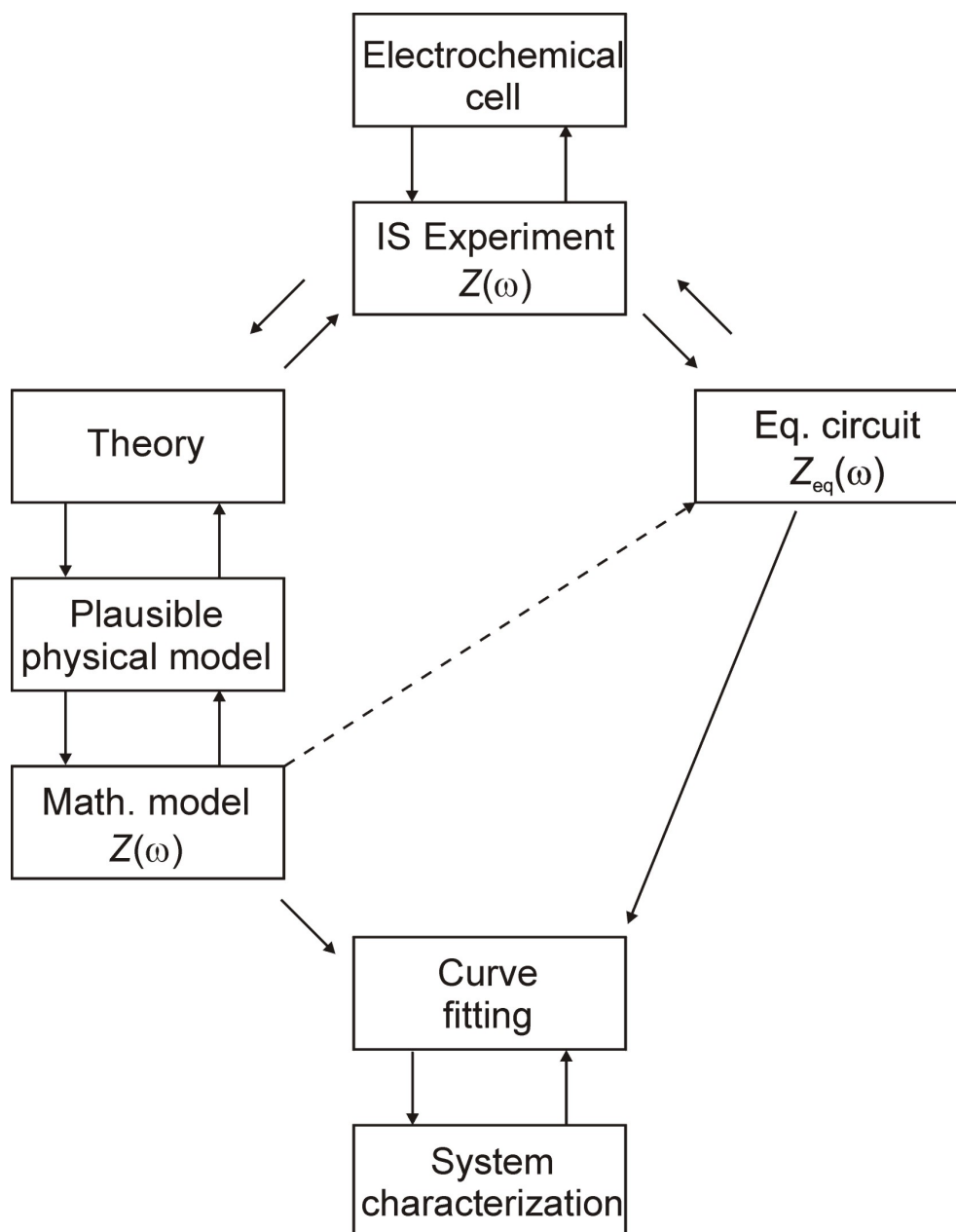


Figure 4.4: Diagram describing the work flow from measuring to interpreting the impedance data [81].

4.2.2 Scanning Electron Microscope

The samples surface and cross section were investigated. For this, the etched samples were cleaved and first dried at $\approx 200^\circ$ C. After drying the porous substrates were placed in the SEM chamber where a vacuum in the range of 10^{-6} mbar was established. The SEM was a Philips XL series scanning electron microscope.

4.2.3 Atomic Force Microscope

The AFM was used to investigate the roughness on the pore walls and coupling interface. Likewise in the case of the SEM investigation, the samples were first cleaved. A special sharp tip provided by Veeco, GmbH, Germany was used. The pore walls were scanned in cross section as shown in Fig.4.5.

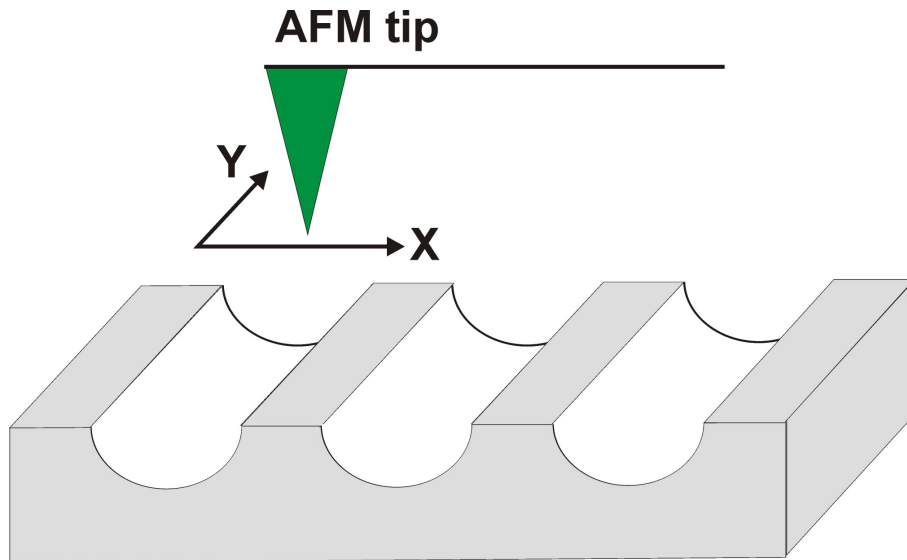


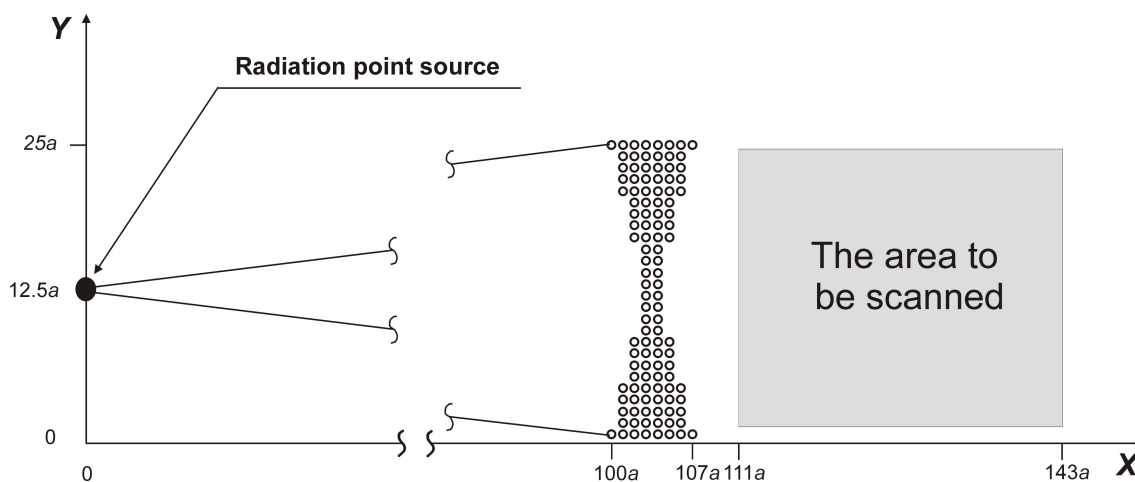
Figure 4.5: *The AFM scan methodology for determining the roughness on the pore walls.*

Each experiment involved scans in X as well as in Y direction. The AFM was a Park Scientific Instruments tool. The measurements were performed in a contact mode.

4.3 Photonic Crystals measurements

4.3.1 Microwave measurements

In order to approximate an incident homogeneous, plane wave at the frontal surface of the lens, a dipole was placed at a distance of $100a = 2.8m$ in front of it. This distance is kept unchanged for all measurements unless otherwise specified. The sending antenna was fed by an HP83752B

Figure 4.6: *The microwave measurements design.*

synthesized sweeper with a power of 16 dBm. In order to measure the electromagnetic field behind the lens, a receiving antenna was mounted on a (XYZ)-table (see figures 2 and 3). It was moved over an area of 700 mm by 800 mm and every 5 mm the field was measured. Hence, the total number of points measured was 22701. A drawing of the measurement design is shown in Fig. 4.6.

The received signal was amplified by an HP83051A microwave system amplifier. This amplified signal was fed into an ACSP2506-SN0898 detector diode. Since the source signal was amplitude modulated, the detected signal had a frequency of 1 kHz. This signal was processed by a Stanford Research Systems ST530 lock-in amplifier. The time constant used for the filter was selected to 300 ms, hence the sensitivity of the field scanner was relatively high. The whole system was controlled automatically by a microcomputer.

Because the measurement of the field distributions may be distorted by external signals and interferences caused by reflections, the set-up was placed into an anechoic chamber. The field distributions were measured from $\lambda = 2.5$ to 5.5cm (5.45GHz to 12GHz). The polarizations measured were TE (the magnetic field component of the incident wave is parallel to the dielectric rods) and TM (electric field parallel to rods). Doing this, the direction of the sending and receiving dipole was turned and the measurement procedure was repeated.

In spite of the high effort using an anechoic chamber, one cannot completely avoid reflections: the distortion of the electromagnetic field distribution has to be considered. Moreover the dipoles (35 mm length) exhibit a certain frequency characteristic. Therefore it was decided to relate the measurements ($E(x, y)$) to free space measurements without the lens ($E_0(x, y)$).

The performance of the lens is expressed using a ration called intensity gain (IG) defined as:

$$IG = \frac{E(x, y)}{E_0(x, y)} \quad (4.2)$$

Throughout the work the data are presented as a spacial distribution of the IG.

The rods for building the PC consisted of Al_2O_3 material, supplied by FRIATEC AG, Germany; with a nominal purity of 99.8 % and polished surfaces. The rods dielectric constant $\epsilon = 9$. The rods height was 50 cm, hence a factor 10 higher than the longest wavelength employed for the measurements. The rods where fixed between two styropores plates which have a dielectric constant for microwaves, $\epsilon \approx 1$. The location of the rods in the styropore plates were defined by a high precision borer controlled by a robot arm which moves with a precision of 0.1 mm.

5 Modeling electrochemical phenomena at the Si electrode

5.1 Current oscillations

5.1.1 General results and representations

In this chapter we will present simulations that were done under potentiostatic conditions; i.e. constant external potential, partially because the results presented here are new and/or from a larger area than earlier simulation runs [82, 18], partially to introduce important features of the simulations and their interpretation for the most simple case. The CBM produces features more complex than envisioned in its conception (as a good model should) and the results of a simulation may not only be unexpected and in need of an interpretation, but will tend to change the simplistic viewpoint that went into the initial model construction.

The "standard" system modelled consisted of a p-Si electrode with (100) surface orientation. The HF electrolyte concentration was chosen to be 0.024 mol L^{-1} . According to our experiments this corresponds to an etching rate of 0.04 nm/cm^2 ; this value being close to the one calculated by Sere et al. [83] [66]. Different anodization potentials ranging from 3.5 V to 8 V, with an increment of 0.5 V, were used. The area covered by the simulation was (300 x 300) nm^2 at a pixel size of 1.5 nm. The first or primary quantities of interest are simply the current density vs. time curves, i.e. $j_{an}(t)$, which allows by "inspection" to deduce the oscillation frequency n_{osc} and period $T_{osc} = 1/\nu_{osc}$ and the damping time constant τ_D .

Fig. 5.1 shows a typical result for 6 V anodization potential. The simulation yields pronounced current density oscillations as illustrated in the graph; also shown are four "snapshots" or "screenshots" of the oxide thickness and the potential losses taken at four characteristic times in the oscillation cycle as indicated. These screenshots were chosen to illustrate the initiation and synchronization of the CBs as well as the relatively quiescent state. Again, the whole area constitutes pretty much one "classical" domain by definition, simply because we have strong oscillations with currents close to zero in the minimum.

A new cycle will start with the nucleation of single and mostly uncorrelated CBs in the

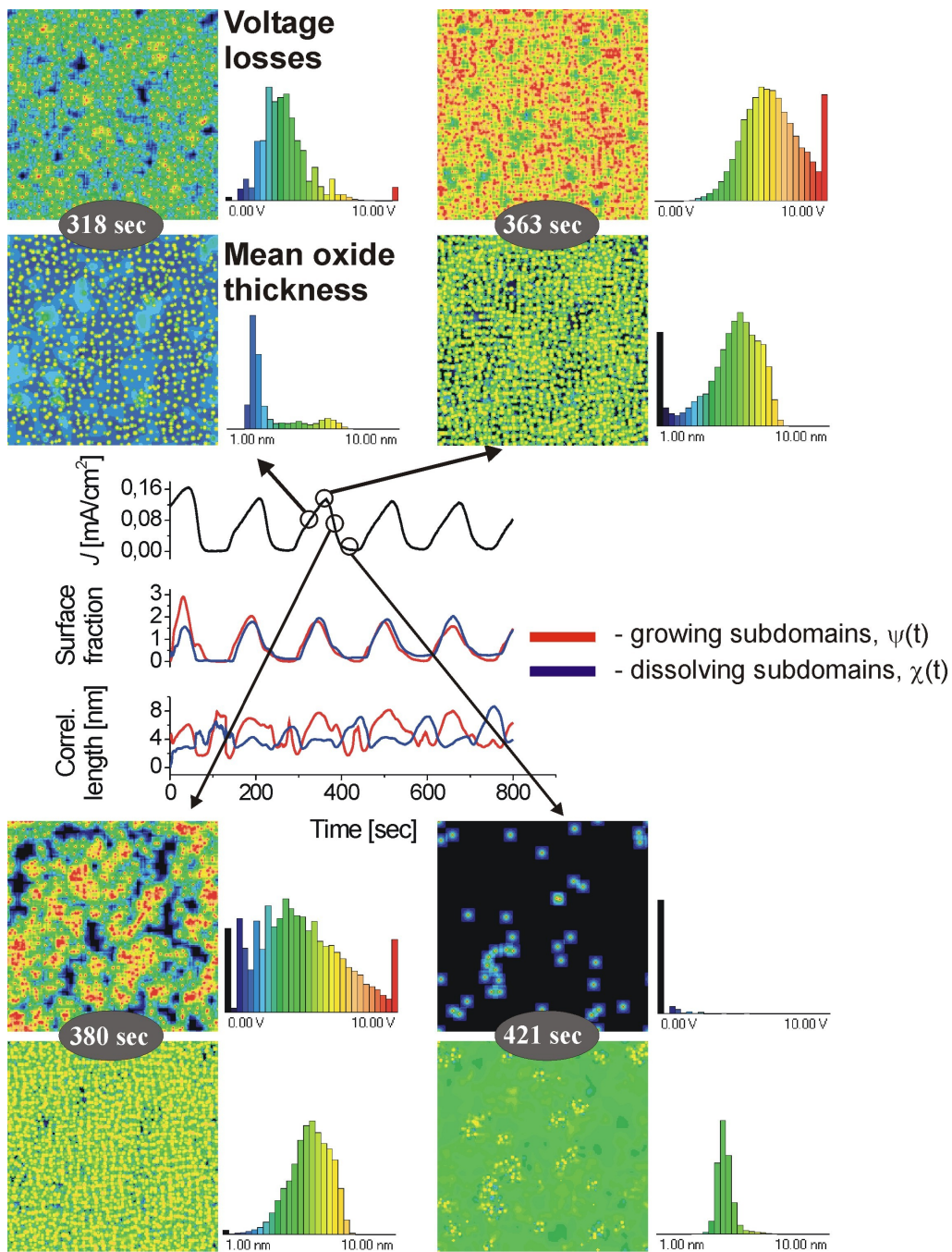


Figure 5.1: Example of a fairly stable current oscillation at $U_{an} = 6V$ together with four screenshots of the oxide thickness and the voltage losses at the times indicated. The large bars in the histograms at the end of the scale show the sum of all values outside the range and thus are thus not "real". The time development of the four most important fit parameters for the AFAP are shown, too; for details refer to the text.

low current phase as soon as the oxide has been sufficiently thinned by chemical dissolution; this is clearly visible at $t = 421$ s (a situation similar to the one shown in Fig. 2.12). The synchronization or phase correlation of the spatially separated CB clusters or subdomains is a direct result of the rather uniform starting conditions. While this would be a static synchronization in the sense introduced in Sec 2.4, it is a direct consequence of a dynamic synchronization, taking place during the previous current cycle. By now the reader should be aware of the fact that any linear description of what is going on encounters the "egg and hen" problem - there is no clear cause - effect relation, but a closed "logical circle".

As the oxide thinning continues, a rapidly increasing number of CBs is initiated and some dynamic synchronization takes place, e.g. at $t = 318$ s. Areas of still thinning oxide (blue) separate from areas of oxide growth (yellow) - clearly visible in the histogram. Nevertheless, the phase as defined before is similar everywhere. Note, for example, that in "phase space" the dark blue parts in the oxide thickness map (CB about to start) signify a phase comparable to the yellow area (CB almost over). Synchronization occurs because the CBs in active subdomains all turn off at about the same time by the mechanism discussed in Sec. 2.4, leaving back a passive subdomain that will quickly turn "unicolour" by the smoothing action of oxide dissolution. The current in this time frame is partially carried by CBs that have been initiated earlier but are still active, but is mostly due to CBs initiated within the time frame considered. Close inspection of the oxide thickness maps (also in the other figures containing those maps) show that there are always small areas of very thin oxide ("blue dots") in an active subdomain. This results from the de-synchronizing mechanism discussed before, which tends to prevent the nucleation of new CBs close to an active one because there is a reduced or even vanished electrical field, and thus allows severe thinning by chemical dissolution between active CBs. It is important to note that within an active subdomain there is a lot of "activity" on small scales in space and time that cannot be captured by a few screen shots, but presently only by movies and, to a much smaller extent by the correlation lengths obtained from the fitting routine described below.

At the peak of the current ($t = 363$ s), the average oxide thickness has considerably increased but there are still thin patches that can initiate the new CBs. Nevertheless, the rate of "old" CBs being extinguished now becomes larger than the initiation rate. On the downward slope of the current the production rate of new CBs is far smaller than the stopping rate of old ones, the current drops sharply. Simultaneously the oxide thickness starts to decrease because chemical dissolution now removes more oxide than is produced. It is interesting in this context to compare the situations at the current amplitude midpoints in the upward and downward part ($t = 318$ s and $t = 380$ s), where the current is identical, but the maps rather different. This is due to the fact that in the upward part the current is mostly due to CBs that start in

this time frame, whereas in the downward part it is mostly carried by "old" CBs.

Chemical etching smooths the relatively rough oxide as can be clearly seen in the $t = 421$ s screenshot. Conditions are now rather uniform, even if one started from a random oxide thickness distribution, and this helps to keep the process synchronized.

What can be seen in the oxide thickness maps of Fig. 5.1 by visual inspection (particularly well in the screenshot at 421 s) are the "smooth" and "rough" areas or subdomains, correlated to mainly oxide dissolution and oxide production via active CBs. The potential loss maps show that even more pronounced (with oxide-growing "rough" areas always "red-shifted" with respect to the background). It is evident (in particular with the 380 s potential loss map) that the two kinds of subdomains are rather irregular or non-circular; the correlation length thus is not a measure of their area. Increasing correlation lengths (as shown later) therefore may only indicate that subdomains are getting somewhat more "roundish", but not necessarily bigger.

At and after the current maximum, the active subdomains percolate and produce a large new passive subdomain pretty much identical at this point with the domain itself, which will get smoother (with respect to the oxide thickness distribution) during the downward turn of the current because the oxide dissolution smoothes the surface, and some newly nucleated CBs remove particularly thin parts. Together, a rather narrow oxide thickness distribution result as shown at $t = 421$ s, which provides the uniform background into which new small and sufficiently synchronized active CB subdomains develop in the next cycle. Synchronization of the spatially separated CB clusters or subdomains comes from rather uniform starting conditions - and this brings us back to the beginning of the cycle as described above.

The correlation length (CL) for the growing domains behaves in a quite similar way; it oscillates almost in phase with the current density. Up to the current peak at $t = 363$ s the CL increases, indicating a continuous increase of newly nucleating CBs. The decrease in the current density, which is caused by more CBs turning off than on, is also perfectly correlated with the decrease in the CL for growing domains. An aberrant behaviour, however, expresses itself in the intermediate CL peak at the current minimum. This most likely relates to the nucleation of new CBs in areas, which until this moment underwent only dissolution and where no CBs could nucleate since the potential losses from the neighbouring CBs were too strong. However, even after this intermediate peak the CL will decrease again, and this is caused by the fact that the next batch of freshly nucleated CBs are very strongly localized and too far away from each other to be closely correlated.

The CL for the dissolving domains is essentially anticyclic, which is what would be expected. Its time sequence also shows some finer structure related to the CB dynamics, but we will refrain from a detailed discussion at this point. Suffice it to mention that the data compression

as described in the foregoing does allow to a certain extent to arrive at a better interpretation of what is actually going on.

Figure 5.1, for the sake of completeness, also shows the time development for the surface fractions as defined before. While quite intriguing curves resulted, their interpretation will not be attempted here.

5.2 Damped current oscillations

Having progressed to this point, it is now of interest to look at the simulation of damped current oscillations, which must, by definition end in a loss of synchronization and the presence of several domains with random phases. One example is shown in Fig. 5.2.

On a first glance, nothing resembling "naive" domains is visible. On a second glance, keeping in mind what has been pointed out before, and just looking at the potential loss maps, one sees that there is indeed a large frazzled domain in the map related to the second current maximum, $t = 149$ s. The areas in bright red (and the areas in dark blue!) have comparable phases and percolate. In the fourth current maximum at $t = 365$ s, carrying only about 60 % of the maximum current, the red-dark-blue "domain" is decidedly smaller and the connected greenish areas - correlated to domains with other phases - are larger. Both correlation lengths oscillate weakly while macroscopic oscillation in the current density can still be observed, and then become stationary. Their behaviour during the oscillations is similar to that discussed for the stable oscillations, although both parameters are very noisy. Due to comparatively lower anodization potential, the overall number of active CBs on the surface is also smaller, which clearly leads to smaller CLs.

Once the oscillations are damped, both CLs come to the same value and exhibit no clear macroscopic oscillation, just as the current density does. At this point the whole surface is oscillating at random phases (equivalent to many domains). This is also very nicely pictured by the potential losses maps taken at different (still slightly visible) peaks in the damped region of the current density.

At this point it becomes clear that a discussion of simulation results in the framework of simple "classical" domains does not do justice to what really is going on at the electrode, and this justifies the deeper concept of domains and especially subdomains as presented in Sec. 5.1.

It remains to be seen if (difficult to calculate) maps of the CB phases will produce clearer visual images of the domains, but to some extent this is a moot question. Everything of physical interest is already contained in the data, and all measurable quantities are easily derived as will be shown in what follows.

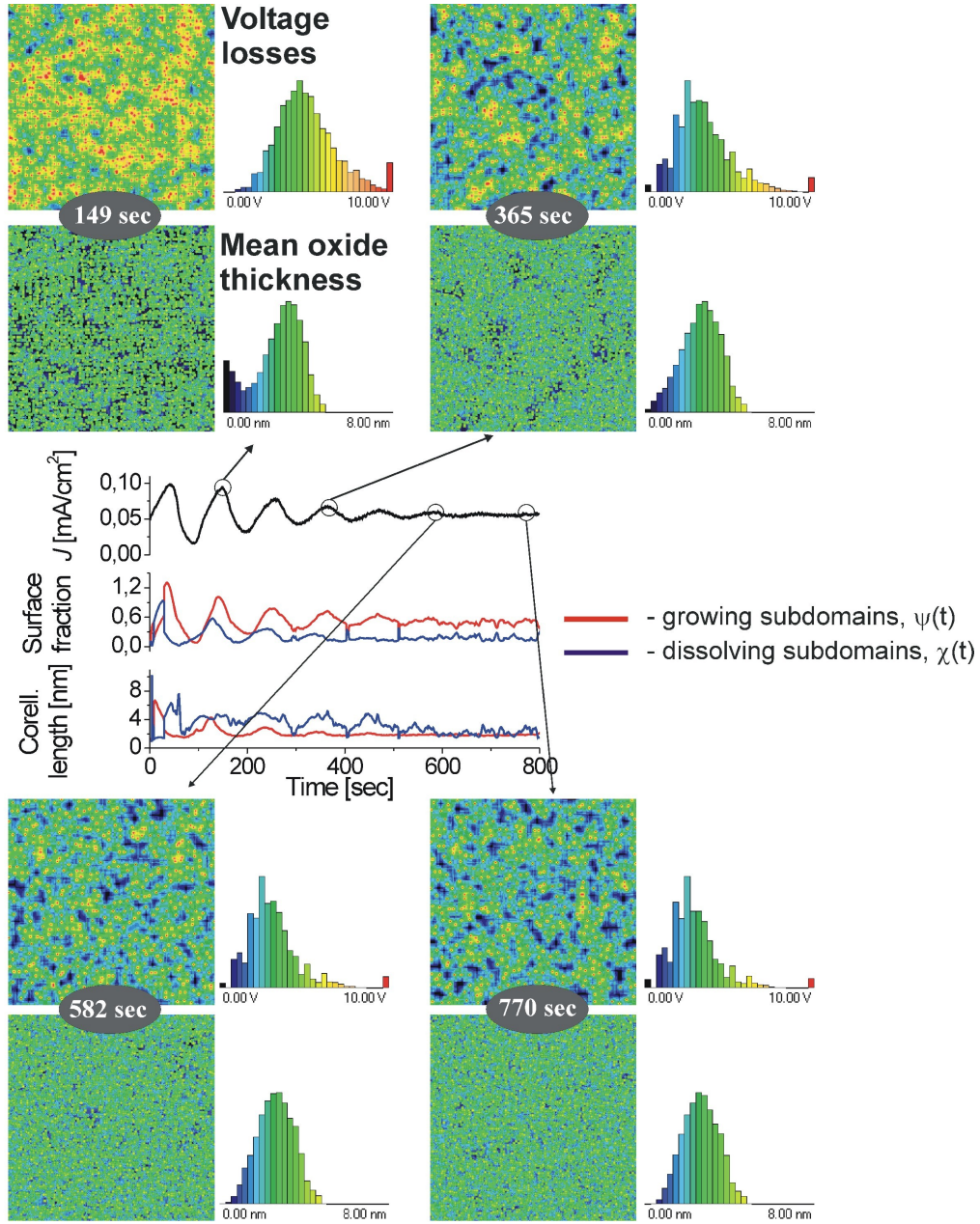


Figure 5.2: Damped current oscillations with snapshots of the oxide thickness and the voltage losses; the time development of the correlation lengths and the subdomain surface fractions are also given.

5.2.1 Potential dependence of prime quantities

The nucleation of a new CB will generate potential losses in its neighborhood according to the Eq. 2.17 and thus lower the electric field strength in its surroundings as shown in the potential loss maps in several figures. According to Eqs.2.13, this decreases the probability for the nucleation of a new CB, or the lifetime of an existing CB, respectively. This implies that the degree of synchronization depends on the average number of active CBs, or, since active CBs carry all the current, the average current. Weak synchronization will lead to damped oscillations, described by exponential decay of the amplitudes with a time constant t_d , and this is what will be observed at the onset of oscillations around the current minimum after the $I_o x$ peak. However, it is a well established experimental observation that increasing the anodization potential, while hardly changing the average current, leads to more stable oscillations, i.e. the damping time constant t_d will increase substantially with increasing potential.

The CBM should reproduce this behaviour without any additional adjustment. That this is indeed the case is shown in Fig. 5.3a. The current vs. time results are shown for three values of the potential, and from a number of simulations at various potentials the oscillation period T_{osc} and the damping time constant t_d have been extracted and plotted. Starting with strongly damped oscillations for $U_{an} = 3.5$ V, the oscillations become rather stable at $U_{an} = 5.5$ V and beyond. The oscillation period increases linearly with the applied potential; this is shown in Fig. 5.3b, together with the damping time constant in Fig. 5.3c. These results are in good agreement with measured ones as shown in Fig. 5.3d) - e) taken from [84].

It remains to interpret the potential dependence of the damping time constant, a quantitative result that the model produced "automatically". In this case it is easy: For all else being equal, a higher anodization potential increases the nucleation probability for new CBs and decreases the stopping probability for existing CBs. In other words, the effects of the de-synchronization mechanism are smaller and this favours synchronization. All else, of course, remains not equal if the potential is raised, but whatever happens in a more subtle way and influences the synchronization/de-synchronization behaviour (e.g. changes in the thickness distribution of the oxide and the frequency of the oscillations) will be "automatically " taken care of by the CBM.

As can be seen from Fig. 5.3c, oscillations decay more or less instantaneously below a minimum potential of about 4.5 V, after that t_d increases linearly. At least for the parameter space scanned here, oscillations are never undamped (in accordance with [85]), although it may take many oscillation periods before that becomes noticeable.

Figure 5.4 gives some examples for the average oxide thickness, the oxide roughness and the specific capacitance for damped oscillations (a) - c) and stable oscillations (d) - f). The slight

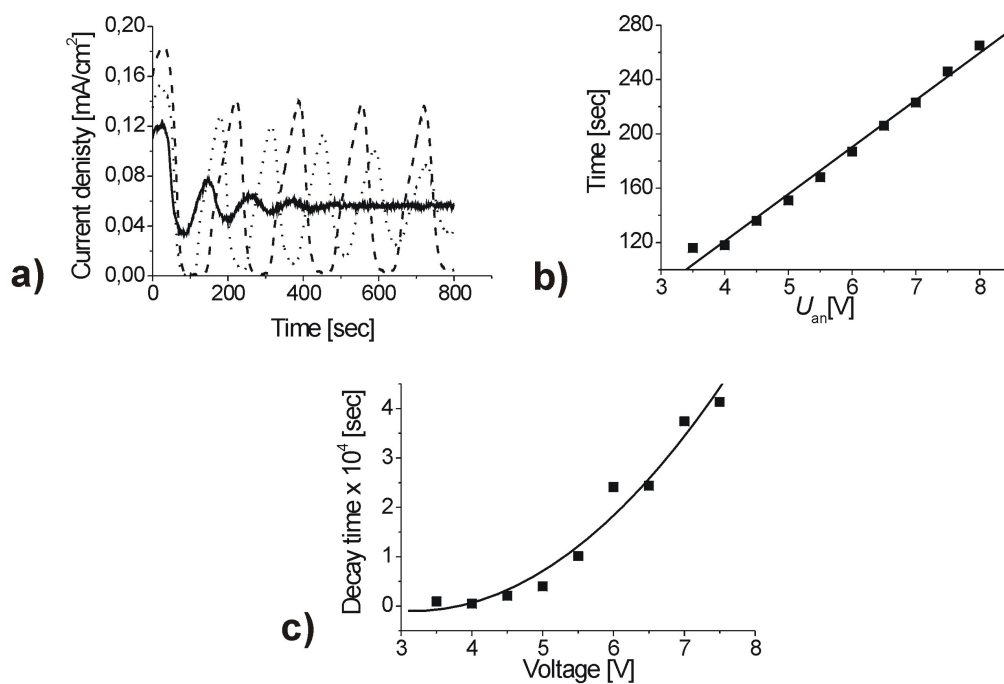


Figure 5.3: *Current density oscillations as a function of the applied voltage. Current density vs. time showing damped oscillations with different degrees of damping (a). Following anodization voltage was used: solid line 3.5 V; dotted line 4.5 V; dashed line 5.5 V. Oscillation period $T = 1/\nu$; increasing linearly with time (b). Decay time constant τ_d of the oscillations (c).*

difference in phase of the oxide roughness oscillations and current density oscillations (Fig. 5.4 a), d) is important. The maximum in the oxide roughness coincides with the maximum of the active CB number (not displayed) - as it should. A large density of CBs will always induce faster synchronization as compared to a smaller density. The minima in the current and the oxide roughness coincide rather well, indicating that as soon as the current drops, i.e. active CBs "die" and hardly any new ones are nucleated, the dissolution of the oxide is the predominant oxide modifier in the system. This will smooth the oxide surface (but not the interface) and the roughness will decrease - a fact that is clearly seen in Fig. 5.4 a) and d).

5.3 Current oscillations induced by extrinsic synchronization

Insufficient direct or dynamic synchronization leads to damped oscillations as pointed out in Sec. 2.4. Experimentally it was shown that oscillations could be restarted after they vanished by suddenly changing the applied potential to a higher or lower value [41].

This experiment is easily implemented in the CBM; Figure 5.5 shows some simulation results. A typical (damped) oscillation for 4 V is started and run until it has all but disappeared. Then the potential is either decreased to 3 V (Fig. 5.5a), or increased to 5 V (Fig. 5.5b). In both cases the system starts to oscillate again, just as found in experiments [85].

Again, the model reproduces the experimental reality, but now this needs to be interpreted. From the viewpoint of the CBM both results are easy to understand. A damped oscillation finally results in some relatively constant density of CBs over time with random phases. If the potential is suddenly decreased, active CBs will stop prematurely, and new ones will not be nucleated. The current drops to (almost) zero, because most current bursts stop at the same time - i.e. they are now synchronized. Activity starts again as soon as the oxide has thinned down sufficiently, and since this process homogenizes its thickness to some extent, many CBs start within a narrow time frame, i.e. they are synchronized once more.

If the potential is increased, the situation is even more straightforward. Once the potential is increased to 5 V, the "history" of the CBs on the electrode surface is not so important any more. Most CBs will keep "burning", and new ones are nucleated right away. The current will immediately increase; it will come down, as discussed before, as soon as a synchronized domain has formed. Again, the electrode has been reset to the conditions typically prevalent at the start of a 5 V cycle.

Chazalviel and Ozanam [36] explain this (and other) oscillatory phenomenae as a result of some "resonance" effect that is taking place at the electrode under perturbation. The results

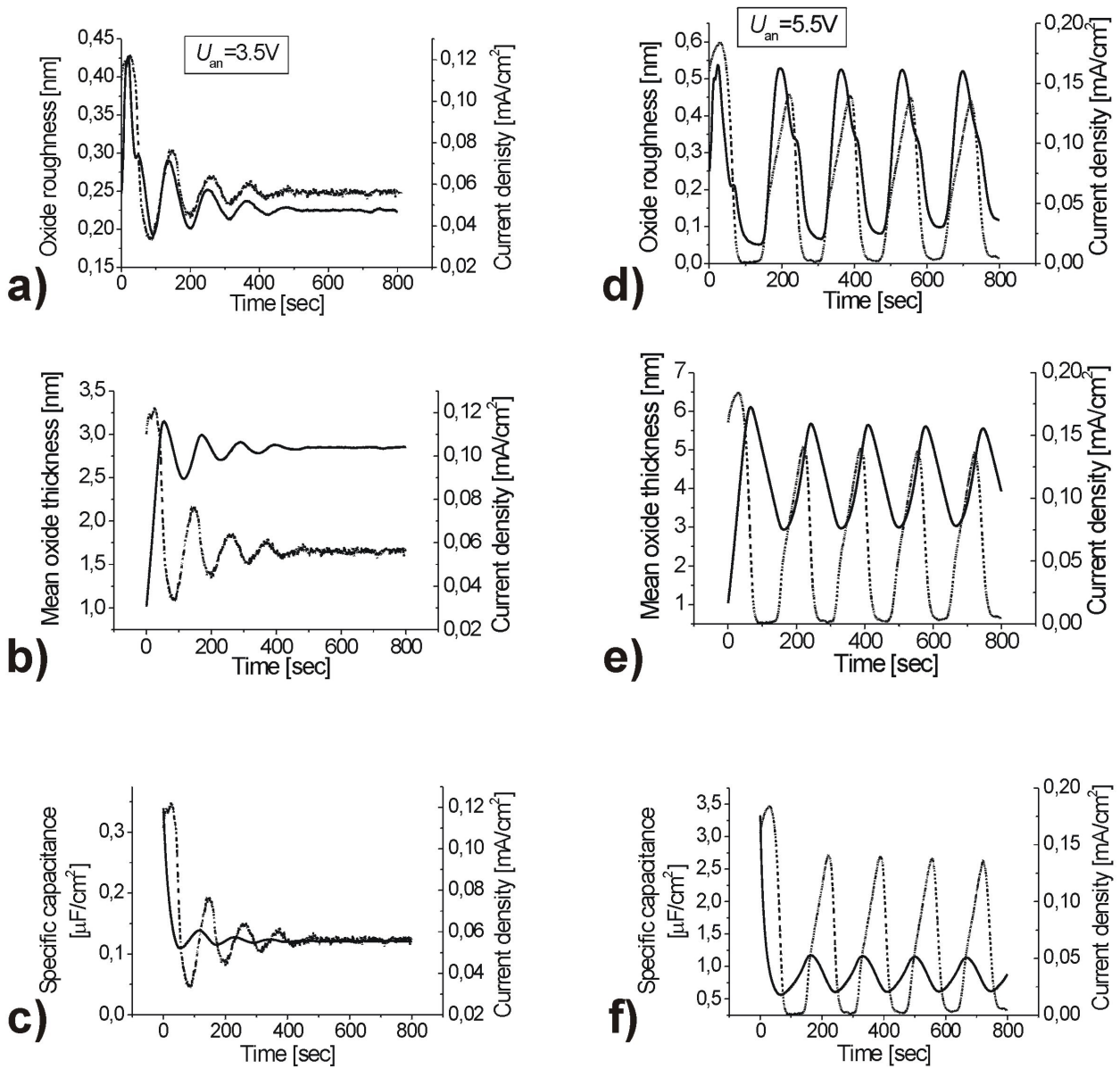


Figure 5.4: Calculations of the oxide roughness Y (a) and (d), average thickness $\langle s \rangle$ (b) and (e), and capacitance C (c) and (f). Considered are damped oscillations (a-c) and stable oscillations (d-f). All the plots also contain the current density curve (dashed line).

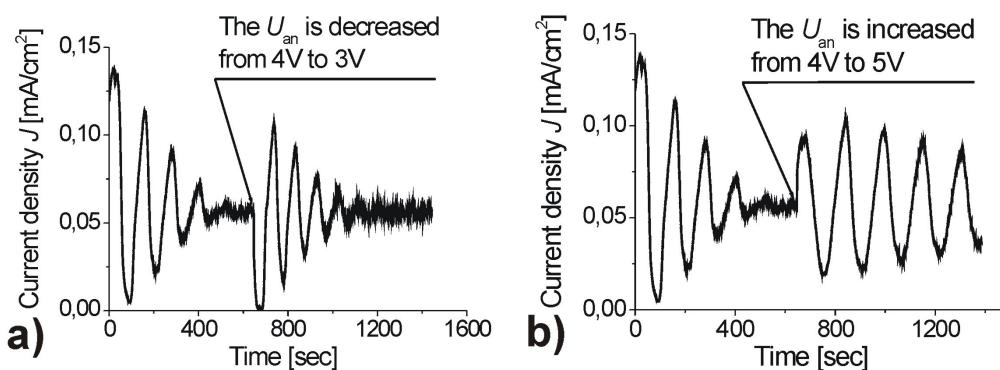


Figure 5.5: Voltage changes induce new oscillations. Decreasing the voltage by 1 V (a), increasing the voltage by 1 V (b).

presented here reproduced the measurements shown in [85]. The term "resonance" with all the implications it carries is not needed, however, to understand the phenomenon.

5.4 Forced current oscillations

So far, strict potentiostatic conditions were used; at best the potential was changed in sudden jumps. Considering the electrode as a system of stochastic micro-oscillators with a certain (average) time constant $1/\nu_{osc}$, new effects can be expected if the potential is not kept constant but is modulated with a (cycle) frequency $\omega_{mod} = 2\pi\nu_{mod}$ of its own, e.g. sinusoidally as

$$U_{an} = U_{an} + \Delta U_{\omega} \sin \omega_{mod} t \quad (5.1)$$

For all following simulations and experiments the amplitude ΔU_{ω} is chosen to be 1.5 V whereas ω_{mod} is a multiple of the intrinsic oscillation frequency $2\pi\nu_{osc}$; i.e. the oscillation frequency obtained for constant anodization potential (4 V in the case shown here).

Fig. 5.6a and -b shows a direct comparison of "simple" oscillations from the simulations and an experiment at a potential of $U_{an} = 4$ V. The two oscillation frequencies are $\nu_{osc} = 9$ mHz for the simulation and $\nu_{osc} = 20$ mHz for the experiment. The difference is trivial; it would be no problem to match the simulated frequency to the observed one, but that is not the issue here. In both cases the oscillations essentially disappear after 4 - 6 cycles; which is more important here than a perfect match of the frequency. The modulations used in the simulation and the experiment refers to the intrinsic frequency of each case. The results can be seen in Fig. 5.6c) and -d. In both cases the current density oscillations will couple to the external frequency, and the oscillations now become stable in time, albeit on occasion only after a short transitory period in the experimental case. This transitory period (most pronounced in Fig. 5.6d) may

simply be due to a kind of "initialization" of the real Si surface, which is covered with a native oxide and possibly some organic residue that need to be removed first.

Figures 5.6e and -f show the current density oscillations when the anodization potential is modulated with half the frequency of the intrinsic oscillations. The resulting oscillation contains both frequencies in some kind of beat pattern. The same can be observed in Fig. 5.7g and -h, where the anodization potential is modulated with twice the intrinsic frequency. Some beating is observed for all modulation frequencies ω_{mod} , harmonics were chosen here to maximize the effect of producing more stable oscillations by modulations. The detailed experimental conditions used for the measurements in Fig. 5.6 can be found in [86]; essentially an HF(aq) electrolyte concentration of 0.024 mol L⁻¹, was used for (100) p-type (20-30) Wcm Si sample of 1cm² area with a metallization layer on the back ensuring a good ohmic backside contact. In comparison to the simulations, where the sample area is set to be (300 x 300) nm² = 0.09 m², the area used in the experiments is several orders of magnitudes larger. Keeping this in mind, together with consideration of the usual scaling problems for this kind of simulation (see also the discussion), the agreement is quite good.

5.5 Potential oscillations

5.5.1 General remarks

Potential oscillations, i.e. oscillations measured between the reference electrode and the sense electrode on the sample backside, can occur at a Si/HF interface under galvanostatic conditions, i.e. for a constant anodization current. This fact already proves that the physical mechanism behind the oscillations must be more complicated than a "simple" positive / negative feedback stochastic oscillator running in an area of the global characteristics where a differential negative resistance is observed [87]. That is also the reason why stable potential oscillations are relatively hard to obtain, as also shown indirectly by the relatively small number of published papers dealing with this topic. For high anodization currents [50, 51] and an "exotic" electrolyte [88] not containing HF, Parkhutik found long lasting stable oscillations [89]. Lehmann investigated the potential and the oxide thickness oscillations at relatively high electrolyte concentrations [49, 20].

Potential oscillations are qualitatively quite different from current oscillations for a variety of reasons that are cursorily given and compared in Table 5.1. Assumed is a certain capacity C of the system and a certain total series resistance R_S . The table contains a few self-explanatory points, but mainly serves to point out the major difference of potential oscillations to current oscillations and to introduce some of the finer points for the implementation of the CBM as

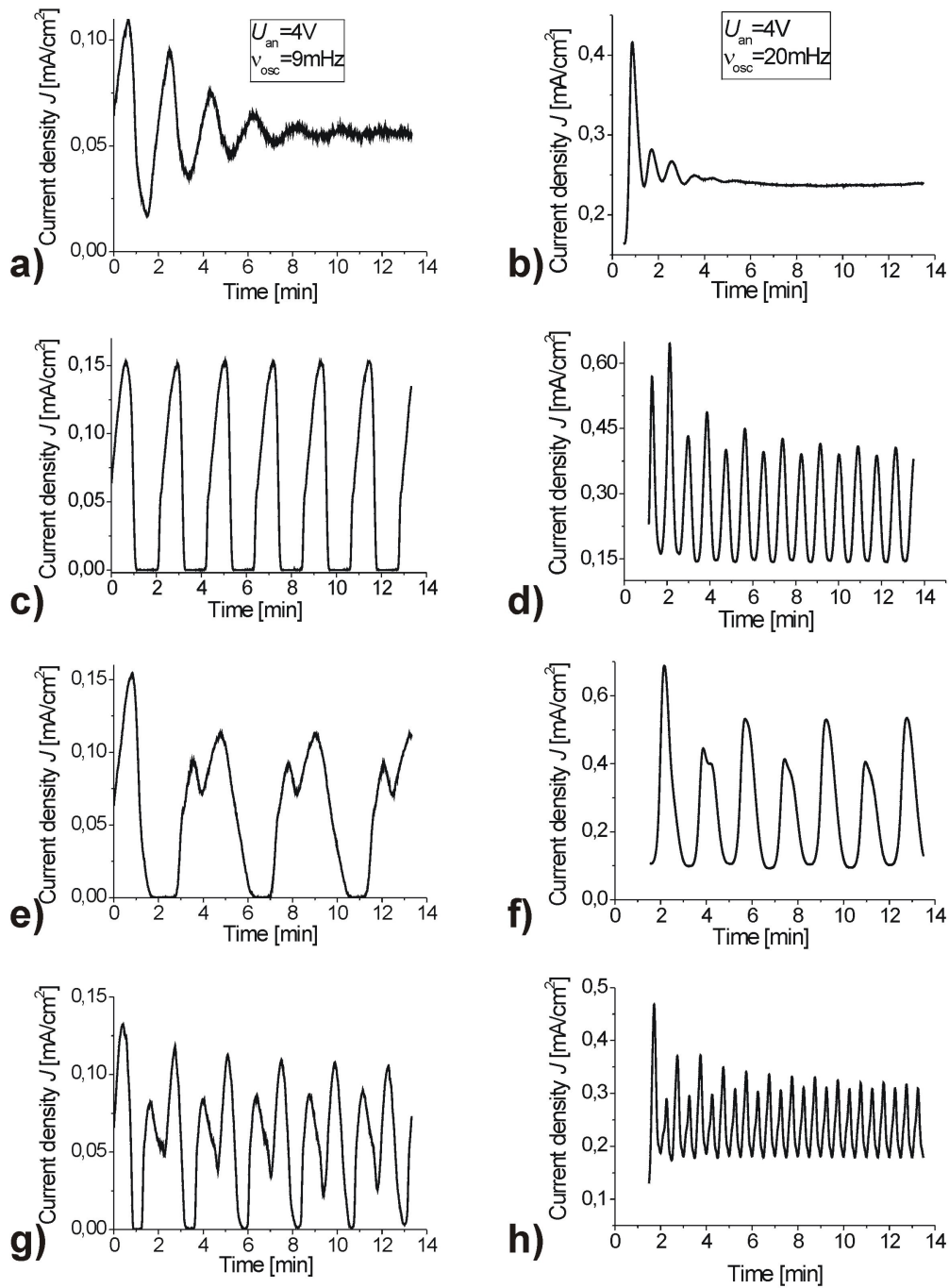


Figure 5.6: *Simulated (left column) and measured (right column) current density oscillation for forced oscillations and an average anodization voltage $U_{an} = 4$ V. Reference with zero amplitude, i.e. no modulation (a) and (b). Modulation frequency $\omega = 2\pi\nu_{osc}$ (c) and (d). Modulation frequency $\omega = \pi\nu_{osc}$ (e) and (f). Modulation frequency $\omega = 4\pi\nu_{osc}$ (g) and (h).*

Table 5.1: Comparison of galvanostatic and potentiostatic conditions for electrode oscillations.

Parameter	Current oscillation	Potential oscillations
Total current density j_{an}	$j_{an} = j_{an}(t)$	$j_{an} = const.$
Local current density $j_{loc}(x, y, t)$	CBs $\Rightarrow j_{an}(t) = \sum j_{loc}(x, y, t)$	CBs $\Rightarrow j_{an}(t) = \sum j_{loc}(x, y, t)$ i.e. local currents still oscillate!
External potential $U_{an}(t)$	$U_{an} = const.$	$U_{an} = U_{an}(t) =$ $V_{SiO}(x, y, t) + R_S I_{an}$
Local potential on the Si surfaces $V_{SiO}(x, y, t)$	equipotential surface
Correlations between CB micro-oscillators	Random phases: $I_{an} = const.$	Random phases: $U_{an} = const.$
Displacement current density j_{cap}	Phase coupling: $I_{an} = I_{an}(t)$	Phase coupling: $U_{an} = U_{an}(t)$
Basic oscillation mechanism	$j_{cap} \approx U_{an} \times dC/dt$	$j_{cap} \approx C \times dU_{an}/dt$
	Unimportant	Important
	CB interaction	CB interaction
	\Rightarrow synchronization and de-synchronization \Rightarrow domain formation $\Rightarrow j_{an}$ oscillations	\Rightarrow synchronization and de-synchronization \Rightarrow domain formation \Rightarrow Resulting j_{an} oscillation suppressed by potential oscillations
Shape	Simple, sinusoidal	More complex, saw-tooth, double peak, ...
Run-away effects	No; $j_{an}(t)$ is always self-limiting	Yes; U_{an} may exceed all limits. New effects.
Experiment	Stable oscillations easy to obtain at all HF conc.	More difficult to obtain, especially at small HF conc.

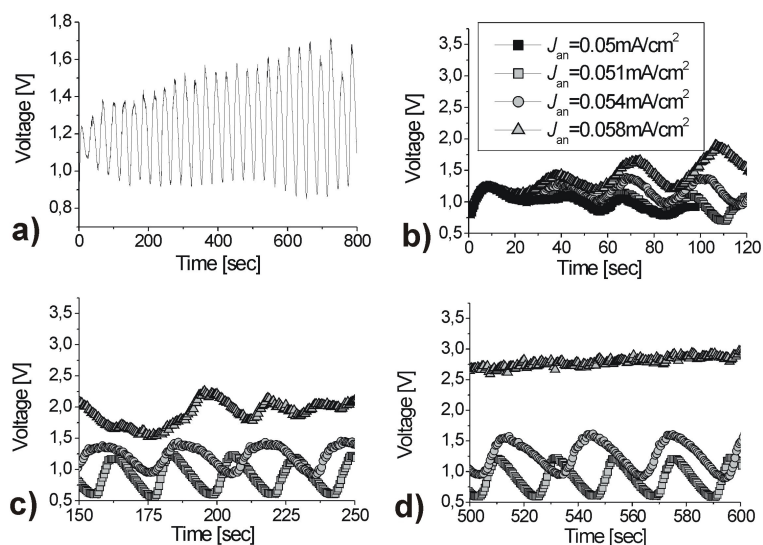


Figure 5.7: The first simulated voltage oscillations at a Si electrode. Stable voltage oscillations for an anodization current of $J_{an} = 0.054 \text{ mA/cm}^2$ (a). Voltage oscillations at slightly different (see inset in (b)) anodization currents (b) - (d), the time period 150 s - 250 s (c), the 500 s - 600 s interval (d).

mentioned in Sec. 2.4.

1. The potential is an intensive variable; it does not depend on the sample size. More simply put, the potential, in a first approximation, is the same everywhere at the sample surface at any instance in time as long as no lateral currents are flowing. This does not contradict the de-synchronization mechanism introduced in Sec. 2.4, which firstly introduces only deviations from an equipotential surface on a nanoscopic scale by allowing lateral current flow components, and secondly is an expression of what may happen if one looks beyond a first approximation.
2. The current still could have any arbitrary local value, but the sum of the current over all pixels must be constant at all times.
3. The oxide capacitor C , as defined and calculated in Sec. 5.2.1, draws a displacement current j_{cap} , which must be included in the current flow balance. For current oscillations, shown in Sec. 5.1, j_{cap} was neglected since it is quite small. For potential oscillations, it must be included, however, and this provides another feedback mechanism.
4. The potential $V_{SiO_2}(x, y)$ at the sample surface is not identical to the external potential U_{an} , but always diminished by $R_{ser}I_{an}$ i.e. the potential drop in the total series resistor. It is also varying laterally around active CBs due to the mechanism discussed before. For the same reason R_{ser} is not an absolute constant but depends somewhat on the number

of active CBs and thus provides another feedback mechanism that can be crucial for the occurrence of oscillations (cf., e.g. [87]). The part of R_s coming from the electrolyte conductivity etc., was of small importance for the results shown here (and in Sec. 5.1) and will thus be neglected, while the CB-related part is fully accounted for.

5. The basic mechanisms for the synchronization (or phase correlations) of CB's due to local interactions have not changed under galvanostatic conditions; they are still due to local interactions. Current oscillations would result, and that can only be avoided by changing the potential "in reverse": if the current tends to go up, the potential must come down and vice versa. This is what a galvanostat does (which is nothing but a constant potential source with a hardware feedback control loop) and that is what the CBM does for galvanostatic "experiments" with a software feedback loop.
6. While there is always some well defined average current for any (reasonable) potential applied to the system, the reverse statement is not true: currents fed into the system that are too large will grow more oxide than can be dissolved by the HF at any condition. Galvanostatic conditions then necessitate continuous potential increases, i.e. a steady state in the form of stable oscillations, damped oscillations, or no oscillations but constant potential, is never reached. The system virtually "explodes" (sometimes experimentally, too, if no external fuse blows and a sufficiently powerful potentiostat is used).

In hindsight, it is far easier to conceive of electrode oscillations not as current or potential oscillations *per se*, but as electrode impedance oscillations, which, together with external series resistances and feedback loops, lead to the effects observed under the conditions chosen.

It is worthwhile to mention that pronounced potential oscillations have also been found during pore growth; the earliest and most detailed work was published for InP, together with a first simple "resistor" model [17] based on CB dynamics. While this approach was (and is) valid for potential oscillations occurring if the current flows through pore tips exclusively, it is not sufficient to describe the potential oscillations occurring during electropolishing as is the case here.

5.6 Results of simulations

Simulating potential oscillations with the CBM should be possible in principle, because the basic claim of the CBM is that it contains all necessary ingredients for all electrode phenomena found within the confines of the model as discussed in Sec. 2.4. Nevertheless, the algorithms

have to be changed to account for the constant current condition, and some finer points like the charging/discharging of the oxide capacitor via the dC/dt term, and in particular via the dU/dt term, which is no longer zero, should be considered. In short, the following measures were taken:

- For every time frame (typically 5 ms) the total current was compared to the preset current; deviations cause a matching potential change for the next time frame. For reasonable time frames this causes rather noisy constant current conditions and introduces a kind of "numerical" time constant that acts like a capacitor. This is essentially what a potentiostat does, too, except that its operation is far smoother than the simulation.
- The capacitive displacement current as defined above was included in the simulation.
- The probability curves for switching CBs on and off had to be slightly modified - they have to be somewhat "softer" compared to the potentiostatic case.

Putting everything together, it was possible for the first time to simulate potential oscillations at the Si electrode; a typical result is shown in Fig 5.7.

The necessary change of the probability functions was a bit puzzling at first, but appears to be a logical necessity upon closer inspection: As discussed earlier, the probability functions not only define the dynamics of the CBM, but are also directly related to the oxide quality. During the current oscillations, the mean oxide thickness values are always well above 2 nm, however, this is not the case for the potential oscillations [20], where the oxide thickness locally and temporarily reaches values as small as 0.7 nm. This magnitude is already comparable to the suboxide thickness; suboxide here meaning basically a different form of SiO_2 at the Si - SiO_2 interface. Independent of the peculiar properties of the suboxide, the breakdown properties of sub-nm oxides must be expected to be different from that of "thick" generic anodic SiO_2 and that must change the probability functions in the "softer" direction. In essence, it was necessary and sufficient to shift the stopping probability function in Fig. 2.9 in the direction of the higher oxide thickness, i.e. the magnitude of E_{min} in Eq. 2.14 was set to 0.1 V/nm.

Figure 5.7a) shows simulated (nearly) stable potential oscillations at a current density of $j_{an} = 0.054 \text{ mA/cm}^2$. Although the amplitude of the oscillations is slowly increasing with time, the frequency and average potential remain rather constant. Fig. 5.7b) - d) demonstrate the sensitivity of this type of oscillation to small changes in the current density. For $j_{an} = 0.05 \text{ mA/cm}^2$ (filled squares curve) the oscillation is heavily damped and disappears after a few cycles, while for $j_{an} = 0.051 \text{ mA/cm}^2$ and $j_{an} = 0.054 \text{ mA/cm}^2$ (empty squares and circles, respectively) stable oscillations are obtained. For $j_{an} = 0.058 \text{ mA/cm}^2$ (empty triangles) so-called "exploding" oscillations result - the potential increases steadily beyond any limits.

Three time cuts are shown in Fig. 5.7 b) - d) rather than one curve so as not to obscure details. Note that at 0.05 mA/cm^2 the oscillations disappeared after less than 100 s, but that an increase of the current density of just 2% will cause oscillations stable for at least 800 s. An interesting behaviour can be observed for the oscillation at $j_{an} = 0.058 \text{ mA/cm}^2$. It exhibits a relatively stable oscillatory behaviour during the first 120 s, at least with regard to the frequency. Somewhat later it loses its "monochromatic" behaviour and becomes "coloured" and unstable, i.e. it oscillates with several frequencies until it is just "noisy". This is a hallmark of insufficient synchronization of the CBs caused by the fragmentation of the surface in domains that are in different phases at any instance of time (e.g. mostly dissolving oxide or mostly growing oxide).

In general, the behaviour shown in Fig. 5.7b) - d) is compatible with the experimental findings that stable potential oscillations are very difficult to obtain, especially at very low electrolyte concentrations. According to Hasse [84] and Prange [90] stable potential oscillations are found in a very narrow current interval. Usually a change in the anodization current within 10% will lead to either strongly damped or "exploding" oscillations, a feature that is essentially reproduced in the simulation results presented here. Hasse [84] had to apply a constant current of 0.12 mA/cm^2 for about 60s first, followed by a decrease of the current to the "working" level of 0.04 mA/cm^2 in order to be able to obtain stable potential oscillations. Prange [90] and Lehmann [20] used highly concentrated electrolytes (5 wt% HF), where it is somewhat easier to produce potential oscillations.

An analysis of the oscillation period over a narrow interval of current densities, i.e. $J_{an} \in [0.05; 0.06 \text{ mA/cm}^2]$ shows that with increasing anodization current the oscillations period will increase as well, as shown in Fig. 5.8a). In order to have some assessment of this, a linear fit of the average potential as a function of time was made; the slope of these fit curves are shown in Fig. 5.8 b). Damped oscillation would exhibit a negative slope, while zero slope indicates the range of stable oscillations; slopes > 0 indicate "exploding" oscillations. The results confirm once more that the range for stable oscillation is indeed very narrow, and that a small change in the current will drive the system in a non-stable oscillatory state.

As in the case of current oscillations, the CBM model simulations allow to extract many more quantitative data. Figure 5.9a) shows the mean oxide thickness for the "standard" potential oscillation at $J_{an} = 0.054 \text{ mA/cm}^2$ at high resolution in the time interval 400 s - 600 s. together with the potential oscillations for reference. As one can see, the mean oxide thickness oscillates with the same period as the potential; the only difference being that the oxide oscillation is advanced in phase. Lehmann observed experimentally a phase difference between the mean oxide thickness and the potential [20]. Another important simulation result is that the mean oxide thickness never reaches zero, which is also in full accordance with

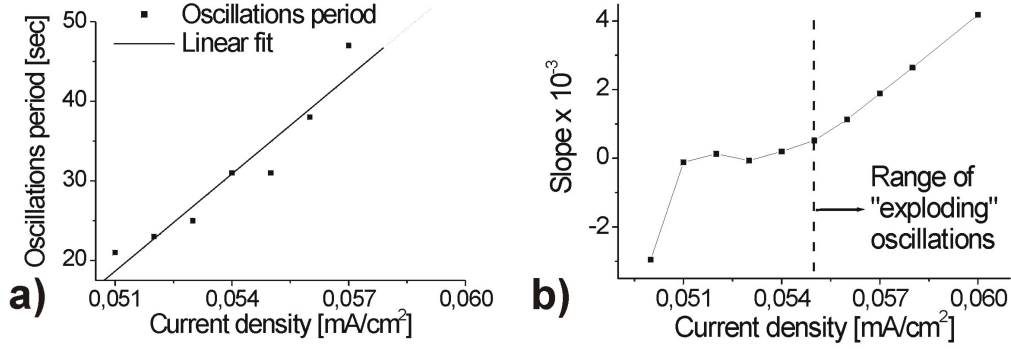


Figure 5.8: The oscillations period $T_{osc} = 1/\nu_{osc}$ as determined from the time interval from 100 s to 600 s (a). Slope of the average voltage (linear fit) slopes > 0 indicate "exploding" oscillations (b).

the measured data [20]. Figure 5.9a shows a very weak variation of the oxide thickness, i.e. peak-to-peak amplitudes of about 0.01 nm, furthermore the average oxide thickness does not vary significantly, at least in the range of stable oscillations. Figure 5.9b shows the behaviour of the oxide thickness for the full time scale for two distinct anodization currents, i.e. $J_{an} = 0.054 \text{ mA/cm}^2$ (stable) and $J_{an} = 0.05 \text{ mA/cm}^2$ (strongly damped). In contrast to the stable oscillations, the oxide thickness will continuously decrease for the damped case, arriving at an oxide thickness less than 0.65nm, which is deemed an unphysical value and causes the simulation program to simply stop (as indicated in Fig. 5.7b) and Fig. 5.9b). Very small values for the oxide thickness as presented in Fig. 5.9b indicates that the capacitive effects outlined above can become large. Generally, the total current, i.e. the anodization current at the electrode, is always given by

$$J_{an} = J_{cap} + J_{ox} \quad (5.2)$$

and the oxidation current J_{ox} will be given by the algebraic sum of the active CBs times their specific current ICB at any specific instance in time, i.e.

$$J_{ox} = \frac{\sum_n I_{CB_n}}{A_{electrode}} \quad (5.3)$$

where n is the number of the CBs and $A_{electrode}$ is the area of the electrode. From the definition of a capacitance $C = Q/U$ (Q = charge stored in C at U) it follows for the capacitive current density $J_{cap} = dQ/dt$

$$J_{cap} = \frac{dQ}{dt} = \frac{dC}{dt}U + \frac{dU}{dt}C \quad (5.4)$$

Relation 5.2 will add the desired capacitive effects to the model. The parameter C in Eq. 5.4 is the oxide capacitance, which in turn depends on the oxide thickness; which is continuously

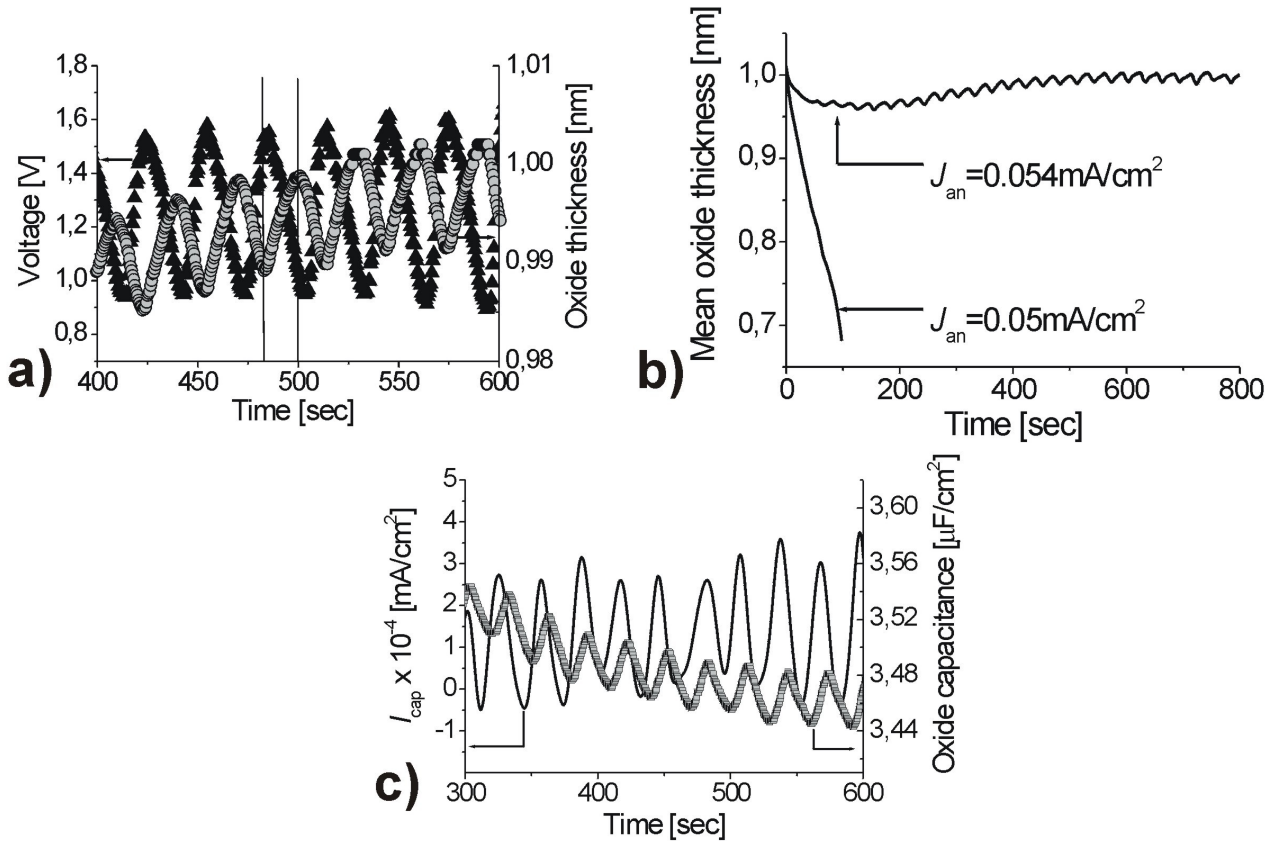


Figure 5.9: Voltage oscillations together with oxide thickness oscillation at anodization current $J_{an} = 0.054 \text{ mA/cm}^2$ (a). The left ordinate axis belongs to the voltage, the right one to the oxide thickness. Oxide thickness oscillations belonging to damped and stable oscillations, respectively (b). Oscillation of the capacitive current, after a FFT filtering, together with the oxide capacitance at $J_{an} = 0.054 \text{ mA/cm}^2$ (c).

calculated by the simulation program at any instance in time. C can thus easily be calculated (assuming a dielectric constant of $\epsilon = 3.9$ and the capacitive effects are thus intrinsically contained in the CBM. Figure 5.9c) gives an idea of the magnitude of the capacitive effects; it shows the calculated capacitance and the capacitive current for the standard case $J_{an} = 0.054 \text{ mA/cm}^2$ in the time interval between 270 s and 400 s. The oscillatory behavior of the capacitance and the capacitive current is clearly visible, although the current curve is very noisy (here plotted after a FFT filtering). The capacitive current is in the order of 10^{-4} mA/cm^2 and thus at least two orders of magnitude smaller as the anodization current; it is, however, underestimated due to numerical idiosyncrasies explained. The capacitive behavior, however, is part of a feedback cycle and an absolute "must" in order to bring the electrode into the oscillatory state. While this may appear astonishing, turning off the capacitive effects produces "exploding" oscillations only.

5.7 Interpretation and more detailed simulations

As before, all kinds of maps can be produced, most interesting here are oxide thickness maps and potential losses as shown in Fig. 5.10. Again, the model may be "smarter" than its creators, meaning that it produces results that were not predicted and that need retrospective interpretation. Figure 5.10 shows a case in question, namely a small section of the mean oxide thickness curve for the standard case of $J_{an} = 0.054 \text{ mA/cm}^2$ taken from Fig. 5.7a together with the potential curve, the correlation lengths and the surface fractions, and snapshots of the oxide thickness distribution at the times indicated on the potential curve. Each oxide thickness map is accompanied by a histogram, displaying quantitatively the oxide thickness distribution. In the first map, taken at 284 s (before the potential reaches its minimum), significant differences in the oxide thickness can be seen and the thicker areas correlate loosely with the areas containing active CBs as shown in the potential loss maps. At this moment a given number of CBs are active and produce oxide. As time progresses ($t = 293 \text{ s}$), the mean oxide thickness increases while the potential decreases. This is simply due to CBs still "burning" and producing oxide, even if the potential decreases. At the same time, new CBs nucleate in the thin areas; as a consequence, the potential loss map shows active CBs in the same area as in the time frame considered before, but also new active areas. As time progresses, too many CBs stop and the potential has to go up again. The active areas now correlate visibly but not perfectly with the areas that were quiet before. As can be seen, the relation between active regions and passive regions in the potential loss maps is roughly the same in all screenshots - as it should be. Moreover, on any point of the electrode we have local current oscillations that are synchronized to such an extent that the galvanostatic

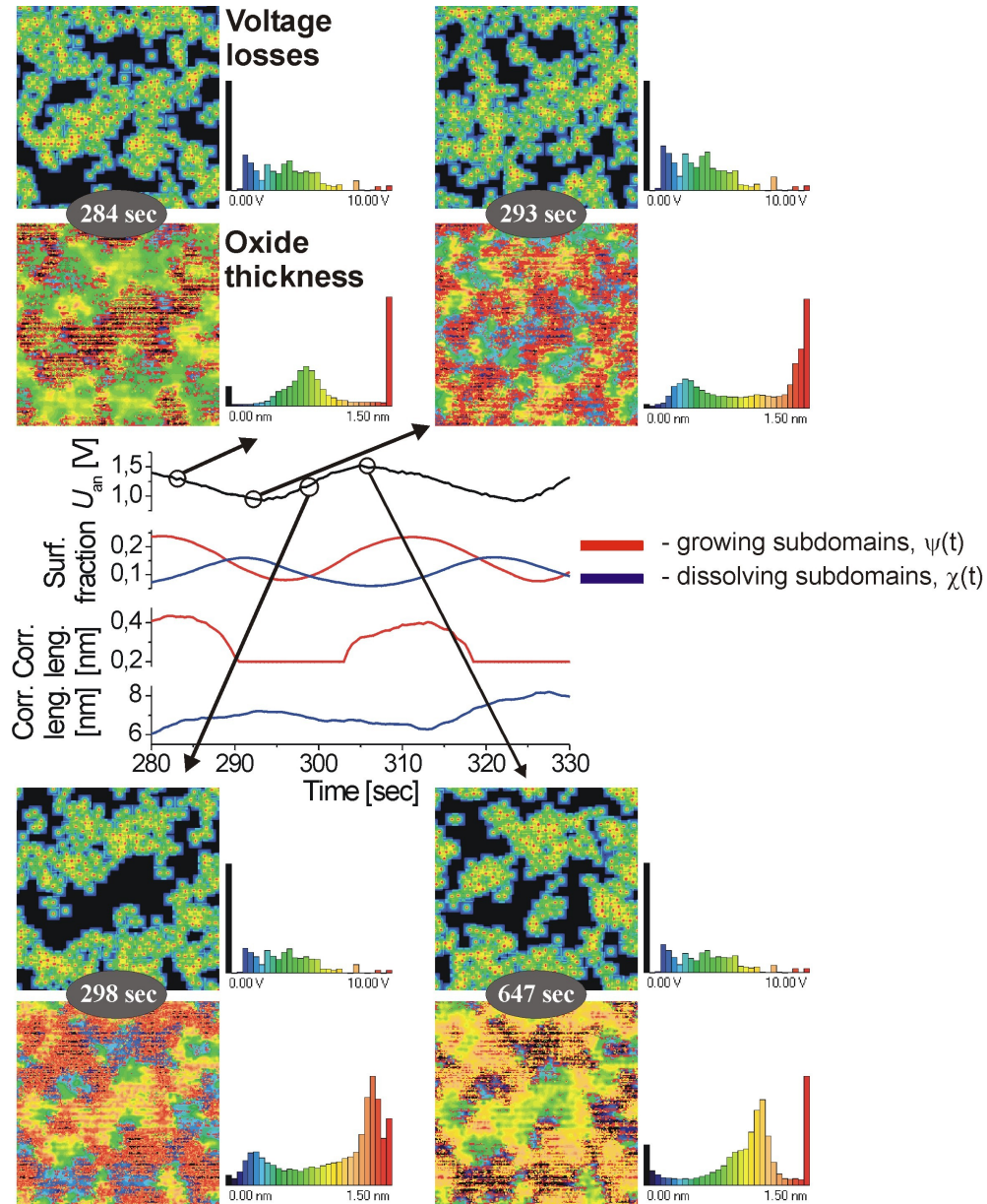


Figure 5.10: A sequence of oscillations at $J_{an} = 0.054 \text{ mA/cm}^2$ (the complete oscillation can be seen in Fig. 5.7a). Snapshots of the oxide thickness distribution at different points on the oscillation phase as well as the fitting parameters for the AFAF are given.

condition, averaging the current to I_0 at any point in time, can only be maintained by potential oscillations.

Of particular interest is the relation between the potential variation and the change in the oxide thickness for "exploding" oscillations. This can be seen in Fig. 5.9 where the potential development for an anodization current $J_{an} = 0.058$ mA/cm² is shown. The difference between the anodization current $J_{an} = 0.058$ mA/cm² for this case and for the $J_{an} = 0.054$ mA/cm² producing the rather stable oscillations in Fig. 5.10 is 0.004 mA or 6.9 %. Nevertheless, about 2000 additional CBs are needed at any time to carry the additional current. The system now is no longer able to dissolve the additional oxide produced by these 2000 additional CBs and the mean oxide thickness increases slowly with time as can be seen directly from the histograms. More over, the "camel-back" distribution of oxide thickness with maxima at thin and thick oxides that is always present for stable oscillations (cf. Fig. 5.10) disappears and gives place to a bell-shaped distribution with a maximum that increases with time. Note that the oxide thickness scales are different in Fig. 5.10 and Fig. 5.11: On the scale shown in Fig. 5.11, the oxide thickness screenshots in Fig. 5.10 would look rather monochrome. The potential loss maps look rather similar in both cases - as they should, considering that almost the same current is flowing in both cases. Movies of the potential loss, however, are quite different in the oscillation regime and in the non-oscillating part. While in the former case the active (yellowish) regions move in a more orderly fashion over the sample surface, their behaviour in the latter case is more hectic and random.

Fig. 5.10 showed part of the reference case for stable oscillations between 280 s and 330 s at $J_{an} = 0.054$ mA/cm²; the potential together with the correlation lengths parameters is plotted. It can be seen that the correlation length $\psi(t)$ for the growing oxide subdomains has a considerable phase lag compared to the correlation length $\chi(t)$ of the oxide dissolution subdomain, and that the minimum on the potential curve coincides with the minimum of the correlation length for the growing subdomain. The potential increase is obviously connected to the correlation length increase of the subdomains where the oxide growth takes place. This is a supplementary proof that the increase in the potential is caused by the need to start new CBs on the electrode surface. The increase of the correlation length $\chi(t)$ in parallel to $\psi(t)$ indicates that on the first phase of the potential increase new CBs nucleate indeed, but dissolution still is the predominant process.

The $\chi(t)$ curve starts to descend at about the inflection point of the upwards part of the potential oscillation. This is easy to understand. At the inflection point the potential reached a value that favours both the nucleation of new of CBs and the "burning" of the already existing CBs (i.e. it "keeps alive" the CBs); the growing subdomains thus expand at the expense of the oxide dissolving subdomains. The correlation length $\psi(t)$ of the dissolving subdomains

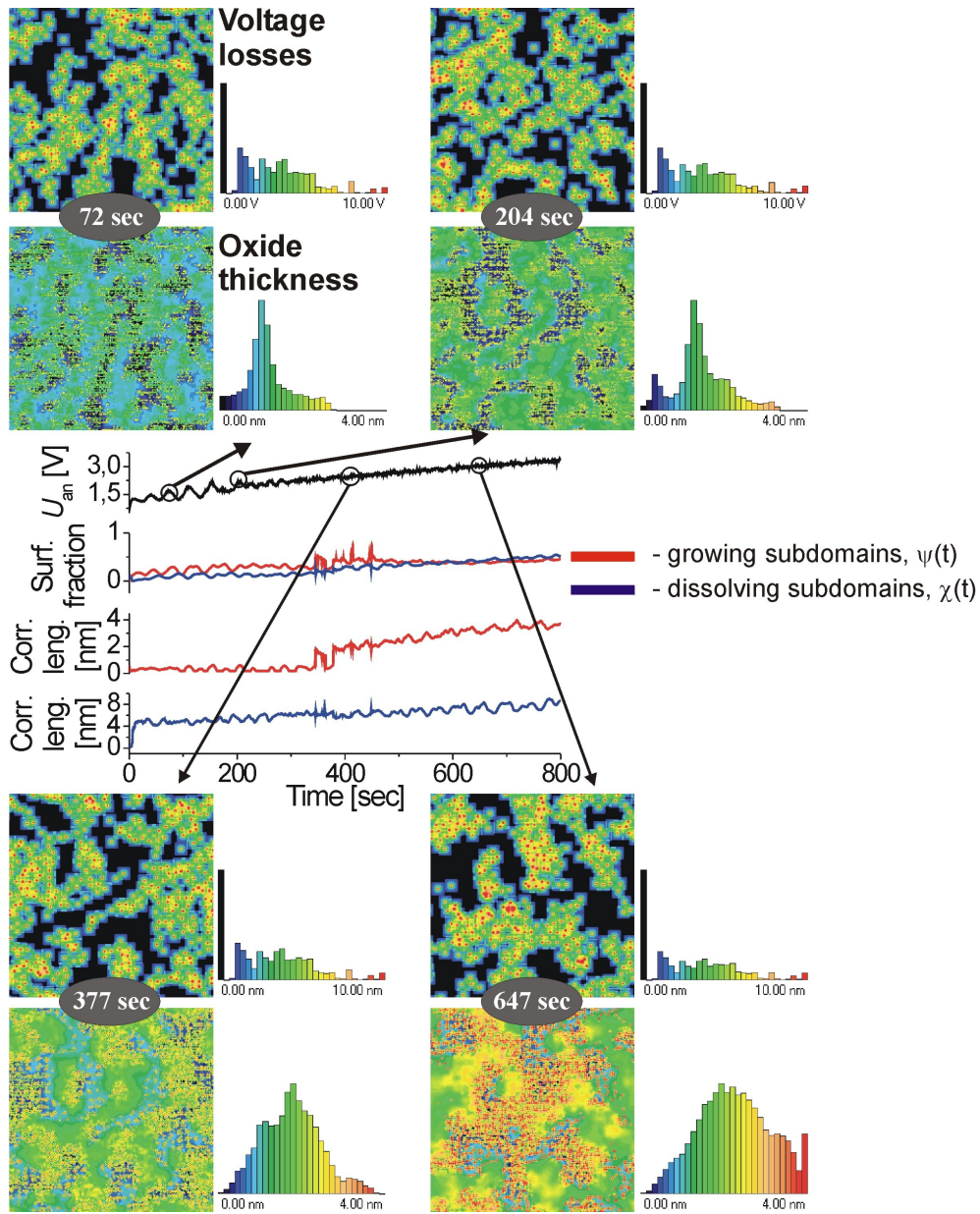


Figure 5.11: "Exploding" voltage oscillations for $J_{an} = 0.058 \text{ mA/cm}^2$ with oxide thickness snapshots at different moments on the oscillations curve.

therefore decreases. Contrariwise, the correlation length $\psi(t)$ of the growing subdomains does not simply increase, but fluctuates at a high level because there is no strong correlation between the "old" and the "new" areas. After some time, the cycle will repeat as discussed. Even though the $\chi(t)$ and $\psi(t)$ curves tend to have the same behaviour in time, the exact shape is very different for each oscillation period. This is a supplementary argument that the processes at the electrode surface are very stochastic on a microscopic scale, but can nevertheless lead to the same macroscopic behaviour. Analyzing the "exploding" oscillations obtained for $J_{an} = 0.058 \text{ mA/cm}^2$ and shown in Fig. 5.11 provides new insights and justifies claims made before. In this case the average value for $\chi(t)$ increases linearly, whereas $\psi(t)$ remains almost constant. While the oscillation has all but disappeared in the potential curve, it is still present in both correlation lengths, in particular in $\chi(t)$. However, the $\chi(t)$ curve shows clear signs of frequency doubling, and the $\psi(t)$ curve already oscillates rather "chaotically" and this may be taken as evidence that the loss of clear potential oscillations could also be interpreted as a transition from order to chaos. Be that as it may, the increase of the correlation length of oxide dissolving subdomains in perfect harmony with the potential increase shows directly that the oxide dissolving subdomains become rounder, more compact, because they cannot grow substantially in size. Knowing this, it can be clearly recognized in the maps of Fig. 5.11. This implies that it becomes increasingly more difficult for CBs to nucleate in, or penetrate into these areas; instead the potential has to go up to keep a constant number burning. In the active areas, the CB activity is visibly more hectic and random - and that is exactly what was claimed above for what one would see in a movie.

While many more examples could be given, it should be clear by now that the present implementation of the CBM goes far in simulating the Si electrode behaviour in the oscillatory regime of the characteristics and that useful data compression routines have been found and applied.

5.8 Discussion

5.8.1 Merits and limits of the current-burst model

It is clear from what has been presented that the current-burst model can quantitatively reproduce many, if not all, observed features of current and potential oscillations at a Si electrode in diluted HF; in particular potential oscillations under galvanostatic conditions. Competing models, e.g., [46, 47, 48] so far could not produce as many phenomena, are inherently more complicated and somewhat vague about the physical mechanisms behind the parameters considered.

The CBM is based on just one basic *assumption* or "axiom" - the probability functions for starting and stopping a CB - and many *approximations*. The basic assumption is rather natural, however, since it is generally accepted that current will start to flow before the oxide thickness is zero. However, tying current flow in a unique and reversible way to the oxide thickness (e.g. assuming that the current density is proportional to some (negative) power of the oxide thickness), will always produce a steady-state configuration with a constant oxide thickness, independent of the starting distributions of the oxide thickness. A non-linear or stochastic component is needed in relating oxide thickness and current, and the choice of some "ionic breakdown" probability is not unreasonable. Considering that this is the usual assumption for electronic breakdown, and considering that it might well be the electronic breakdown that triggers the ionic breakdown as pointed out in [91], the basic assumption of the CBM appears reasonable.

Another option would be "mechanical" oxide breakdown, e.g. crack formation somehow tied to the oxide thickness in a non-linear and stochastic way with some consequences for current flow. This is the approach tried in [48]. While this works, too (but to a far smaller extent than the CBM), it needs far more assumptions (including unphysical ones like crack formation in layers under compressive stress) and many approximations are needed, as well as an adjustable parameter.

The approximations of the CBM contain the exact numerical values of essentially uncritical numbers like the dissolution speed of SiO₂ in HF of a given concentration, or the current in a CB, some rather uncritical omissions like the capacitive effects for potentiostatic current oscillations; but also omissions of potentially important effects like mechanical stress in the oxide, electron tunneling through the oxide, diffusion limitations, Nernst potentials induced by concentration gradients or local pH variations produced by local current fluctuations.

It is worthwhile at this point to discuss the limitations, assumptions and approximations of the CBM more closely. There are presently essentially two physical and two modeling limitations. The physical limitations are: i) the surface of the Si must be covered with oxide at all times, and ii) all current produces oxide. While deviations from those conditions encountered in experiments will probably not change the over-all behavior very much, the algorithms presently used might produce "artifacts".

The modeling limitations first concern low values of the HF concentration or the current density; as before the algorithms used might produce artifacts for physically harmless situations encountered at larger HF concentrations. Second, the numerics involved in any Monte Carlo program do not allow simple scaling to larger sample areas. A simulation run of a (1 x 1) μm^2 sample takes 20 days or so, and realistic sample sizes are out of reach.

While the physical limitation and the modeling limitation with respect to the sample size

are more or less trivial, the HF concentration issue is critical.

It is easy to run the program for increasingly larger HF concentrations, but then the spread in oxide thickness increases. Temporarily and locally the thickness may reach values as low as 0.65 nm with no CB nucleation because of the de-synchronizing effects of active CB's nearby; in this case the program simply stops. While in physical reality this may happen without major changes in what is generally going on, new effects could and would take place that are not yet part of the CBM. Electron tunneling through very thin oxides, with oxygen and not SiO₂ production as the concomitant chemical process, is a safe bet. However, since tunneling is highly non-linear in nature, an implementation into the Monte Carlo program is not straightforward. Moreover, if the oxide disappears completely, direct dissolution via CBs through a hydrogen passivation "barrier" may take over for a short time; again a process that is not yet part of the program.

Oxide thicknesses in excess of roughly 10 nm may also be encountered within the available parameter space, in this case stress-induced effects may occur, including extremes like (periodic) flaking off of the oxide as observed in [50]. Again, while physically simple, this is not straightforward to implement in the simulation, in particular because it is not quite clear what will happen. Simply postulating crack formation in an oxide that is under compressive stress as the major mechanisms behind micro-oscillators and synchronization as done in [48] appears far-fetched and not very likely. We are thus left with a slightly paradoxical situation. While the physics of the CBM or simply of the general situation tends to imply that more effects come into play at larger HF concentrations, i.e. everything gets far more complicated, experiments seem to indicate the opposite: it is far easier to find strong stable current and especially potential oscillations at large HF concentrations. This might be seen as an indication that at least some of the many possible effects discussed above may be neglected, or that they simply provide for positive feedback, strengthening synchronization, without changing the basic mechanisms all that much. It goes without saying that all the effects mentioned must be considered, at last in principle, in all competing models, too.

On the other hand, some effects discussed in the literature like field-enhanced diffusion of oxygen in SiO₂ layers or enhanced SiO₂ dissolution at high field strength are already included in the CBM. If the oxide at some point (x,y) is a bit thinner than on average and the effects mentioned become noticeable, it will simply produce a CB somewhat earlier than without these effects and thus change the distribution function somewhat. Since the distribution functions are, to some small extent, free parameters of the system, any such effects, if existent, are already included.

As pointed out before, the CBM is based on Monte-Carlo simulations and therefore restricted to small sample sizes that can be handled by standard hardware. The parameters were selected

in such a way that oscillations resulted, but that does not necessarily imply that this set of conditions would produce oscillations on a typical (1 x 1) cm² sample. However, since the simulations on (200 x 200) nm² sized "samples" agreed rather well with experimental results obtained for the parameter set used as far as it could be compared, the size problem may not be all that serious.

5.8.2 Possible extensions of the CBM and future work

It is tempting to extend the CBM to other phenomena encountered in electrochemistry, it is, however, too early to make definite claims. The following list therefore must be seen as tentative; while the effects mentioned might find explanations in terms of suitably modified CBM, there might be other explanations, too.

Effects under anodic oxidation conditions: in [56, 92] some new phenomenae with respect to anodic oxide formation were reported. In particular, a steady-state anodic oxide was found with peculiar micro- and macrostructure. Viewed under high magnifications, the oxide seems to be composed of spherical particles with diameters of some 10 nm. This would just be what would be expected as a result of one CB for the conditions given. If interpreted in this way, the active phase of a current burst would lead to rather violent local oxide formation, producing [H⁺], and thus increasing the local pH value considerably. This in turn slows oxide dissolution; it may not take place at all during the oxide formation [28]. This is a feature that is certain to occur and it can easily be incorporated in the program code; it will be interesting to see how this pH-based feedback mechanism will change the results already obtained.

Pore formation in anodically etched semiconductors often produces rather regular structures, up to self-organized single pore crystals [93]. This may be seen as a current oscillation in space instead of in time. While this fact by itself is not linked in an obvious way to the CBM, the additional observation of strong current or potential oscillations often occurring ion parallel to strong current oscillations in space (i.e. well expressed pore patterns) [54, 93, 94], does give a strong hint that some CBM related mechanism is at work; cf., e.g., [91, 95], where some more speculations about possible connections have been made.

In this context it is worthwhile to mention that any barrier to current flow, not just SiO₂, might induce CB behaviour. In particular, current flow through hydrogen passivated Si surfaces might follow CB patterns; with probability functions that also contain the crystallographic orientation of the surface as a parameter. While a mechanism based on this goes a long way to explain certain features of pore growth in Si (cf. [52]), it is purely qualitative at present and not necessarily the only possible explanation. It is worthwhile to point out here, that an extension of the CBM to pore growth is simple in principle, but rather difficult

to implement quantitatively because only a full three-dimension treatment of the dissolution process could do justice to this problem.

As has been shown, current flow via the CBM does not always produce oscillations, then the CBM model therefore should be able to reproduce the current - potential characteristics of the Si - HF system at least in that part where the basic assumptions are met. First attempts in this direction were met with some success; however, the limitations of the present software as discussed above also become quite clear. While it will take a dedicated effort to move the CBM in this direction; the authors feel quite confident that it would be met with success. Last, it shall be mentioned that any material that dissolves anodically via oxide formation might be doing this via CBs. In other words, oscillatory phenomena observed during the anodic dissolution of metals might also be due a CB mechanism. However, it is also quite possible that the unique qualities of SiO₂ restrict the CBM to Si only. Time and more research will tell.

6 Experimental work on porous Si for photonic applications

6.1 Etching of special structures

6.1.1 Introduction

The structures to be etched in this work represent ordered macropores of Si which are to be used as PC. Since this tandem always implies the coupling of light into a periodic material, i.e. the macroporous Si, for the fabrication of the porous Si one has to take into account special issues related to the interaction of the radiation with the PC.

As it was explained in the Section 3.2, $v_g \rightarrow 0$ in PCs at the frequencies where the PBS is flat. While on the PBS these regions can be broad enough, the geometry of the porous stack is defined to meet the strictly defined absorption line of the gas to be measured. This imposes strong constraints with respect to the precision of the pore diameters and their distribution.

Additionally, some special requirements must be met with respect to the radiation coupling into the PC. Considering that the light propagates in PCs in the form of Bloch waves, it is necessary that the symmetry of the Bloch modes ensures the coupling of the incoming plane wave. For the structures etched for the sensor, the distribution of the modes is 41% inside the air holes and the rest in the Si matrix.

Working with frequencies at the flat part of the PBS involves very high reflections and hence very low transmission at the interface between the air and the active device. Regular solutions known from geometrical optics, e.g. Anti Reflection Coatings (ARC), are hardly applicable here. This is due to the fact that the degree of coupling is not only dependent on the refractive index contrast but also on the geometry of the interface. Two main techniques are proposed as solutions: etching of (i) an adiabatic taper and (ii) an Anti Reflection Layer (ARL). While the optical yields of these two approaches go beyond the scope of this thesis, in what follows the peculiarities of both geometries will be discussed in short from the point of view of the electrochemical etching.

6.1.2 Adiabatic taper

As mentioned above, for an efficient coupling of the radiation into the PC some special manipulation on the etched structure is needed. Having a group velocity that is very small, $v_g \rightarrow 0$, means that the refractive index of the PC, which in this case is an effective n_{eff} , is very large since $v_g = \partial\omega/\partial\kappa = c/n_{eff} \rightarrow 0$, where c is the speed of light. According to the Fresnel equations the reflection will be given by:

$$R = \left(\frac{n_{air} - n_{mat}}{n_{air} + n_{mat}} \right)^2 \quad (6.1)$$

It can be seen that for the case of very large n of the PC the reflections will be very high, which correspondingly leads to very low intensities in the crystal. The v_g aimed for the sensor functionality is in the order of $v_g \approx c/100$ which means for the refractive index $n_{eff} \approx 100$. According to Eq. 6.1 this will result in a negligible transmission through the device and hence no spectroscopic sensor can work at such low level of transmitted radiation.

Since smaller n_{eff} lead to an increase of the radiation transmission, the adiabatic taper is the first approach chosen for solving this problem [96]. The main idea behind this concept is tuning the lattice constant such that the radiation of the gas frequency first enters a region where it propagates with a $v_g \cong c$, i.e. having a $n_{eff} \rightarrow 1$. Further, as the light propagates into the depth of this incidence region, its lattice constant will be gradually changed to the one at which the radiation has $v_g \rightarrow 0$.

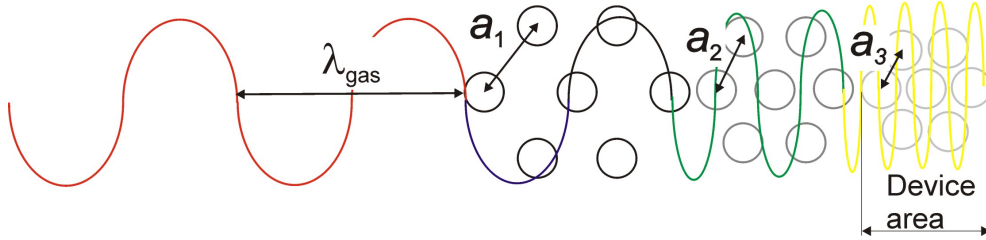


Figure 6.1: *The concept of the adiabatic taper for coupling more radiation.*

In Fig. 6.1 the theoretical concept of the adiabatic taper is shown. One starts with a lattice constant for the PC for which the radiation at the corresponding frequency has a n_{eff} close to 1. This will be further changed toward the right geometry. In the drawing this is indicated by having $a_1 > a_2 > a_3$ whereby a_3 is the right lattice constant. (The situation depicted in Fig. 6.1 represents only a particular case and for different classes of the PCs the direction toward the larger n_{eff} must not necessarily be achieved by reducing the lattice constant. It is generally a function of the specific geometry of the PC.)

Since the macropore etching in n-Si allows on the same surface different geometries of

the pores, i.e. regions with macropores with different diameters and lattice constants, the adiabatic taper could be also etched. However, beyond the theoretical concept no experimental work was continued in this direction. The main reason being the packing robustness of this structure. Only a 1% variation in the r/a over different regions on the taper (r - pores diameter and a - lattice constant) leads to a complete vanishing of the coupled radiation. Having different geometries on the same sample, although theoretically allowed (see the principles of the Lehmann compensation), a precision higher than 1% is at present unrealistic.

6.1.3 Anti reflection layer

The next concept aiming a better coupling of the radiation into the PC is the formation, prior to the porous stack, of an ARL. This approach resembles, to some extent, the known ARC technique from the geometrical optics. Nevertheless, the ARL idea has its distinction compared to the ARC, which cannot be applied in its classical form for the class of problems to be solved here.

An ARC has a thickness that is usually defined as $d_{ARC} = \lambda/4n_{ARC}$ [75]. The n_{ARC} is related as follows to the refractive indexes of the surface to be coated, n_{eff}^{PC} and the incidence medium n_{air} : $n_{ARC} = \sqrt{n_{eff}^{PC}n_{air}}$. Due to a very high n_{eff}^{PC} the n_{ARC} will also reach a very high magnitude which leads to unrealistically small thicknesses of the ARC: d_{ARC} would have to be in order of a few 100 nm. Technologically this is very difficult to realize with a very high spatial precision.

Geppert [97] found that a corrugated surface of the cleaved PC made from macroporous Si which is covered by bulk Si with a thickness d_{ARL} , will increase the transmission of the radiation of a specific wavelength by a factor of 2 from 38% to 76%. The optimal thickness of the ARL found by the author is in the range of $d_{ARL} = 0.57a$ to $0.6a$, where $a = 4.2\mu m$ is the lattice constant of the rest of the PC. The thickness of the ARL in this case is in the range of $2.5\mu m$. The tolerance in the fabrication that can be obtained at this scale additionally to the broad range for the d_{ARL} given by the calculations make this approach a feasible one.

The technique for obtaining the ARL via electrochemical etching is shown schematically in Fig. 6.2a. The device area represents the triangular lattice of macropores with the lattice constant a . The complete area of the device is in the range of $1 \times 1 \text{ mm}^2$. From the last row of pores to the edge of the active device remains a piece of bulk Si, which represents the ARL. Each device will be separated from its neighbors by etching a trench of slightly more than $3 \mu m$ in the thickness.

Figure 6.2b shows the cross-section of the etched trench. A single Si sample to be etched consists of more devices separated by such trenches. After etching, several chips can be cleaved

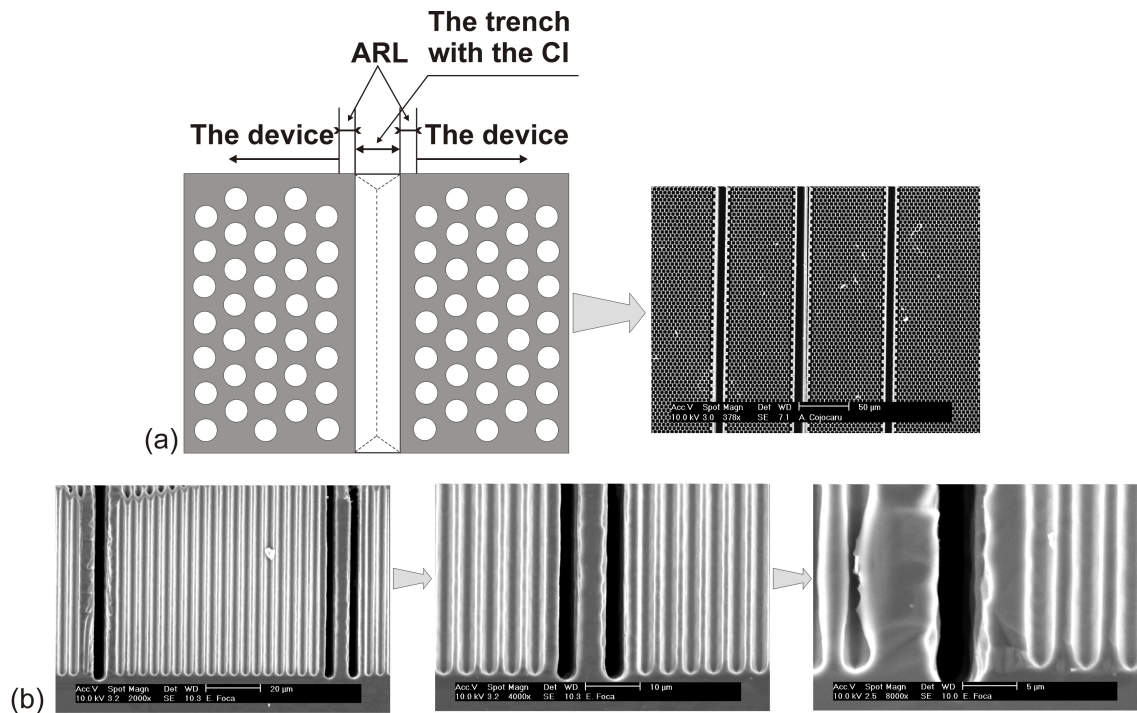


Figure 6.2: *The concept of the ARL and the technique how it is electrochemically etched (a). The SEM pictures of the trench cross-section (b).*

from a Si sample. It is important to note, that the trench wall represents the Coupling Interface (CI) for each individual chip. Since the trench is obtained via the electrochemical etching, the production process must be quite precise in order to ensure a low roughness on the CI. Note also that the lateral size of the chip is 1 mm which imposes quite strict etching conditions for obtaining the smooth walls of the trench. In Fig. 6.2b, although pores and trenches appear to be very homogeneously etched, some roughness on the wall is quite apparent. More on this issue is presented in Section 6.4.

The geometry with ARL and trench is used for all samples in this work. In the next sections several important issues with respect to the etching of such structures will be addressed.

6.2 FFT impedance spectroscopy for the control of pore growth

6.2.1 Introduction

The growth of pores is a very complex process that is dependent on many parameters, as it was shown in the theoretical part. Controlling the pores growth, i.e. optimizing the etching parameters, can be done by: (i) passive control or (ii) active control.

The first case applies even when the etching parameters are corrected for experiment n after experiment $n - 1$ is finished - *ex-situ*. In this case the analytical and decisive work is done after the etching process is finalized. Analyzing the porous structure and comparing to the expected result a decision upon the correction of the etching parameters according to some predefined models, e.g. in this work the CBM, will be made. For a typical etching time of about 10 hours it becomes obvious that the optimization process takes extremely long. This is further worsened by the fact that most of the situations needing very precise adjustment occur in the last phase of the etching process, i.e. any newly chosen etching parameters show their impact only after the end of a full-length etching.

The second case is a more powerful method, which involves the correction of the etching parameters during the experiment - *in-situ*. For this, however, the quality and features of the porous structure have to be "guessed" either from the direct data, i.e. evolution of the etching current or illumination (depending on the type of the experiment) or by using a characterization tool that delivers information about the porous structure while the experiment is running. Such an investigation tool would be not only interesting with respect to the technological analysis, but will indeed yield precious information about the pore growth process which will shed more light on the understanding of the electrochemistry of the pore growth, i.e. the purely scientific benefit cannot be neglected. The simplest tool to imagine would be the use of some kind of microscope, a scanning tip, etc. However constellations like the one mentioned are hardly possible since one deals with very corrosive milieus and always acts in a liquid environment. The chosen *in-situ* investigation technique, impedance spectroscopy, is widespread in electrochemistry. Since we deal here with very dynamic systems (electrode surface is changing very fast since the pores continuously grow), the FFT-impedance technique [98], is very adequate for this type of measurements.

Since this work is mainly dealing with macropore formation in n-type Si, as already elucidated in the introductory part, the central etching parameters are: etching current, anodization voltage and illumination intensity. Doing any type of IS on such a system involves first applying a perturbation on one of these parameters as input and "reading" the answer of the others. Thus any such combination might form an impedance mode.

6.2.2 Voltage impedance

In the case of voltage impedance done in this work the perturbation signal is applied to the anodization voltage which results in a change of the etching current. This is schematically shown in Fig. 6.3 where a typical IV-characteristic of n-Si in contact with HF is shown, under BSI. One can see that any change in the voltage will indeed trigger an answer in the current,

which allows to calculate the impedance according to the generic formula.

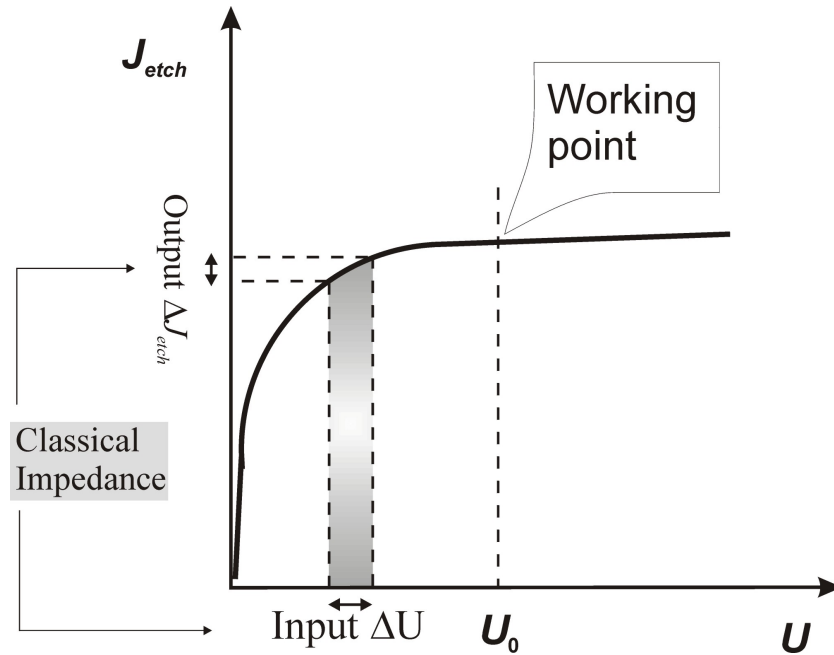


Figure 6.3: Illustration of the concept for the IS in voltage.

Actually, during the pore growth, the etching voltage is chosen such that one remains in the saturation range of the IV-curve, i.e. the point U_0 in Fig. 6.3. In this case, any perturbation in the voltage will generate a very minute signal as answer in the current (due to the flatness of the curve). For such a measurement there is a high risk of data contamination by excessive noise. This is especially true at small frequencies which by themselves are somewhat problematic, since growth of pores leads to a strongly drifting system. However these problems can be overcome by using appropriate hard- and software.

Figure 6.4 shows the Nyquist plot of a measured impedance. The squares indicate the measured data. Two semicircles can be observed. The first one, in the negative range of the $\text{Im}\{Z\}$, shows a typical capacitive behavior. Due to a very rough (since porous) surface, it is however, not obvious which capacitance it does describe. However, due to the fact that it stays nearly constant in time, it most likely describes the interface at the pores tips. Finally, the capacitive semicircle is described by a generic circuit: a parallel resistance R_p and a parallel capacitance C_p .

More interesting is the second semicircle which can be seen in the positive region of the $\text{Im}\{Z\}$. In electrical engineering such a behavior would be ascribed to an inductance, i.e. a coil. Such an element, however, does not have any analogue as electrochemical process. Here a negative semicircle will be rather described by a time constant $\tau = RC$ and a ΔR_p which is a measure of the semicircle opening. The total impedance of the equivalent circuit for the

voltage impedance has the following form:

$$Z(\omega) = R_s + \frac{1}{\left(\frac{i\omega\tau}{(R_p + \Delta R_p)(1+i\omega\tau)} + \frac{1}{R_p(1+i\omega\tau)}\right) + i\omega C_p} \quad (6.2)$$

Following the standard interpretation of such a model, R_s describes ohmic losses, C_p describes the capacitance of the interface, and R_p the chemical transfer resistance of the chemical dissolution process. The chemical dissolution splits up into a fast and a slow process, the later characterized by a relaxation time τ . The difference ΔR_p describes the increase in the chemical transfer resistance at higher frequencies.

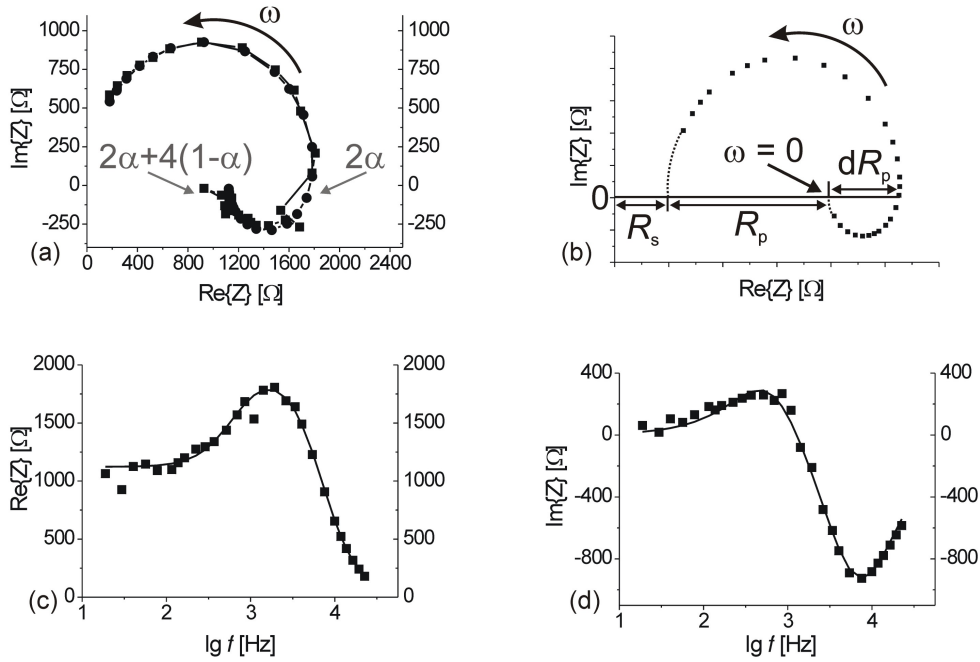


Figure 6.4: The Nyquist plot of the measured voltage impedance together with the fitting curve (a). The Bode plot for the imaginary (b) and the real (c) part of the calculated impedance; indicated are also the fitting curves.

The Fig. 6.4a shows the measured Nyquist plot, squares curve, together with corresponding fit represented by the circles curve. One can see the perfect fit of the curves as well as their correct frequency dependence. The distribution of the resistances involved in the fitting model from Eq. 6.2 is illustrated in Fig. 6.4b. Figures 6.4c and -d show the corresponding Bode plots where a perfect fit of the model with the measured data can also be observed.

"Inductive" loops are well known from spectra measured during the anodic dissolution of metals [81], e.g. Fe in H_2SO_4 . One explanation in this case was the formation of a H_2 layer on the electrode surface which blocks the anodic processes [99, 100]. Another explanation involved the blocking of the electrode by the formation of a porous Fe_2SO_4 layer; a consistent

mathematical model sustains this explanation [4]. The formation of porous CuCl is responsible for the blocking of a Cu electrode and hence the inductive loop during the anodization of Cu in HCl [101, 102]. In general, for anodization of metals the inductive loop is ascribed to the formation of a blocking layer that hampers the reactions at the electrode surface.

Similar inductive loops are found in semiconductors electrochemistry as well. Searson et al. [103] found such loops in n, p⁻, p⁺, n⁺ - Si at potentials slightly higher than the OPC. However, as soon as the potential reaches the electropolishing regime, the inductive loops disappeared. They were attributed to the formation of an oxide layer on the Si surface, adsorption of some organic layers, or H₂ adsorption. While the last two explanations are less probable, the capacitance calculated from the inductive loop did not match very well with the typical capacitance of the SiO₂ films with the same thickness (the discrepancy was by orders of magnitudes higher as compared to the thermal oxides). The same authors later suggested an explanation in which the inductive loop is attributed to the increasing potential drop across the Helmholtz double layer [104]. Ozanam et al. [42] give a more consistent explanation for the inductive loop; they ascribe it exclusively to the pore formation regime, or more generally to a roughening process of the electrode, or to a relaxation of the electrode coverage by adsorbed species.

Since *ex-situ* measurements, i.e. (not during porosification) on rough and also porous electrodes did not show any inductive behavior [105, 106, 107, 108, 109], one can assume, with a high degree of confidence, that the inductive character of the impedance is not determined by the surface inhomogeneity of the electrodes. The diffusion limitation induced by the porous nature of the electrode was extensively investigated by IS. The experiments did not show any inductive behavior either [110, 111]. Under these circumstances it is worthwhile to consider that the inductive loop, during the etching of Si in HF, is a relaxation process related to the chemical reactions occurring during the etching of Si.

There are two commonly accepted main reactions known for the dissolution of Si: divalent and tetravalent. During the first process electron injection takes place [20, 29]. Vanmaekelbergh et al. [112] related the electron injection during the divalent dissolution of Si to the inductive character of the impedance. The authors also present an extensive mathematical model for describing the loop. Lewerenz et al. [113] attributed such behavior of the impedance to the electron injection as well, while investigating the photocurrent multiplication at the n-Si/electrolyte interface.

It is more realistic not to limit the interpretation of the inductive loop to the electron injection process in the semiconductor, but to give it a more general character; namely that it might describe the whole spectrum of the electrochemical reactions during the the pore formation process. Since the measured R_p and ΔR_p represent solely the chemical reaction

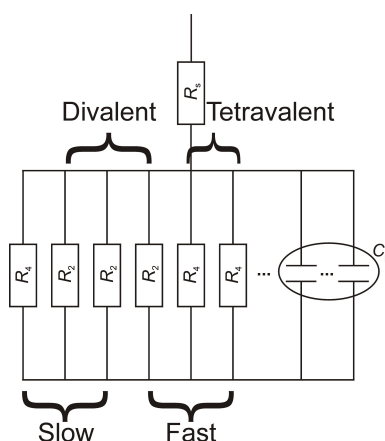


Figure 6.5: Illustration of the pore tip state as measured by the impedance spectroscopy.

transfer resistance they can be further related to the total anodization current. At the pore tips the dissolution process is represented by an interplay of the divalent and tetravalent dissolution. The valence of the dissolution process can be considered to be:

$$n = 2\alpha + 4(1 - \alpha) \quad (6.3)$$

where α and $(1 - \alpha)$ are the respective fraction of the divalent and tetravalent dissolution.

The pore tip, from the point of view of the electrochemical reactions, may be envisioned to behave as pictured in Fig. 6.5. It is characterized by a very complex state where the divalent and tetravalent electrochemical reactions take place simultaneously. The resistances symbolize local areas where the dissolution takes place via one of the reactions, i.e. R_2 - valence 2 and R_4 - valence 4. Capacitances are in parallel to the resistances. The whole array of capacitances symbolize the pore tip.

The main message of the picture in Fig. 6.5 is that "slow" and "fast" processes are not limited to the time constants of the divalent or tetravalent reactions. The situation may be more complicated where the respective reactions are interconnected up to such a degree that "slow" and "fast" would rather mean group of them that can or not follow at high frequencies.

Since the inductive loop starts at very low frequencies and spans over a well defined frequency range, one can propose the following scenario of the electrochemical reactions frequency dependence: at low frequency all chemical reactions will be seen that take place at the pore tips; as soon as the frequency increases only the fastest electrochemical reactions can follow.

In this case Eq. 6.3 takes on a more general form:

$$n = n_1\beta + n_2(1 - \beta) \quad (6.4)$$

where β is the fraction of the fast chemical reactions and n_1 is the valence of the fast

reactions and n_2 that of the slow ones. The following model results:

$$\text{For } \omega \longrightarrow 0 \quad \Rightarrow \quad \Delta U = \Delta I_1 \cdot R_p = (n_1\beta + n_2(1 - \beta)) \cdot \mathbf{N} \cdot R_p \quad (6.5)$$

$$\text{For } \omega \gg \quad \Rightarrow \quad \Delta U = \Delta I_2 \cdot (R_p + dR_p) = n_1\beta \cdot \mathbf{N} \cdot (R_p + dR_p) \quad (6.6)$$

ΔU is the anodization voltage and ΔI are the fractions of the anodization current correspondingly. The number N is a proportionality factor; in fact it indicates the total number of the dissolved Si atoms. Equation 6.5 describes the slow and fast reactions occurring simultaneously and Eq. 6.6 describes only fast reactions occur. Equations 6.5 and 6.6 can be further on rewritten as:

$$\frac{R_p}{R_p + dR_p} = \frac{n_1\beta}{n_1\beta + n_2(1 - \beta)} \quad (6.7)$$

For known values of the n_1 and n_2 , one can calculate β from the measured resistances. This allows further assessment of the average dissolution valence at the pore tips by using Eq. 6.4. It is worthwhile to discuss the following 4 scenarios for possible n_1 and n_2 during the macropore formation in n-Si:

1. Assuming the blocking oxide layer to be the reason for the inductive part of the impedance, the oxide formation, i.e. the 4-valent reaction, will be the slowest process. In this case one has the following magnitudes: $n_1 = 2$, $n_2 = 4$ and $\beta = \alpha$.
2. Assuming the formation of the hydrogen bonds implies that the H - passivation, to be the slowest reaction, than the divalent dissolution will not follow at high frequencies, which leads to the following magnitudes: $n_1 = 4$, $n_2 = 2$ and $\beta = 1 - \alpha$.
3. If the electron injection would be the slowest process, the picture is similar to what is described in 2.
4. n_1 and n_2 might even be some arbitrary numbers. In this case the analysis seems to be useless since the exact electrochemical reactions will be difficult to identify.

In what follows only the 1st and to some extent the 4th possibilities have been used because 2 and 3 would lead to a completely wrong time dependence of the valence. Additionally, for the possibility 3 negative values of β , for certain regimes of pore formation, can be found which does not make sense at all. In this case Eq. 6.7 after some rearrangements has the form:

$$\frac{dR_p}{R_p + dR_p} = 1 - \frac{2\beta}{2\beta + 4(1 - \beta)} = \frac{2 - 2\beta}{2 - \beta} \quad (6.8)$$

From Eq. 6.8 β can be obtained:

$$\beta = \frac{2R_p}{dR_p + 2R_p} \quad (6.9)$$

Plugging β in Eq. 6.4 one obtains:

$$n \quad \text{2-fast and 4-slow} = \frac{4(R_p + dR_p)}{dR_p + 2R_p} \quad (6.10)$$

For the sake of comparison, by following the same steps, the valence is calculated assuming the scenario 2:

$$n \quad \text{2-fast and 4-slow} = \frac{4dR_p}{2dR_p - R_p} \quad (6.11)$$

After a careful analysis of Eqs. 6.10 and 6.11 it can be seen that if one leads to an decaying curve as a function of time, the other will exactly mirror this behavior. It is known that as macropore is growing the leakage current becomes more predominant as a function of time. Leakage current is a purely divalent process, hence it is expected that the average valence, maximum possible 4 at the pore tip, will decrease as a function of time. Such a behavior was shown by the valence calculated according to the Eq. 6.10. By contrast Eq. 6.11 led always to increasing curves of the valence and the calculated magnitudes could reach values much beyond 6. This is however not possible, hence serving as an additional argument that Eq. 6.10 is more appropriate, i.e. that the 2-valent is the fast process and the 4-valent is the slow one.

Experimentally, it is found that during optimal macropore growth, characterized by perfect geometrical features (constant diameter with depth and across the sample, no cross-talk between the pores and intact surface) the measured average dissolution valence has values close to 3. The direct implication of this is that the fraction of the tetravalent and divalent dissolution is equal during the pore growth. Giving the twice larger volume of SiO₂ compared to the volume of Si to be oxidized, this could lead to the condition when the pore tip is fully covered by a layer of oxide. Later in the text it will be shown how this fits with the finding that the divalent dissolution is present as well.

Extending this interpretation to all data obtained from the voltage impedance for macropore formation under BSI condition for all kinds of etching conditions is nearly impossible since a lot of electrochemical dissolution processes can occur in parallel, e.g. the (desired) photoinduced dissolution of Si at the pore tips, the (undesired) dissolution of Si by electrical breakthrough current at the pore walls, or the formation of side pores. Therefore the commonly measured voltage impedance can produce spectra much more complicated than those expected for the

formation of "nice" macropores as described in this work.

Basically two processes can be mirrored in the voltage impedance. They may occur at the same area, e.g. at the pore tip, or may be spatially separated, e.g. one reaction at the pore tip, the other at the pore walls. This information can not be deconvoluted from the impedance data directly. There is indirect information, however, which one can get from comparing the resulting macropore structures and the impedance data recorded while etching the macropores.

6.2.3 Experimental Results and Discussion to the Voltage Impedance

Interpretation of the impedance data

Figure 6.6 shows the fitted data obtained for two types of experiments: small diameter pores, i.e. large interspacing between the pores, Fig. 6.6a, and pores with large diameter, i.e. small pores interspacing, Fig. 6.6b. These experiments are intentionally chosen in order to compare the behavior of the impedance for the case when the SCRs of the neighbored pores do not overlap, i.e. large pore interspacing, with the impedance data for the pores where the SCR do overlap (and, additionally, a too high etching voltage generates mesopores on the walls and leads to the formation of the star- or petal-shaped pores). One has to mention here that the prestructured samples were not designed for such diameters, i.e. the etching process is not stable and only hardly leads to the formation of homogeneous pores. For the large diameter pores the fitting model from Eq. 6.2 could be applied only ca. 80 min after the etching started. The curve in Fig. 6.6c shows the measured R_s for the case of the pores with a small interspacing. The increase of the R_s at the beginning reflects the pore nucleation, which restricts current flow to the pore tips and thus decreases the area for the ohmic path according to $R = \frac{\rho l}{A}$. The reduction of the R_s after 50 minutes corresponds to the strong increase of the area (building of the pore walls). Even if only a small current density (compared to the pore tip) is flowing through the pore walls, this becomes a large contribution to the current and therefore to the ohmic resistance. The competition between increasing area (reducing R_s) and increasing pore length (increasing R_s) leads to the stabilization at a constant value.

By contrast, for the large diameter pores, due to the overlap of the SCR and additionally by keeping the voltage small enough, the leakage current is much smaller as compared to small diameter pores. This leads to the fact that as the pore advances, mainly the pore tip remains as active area which ensures the increase of the R_s due to the continuous decrease of the electrolyte concentration at the pore tip. Exactly this behavior of the R_s can be seen, which continuously grows as a function of time. In Fig. 6.6c only the qualitative behavior of the curves is relevant, the absolute values can also depend on the exact number of the etching run per electrolyte.

From the simple geometrical relation for the resistance (i.e. $R = \frac{\rho l}{A}$) one can understand several features of the time dependence of the impedance data which are reflected in the pore morphology. While pores are formed, the sample area increases constantly, which would imply a decrease of the chemical transfer resistances R_p and ΔR_p . But the experiments show, see the next section, a continuous increase of R_p and ΔR_p . So the chemical reactions will be limited to a certain area - the pore tip.

Comparing the behavior of the R_p , Fig. 6.6d, as a function of time for the small and big

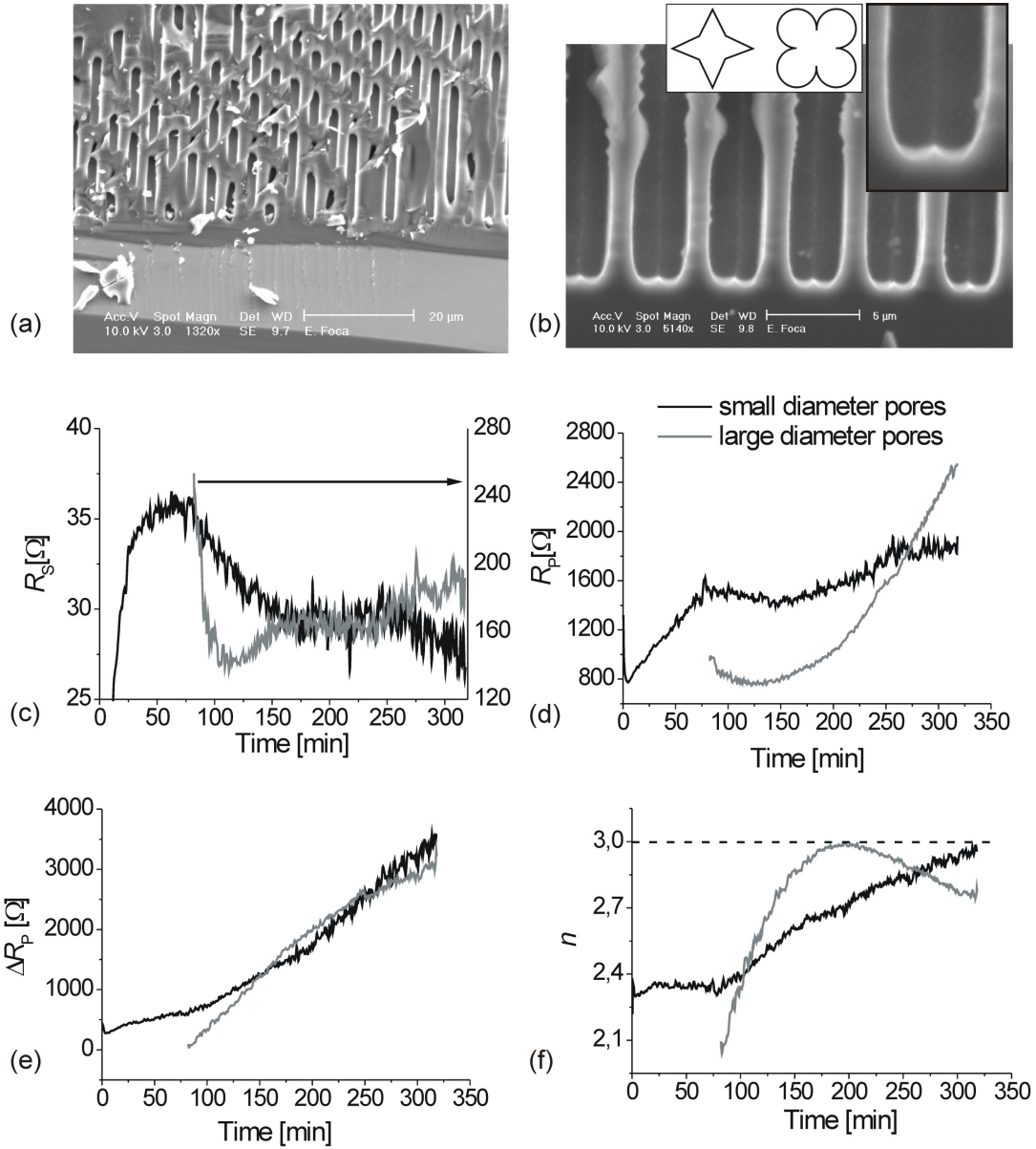


Figure 6.6: The data extracted from the voltage impedance for the case of macropores with a large (a) and small (b) interspacing. The following parameters are displayed: R_s (c), R_p (d), dR_p (e) and n (f). The inset on the SEM picture in (b) shows a magnification of the pore tip as well as two possible shapes of the macropores.

diameter pores one can see that for small diameter pores R_p increases much slower as compared to the big diameters. This slower increase is explained, as was the case of R_s , by a continuous increase of the active surface caused by as a result of a strong leakage current. Interesting enough, the ΔR_p in Fig. 6.6e, has almost the same behavior for both samples indicating that in both cases it describes the same electrochemical reaction that cannot follow at higher frequencies.

Figure 6.6e, shows the calculated dissolution valence from the impedance data. For the small diameter pores, at the beginning of the experiment, i.e. while pores nucleate, this number starts near 2.4. This happens not only for the experiments shown here, but for nearly all macropore experiments that have been analyzed. For stable pore formation this number increases and reaches a value around 3 when good macropores are etched. As long as n stays constant around 3 no other chemical reactions (especially leakage current through the pore walls) is relevantly large. According to this interpretation the pore nucleation process belonging to the small interspacing took about 100 min and good pores have never been etched stably since for no time, the valence $n \cong 3$ could be reached, i.e. even for short pores the leakage current is large.

At the same time, for large diameter pores, after about 170 min, stable pores growth is reached and $n = 3$ remains for a certain time at this level. The decrease of n after 220 min is related to an eventually increase of the leakage current through the pore walls. This leakage current destroys the pore walls which has been confirmed by SEM analysis and it becomes amplified through the sharp parts of the macropores (i.e. due to their petal- or star shape). As a result of SCR overlapping, the leakage current through the pore walls is reduced, at least before the pore shape is petal- or star like.

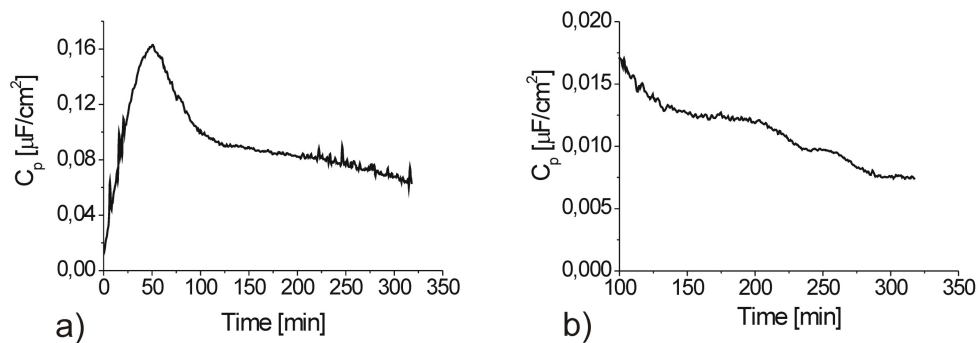


Figure 6.7: The calculated parallel capacitance for the small diameter pores (a) and the large diameter pores (b).

Figure 6.7 shows the measured capacitances for small diameter pores, Fig. 6.7a and for large diameter pores, Fig. 6.7b. In both cases it is primarily defined by the SCR at the pore

tips. If C_p is calculated by applying the regular formula for the capacitance for the SCR at the pore tip (considering the SCR thickness at the tips to be slightly smaller than at the pore walls [20]) and multiplied with the number of pores (due to their parallel connection), the obtained magnitudes match very well with the values shown in Fig. 6.7a. However, for the case of the larger pores, it has generally smaller values and this is due to the inhomogeneous state of the pore tip. The total capacity of the pore tip in this case is not uniquely defined by the capacitance of the SCR.

Without losing generality, it has to be mentioned that the formation of the pores leads to etching of some special geometries representing the pore tips in connection with the walls and even some sharp geometries on the walls. All these lead to the fact that the concept of the capacitance, known for the plate capacitor, is hardly applicable here if not wrong at all. This makes the interpretation of the measured capacitances very difficult. It was observed from many experiments, however, that the capacitance has to remain almost constant as a function of time if only stable macropore growth is desired. Some more research is needed for ordering the quantities obtained as C_p to the measured SCR, or eventually SiO_2 , layer covering the pore tip.

Figure 6.8 shows SEM pictures of the samples cross-sections for inhomogeneous and homogeneous¹ pore growth regimes accompanied by the corresponding calculated valence. From the SEM and AFM investigations the pores in Fig. 6.8a combine good and bad quality, thus qualified as inhomogeneous, as compared to the pores in -c where they satisfy all the criteria to be considered as homogeneously grown. Apart from the difference in the visual investigation of pores, a clear trend can be observed in the behavior of the calculated valence for inhomogeneous and homogeneous pores.

For the inhomogeneous pores, Fig. 6.8b, the calculated valence hardly reaches the magnitude 3. As the applied voltage, during the experiment run, is chosen to be more adequate for the optimized state of the pores growth regime, i.e. for etching homogeneous pores, the valence stabilizes at 3 and remains at this value for about 200 min. After 300 min, however, when the pores are deep enough, i.e. ca. 200 μm , the leakage current starts to increase dramatically and the valence starts to drop toward the divalent dissolution. The SEM picture in Fig. 6.8a perfectly reflects the symbioses of "good" and "bad" pores which is characterized by regions with relatively homogeneous pores and regions with macropores being chaotically grown from the point of view of their diameter and also interspacing.

Having the same electrolyte, but a better etching potential leads to the formation of the very nice macropores, see Fig. 6.8c. Figure 6.8d shows the behavior of the valence as a function of time where the characteristic shape can be observed. It starts at around 2.4, which is a

¹See the meaning of these definitions in Section 4.1.1.

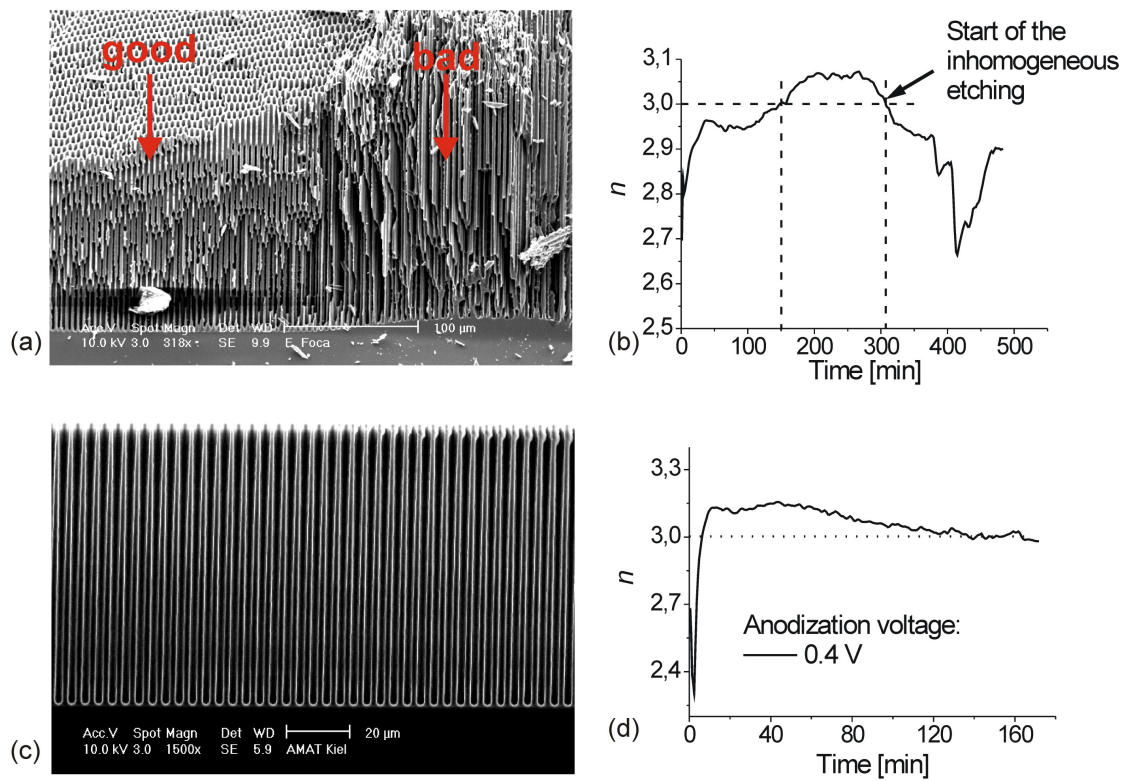


Figure 6.8: SEM picture of the sample cross section for inhomogeneous pores (a) and corresponding calculated valence (b). SEM picture of homogeneously grown pores (c) and the corresponding calculated valence (d).

common characteristic for the nucleation phase. Later the valence approaches asymptotically 3 while the pore growth process is homogeneously running.

As it was already mentioned, good macropores quality involve: constant diameter with the depth; constant diameter of the pores across the sample; surface not destroyed and no cross-talk between the pores. In the previous section it was shown that macropores of very good quality exhibit an average dissolution valence which is $\cong 3$. As soon as the valence considerably drops below this value, worsening of the pores quality can be observed. Even if the interpretation of the calculated number n , as valence with Eq. 6.8, is improper, the relation of the measured resistances remains as a direct quantifier of the pore quality. However, the obtained magnitudes for n fit very well the experimental findings for the valence. By using gravymetry Rönnebeck et al. [114, 115] calculated the valence obtained during the macropore formation in n-Si and found it to be 2.7, or more generally $n \leq 3$. This justifies why further on the magnitude n will be considered to be the dissolution valence.

Note also that without doing impedance during the pore etching the only means to recognize if the pores are normally growing is to follow the illumination intensity variance in time. For the sample shown in Fig. 6.8b the illumination intensity gave signs for a problematic etching only after 400 min. Before that time was impossible to recognize a problematic pore growth process. By means of the impedance, however, already at the minute 250 it could be observed that the etching process is not under optimized conditions. Having the valence as a quality tool allows at an early time the readjustment of the etching parameters which could easily save the etched structure. After 400 min no action is able to reestablish the normal etching process and the porous structure is considerably destroyed. Hence the voltage impedance becomes a very powerful tool that can be effectively used in order to in-situ controll the etching process.

Interpretation of the dissolution valence

It is interesting to see how does the dissolution valence changes as a function of the applied voltage during the macropore formation. To investigate this, macropores were grown under different etching potentials. The etching conditions were: $3\mu m$ diameter, $150\mu m$ depth and $T = 20^\circ C$ for the electrolyte, and $c_{HF} = 5wt\%$. Figure 6.9a shows the initial IV curve of the Si-HF system in which the macropores were grown. The dotted verticale line indicates the beginning of the saturation regime and hence the minimum value, $U = 0.2V$, for the anodization voltage needed so that the pores grow under the optimal conditions. Figure 6.9b shows the measured valence for $U = 0.05V$, which is a potential considerably lower than the saturation voltage, usually leading to very bad macropore growth. It can be seen that the dissolution valence hardly reaches values higher than 2.7 and soon drops toward 2.3, leading to predominantly divalent dissolution of the pore tips. In order to assess the special behavior

of the etching at such a low voltage, the etching time was selected to be longer than in the rest of the experiments.

Figure 6.9c shows the dissolution valence calculated from the impedance measurements done for the etching runs at different voltages, starting with the lower limit of the saturation voltage. The best quality of pores could be obtained for voltages in the interval $0.2V < U < 0.6V$. Once the etching voltage exceeded this interval, e.g. see the valence for $U = 0.8V$ in Fig. 6.9c, the pore quality was worsened, which could lead to the formation of the star shape pores, common indication toward a too high voltage, and also to the complete etching of the surface, which is an indication of the high leakage current.

It can be seen that for the investigated voltages below 0.6 V the dissolution valence is very stable around $\cong 3$. It is somewhat smaller for $U = 0.4V$, but this deviation is smaller than 0.1. This leads to the conclusion that $n \cong 3$ is indeed optimal for macropore growth. Using the Eq. 6.3 one can calculate the fraction of the divalent and tetravalent dissolution for this valence. Figure 6.9e shows the fraction of the divalent dissolution. It can be seen, for the optimal conditions of the macropores growth the fraction of the divalent dissolution equals the one of the tetravalent dissolution. However for the voltage $U = 0.8V$ the divalent dissolution becomes less predominant and the tetravalent dissolution dominates.

The conditions deserve special attention when the pore growth is not optimal. The dissolution valence is shown in Fig. 6.9d and the corresponding calculated divalent dissolution part in Fig. 6.9f. One has to mention that generally $U < 1.5$ V still well distinguishable ordered macropores could be found. Their quality is labeled as "bad" due to destroyed surface and not round pore shape. Indeed the dissolution valence for these voltages never reaches 3. For voltages up to 1 V a constant valence around 3.2 is clearly seen, which leads to almost a 60% of tetravalent current. One can also see that for $U = 1.5$ V the valence starts and persists for a long time at a value smaller than $n = 3$. An exact interpretation of these results is rather difficult. One would expect that an increased anodization voltage would lead to more oxide production and hence n should be closer to 3. This can be indeed seen for voltages up to 1 V. However, when this threshold is overcome, the average valence drops below 3 indicating that the amount of the divalent dissolution becomes predominant. Knowing the divalent nature of the leakage current, it appears that at higher voltages, i.e. $U > 1$ V, its fraction is dramatically increased. Even if the SCRs of the neighbouring pores would overlap making the walls insulating, voltages close to (and higher) 1.5 V are big enough to break the junction and initiate the leakage current. The dissolution valence drastically drops right from the beginning of the experiment, this being a clear indication that at such high voltage values the leakage current is present from the start of the etching process. This may be an explanation why the surface for these samples is always destroyed despite a well distinguishable regular pore array.

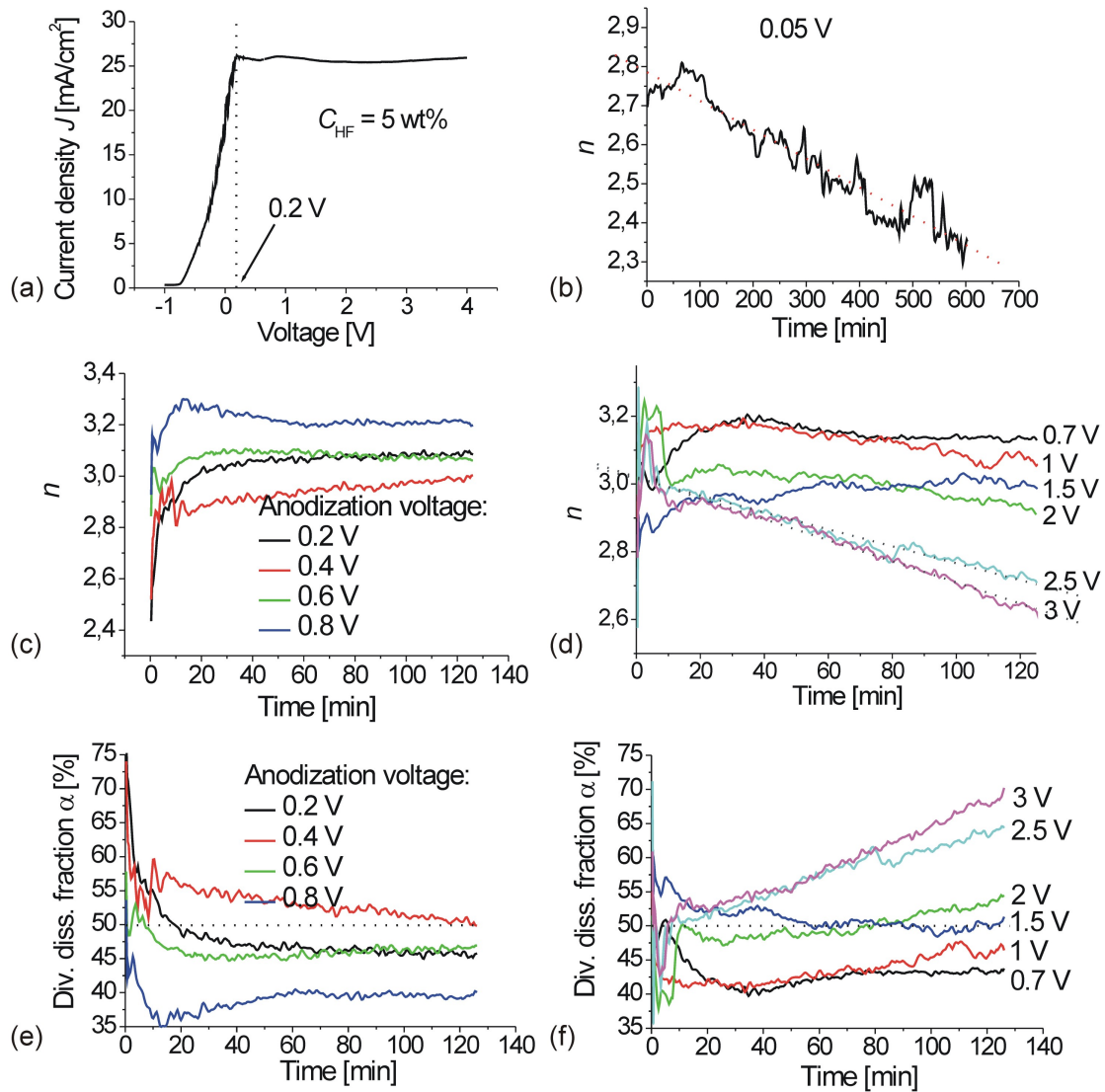


Figure 6.9: The IV curve of the Si-HF interface used for the macropores formation (a). The dissolution valence obtained from the measured impedance data. Potential in the linear regime of the IV curve (b). Potentials close to the optimal growth of macropores (c). Potentials far in the saturation regime (d). The corresponding fractions of the divalent dissolution for different etching voltages (e) and (f).

A model for macropore growth under optimized conditions

The model developed here assumed that at higher frequencies only the divalent dissolution can follow. For the sake of completeness, however, one could assume that it is only the tetravalent dissolution that follows, or even mixtures of univalent (not really known up to know, but quite easy formulated in terms of pure chemistry) and tetravalent dissolution. For both of these cases the corresponding dissolution valence, $n(t)$, was extracted from the impedance data. The results showed that none of the above approaches delivered meaningful data so that it was reasonable to assume that indeed at higher frequencies only the divalent dissolution can be observed.

From the data analyzed in the previous section it follows that the optimal valence for the homogeneous macropores growth is $n \cong 3$. This involves that tetravalent dissolution proceeds with the same rate as the divalent one. Taking into account the higher volume of SiO_2 compared to Si this allowed to conclude that most probably the whole tip of the pore is fully covered with a layer of oxide.

A deeper analysis makes this assumption very plausible since the homogeneously grown macropores, in virtue of their geometrical features, represent round cylinders which preserve no information about the crystallographic characteristics of Si. The earlier advanced macropore growth models by Zhang [116, 103, 104, 117, 69] and Lehmann [26, 118, 32, 20] involving the increase in the electric field at the pores tips due to the curved SCR can be considerably improved for the special case of optimized macropore formation.

The dissolution valence of $\cong 3$ found for stable pore growth implies that the oxidation process proceeding via 4-valent dissolution, is constantly accompanied by the divalent dissolution and proceeding with the same rate. The SiO_2 formation is directly locally coupled to the divalent Si dissolution.

In Fig. 6.10 a scheme is proposed showing the formation of the macropores, under the optimized conditions. One starts considering that "optimized conditions" mean such etching conditions that over the whole etching run each pore has always a closed oxide layer covering its tip. More generally, the etching conditions and environment have to be selected such that the oxidation is considerably favored. The formed oxide layer must be thin, but thick enough in order to preclude the formation of a full SCR at the pore tip. As the etching proceeds, locally the oxide will be dissolved. This leads to the exposure of the bare Si surface to the electrolyte.

Since the prerequisite for the macropores growth, in the framework of the proposed model, is the immediate oxidation of the surface that would be the next step to follow. However, due to a big volume of the SiO_2 the immediate oxidation may be hampered due to the lack in space. That being the reason why first some Si atoms have to be removed from the lattice,

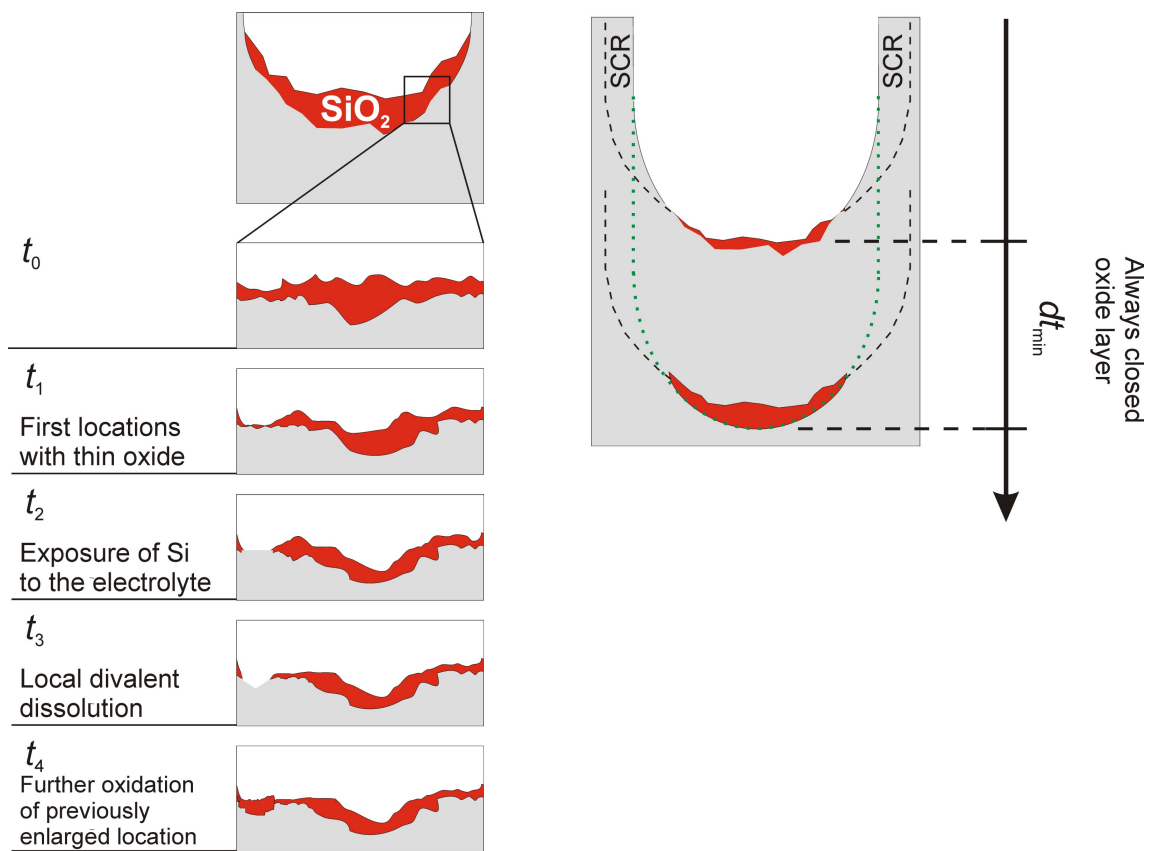


Figure 6.10: A mechanism for the macropore growth under optimized conditions.

i.e. by divalent dissolution, followed by the subsequent oxidation of that place, i.e. tetravalent formation of the oxide. As a result, the net valence will be an average between 2 and 4 valent processes, i.e. $n = 3$. In this way the pore will further advance by continuously dissolving and building oxide at the pores tip. One can speculate that the divalent dissolution may be regarded as a necessary step before oxidation in order to reduce the stress between the SiO_2 and Si.

At this point the definition of a "closed oxide" layer might seem somewhat confusing since (i) the calculated valence shows that the divalent dissolution occurs as well and (ii) in the framework of the model presented here, Fig. 6.10 shows naked Si surfaces, e.g. between t_2 and t_3 or t_3 and t_4 . These two, however, do not contradict the model presented here. First, the divalent dissolution is considered to be a very local process, i.e. only so much Si is directly dissolved necessary for reducing enough the stress so that SiO_2 can be produced. Hence it may be assumed that oxide free locations can not be detected within any imaginable "microscope". Second, the divalent dissolution is a much faster process as compared to the oxide dissolution [29], hence any data acquisition system allowing to "look" at the pore tip even for the smallest time resolution will not be able to "catch" the time spans when the Si surface is not covered by an oxide film. This is also indicated in Fig. 6.10 with a schematic time scale. In this case, $dt_{min} \gg t_4 - t_0$, with dt_{min} the smallest time step for the measuring setup.

The measured average valence during the pore growth, obtained by means of the impedance spectroscopy was found to be around 3. For the same experiment the estimated valence via the gravimetric measurement of the mass law lead to a values of 2.75 which fits well with the one measured by Rönnebeck et al. [114, 115]. This small deviation can generally very well be understood if one considers that the slow reactions are not exactly tetravalent, but have a somewhat smaller valence. This actually mean to allows $n_1 = 2$ and $3 \leq n_2 \leq 4$. It is sufficient to assume $n_2 = 3.8$ and the calculated valence from the impedance data perfectly match the ones estimated via gravimetric methods. It is important to mention that a valence for the oxidation that is different than 4 is generally allowed. From the point of view of theoretical chemistry such a mechanism can be easily formulated. What happens at the pore tip is a set of electrochemical reactions that, in the virtue of the model presented above, efficiently interact and influence each other. In the model for the valence calculation it was assumed that at the higher frequencies only the divalent dissolution processes will follow due being faster. However one can assume that part of these divalent processes are, for some reasons, retained in time by some tetravalent processes. As a result, what is seen in the impedance at a certain instance in time for higher frequencies, only a part of the whole divalent reactions follow, the other is not able. Such a mechanism on average decreases the valence for the Si dissolution. Following this argumentation line, a change of the n value to 3.8 lead to an estimated valence

which was almost identical to the one obtained by the gravimetry. Thus, n_1 and n_2 must be left as fitting parameters which might give further inside about the exact electrochemistry of the electrode.

6.2.4 Photo Impedance

As mentioned in the introductory part "photo impedance" has been used as a second in-situ characterization tool for controlling the macropore growth process. The photo impedance is obtained by imposing a FFT perturbation on the BSI intensity and analyze the change in the etching current. By contrast to the voltage impedance in this case there cannot be developed any model having as routes an equivalent electrical circuit since the response in the current is not a result of the change in the applied voltage.

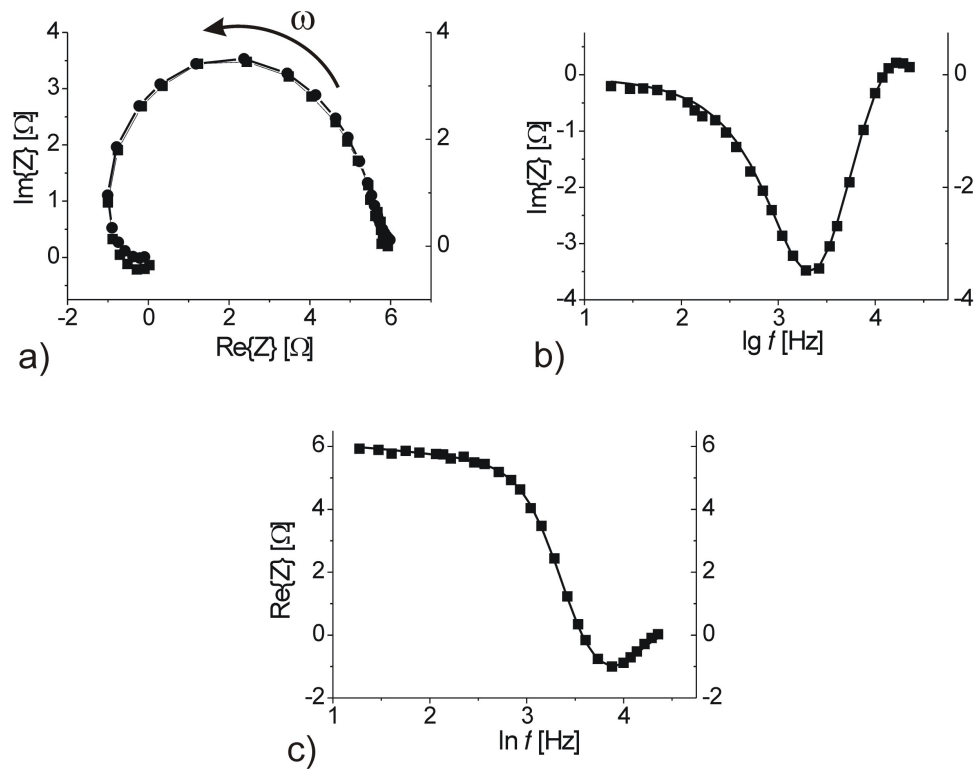


Figure 6.11: *The Nyquist plot of the photoimpedance together with the fitting curve (a). The corresponding Bode plots for the imaginary (b) and the real (c) part of the photoimpedance accompanied by the fitting curves. The squares are measured data and the circles represent the fitting with the corresponding model.*

Figure 6.11a shows the Nyquist plot measured by the photo impedance. The square curves indicate the measured data. Figure 6.11b and -c show the Bode plots for the measured and fitted real and the imaginary part of the photo impedance. One can see a (heavily damped) resonant phenomena in the impedance at higher frequencies. At low frequencies the Warburg characteristics can be recognized which are related to the concentration gradients in the electrolyte.

Note that while the photo impedance is a well established technique [119] doing impedance

during the macropore growth under the BSI is investigated for the first time in the framework of this dissertation. In order to interpret the measured data a special theoretical model had to be developed.

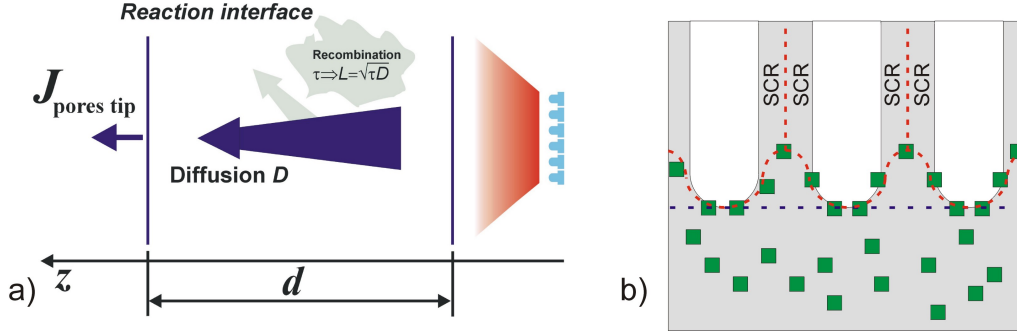


Figure 6.12: *The theoretical model for the photoimpedance (a). Limitations of the proposed model due to the change of the reaction interface and unlocalized current flow (b).*

The photo impedance is mainly fitted by a model which describes the diffusion of photo-generated holes through the n-type wafer, illustrated in Fig. 6.12a. It is described by the continuity equation:

$$\frac{dn}{dt} = D \frac{\partial^2 c}{\partial z^2} - \frac{n - n_0}{\tau} + G(\omega) \quad (6.12)$$

where the first term on the right side in Eq. 6.12 is the diffusion term followed by the part of the hole current lost by the recombination. Further is added a frequency dependent term for the generation rate of the carriers, $G(\omega)$. In order to solve the Eq. 6.12 the following boundary conditions must be applied: the generated holes, apart from the recombined part, are fully consumed at the reaction interface. More general, the reaction interface as illustrated in Fig. 6.12a, are actually the pore tips. The restriction that the holes are fully consumed implies there is no leakage current arising from the diffusion of the holes in the area between the pores and their ulterior consumption as the unwanted current through the walls. In a good approximation the solution for the Eq. 6.12 is:

$$\frac{dJ_{etch}}{dJ_{illu}} = \frac{A}{\cosh \sqrt{i\omega \frac{D^2}{d} + \left(\frac{d}{L}\right)^2}} \quad (6.13)$$

where D is the diffusion coefficient of the holes in Si, d the thickness of the remaining bulk wafer and L the diffusion length of holes. Obviously while the substrate is continuously etched, d will decrease and by subtracting d from the total thickness of the wafer one can obtain the thickness of the porous layer. The diffusion length and the diffusion coefficient are constants of the material. The diffusion length, however, is a parameter that can strongly vary from wafer to wafer and even across the same wafer. This being the reason why only D enters as a

constant in Eq. 6.13, while d and L will be fitting parameters, whereby L is expected to be a constant as a function of time.

Figure 6.11 shows the fitting with the developed model. For the Nyquist plot, circles curve, one can also see a perfect match in the frequency domain with the measured data. Finally, the Bode plots show a very good fit of the theory with the experiment.

6.2.5 Results and Discussion of the Photo Impedance

The experiments with the small and large diameters used for interpreting the voltage impedance are used here as well, see Fig. 6.6.

Figure 6.13 shows the results obtained for the fitting parameters. As one can see the remaining bulk thickness is indeed decreasing as a function of time, showing the continuous etching of the substrate. If one calculates the final thickness ΔS of the porous layer one obtains 128 nm for the thin pores, Fig. 6.13a, and $\Delta S = 250$ nm for the thicker pores, Fig. 6.13b. The real depths of the pores, estimated after the etching by investigating the sample under the SEM, is $\Delta S = 250$ nm in both cases. Obviously the sample with smaller pores shows a strong deviation from this number while the sample with the broad pores gives a good estimation of the porous layer thickness. The deviation for the small diameter pores will be discussed later in combination with the diffusion length.

While the result for d is nearly correct, the result for fitting the diffusion length L shows a systematic error. Figure 6.13c shows the fitted diffusion lengths for both types of the samples. Since the recombination properties of the wafer do not change while the pores are etched, L should be constant; instead we find a continuous decrease of L for both samples. For the case of small diameters the diffusion length drops drastically exhibiting a change in the magnitude of more than $200 \mu\text{m}$ to the end of the experiment compared to its start. The diffusion length for the large diameter pores shows also a decrease, however it is much smaller and there is a considerable time, ca. 50 min, were L is even constant.

Figure 6.13d shows the estimated L for the small diameter pores, but obtained in low concentrated electrolyte, i.e. $c_{HF} = 4\text{wt}\%$, empty square curve. Compared to the previous case, L remains constant for about 60 min which is even somewhat longer compared to what the large diameter pores showed. An experiment done at the same electrolyte concentration, but at lower temperatures, i.e. $T = 17^\circ\text{C}$ exhibit even better behavior. The results are indicated in Fig. 6.13d by the black and grey curves. In these cases the curves remain constant for longer than 100 min. Note also that the grey curve is obtained from an independent experiment with identical experimental conditions as for the one described by the black curve. The same starting value as well as the similar shape of the curves is a good indication that the

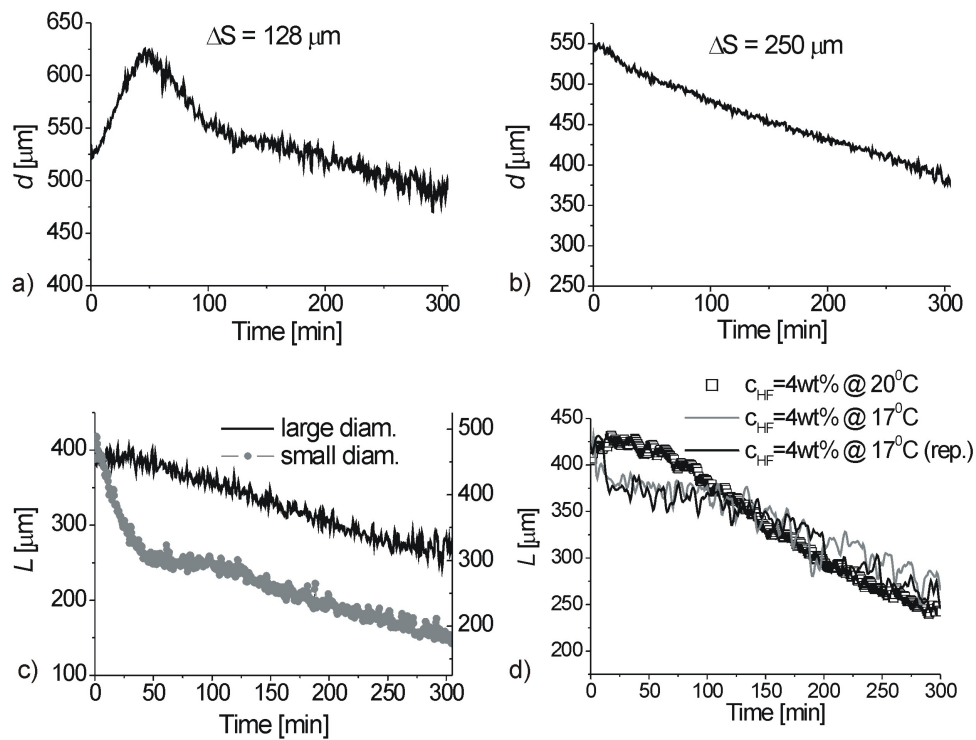


Figure 6.13: *The estimated change of the remained bulk thickness. The curve for the thin pores (a) shows an aberration in comparison with the case of very thick pores (b). The fitted diffusion length remains longer constant for large diameter pores compared to small diameter pores (c). Time dependence of the diffusion length for lower concentrated electrolyte and lower etching temperatures (d).*

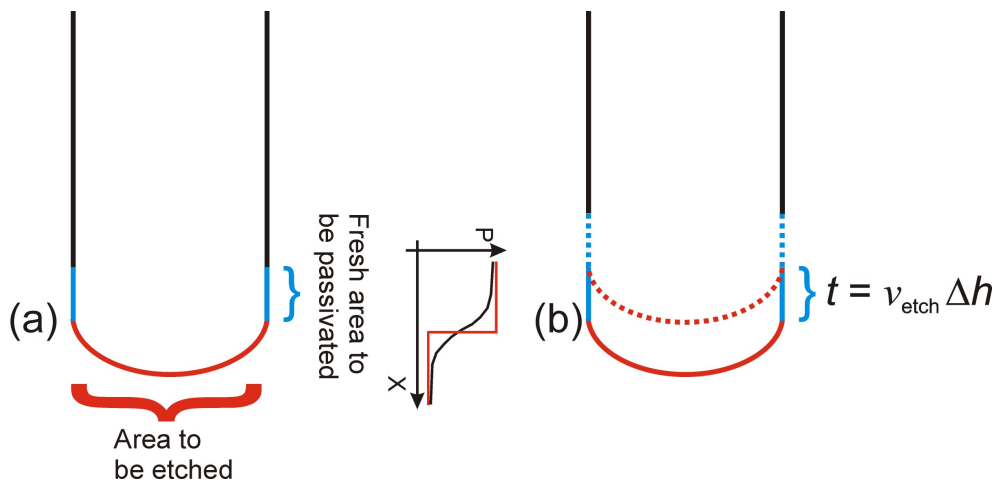


Figure 6.14: *The selectivity between the pore tip and wall from the energetic (a) and kinetic (b) points of view.*

measurements are reproducible.

The decrease of the diffusion length is basically a limitation of the model proposed here. It assumes a full parallel plane as the etching front as illustrated in Fig. 6.12b by the dashed dark blue line. Another strong constraint of the model requires that all photogenerated charges are completely consumed at this front, except the part lost by recombination. A more realistic view is however represented by the red dashed line, Fig. 6.12b. This involves the diffusion of the charges between the pores, to the intersection of the SCR. These charge carriers will be consumed at the freshly emerged parts of the pores wall which are still not sufficient passivated. This conclusion is also supported by the fact that L changes less for the broad pores. Due to the overlap of the SCRs, as it was also mentioned for the voltage impedance, the pore walls become insulating which precludes the diffusion of holes (or at least diminishes it considerably) far away from the pore tips between the pore walls. Thus the chosen boundary conditions are more valid compared to the thin pores where the walls are well conductive and any hole being at the pore tip, if not consumed immediately, has a great chance to diffuse between the pores. The same is responsible for a better assessment of the ΔS for broader pores. However, it is important to mention that in both cases d has the same starting values, which are only 5% different from the real thickness of the wafer. Additionally, at low temperature L is longer constant indicating that slow electrochemistry approaches well the conditions described in the fitting model.

The results shown in Fig. 6.13 allow a deeper understanding of the macropore formation. As shown in Fig. 6.13c and -d the L shows a more realistic behavior for lower electrolyte concentrations, low temperatures and thinner pore walls. Since for different electrolytes the inflection points for the curves describing L is taking place at different depths, one can expect

that the reason for the incorrect determination of the L is only chemistry and the conditions at the pores tips and nearby regions, i.e. freshly emerging parts of the walls. The improvement of the L behavior by the reduced temperature can be explained by analyzing the system from two point of view:

1. **Energetically.** During the pore etching the system tends to minimize its free energy $F = U - TS$. When the temperature is sufficiently low to have a perfect order in the system, the tip of the pore will be passivated with a probability $p = 0$ and the pore walls with $p = 1$. This is schematically indicated in Fig. 6.14a. In this case there exist a strongly defined selectivity between the pore tips and walls which leads to the etching only at the pore tips and best passivation of the pores wall. When the temperature is increased, this leads to the increase of the entropy in the system and hence of the disorder. The probability for the passivation is not longer a perfectly defined step function, but it starts to "melt" (the red curve in the plot). This has the effect of decreasing selectivity between the tips and the walls and as a consequence of bad passivation of the walls, part of the current will be driven through the pore walls. This may explain why at lower temperatures the L remains constant over a longer period of time.
2. **Kinetically.** While the above argument sounds plausible, for lower temperatures one has to regard also the kinetic effects. Obviously, a good and fast passivation of the freshly emerging wall sites has to impede the consumption of the photo generated carriers everywhere but the pores tips. It is hard to assess whether the times required for the Si-H bond formation or dissolution of Si is strongly influenced by the change in the temperature. Instead what is strongly influenced is the speed of the pore growth, i.e. it is slower if the temperature is smaller. If one defines a certain constant time constant K needed for good passivation of a specific area of Si, moving the pore tip with a lower speed allows enough time for very good passivation of the freshly emerged pores walls, schematically shown in Fig. 6.14b. This in turn leads to better protection against further dissolution and hence consumption of the photo generated holes. Note that "good passivation" has not to be underestimated. Assuming a passivation degree of a surface being 99.99% yet means that each 10000th Si atom is not passivated and hence free for being dissolved. Each newly dissolved atom exposes new Si atoms to the acidic medium and the passivation issue becomes again acute. This conclusion can be extend even further and namely in order to be in the optimal macropores growth regime one needs to achieve a specific etching speed which allows enough time for very good passivation of the pore walls.

Generally, to solve this problem, one has to change the static boundary conditions in Eq.

6.12 to a periodic function mirroring the interspacing between the pores, i.e. the shape of the red dashed line in Fig. 6.12b. This is however not an easy task and necessitates some complex mathematical effort. It is complicated since the characteristics of this periodic etching front can have a strong dependence on the etching parameters, i.e. type of the electrolyte, applied voltage, geometrical features of the pores, etc. Additionally, one has to consider that the backside of the sample is generally unpolished and usually full of defects. These defects will efficiently trap the generated carriers. This source of recombination is not included in the model too. Obviously, as the pore advance into the depth the model becomes more sensitive to this effects and imprecisely describes the behavior of the impedance.

Despite the improvements that can be added to the theoretical interpretation of the measured impedance the data extracted from the photo impedance is valuable and to a great extend precise. Suffice it to mention that all the extracted numbers are in the right order of magnitude. The diffusion length has numbers that are only by a few % smaller than the thickness of the wafer which is a good indication that, at least for relatively short pores, this magnitude is meaningful and can be taken as a guiding number in order to learn more about the quality of the wafer. Combined with the voltage impedance, the photo impedance gives additional information about the pore etching process and its data can be further utilized for efficient control of the pore etching.

6.3 The role of alcohols in the electrolytes for pore etching

6.3.1 Introduction

The recipes for the electrolytes for pore etching in n-Si in most of the cases will contain alcohols. This usually simplifies the process of parameter optimization on the way to obtain good pores, whatever this involves for each experimentalist. Yet the reasons why alcohols are so important are not understood. It is often only a question of some "alchemy".

Besides the common etching parameters as applied voltage or current, illumination intensity, electrolyte concentration and temperature, less known, but very important too, is the degree of wetting the surface by the electrolyte. In part, etching ordered structures of pores, especially macropores, becomes almost impossible if the electrolyte does not contain some surfactants [120]. It is also known that the Si surface is generally hydrophobic and it is this state that can be changed by adding tensides and as a result achieving an easier pore etching. However the same effect can be obtained if adding alcohols. Their role is even more complex and besides reducing the surface tension and thus bathing better the electrode, they might have an important impact on the electrochemistry kinetic; more generally also to favor or hamper some specific electrochemical processes. Investigating all these processes is complicated due to the porous nature of the electrode. There are only a few reports in the literature concerning the role of alcohols with regard to the Si dissolution [121], however they cannot describe all the processes taking place at the pores tips and hence their impact on the pore geometries and features.

In this Section these issues are addressed by etching macropores in n-Si and investigating their feature sizes. The used electrolytes contain different types of alcohols. The obtained results are compared to the structures etched in pure water. Generally the macroscopic features of the pores are of primary concern and are discussed in details. This information is used as input for a better understanding of the role of each alcohol.

6.3.2 Experimental results

As already mentioned in the introductory part, besides the better wetting of the surface, resulting in a smaller contact angle, the role of alcohols is not so clear. Frey et al. reported a decreased silica dissolution rate in electrolytes containing ethanol [56]. Lehmann in his work [20] claims that due to the better wetting of the surface, the sticking factor of the etchant species is higher which leads to more homogeneous etching.

The investigation starts from measuring the voltamograms of clean Si surface using different

intensities of the BSI. There is some risk to find pore nucleation at low voltages, however being fast enough with the sweep rate this range is passed very fast and only oxidation of the electrode will take place. The measurements started with -1V and is continued up to 7V with a rate of 0.13 Vs^{-1} . For the BSI intensity it starts with 2V, being the typical range while etching pores and increase it further to 6V in order to see if there are some mass limitations effects leading to slowing the electrochemical reaction at the electrode surface.

The measured voltamograms are shown in Fig. 6.15. As electrolyte the HF was dissolved in: pure water, water with methanol (MetOH), water with ethanol (EtOH), water with 2-propanol. The same order of presenting the results is kept throughout the work unless otherwise specified. The voltamograms are recorded at 2V for the BSI. The etching of the macropores is taking place, regularly, around this illumination intensity.

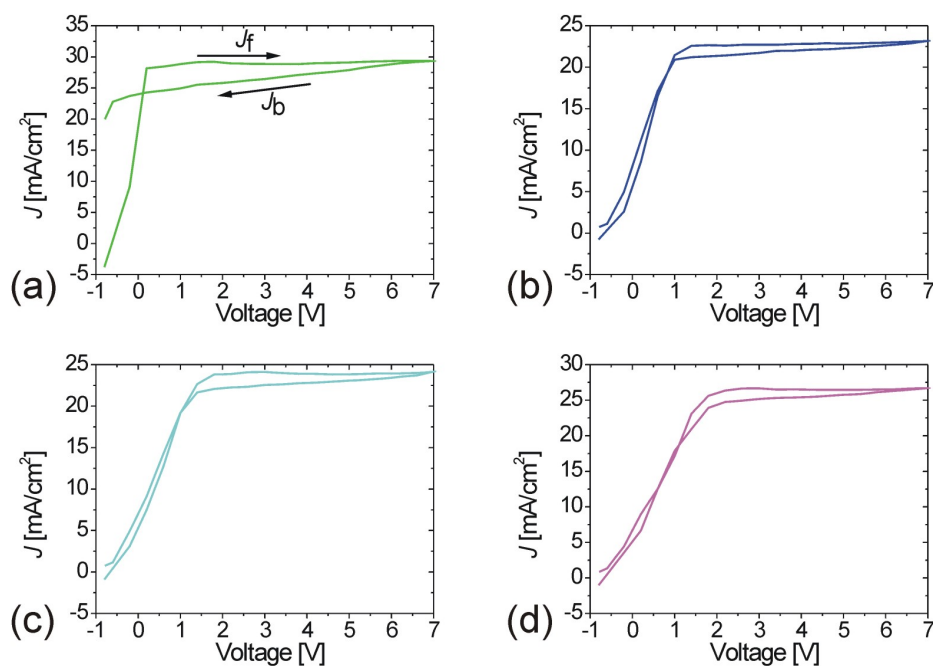


Figure 6.15: The voltamograms measured in the following electrolytes: water (a); methanol (b); ethanol (c); 2-propanol (d). The voltamograms corresponding to 2V BSI for all four electrolytes (e).

In all cases there is a clear difference in the currents for the onward scan compared to the backward one. This is a clear indication that a passivation (or protective) layer is produced which can only be SiO_2 . There might be some formation of the H_2 at the electrode surface. Note that although H_2 formation is extensively treated in the literature, it remains only as a supposition merely because it is required by the proposed dissolution reactions. Otherwise no rigorous H_2 production was observed during the macropore formation.

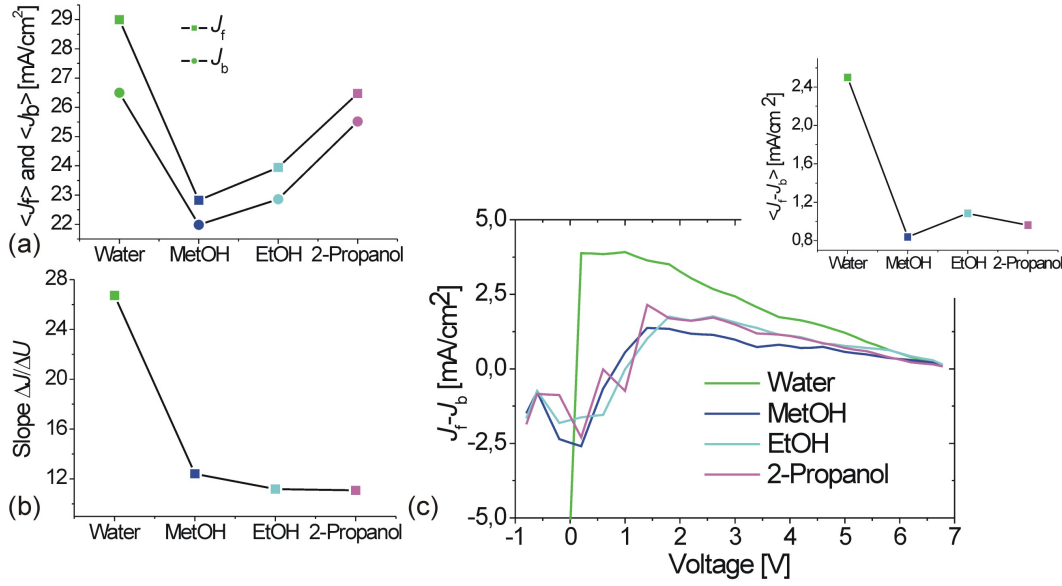


Figure 6.16: Feature of the IV curves at 2 V illumination intensity. The mean value of the J_f (the current on the forward scan) and J_b (the current on the backward scan) in the saturation regime (a). The slope for the linear regime (b). The $J_f - J_b$ as a function of applied voltage (c). The inset shows the mean value of this difference.

Figure 6.15 shows the measured IV curves. Figure 6.16a shows the mean values for the J_f (the current on the forward scan) and J_b (the current on the backward scan) obtained for different electrolytes. These magnitudes are averaged over the saturation regime of the curves; neglecting the linear part at the beginning. One can clearly see that the highest current could be achieved in water containing solution and it drastically decreases if MetOH or EtOH are used. For the case of 2-Propanol J_f is very close to the J_b obtained in water.

The slopes in the linear region of the IV curves are analyzed as well and the results are shown in Fig. 6.16b. Note that for all electrolytes the linear regime is a purely ohmic characteristic of the system. The steepest increase is observed for water being an indication that the electrolyte is the most conductive and leads to little ohmic losses. Instead all alcohols exhibited smaller slopes due to a higher resistivity of these electrolytes. One common feature for the alcohols is that the longer the molecule chain is the smaller the slope is for the linear regime. Having high ohmic losses in alcohols containing electrolytes make the predictions concerning the SiO₂ quality somewhat difficult purely from the IV curves as presented here. This is because the real voltage drop on the Si-HF junction is different for each electrolyte.

In Fig. 6.16c is shown the difference between the J_f and J_b as a function of the applied voltage. The inset shows the averages. One can see that the biggest difference is achieved for water followed by smaller numbers inherent to alcohols.

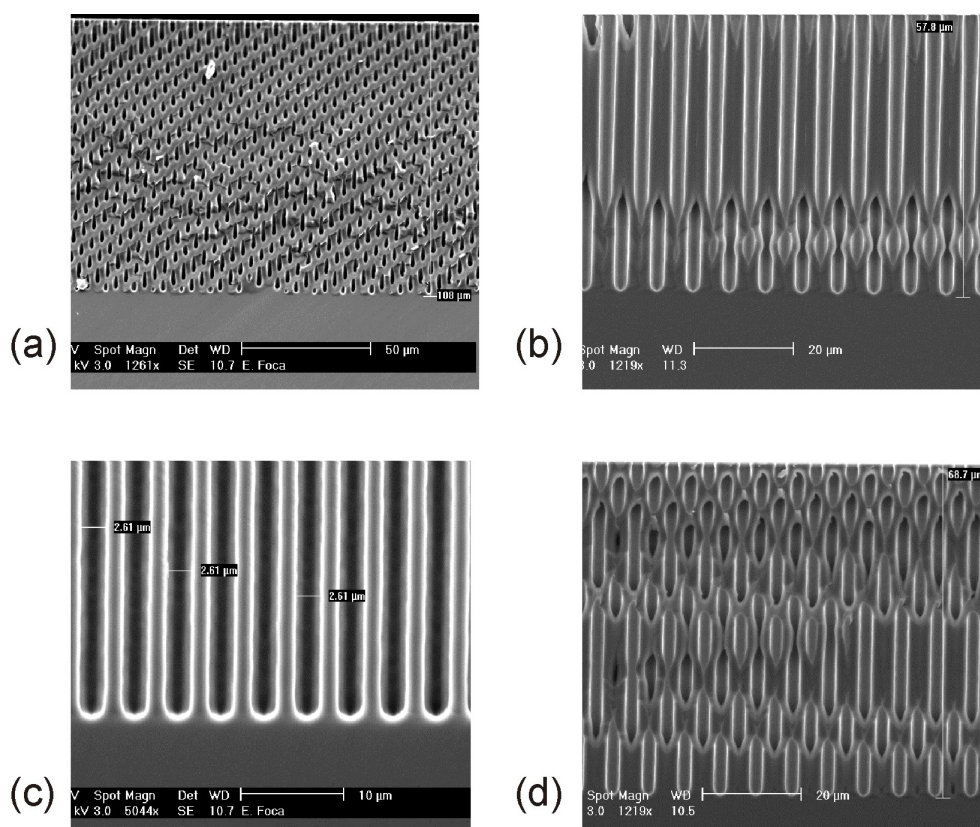


Figure 6.17: SEM pictures of the macroporous layers obtained in electrolytes containing: water (a); methanol (b); ethanol (c); 2-propanol (d).

Figure 6.17 shows the cross sections of the etched samples in the electrolytes under investigation. One can see that all experiments produced good pores. The pore diameters are constant on different regions of the sample. The cleaving artifact in Fig. 6.17a and c (somewhat also in b) shows the pores on several layers where the homogeneity of the etching process can be observed clearly. The case of the 2-propanol shows a difference in the forward and backward currents which is very small and even smaller than for the pure water.

The corresponding structural analysis of the pores is shown in Fig. 6.18. One can see that the pores in alcohol containing electrolytes exhibit larger diameters, Fig. 6.18a. The largest diameter is found for the MetOH and it will consequently decrease for the other two types of the alcohols. In any case, the diameter of the pores obtained in water are the smallest compared to the alcohols.

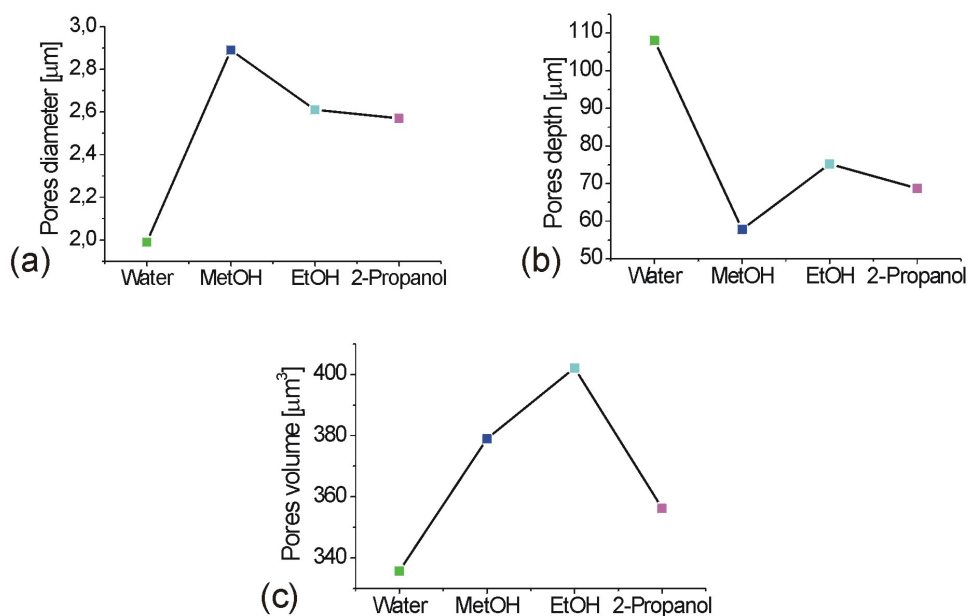


Figure 6.18: Analysis of the pore features made in different electrolytes. The variation of the pores: depth (a), diameter (b), and the volume of a pore (c).

Note that since keeping the same etching current for all types of electrolytes the change in the pore diameter should be compensated by a change in the pore depth. Figure 6.18b shows clearly this effect where it can be seen that the deepest pores could be obtained in aqueous electrolyte and the depth drastically decreases for the alcohols. The same trend is seen for MetOH and EtOH, however the pores etched in 2-Propanol show a depth between the other two alcohols. In order to be able to make some predictions about the dissolution valence in this milieu the volumes of the pores have also been estimated, Fig. 6.18c. The pores obtained in water show the smallest volume and it increases for the alcohols. It follows a clear trend for

the MeOH and EtOH. The pores obtained in 2-Propanol show a volume situated in between these two alcohols, but higher as the pores in water.

6.3.3 Discussion

Prior the discussion of the results one has to make clear that during the pore formation, independent on the electrolyte, the experimental conditions were identical for all samples, i.e. similar: $J_{etch}(t)$, $U(t)$, T , c_{HF} . Any comparison among currents actually means the currents extracted from the IV curve measurements.

For all electrolytes used here, SiO_2 will be produced and consequently dissolved on the electrode. Having smaller current (see the IV curves) in the alcohol containing electrolytes is a clear indication that the SiO_2 is "more" dominant in the Si dissolution. It is because the oxide dissolution rate is indeed smaller for methanol and ethanol as compared to water [122]. As a result the current flow is hampered by the oxide layer. This perfectly fits the findings of Frey et al. [56]. However it can also be interpreted as that the produced oxide in alcoholic solutions is denser and hence of higher quality, whatever the term quality implies in this case. This assumption is also supported by the fact that the currents (extracted from the IV curves) obtained with both alcohols are lower as compared to aqueous electrolyte. Indeed driving less current with the same applied voltage can happen if the oxide is dissolved slower which leads to the formation of more robust oxides. This also fits very well with the experimentally findings of Leisner et al. [123]. In any case the low dissolution rates does not exclude the fact that the anodically produced oxide show a denser structure. This can be also a strong condition for producing good oxide in very acidic environments.

Somewhat confusing is the magnitude $J_f - J_b$ for the alcohols compared to water since it shows smaller values for the alcohols. A straight forward conclusion would actually contradict the previous affirmation that the SiO_2 in alcohols has a denser structure as compared to the oxide formed in water. However, higher ohmic losses in the alcohol containing electrolytes might be an indication that using the same scan speed for all electrolytes does not allow to make precise predictions about the quality of the oxide relying only on the difference $J_f - J_b$.

The current reached in 2-Propanol show values comparable to water. According to the results of Leisner et al. [123] the quality of the oxide in 2-Propanol is indeed worst as compared to MeOH and EtOH, but still better than the oxides formed in water containing electrolytes. This can explain why the current reached in 2-Propanol are higher as compared to the other alcohols, but still smaller than in water. The case of 2-propanol (and also 1-propanol or even isopropanol) is very interesting since it is known that 2-propanol is responsible for the drastic reduction of the etching speeds of SiO_2 [124]. However our curves show the contrary which

is not at all counterintuitive. The 2-propanol is also known for mixing relatively bad with water and in the presence of some salts in water even building clear phase separations [125]. In this case, the behavior of the electrolyte is quite difficult to predict without using some additional investigation methods. It should be pointed out, that pores as deep as 100 μm could be etched. However deeper pores were very difficult to etch due to the blocking of the etching current, via SiO_2 , at the pore tips.

The pore features shown in Fig. 6.18 can be now better understood. While clearly reducing the SiO_2 dissolution rate the electrolytes with alcohols produce pores that have generally bigger diameters and are shallower (for the same etching current). This happens due to the fact that a longer lasting oxide on a certain area unit (at the pore tip) hampers for longer time the current flow via the corresponding area. The current will then flow through new areas leading to the overall enlargement of the pore diameter. Interestingly enough, the pores become wider for the shorter chains of the alcohol and their diameter decrease as the chain becomes longer. Since imposing the same current obviously the pores must compensate their increase in the diameter by decreasing the depth which is perfectly true for the aqueous, MetOH and EtOH containing electrolyte. The case of 2-Propanol is special here because although exhibiting smaller diameter as compared to EtOH the pores are however shallow. The reason for that is perhaps what has already been discussed namely the changes in the electrolyte which the 2-Propanol triggers especially during the pore etching, when a considerably amount of SiF_6^- is released in the electrolyte.

Note that very deep macropores could be etched in p-Si using electrolytes with isopropanol. Even if at the first glance this does not fit with our results, however, the macropores in p-Si are etched under conditions of predominantly divalent dissolution, i.e. no or very little production of the oxide at the pore tip. It is different in n-Si where the optimal condition for the macropores etching involve the continuous and full coverage of the pores tip with an oxide layer. This may be the reason why in n-Si etching of good macropores is difficult with 2-propanol although possible when the etching conditions are such that the divalent dissolution predominates.

Figure 6.18c shows the volume of one pore for the different electrolytes. The increase of the volume, if the alcohols are used, can be explained by assuming that in the alcohol containing electrolytes the Si dissolution valence increases. And this supposition appears plausible if brought together with the experimental data showing the reduction in the SiO_2 dissolution rate if using MetOH and EtOH. The dissolution valence for MetOH compared to EtOH, estimated according to the pore volume, seems to be higher, which hints toward a slower oxide dissolution rate in MetOH compared to EtOH and this fits well to the other results. The propanol, since efficiently hindering the dissolution of oxide exhibits a valence

that is even higher as compared to MeOH. Somewhat counterintuitive is the behavior of water which does not fit in this picture. Estimated from the pore volume this would show a valence much smaller as compared to the alcohols which is basically wrong. Since alcohol containing electrolytes are more resistive as compared to water in the process of finding the optimum voltage for the experiments involving all 4 electrolytes, it was chosen a voltage that is high enough to drive the current for 2-Propanol at the same time this being somewhat too high for the electrolyte with water. As a consequence the part of the leakage current in the aqueous electrolyte becomes considerably high which induces artifacts related to the geometry of the etched pores in water and hence the ulterior appreciation of the pore volume.

Note that we also observed that the pore walls become very smooth for ethanol containing electrolyte. A reduction of the roughness of a factor of 5 compared to aqueous electrolyte could be observed. This can be well explained within the Current Burst Model which, independent of these results, predicted that smooth pore walls can be obtained only in electrolytes where the SiO₂ dissolution rates are drastically reduced. Hence this fits very well to the experimental data presented here.

6.4 Inhibition of pore wall roughness

6.4.1 Introduction

The use of macroporous Si for optical applications imposes certain requirements to the pore structure. To mention only a few: very precise structural features, necessitating control of small diameter variations of the pores (both as a function of depth as well as from pore to pore), deviation of the actual pore nucleation site from the prestructured site, and finally very smooth pore walls, i.e. minimal roughness. In almost all experiments the first two characteristics are easy to be investigated at least with the precision given by the optical and electron microscopes. As far the pores walls roughness is concerned, in order to be assessed it calls for such techniques as e.g. AFM or profilometer. Scanning pore walls with such devices, i.e. curved surfaces of only 1 μm^2 , calls for very long operation times and can very easily become a very expensive experiment due to the very sharp tips needed for the AFM microscope. Very often this is the reason why such features of the pore walls were not investigated unless they become sufficiently pronounced so that even with the regular microscopes can be seen, which is, however, very seldom the case (apart from the conditions when mesopores form on the pore walls).

Nevertheless, pore roughness is one of the "no go" factors for the use of porous materials for optical applications. It is enough to have a roughness of several % of the radiation wavelength and this might already cause severe problems in the functionality of the device. That being also

the reason why this issue is extensively investigated in this work and solutions are proposed in order to surpress the pore roughness.

Geppert in his dissertation [97] was the first to observe that the *Coupling Interface* (CI) on the ARL can have a RMS of up to 530 nm on a $35\mu m$ scale. This was large enough in order to completely preclude radiation coupling at a wavelength of $\lambda \approx 10 \mu m$. Further investigation of the pore walls showed RMS that could reach values as high as 60 nm on a $2 \mu m$ scale. Figure 6.19 shows a series of measurements, organized in a matrix form, that elucidate the wall roughness problematic. Experiments are done with $C_{HF} = 4wt\%$ mixed with 10 ml of 37% HCl (the reasoning for such an electrolyte is discussed later). The figure shows AFM scans at different levels of the porous structure: top, middle, and pore tips. For any level the scans show: a general view of several pores, a scan of a single pore and a scan of a pore wall. A larger roughness can be seen at the top of the porous layer in comparison to the pore tips. Figure 6.13 illustrates that pore wall roughness is an acute problem calling for some investigations and better understanding.

6.4.2 Experimental results

In this section the results obtained from etching in different electrolyte are shown. For any etched sample the RMS roughness on the pores walls is measured. A direct comparison between the samples is difficult since, as shown in the introductory part, the roughness also depends on the depth of the pores. Nevertheless, all AFM scans are done almost at the same height hence obtained values for roughness could serve as a good guide.

The first experiments are performed on pores obtained in regular aqueous solutions, $C_{HF} = 4wt\%$ HF. The etching temperature is $T = 20^\circ C$ and the pore growth is optimized for a depth of $350\mu m$ with a diameter of $3.2\mu m$. The start value for the etching voltage is $0.85V$ kept constant for $130min$ followed by a linear increase up to $1.25V$ in ca. $360min$. The cross section of the porous sample is shown in Fig. 6.20a where a good grown structure can be observed².

The AFM scan on a pore wall is shown in Fig. 6.20b. The scan is done over an area of almost $2 \mu m^2$. The calculated RMS roughness is $60nm$. Compared to the wavelength used in the gas sensor construction this magnitude represents almost 5%. A step like structure on the pore walls can be observed. The typical size is in the range of 100 nm. Most probably these are the (111) crystallographic planes formed due to the flow of the leakage current through the pore walls [126]. This example also clearly shows that the roughening of the pore walls is mainly a post-etching process and some chemistry that passivates better the pores walls or

²For further experiments no SEM pictures of the cross sections will be shown. For all experiments the pores growth is optimized in order to deliver very homogenous pores.

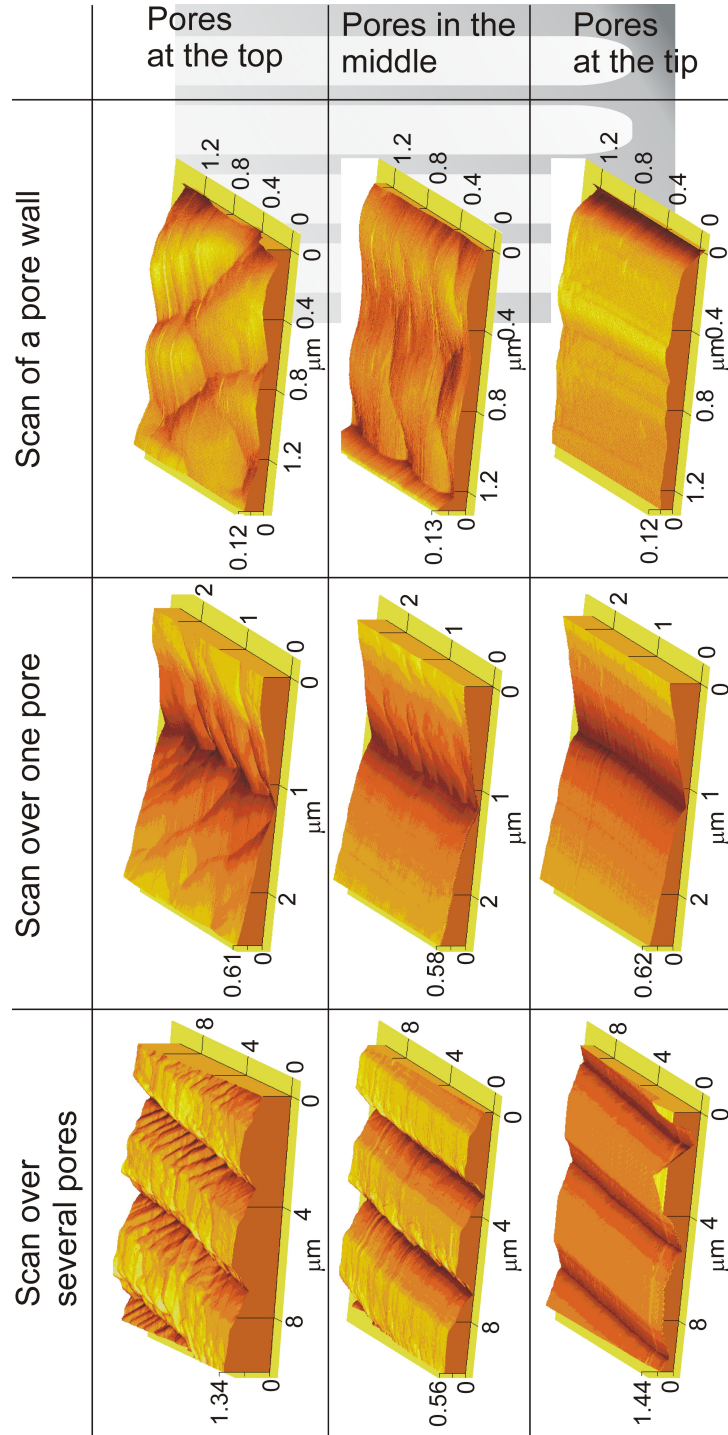


Figure 6.19: A matrix representing AFM scans of pore cross sections at different heights along the pores. Various features are scanned: a group of pores, a single pore and the wall of a pore.

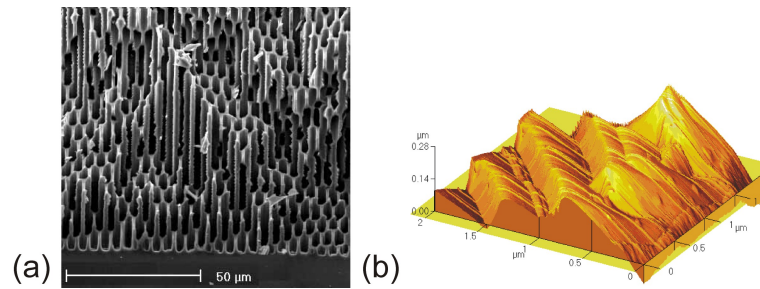


Figure 6.20: Cross section of the etched sample with aqueous electrolyte (a). AFM scan of a pore wall (b).

locally changes the chemistry for reducing the leakage current would be suitable in order to obtain smooth pores.

An aqueous electrolyte with a concentration $C_{HF} = 4wt\%HF$, as used in the previous case, has a $pH \approx 1$. A lower pH value influences the passivation of the Si surface and hence the protection degree of the pore walls. Whatever the term "better" for the passivation means, a direct consequence is the smaller current flow through the pore walls, i.e. a reduced leakage current. Analysing the pore roughness as a function of passivation degree thus becomes reasonable. For this, the next series of experiments involved electrolytes with some addition of the HCl, i.e. to the previously used electrolyte 300ml of $C_{HF} = 4wt\%HF$, 10 ml of 37% HCl are added. This decreased the pH value to ≈ 0.5 .

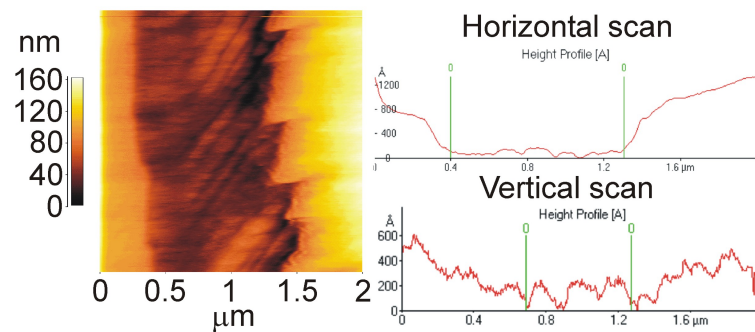


Figure 6.21: AFM scan inside a pore obtained in an electrolyte of $HF(aq.)$ mixed with HCl. The horizontal and vertical heights profiles are shown.

The calculated RMS roughness of these series of samples is $\approx 30nm$ which is a factor 2 smaller as found for pure aqueous electrolytes. Figure 6.21 shows the corresponding AFM scan together with the height profiles along the horizontal and vertical directions. The scan along the horizontal line shows a strong increase close to the end of the sample. From this measurement it is rather difficult to judge whether the formed step is a result of the cleavage of the sample or a real inhomogeneity on the pore wall. Repeated measurement on similar samples did not show such features (see e.g. Fig. 6.19) which generally leads to the conclusion

that this is rather an artifact from the cleavage. Compared to pure water, i.e. higher pH value, for this electrolyte the roughness could be indeed reduced by a factor of 2. Electrolyte with reduced pH value represent very corrosive milieus which can have a negative impact on the quality of the produced oxide at the pore tip and hence on the homogeneity of the etching process in general. That being the reason why very deep macropores, i.e. depths $\geq 500 \mu\text{m}$ are generally very difficult to etch in such electrolytes. In this work homogeneous pores up to a depth of $200 \mu\text{m}$ could be successfully etched with HCl containing electrolytes.

It is known that the clean Si surface, passivated with H^+ is hydrophobic. This might lead to the fact that in the aqueous electrolytes already during the etching process the interface between the semiconductor and liquid is very strained. One cannot easily understand how this is reflected in the pore quality. It can change the sticking factor of HF_2^- , HF , OH^- , H_3O^+ on the surface [29]. This in turn changes the passivation state of the walls as well as the etching conditions at the pore tips. In order to reduce the interface stress the alcohols, see Section 6.3, or the surfactants are extensively used [120]. This considerably enlarges the parameter space for the production of homogeneous porous structures. Besides the use of surfactants another common technique in microelectronics, promoting more uniform covering of the Si surface with HF solution, is the so called *Buffered Oxide Etch* (BOE). The buffering is done by the addition of NH_4F to the HF containing electrolyte. The same procedure is used here where to the 300 ml of $\text{HF}(\text{aq.})$ of $C_{\text{HF}} = 4\text{wt}\%\text{HF}$ are added 5g of NH_4F . The etching is done at $T = 20^\circ\text{C}$. The calculated RMS roughness for the pores obtained in this electrolyte is further reduced to 16 nm.

In microelectronics, the BOE is used in the cleaning process - for removing the SiO_2 . Besides the issues related to the better wetting of the surface another effect that leads to the better cleaning is the reduced SiO_2 dissolution rate in the NH_4F containing electrolytes. As it was already shown in the previous section, the alcohols play a crucial role in reducing the etching rate of the SiO_2 . Thus investigation of the pore wall roughness obtained in the electrolytes containing different type of alcohols is of interest too.

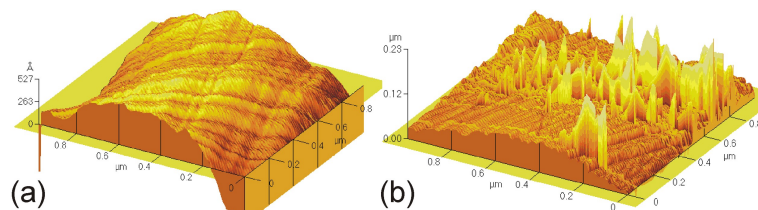


Figure 6.22: *AFM scan inside a pore obtained in an electrolyte of $\text{HF}(\text{aq.})$ mixed with methanol (a) and ethanol (b). In (a) the curved shape of the surface is a measurement artifact and it was planarised for the calculation of the RMS roughness.*

Figure 6.22 shows AFM scans of the pore walls obtained in electrolytes containing methanol,

Fig. 6.22a and ethanol Fig. 6.22b. In both cases an area equivalent to $1\mu m^2$ is investigated. For the case of EtOH some artifacts can be seen inherent to the AFM measurement which however were not considered for the RMS roughness of the samples. The measured roughness for the methanol is 17.5 nm and 16 nm for the ethanol. For these electrolytes the RMS values are very close, however and analysis over a series of samples showed a consistent difference between the RMS values in the corresponding electrolytes.

After showing that decreasing the oxide dissolution rate strongly influences the roughness of the pore walls a natural question arises whether the etching at low temperatures does not lead to the same effect: reduce the oxide dissolution rate and hence surpass the pore walls roughness. Generally low temperatures slow down all processes taking place in the electrochemical dissolution; also the leakage current which is the cause for the roughness of the pore walls. For the sake of completeness, this series of experiments includes also etching at very low temperatures, $T = 10^\circ C$ by using the same electrolyte, 300 ml $c_{HF} = 4wt\%HF$. The calculated roughness is in the range of 12 nm which is a factor 5 smaller than the RMS of the samples obtained in the same electrolyte, at $T = 20^\circ C$.

Although lower temperatures lead to smoother pore walls, the resulting etching time becomes very long. For comparison the etching of $350\mu m$ deep macropores³ etched at $T = 20^\circ C$ lasts 500 min whereas the same depth at $T = 10^\circ C$ will only be reached after more than 800 min. Very long etching time is generally the price that has to be paid for "nicer" pores. Under these circumstances some methods that considerably decrease the pore roughness while keeping short etching times become imperative. Frey et al. proposed solutions for very fast pore etching [127] which were based on surpassing the oxide production and hence reduce the slowest component in the pore growth process, i.e. the oxide dissolution. However their method lead to very inhomogeneous pore nucleation and becomes inapplicable for etching conditions needed in this work.

Generally, not only Si is confronted with a high roughness of the pore walls. A very high pore roughness was observed by Beranek et al. in porous TiO_2 [128]. Tsuchiya et al. [129, 130] used special electrolytes in order to reduce the tubes roughness which consisted of regular etching electrolyte, but which was made viscous by adding some glycerol. In this work the same approach is considered for the etching solution of Si and the next series of experiments involved etching in $c_{HF} = 4wt\%HF$ obtained from 300 ml of DI water whereas 200 ml of the DI water is mixed with 0.5 g of Carboxymethylcellulose Sodium Salt. Figure 6.23a shows a SEM picture of the cross section of the porous layer obtained in this electrolyte together with the AFM scan of the pore wall. One can see a very homogenous growth of the pores as well as a very small RMS roughness which is as little as 9nm.

³Which are quite shallow for most of the optical applications.

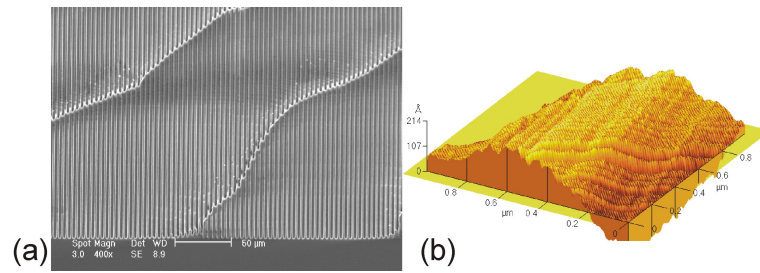


Figure 6.23: Cross section of the etched sample with viscous electrolyte (a). AFM scan of a pore wall (b).

Figure 6.23b shows an AFM scan of a pore wall obtained in a viscous electrolyte. The very low roughness of the wall which is comparable to the wall picture obtained at the tip of the pores in Fig. 6.19 is obvious. The calculated roughness values is below 9 nm which is considerably lower as compared to the aqueous electrolytes. This value is even lower than to the RMS roughness in aqueous electrolytes at $T = 10^{\circ}C$ while providing the etching time inherent to the electrolyte temperature equivalent to $T = 20^{\circ}C$. It takes only 60 min longer, compared to the aqueous etching at $T = 20^{\circ}C$, in order to achieve comparable pore depths. Thus viscous electrolytes not only provide very smooth pore walls, but also the pores could be etched at relatively high speeds.

The same technique for overcoming the pore walls roughness could be applied in order to smoothen the CI. The CI, additionally of being rough as the result of etching *per se*, since obtained as a result of collapsing of more macropores, the roughness can be caused by the imperfect etching, i.e. not enough etching of the pore walls in the trench Fig. 6.2.

Figure 6.24a and -b show AFM scans done along different axes which show a very smooth CI surface. Note that the scanned surface is $20 \times 20 \mu m^2$. The RMS roughness calculated along the X direction is 40nm and that along the Y direction is 20nm. The roughness obtained in this electrolyte is thus a factor 100 smaller than on the same samples by using aqueous electrolytes [97]. Figure 6.24c shows a SEM picture of a very good trench together with homogeneously etched pores.

6.4.3 Discussion

The results presented here show clearly that the roughening of the pores walls is caused by the leakage current flows through the pore walls. An important conclusion at this point is that the leakage current makes the pores rough.

Figure 6.25 summarizes all measured roughnesses obtained in the experimental part. One can see that the highest is exhibited by electrolytes containing water. The AFM scans reveal also a high roughness of the surface which is described by some step like profile. It is not so

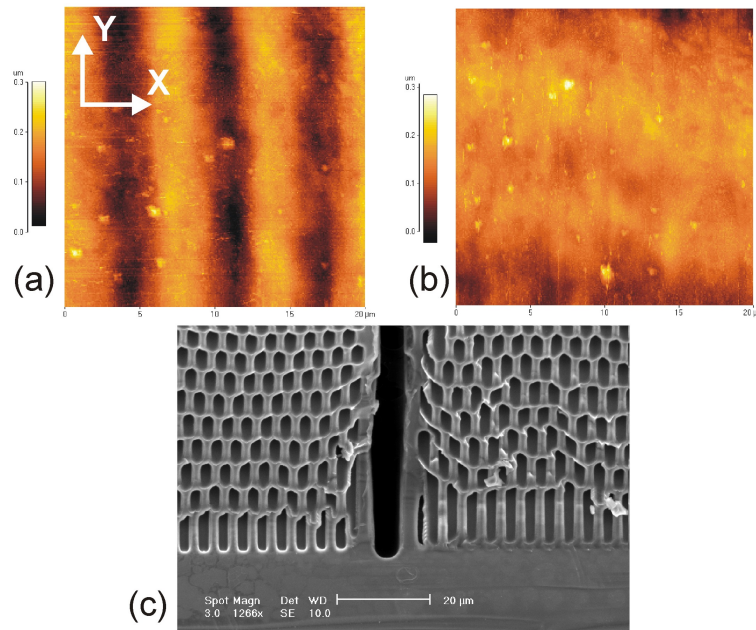


Figure 6.24: AFM scan of the CI in X (a) and Y (b) direction. The cross-section shows a very good etched trench together with homogenous pores (c).

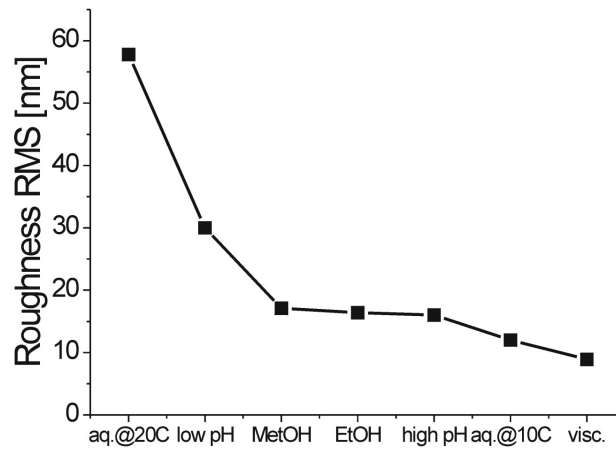


Figure 6.25: The calculated RMS roughness from all experiments casted in one plot.

obvious whether these steps represent the known (111) planes found at the pore walls [126]. Judging from the size of these steps they rather fit to the size of the SCR at the pore wall. In this case this size scale might be the height to which the oxide formed at the tip extends up along the walls. High electrolyte temperatures drive the etching proceeds very fast which might lead to a bad passivation of the freshly emerged sites of the walls and as a consequence high leakage current.

Reducing the pH value would generally increase the number of the protons in the solution. Note that this will however not passivate better the electrode, at least in the anodic state when this take place via the dissociation of the HF molecule at the Si surface [131]. Considering the dissociation reaction constant to be $K = [H^+][F^-]/[HF]$ increasing the concentration of the $[H^+]$ will automatically lead to the increase of the $[HF]$ molecules concentration. Since these are the species passivating the pore walls as a consequence the passivation degree becomes higher and hence is reduced the leakage current. This can serve as a possible explanation why for lower pH values the pores walls are smoother as compared to pure water.

Reducing the oxide dissolution rate leads to a slower etching of the pores, according to the advanced model in Section 7. The reason why this has a favorable impact on the pore roughness can be explained as follows. First, the reduced etching speed allows more time for the freshly formed surface to become passivated. Second, it is related to the quality of the oxide at the tip. According to the CBM a reduced oxide dissolution rate leads to the smoothening of the surface. While etching under conditions favoring the SiO₂ production they will disfavor the divalent dissolution and hence also the leakage current. As a result the pores will become less rough.

The results obtained in different alcohols are similar to those in an electrolyte buffered with NH₄F produces. The buffering shows additionally that besides the kinetic arguments, using an electrolyte which wets better the surface helps to decrease the roughness too. For complete understanding of "better battening" effect some additional experiments are needed however the argument with increasing the sticking factor of the $[HF]$ molecule to the surface in such electrolytes has its merits [29].

Lower temperatures also favors smooth etching of pores. The arguments supporting this conclusion were extensively discussed in Section 6.2.5.

The role of the viscous electrolytes is not really understood. The known feature of a viscous electrolyte is that the diffusion constant of all species in the electrolyte is inverse proportional to its viscosity constant: $D = 1/\xi$, where ξ is the viscosity constant. The effect of such diffusion limitations is favorable for the tip as well as for the walls. At the tips, limiting the diffusion of HF₂⁻ and HF causes an excess of available holes which tends to make the tetravalent dissolution and hence rigorous oxide formation a predominant process. This in

turn leads to a very homogeneous etching. At the pore walls the passivation might take place with a lower rate as compared to aqueous electrolytes, however an H_3O^+ ion is much lighter than any etchant species. As a consequence, due to the mass transport issues, the passivation of the walls becomes more probable as their etching.

6.5 Composite materials for PC applications

6.5.1 Introduction

Filling pores in semiconductors with different types of materials, e.g. with metals, polymers, or other semiconductors, etc., is an emerging aspect of porous semiconductors with interesting potential applications. Filling a second kind of material into porous structures that has either very small dimensions, or huge aspect ratios, or both, is a new kind of "art" in the field of producing novel (nano)composite materials [132, 133, 134] and opens the way to a new branch of (nano)technology and composite materials.

Filling macropores with Cu by electroplating provides a good model system since much work has been done in the field of Cu plating on metals [135, 136, 137] or semiconductor surfaces [132, 138, 139, 140, 141, 142, 143, 144, 145, 146]. For example, the so-called damascene Cu electroplating process introduced in 1997 [147, 142] with the intention to replace Al is now routinely used in microelectronic technology for interconnects. While Cu is deposited into narrow trenches, their depth is rather in the sub-micrometer range. The process uses a thin Cu seed layer and some three or four (or even more) additives in the Cu^{2+} bath solution [148]. The detailed mechanisms were investigated for many years [143, 144, 145], but are still not completely understood.

The reduction of Cu^{2+} ions during electrodeposition consumes either electrons from the semiconductor or injects holes into the semiconductor. Whether a conduction band process (electron-extraction) dominates, or a valence band process (hole-injection), depends on the doping type (n- or p-type) of the semiconductor, the redox potential of the metallic ion, the solution composition and pH value, the polarization potential, and so on [139, 69]. Electroless Cu deposition into Si pores has been investigated, too, but usually resulted in the formation of Cu_2O and SiO_2 clusters on the pore wall, i.e. the reduced and oxidized products of copper ions and silicon, respectively [132, 146]. Hole-injection into silicon thus seems to be the main reaction under those conditions since holes are needed for the oxidation of silicon. A very detailed analysis on the electroless deposition of Cu on porous InP was communicated recently [149], but a uniform Cu deposition could only be realized at a low temperature of 3.5°C . Mostly only the deposition of Pt [150, 151], Au or Cu on bare Si or Ge [152] surfaces is reported.

Filling macropores with Cu is a far more demanding process than the Cu plating or the Cu damascene process, in particular for p-type Si where the easy conduction band process is not possible. Filling of macropores in p-type Si (diameter ca. 0.5 μm , length ca. 50 μm) by electroplating has been attempted with some success by employing backside illumination [153, 154] for producing holes and guide them to the pore tip analogous to the standard

macropore etching process. Attempts to fill deep pores with an electroless technique have been made, too [155], but no data about the filling homogeneity were provided. Sato et al. filled macropores in n-Si with Ni [156]. They reported a homogenous filling of deep trenches with diameter as large as 5mm. Several other reports on the pore filling with metals were not conducted on Si-templates [157, 158, 159]. However, pore depths were in the order of several micrometers or less, and independent seeding processes were often used. Remarkably, single Cu crystals were obtained by electrodeposition under some conditions [157, 158, 159].

It can be concluded that filling deep macropores with diameters of micrometers and aspect ratios of > 50 presents a considerable challenge. Using electroplating may not be easy, but it has the potential for satisfactory results. Standard methods like chemical vapor deposition are not easily available for metals, and physical techniques, e.g. physical vapor deposition or *Atomic Layer Deposition* (ALD) often have severe shortcomings and tend to be rather expensive. The common drawback of most methods is that for deep and large macropores the so-called "bottleneck" effect occurs, i.e. the closing of the pore entrance before it is fully and homogeneously filled with the metal (or possible other fillings). This problem becomes more accentuated for deeper pores and a depth of several tens of micrometers might already be too large for homogeneous filling.

The aim of this work was the optimization of the very deep macropores filling in n-type Si with a diameter of $2 \mu\text{m}$ and as deep as $150 \mu\text{m}$ with Cu by means of electroplating. These macropores could be homogeneously filled without encountering the bottleneck effect, which means the filling begins from bottom towards the tip of the pore. The main electrochemical processes related to the metal electrodeposition inside the very deep pores are identified. The goal is not to deliver some concrete numbers for the experimental conditions, but rather to shed light on the common problems occurring while electroplating metals in porous templates. Finally, the principles of the electroplating process used are discussed, as well as its potential application for other systems. The process reported here may offer a cheap and quick way to fill pores with many metals (i.e. Fe, Ag, etc.) or other materials such as polymers. The knowledge gain from filling deep trenches in Si is used for filling other templates as GaAs, Ge and InP. It is shown that these semiconductors, exhibiting peculiar pores geometries [160, 14, 16], impose different filling conditions and special pretreatments of the samples before deposition.

Finally, the proposed technique might be used for the production of a PC. The filling of metals into pores can be replaced by filling other materials so that adequate refractive index contrast could be obtained.

6.5.2 Experimental results

For uniform filling of the pores from the pore tip to the top, a nucleation process, i.e. seed formation, at the pore tip is crucial. This step is important, reported also in Ref. [155, 157, 158, 159, 161]. After the nuclei have been formed, further deposition of Cu on the rest of the surface must be suppressed. In order to achieve a high nucleation density, a high current (or potential) pulse is applied at the beginning [139, 140, 141]. In the galvanostatic experiments, a high current pulse⁴ of 1.0 mA/cm² for 10 min was used to induce the nucleation (we will use from here on only absolute values for the deposition current). The corresponding current and potential vs. time curves can be seen in Fig. 6.26a (phase I). The potential strongly increases at the very beginning (while the voltage decreases; note the negative potential axis on the graph), while the applied current was kept constant. This behavior is an indication that the nucleation process has taken place and that a growth process has started afterwards.

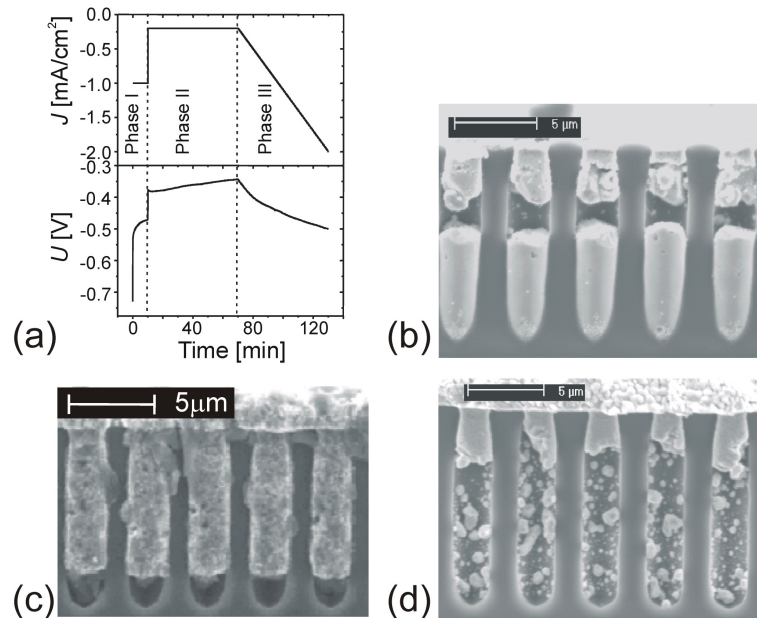


Figure 6.26: *Inhomogeneous pore filling. Current density and potential vs. time (a) for the filled pores shown in (b); bottleneck formation (b); filling obtained only with a linear increase of the current (c); filling obtained with a constant current (d).*

The parameters of the current pulse must be carefully selected. Current densities too high might produce nuclei formation not only at the pore tip, but also on the pore walls or even on the surface. More seriously, it may lead to parasitic reactions such as the decomposition of water, which will produce H₂ in the pores. By contrast, too small current densities may lead to nuclei formation only on some selected pores tips and then to inhomogeneous filling in the sense that not all pores are finally filled [139].

⁴Since electroplating is done in the cathodization regime, the currents values have to be considered negative.

After initial nucleation, corresponding to the strong potential increase during the first seconds of the experiment (Fig. 6.26a), the (small) nuclei must be allowed to grow laterally until the bottom of the pore is totally covered, in order to form a suitable seed for a growing Cu column. For this lateral seed growth phase an appropriate period of time must be chosen. It was found that 10 min is sufficient; this is rather an empirical value, however, since it depends on many factors such as substrate and electrolyte resistivity; electrolyte temperature, etc. In our case the processes for the nuclei formation and growth of the seed may merge into just one step; e.g. 1.0 mA/cm² for 10 min; this is denoted as phase I.

After the seed formation step, the electrodeposition must be decelerated because it must be ensured that the transportation of Cu²⁺ ions does not become the rate-limiting process for the uniform filling [139]. The transportation of the Cu²⁺ ions to the reaction place at the pore tip is rather slow due to the diffusion limitation in deep pores and this necessitates small current densities at this point. While lowering the current density to arbitrarily small values may overcome diffusion limitation problems, too small currents (and therefore also voltage) are counterproductive since the negative potential must remain large enough to achieve the necessary overpotential ("driving force") needed to warrant continuous film growth. The parameters chosen and shown in Fig. 6.26a in phase II will meet both conditions. As can be seen, keeping the current constant in this early growth phase leads to a gradual potential decrease, indicating that the voltage losses in the electrolyte (inside the pores) are reduced since the pores are continuously filled and thus become shallower.

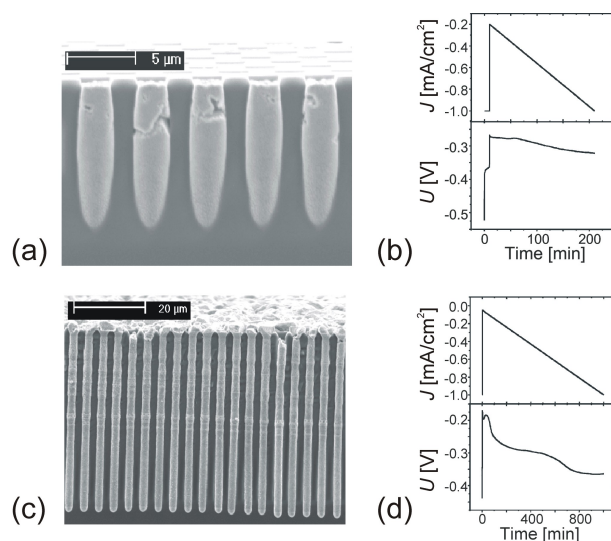


Figure 6.27: SEM pictures of Si macropores uniformly filled with Cu. Just about uniform filling of 10 μm deep pores (a); deposition conditions (b); perfectly filled 60 μm deep macropores (c); deposition conditions (d).

As a consequence, diffusion limitation becomes less severe and the current can be gradually

increased as shown in Fig. 6.26a for phase III. The slope of the current increase must be chosen accordingly since a too high slope will generally lead to the known "bottleneck" effect. This is shown in Fig. 6.26b, where the current density was increased from 0.2 mA/cm^2 to 2 mA/cm^2 in 60 min, causing the closing of the pores' entrances before their complete filling. Generally, a current density that is too large at any time after phase I will always lead to the closure of the pores. The reason is that as soon as the copper ions transport becomes limited process, the most preferable/probable reaction place shifts to the pore entrances for reasons explained later in more details.

The situation in Fig. 6.26c corresponds to a case where the current is increased from 0.2 mA/cm^2 to 1 mA/cm^2 in 200 min without using the pulse for the seed formation in phase I. In this case the deposition does not start from the pore tip. It also shows that if nuclei are allowed to grow across the pore to form a seed, the Cu eventually deposited inside the pores is mottled in appearance and not of good quality.

Figure 6.26d shows the results of a deposition attempt with a constant current density of 0.6 mA/cm^2 after the current pulse for the seed formation but without phase III. Evidently the deposition could not be focused on the tip and nucleation mostly took place all over the pore walls. It is thus clear that all phases of pore filling need to be optimized, and it is equally clear that the issue becomes even more involved for pores deeper than the $10 - 15 \mu\text{m}$ pores in Fig. 6.26.

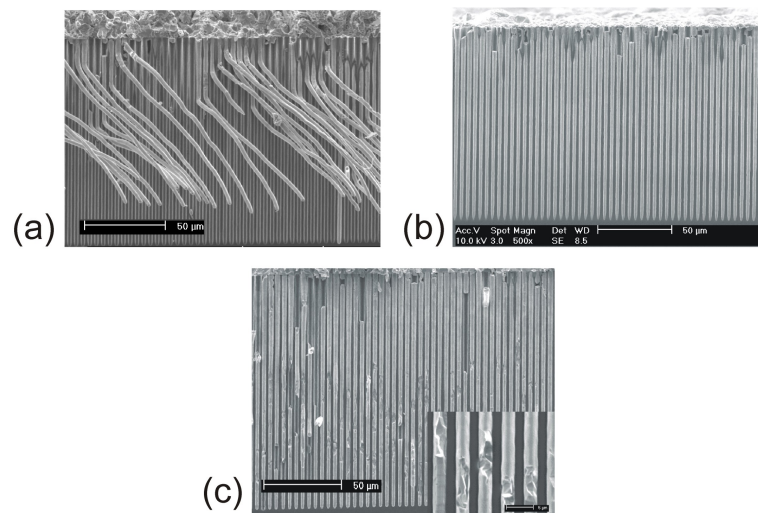


Figure 6.28: *Filling of $150 \mu\text{m}$ deep macropores showing "artifacts" due to symmetry breaking upon cleaving (a); Complete filling of $150 \mu\text{m}$ deep macropores (b); Complete filling, but with some imperfections in the Cu rods (magnified view in the inset) (c).*

Uniformly filled pores obtained under optimized conditions are shown in Fig. 6.27. In Fig. 6.27a there is still a small bottleneck effect expressed in some defects in the Cu bulk. The Si

sample surface is completely clean, however, indicating that the deposition starts at the pore tips rather than on the semiconductor surface indeed. The current and the potential for this case are shown in Fig. 6.27b. Phase I was too short to be seen in Fig. 6.27d while phase II was omitted for the sake of simplicity, and a linear increase of the current with a small slope and end value was carefully chosen for the phase III.

Following the line of reasoning described above, macropores with a depth of up to 60 μm could be filled uniformly as shown in Fig. 6.27c, suggesting the validity of our approach. In Fig. 6.27c one can also see some variation of the macropore diameters, which, however, was not an impediment for the homogeneous filling of the pores with Cu. By contrast to the picture in Fig. 6.27a, a thin layer of Cu has formed on the top of the sample; but this most likely happened after the pores were filled. The current and the potential for this case are shown in Fig. 6.27d.

It should be pointed out that the duration of phase I for the deep pores was shorter than for the shallower pores, cf. Fig. 6.27b with Fig. 6.27d. While this may seem to be counterintuitive, the need for suppressing random nucleation somewhere on the large pore wall area for the deep pores is more important than allowing long time for the seed nucleation/growth process. Fig. 6.26b illustrates this up to a point: the small whitish specks on the copper poles on the Si walls in the unfilled part of the pore are Cu nuclei that did not grow, indicating that the nucleation process was just about too long.

Figure 6.28 shows the results obtained with 150 μm deep macropores. The experimental conditions include 1min at 1mA/cm² for the seed growth with ulterior linear increase of the current from 0.01 mA/cm² to 1 mA/cm² for 3000 min. Remark that the time for the phase 1 is reduced to 1min as compared to 10min for the case of 60 μm . In no case 1 min is sufficient for the complete grow of the seed, however, it cannot be waited longer on the phase I due to a very strong diffusion limitations of Cu ions in very deep pores. If keeping the current at 1mA/cm² for longer time the bottleneck will occur and the pores entrance is very soon closed. The seed is let to grow further while reducing the current to 0.01 mA/cm².

Here it is important to mention that interpretation of the cross-sectional pictures must be done carefully. The Cu rod inside a pore does not fracture like the porous Si template. It can remain on the sample piece to be investigated with the SEM, but it can also be removed from the pore. If the fracture plane fluctuates, the Cu rod will be sheared off and remain on the part with the larger fraction of the pore. The Cu rods may even be pulled up or pulled out and bent, as shown in Fig. 6.28a. Nevertheless, Fig. 6.28a essentially shows perfect pore filling, as does Fig. 6.28b in a more conventional way. That the few "missing" pieces of Cu are indeed due to the artifacts produced by cleaving was independently demonstrated by carefully beveling the sample by mechanical polishing on an inclined plane so that the Cu

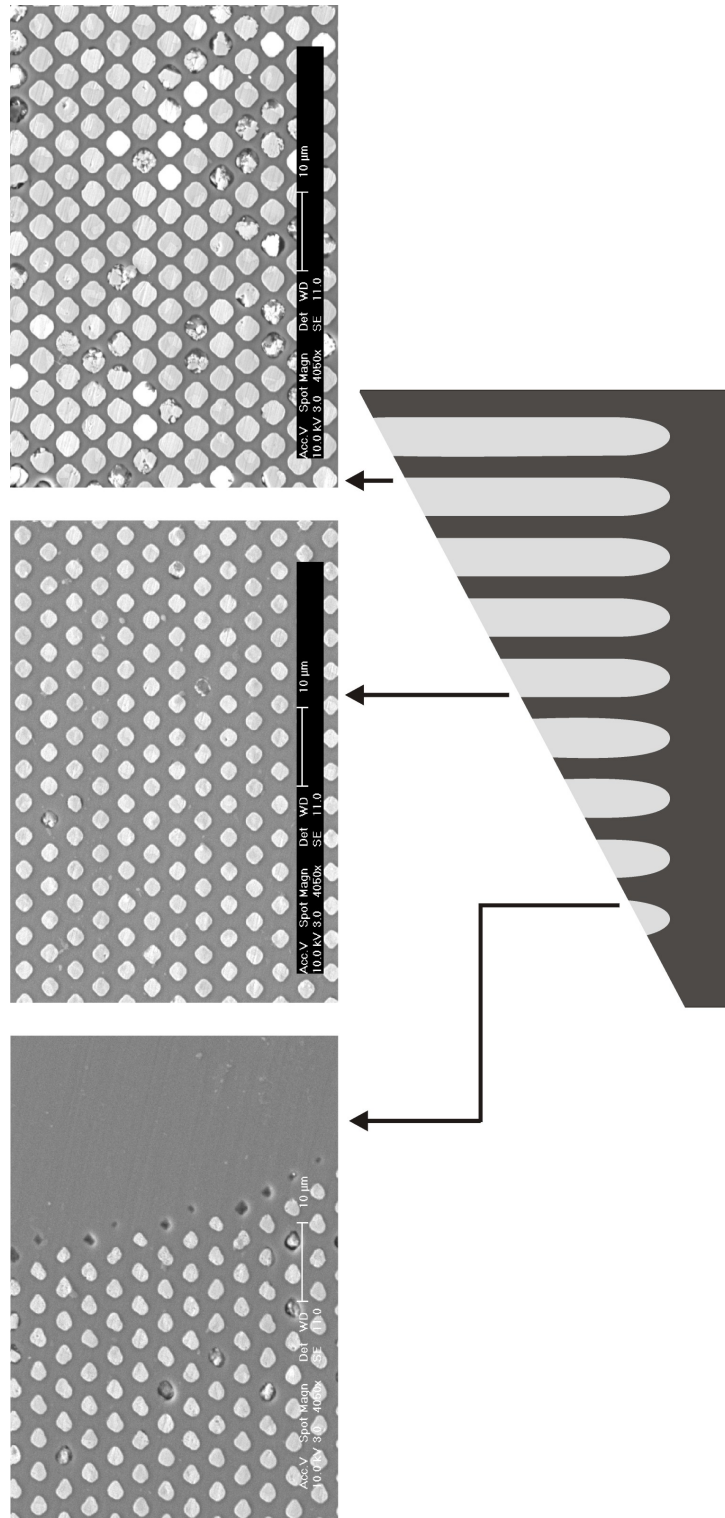


Figure 6.29: Beveled surface and SEM pictures taken at different locations showing the surface of the sample.

filling could be seen at any depth, Fig. 6.29. Figure 6.28c illustrates that perfect filling is difficult; showing Cu rods with some imperfections obtained in an experiment slightly outside the optimum current profile conditions.

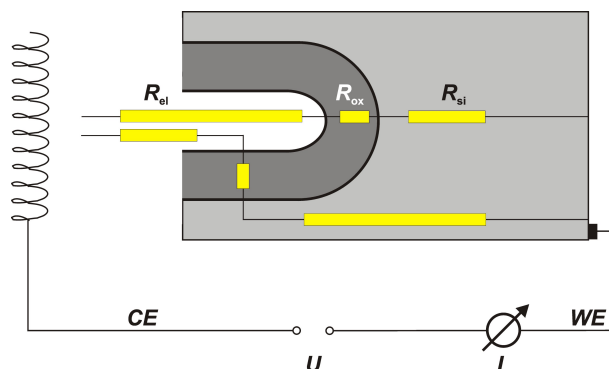


Figure 6.30: *The resistance paths for the current flow. The yellow resistances show the path of the smallest resistance.*

Deep pores with aspect ratios > 100 thus can be filled with Cu by electroplating. However, besides the challenges related to finding the optimal parameter set, a major disadvantage might be that long deposition times are needed. A typical time scale for filling $150 \mu\text{m}$ deep macropores is about 50 hours. This may be an indication that besides the diffusion limitation other factors slowing the process must be taken into account, for example the rearrangement of the copper atoms on the deposited copper pole surface or the low electron density of semiconductors [139].

6.5.3 Discussion

Understanding electroplating from solutions with considerably higher resistivity as compared to the templates is still puzzling. Current flow should occur along the path of the least resistance and thus in the Si and not in the pore (since the resistivity of the solution is at least by a factor of 7 larger than the one of the substrate). This is schematically represented in Fig. 6.30. Therefore it is not obvious why the deposition process should start at the pore tips and not at the semiconductor surface. This topic is rarely addressed in the literature, i.e. describing the electroplating in deep pores. Sauer et al. showed that at least with regard to porous Al, the filling of the pores is possible only if pulsed current is applied [161]. Almost the same technique is reported to be successful for filling InP templates with Cu [162]. Sauer et al. also present a comprehensible electrostatic model which perfectly supports their experimental findings. However it cannot be directly applied here solely because we have to do with very high electrolyte resistivity and very deep pores ($150 \mu\text{m}$ compared to $2 \mu\text{m}$ in Ref. [161]).

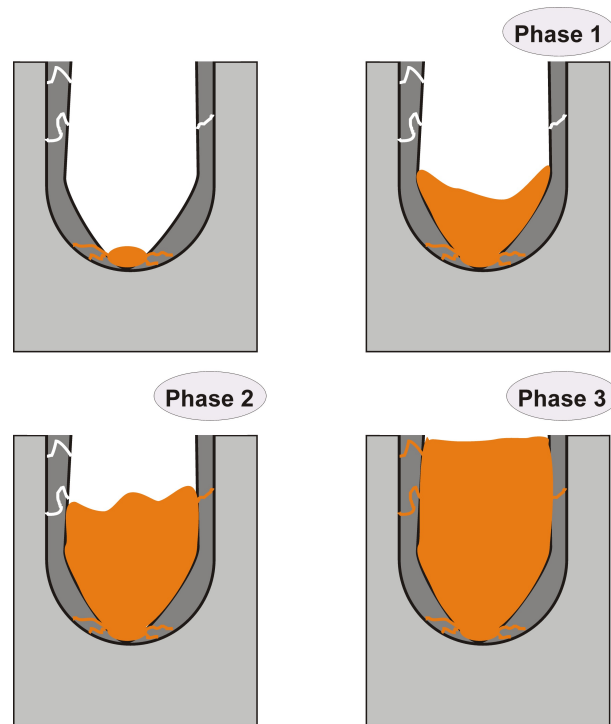


Figure 6.31: A model explaining the deposition of Cu in very deep macropores. The phases indicated in the picture have to be correlated with the ones in Fig. 6.26a.

A possible scheme for the deposition of Cu in macroporous Si is presented in Fig. 6.31. Since the samples have been exposed to air and were sonicated in CuSO₄ solution prior to deposition and dipped in Piranha solution (98 % H₂SO₄ : 30 % H₂O₂, 1:1) for 10 min, it is clear that the pores surface was covered with thick oxide of a thickness that might range between 8 and 12 nm [80]. This oxide layer is an excellent insulator and can withstand field strengths in the order of $> 1\text{V/nm}$ as encountered during in the experiments in the relatively flat parts of the sample (surfaces and pore walls). At the pore tips, however, the field strength is substantially increased so that dielectric breakdown of the oxide occurs and current flow is locally possible, leading to the deposition of the Cu nuclei and their lateral growth into a seed. If no new nucleation occurs, current flow will now proceed through the conducting channel through the oxide. The initial current pulse, which is also a field strength pulse, also helps the process. Nevertheless, even without a protective oxide, the small radius of curvature at the pore tip might enhance the metal ion reduction (as well as the generation of electrons in p-type materials) in comparison to the pore walls or the substrate surface. This could be the case for porous semiconductors with an unstable oxide, this being the case of, e.g., InP, Ge, etc.

This explanation is supported by other observations: the obvious remedy to the resistivity problem outlined above is to decrease the resistivity of electrolyte. However, experiments using

an electrolyte with an increased concentration of H_2SO_4 and a resistivity of about $0.6 \Omega\text{cm}$ (or more) did not improve the filling situation significantly, which indicates that breakdown of the oxide layer at the pore tip is still the critical process in this case, too.

Once the Cu seed is formed inside the pore one has to account for some additional phenomena. If some pores are filled somewhat faster for whatever reasons the deposition rate will increase even more. The process thus tends to be unstable which might lead to very non-uniform deposition conditions across the sample. This sort of instability will become more critical when filling deeper pores, Fig. 6.28c might serve as an example of this.

Since it was invoked a small radius of curvature at the tip as the main reason for starting the deposition at the pore tip (due to the very high electric field strength), it should be evident that for the case of macropores with completely smooth pore wall the radius of curvature on the walls tends to infinity. One has to point out, however, that macropores very often grow with relatively rough walls. This implies the existence of locations on the walls where the radius of curvature is small. According to the schemata proposed above this would imply that the deposition might also start there. This however happens only under unoptimized conditions, i.e. too high/long initial current pulse as one can see in Fig. 1b-d.

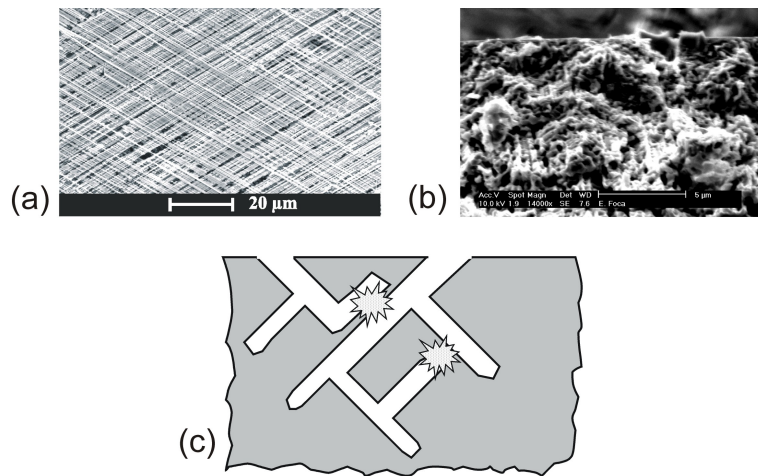


Figure 6.32: A cross section of a domain with pores in GaAs, reproduced from Ref. [160] (a). SEM of a cross section through a destroyed GaAs porous structure after the deposition (b). The schematics of the pores in GaAs which might serve as traps for the formed H_2 (c).

On a next stage it is tested if the same conclusion applies to other porous semiconductors. As a potential candidate GaAs is chosen with pores growing in a fractal-like domain. Peculiar about the pores is that although they are very shallow, they are oriented at a specific angle to the surface, i.e. are not perpendicular as is the case of the macropores in Si. Moreover, the wall thickness is very small resulting in a very fragile skeleton as compared to Si. The cross

section of such a porous structure is shown in Fig. 6.32a reproduced from Ref. [160]. Note that according to the authors each pore will branch into its descendants growing into (111) directions, inclusive toward the surface. Filling such a structure with Cu by using a constant current will immediately lead to a picture similar to Fig. 6.32b. As it can be seen, no porous structure can be recognized rather a sponge like form is found. The first explanation for this effect is shown in Fig. 6.32c. Each of the descendant pore has to grow up to the surface and even pierce it. However, this is not always the case. Some of the pores will form some sort of traps. This traps form a perfect location where the H_2 is formed and also trapped. Over the whole sample this might lead to some local explosions which completely destroy the porous structure. An EDX analysis of these samples revealed some Cu inside the pores, however it is not massively present.

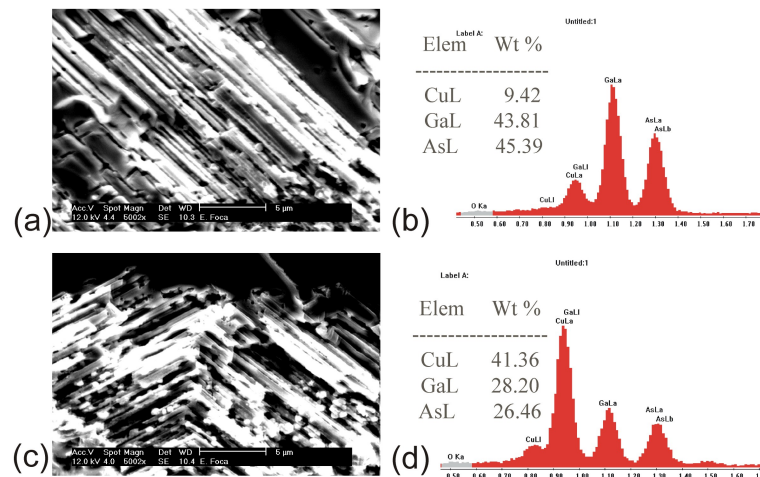


Figure 6.33: *The SEM picture of the filled GaAs sample after being oxidized 5 min (a) and 15 min (c) in H_2O_2 and the corresponding EDX spectra of the respective samples (b) for (a) and (d) for (c).*

Another reason why the filling in GaAs does not work is the quality of the oxide produced on this semiconductor. Being very thin and easily dissolvable, one confronts here even stronger as in Si the problem of the location where the deposition starts, i.e. where the seed is formed. Namely, since the surface is completely clean, the deposition might start everywhere and in most of the cases lead quite early to the bottleneck. In order to avoid this the samples were treated in H_2O_2 prior to the deposition. This is a strongly oxidizing agent which ensures the formation of a homogeneous oxide layer on the pores. (Having not very deep pores, one can generally expect that the oxidation is homogeneous.) In Fig. 6.33a a SEM picture is shown after the deposition of Cu into a GaAs sample kept in H_2O_2 for 5 min prior to the deposition. A homogeneous porous structure is clearly seen and somewhat harder can be seen the Cu inside the pores. An EDX analysis presented in Fig. 6.33b of the same sample shows a weight

% of Cu in the range of 9.5 wt%. A longer oxidation of the sample in H_2O_2 , about 15 min, leads to the formation of thicker oxide and hence improves the filling of the pores. The SEM picture of such a sample after the deposition is shown in Fig. 6.33c. On the sample an EDX analysis is made with the same spot size as in the previous case, Fig. 6.33d. As it can be seen there is considerably more Cu in the structure. One can also see that the amount of Ga and As is somewhat diminished due to the fact that the oxidation in H_2O_2 is also accompanied by the oxide dissolution due to the very unstable form of the oxide.

At this point the role of the oxide as a insulation layer on the pores walls becomes obvious. Filling pores in GaAs as well as in Si is possible only after some oxidation occurred. The observation that the Cu rods slip easily inside the pores, i.e. that they are not attached to the Si or SiO_2 supports the view that they grow as (single) crystals from a seed layer at the pore tips and have hardly any interaction at all with the pore walls, as shown in Fig. 6.28a.

While the Cu in well-filled pores looks rather uniform and smooth, no direct conclusion can be drawn as to its crystalline perfection and texture. Earlier works reported that single Cu crystals could be found with an orientation of Cu (111), or the growth direction is mainly along with $\langle 111 \rangle$ [155, 157, 158, 159, 163, 164]. In this context it is of interest how the deposition proceeds after the pores have been filled. On occasions the Cu will further grow on the surface in form of the "needles" having as basis a filled pore. Rather large crystallites have been formed in continuation of the Cu rod coming from the pore; indicating a high degree of order. This may be seen as an indication that the growth of the Cu inside the pore is also along some preferential direction.

6.6 Conclusions

In the framework of this work special structures formed by macropores in Si are etched. The etched structures are aimed for being used as optical devices which imposed strict conditions with respect to their quality. It is the first time that in n-Si with BSI regular porous regions separated by large trenches are etched. The special application of the etched structures impose strict restrictions to the quality of the trench walls and pores in general. The methods developed allow to etch:

- very deep pores;
- constant diameter with the depth;
- constant diameter across the sample;
- no cross-talk between the pores;

- intact surface of the sample;
- pores with very smooth walls.

The strong requirement with respect to the optical quality of the etched structures are successfully accomplished as a result of deep understanding of the macropore etching mechanisms in n-Si.

In order to better control and understand the pore growth, FFT-IS was extensively used. In particular, for the first time such an analysis is applied *in-situ* during the pore growth. For etching n-Si with BSI a new impedance photo impedance mode was introduced. For both types of impedance modes theoretical models were developed which allowed to interpret the measured data.

The data extracted from the voltage impedance allowed to estimate the dissolution valence at the pore tip at any instance in time. This is the first time that such a precise information about the development of the pore tip state could be obtained. By comparing the estimated valence with the quality of the pores, it could be concluded that the optimal pore growth takes place with a valence of $n \cong 3$. This justifies the assumption that the pores advance while producing, and ulterior dissolving, oxide at the pore tips. As a consequence a special model could be developed which explains the growth mechanism of the macropores under optimized conditions.

The newly introduced mode, photo-impedance, delivers additional data concerning the pore growth. Peculiarly for this mode of impedance is the characterization of the n-Si electrode. The theoretical model fitting the data can be used to extract such parameters as the depth of the pores or the diffusion length of the sample. For the diffusion length a systematic deviation of the measured data from the theoretically expected ones were found. In order to understand the routes of this aberration special experiments have been made which clearly indicate the direction in which the theoretical model could be improved. Not less important, these experiments give new insights into understanding of macropore growth. The main conclusion is that for obtaining good macropores the growing speed has to be adequately chosen, which in most of the cases necessities that the tip is fully covered by SiO₂. Hence both modes of the impedance lead to the same final conclusion for optimal homogeneous macropores growth in n-Si.

Finally, the data extracted from these two types of impedance can be used for *in-situ* controll of the etching process and thus save a considerable amount of time for the optimization of the etching process.

A systematic study of the influence of alcohols on the pore geometry has been performed. Along with the findings of other scientific groups, an important step in understanding their

effect on the formation of pores could be made. The influence they have on dissolution kinetic of the SiO_2 has a great impact on both the size feature of the pores as well as on their quality. In particular by using alcohols, very smooth pores could be obtained and partially explained. Finally, it sheds more light on the mechanism of macropores formation in n-Si and triggers further investigation for deeper understanding of the role of alcohols on the Si - liquid interface.

The topic related to the pore walls roughness is completely absent in the literature. Thus, in the framework of this dissertation, it is the first time that this issue was extensively investigated. By means of using different electrolytes the roughness could be reduced from 60 nm to 8 nm on a $2 \times 2 \mu\text{m}^2$ scale and from 530 nm to 40 nm on a scale of $35 \times 35 \mu\text{m}^2$. It is also for the first time that viscous electrolytes were used for etching macropores in n-Si. They allowed a reasonable etching speed; at the same time yielding perfectly smooth pore walls. The results pave the way for an extensive investigation of the role of viscous electrolyte on macropore etching.

The fabrication of composite materials by using porous templates was investigated. Macropores as deep as $150 \mu\text{m}$ could be filled by electroplating. Additionally, a theoretical approach was proposed which can explain the inherent phenomena to the electrochemical deposition. It fits well to the experimental findings shown in this work. The gained knowledge was further applied to some other semiconductors like GaAs and Ge [162]. Also for the first time extremely fragile porous structure in GaAs could be filled up to a considerable degree with Cu by electroplating. As a remarkable result, the proposed theory can therefore be extended to other semiconductors and fillings.

Finally the feasibility of using macroporous n-Si for the fabrication of the PCs is shown. In this work specific demands imposed by this peculiar optical components could be identified and solutions were proposed. The research is further extended in the direction of producing composite materials which can be also used as types of PCs. The knowledge gained in this chapter helps to assess: how realistic is the implementation of different optical components functioning at different wavelengths.

7 Experimental work on optical elements based on Photonic Crystals

7.1 Calculation methods

In order to calculate the distribution of the electric field intensity in a system consisting of dielectric cylinders a method similar to the one described in [165] is used. Let's consider a PC consisting of dielectric cylinders which interact with electromagnetic wave with the wavelength λ . A polar coordinate system for the plane (XOY) perpendicularly cutting the cylinders axis: $R = (R, \alpha)$ is used. Let $E = E(R)$ be the electric field strength oriented along (0Z) axes. Let's consider the electromagnetic field in the vicinity of a cylinder j with the coordinates in the plane (XOY) given by $R_j = (R_j, \alpha_j)$. The electric field strength $E(R)$ for the corresponding cylinder will consist of two components: first, the electric field originating from the radiation source $E_{source}(R)$ and the electric field scattered by the group of the cylinders in the regarded assembly, $E_{scatt}(R)$. The total electric field strength will then given by:

$$E(R) = \sum_{m=-M}^M (a_m(j) J_m(k_0 R_{R_j}) + B_m(j) H_m(k_0 R_{R_j})) \exp(Im\{\alpha_{R_j}\}) \quad (7.1)$$

where $k_0 = \frac{2\pi}{\lambda}$, $R_{R_j} = R - R_j = (R_{R_j}, \alpha_{R_j})$, J_m and H_m are the corresponding Bessel and Hankel function of the first rank. The parameter M would have to be set to $M = \infty$, however for most practical situation $M = 2$ shows reasonable results. The summation is done in the interval $-M \leq m \leq M$.

The parameter:

$$D_m(j) = \frac{B_m(j)}{a_m(j)} \quad (7.2)$$

is an exact solution of the Maxwell equations for a single cylinder. As a result, it follows:

$$D_m(j) = \frac{k J_m(k_0 r) J'_m(kr) - k_0 J'_m(k_0 r) J_m(kr)}{k_0 J_m(kr) H'_m(k_0 r) - k H_m(kr) J'_m(k_0 r)} \quad (7.3)$$

where $k = \frac{k_0}{\sqrt{\epsilon_2}}$.

Considering that the dispersion from each cylinder is rather weak and leaving only the terms for the zeroth and first ranks for the dispersion a system of the self consistent equations follows:

$$B_m(i) = a_m^0(i) D_m(i) + \sum_{N,M,i \neq j} B_l(j) D_m(i) H_{l-m}(k_o R_{ij}) \exp(i(l-m)(\pi + \alpha_{ij})) \quad (7.4)$$

where $a_m^0(i)$ is the amplitude of external radiation, $R_{ij} = R_j - R_i = (R_{ij}, \alpha_{ij})$. The summation is made over the parameter $-M \leq l \leq M$ and $-N \leq j \leq N$. After solving the Eq. 7.3 a set of $B_m(i)$ is obtained. This information is already enough for qualitative description of the following phenomena.

Let's assume that one needs to assess the intensity of the electromagnetic field in a certain point in the vicinity of the cylinders system. In order to solve this problem, the point of interest is replaced by a cylinder with an infinitively small diameter and one tries to find the electromagnetic field in this point. It is necessary to write and solve the Eq. 7.3 in this case, however, for $N + 1$ cylinders. It can be considered that introducing a new infinitively small cylinder in the system does not change the magnitudes $B_m(i)$ for $N \leq i \leq 1$. What happens is actually $D_m(N + 1) \rightarrow 0$ and $B_m(N + 1) \rightarrow 0$ concomitantly, and that is why the magnitudes $B_m(N + 1)$, according to the theory of excitations, are in the first decaying rank of the very small magnitudes $D_m(N + 1)$. As a result the following formula is obtained:

$$B_m(i) = \sum_{l=-M}^M B_l(j) D_m(i) H_{l-m}(k_o R_{ij}) \exp(i(l-m)(\pi + \alpha_{ij})) \quad (7.5)$$

where $i = (N + 1)$ and $N \geq j \geq 1$. The summation is done over l , $-M \leq l \leq M$ and over the parameter j . In order to find the exact value of the $E(R)$ in the center of the i^{th} cylinder, $i = (N + 1)$ ($R = R_{N+1}$) by means of the Eq. 7.2, a further $a_m(N + 1)$ is needed to be found. One has to mention here that for the cases treated in this work only one component proved to be sufficient, a_m for $m = 0$. By using Eq. 7.1 one can finally write:

$$E(R_{N+1}) = \frac{B_0(N + 1)}{D_0(N + 1)} = \sum_{l=-M}^M B_l(j) D_m(i) H_{l-m}(k_o R_{(N+1)j}) \exp(il(\pi + \alpha_{(N+1)j})) \quad (7.6)$$

If another polarization has to be considered, i.e. the electric field is perpendicular to the cylinders axes, all equations from above can be employed. In this case, however, the electric field has to be replaced by the magnetic field. In this case all formulas remain the same with the exception of Eq. 7.3, where the corresponding changes have to be done.

7.2 Concave lenses

As discussed in the Section 3.1.2 each PC has a clearly defined wavelength interval where it behaves as an optically homogeneous material with $n_{eff} < 1$. This regime allows for an enticing beam propagation inside the PCs and thus many interesting application could be envisioned. Particularly novel types of optical components can be designed based on these metamaterials e.g. such basic optical devices as lenses exhibiting additional interesting properties.

Having a material with $n < 1$ surrounded by air, a focusing lens can be fabricated if the material is shaped in a concave form. According to Snell's law, a convex lens will diverge radiation originating from a point source, Fig. 7.1a, while only a concave lens allows focusing, see Fig. 7.1b.

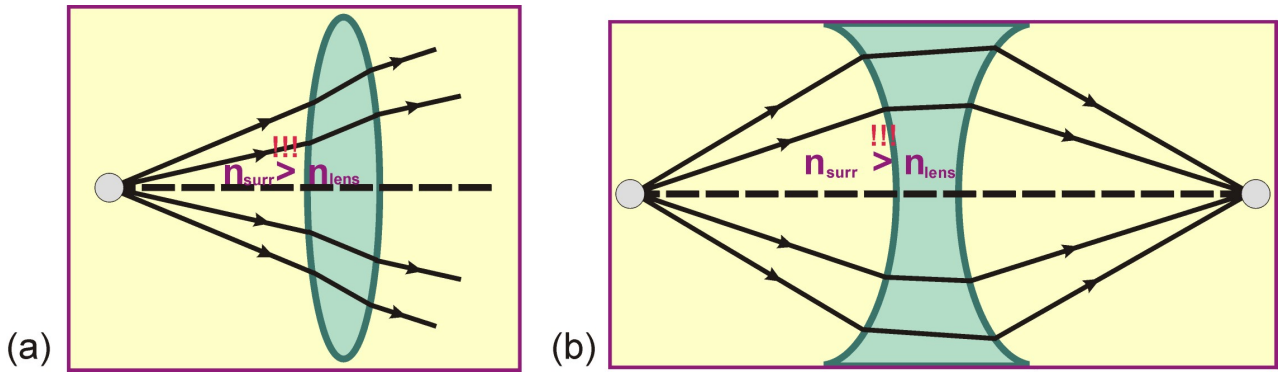


Figure 7.1: *The action of lenses made of optically homogenous material with $n < 0$ surrounded by vacuum (i.e. $n = 1$). A lens with the: (a) convex form diverges the beam from a point source; (b) concave form focuses the beam from a point source.*

In this work two distinct types of lenses are treated. The main difference between them is the lattice type used for the arrangement of the dielectric cylinders, i.e. the primary structural parameters of the lenses. First a square lattice is treated followed by lens based on the triangular lattice. In both cases the design resides on five key steps:

1. Determine the frequencies where n_{eff} exists and has unusual values within the explored frequency range (here, 5GHz to 15GHz);
2. "Cut" a suitable lens from this PC, i.e. arrange the cylinders such that they resemble a contour for a concave lens;
3. Calculate the properties of this lens directly and optimize its performance by fine adjustment of available parameters;
4. Test the lens experimentally and compare the results with the theoretical ones.

7.2.1 Square lattice lens

As the title of this section suggests a lens made from a PC with the cylinders arranged in a square lattice will be treated here. The radius of the dielectric cylinders is chosen such that $r = 0.18 \cdot a$, where a is the lattice constant of the PC. The Photonic Band Structure (PBS) are analyzed for both polarizations.

Figure 7.2 represents the PBS for the TE polarization (Fig. 7.2a) and for the TM polarization (Fig. 7.2b). For the TM polarization a PBG can be clearly seen. Looking at the frequencies for which the wave vector \mathbf{k} is at the Γ point and openings of the bands one can identify those frequency regions where according to Notomi [73] the PC has $n_{eff} < 1$, such an n_{eff} further on called an "unusual index of refraction". The conclusion is condensed in the Table 7.1.

Table 7.1: Frequency intervals with unusual index for the PC with a square lattice type.

TE polarization	TM polarization
$\frac{a}{\lambda} \in [0.5; 0.66]$	$\frac{a}{\lambda} \in [0.59; 0.93]$
$\frac{a}{\lambda} \in [0.82; 0.98]$	$\frac{a}{\lambda} \in [1.07; 1.15]$
$\frac{a}{\lambda} \in [1; 1.1]$	

Having identified the frequency intervals with unusual index of refraction the next step is to find out an optimal arrangement of the cylinders such that a concave lens could be obtained. Numerous simulations proved that the most efficient arrangement is like the one shown in Fig. 7.3¹.

As can be seen from Fig. 7.3a the lens consists of 112 cylinders. The lattice constant of the original PC is $a = 2.8\text{cm}$ which results in a diameter of the cylinders $d = 1\text{cm}$. These dimensions can be seen in Fig. 7.3b where the top view of the lens is shown. Along the lens face a circumference arc is traced with the radius $R = 66.37\text{cm}$. It was selected such that it intersects most of the cylinders located at the lens face. This number was used as the lens radius of the curvature. As a radiation point source a dipole was used placed at $100a$ from the lens "vertex" (which traverses the device between the two central rows).

In what follows a detailed analysis of the lens performance in the frequency intervals listed in Table 7.1 will be done separately for each polarization. Other frequencies not included in the mentioned intervals will be analyzed too.

¹This sentence misses some generality since an infinite number of possible cylinders arrangements that will emulate a concave lens exist. Analyzing all of them is simply impossible that is why this lens represents the best among the most straightforward arrangements.

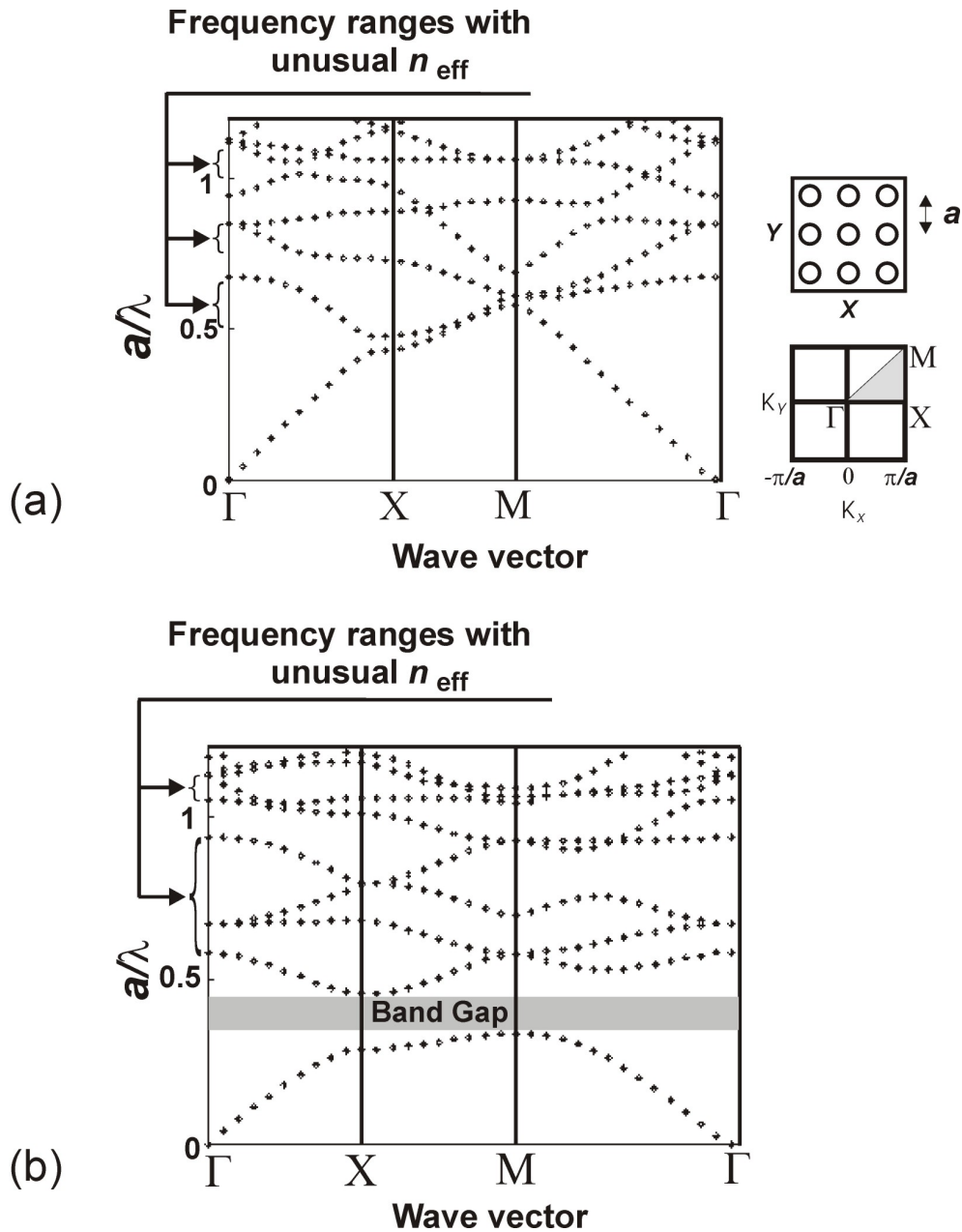


Figure 7.2: The PBS for the PCs consisting of alumina cylinders arranged in a square lattice. The calculations are done for the TE polarization (a) and for the TM polarization (b). On both diagrams are indicated the frequency intervals where the PCs can be ascribed an unusual index of refraction.

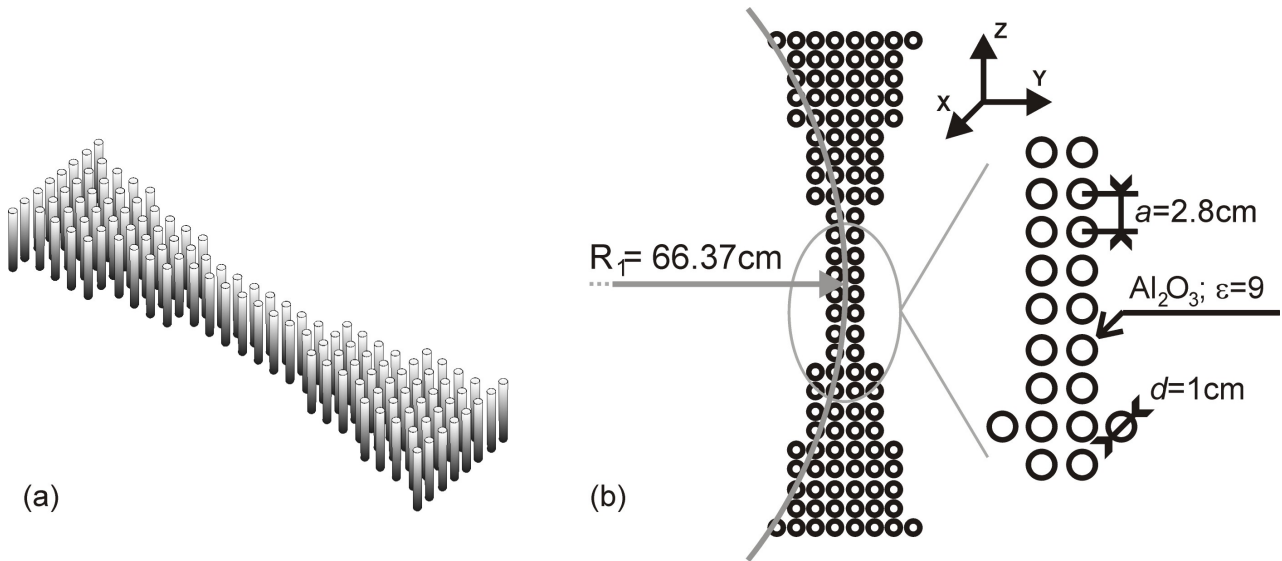


Figure 7.3: Simulations showed that this is the most efficient arrangement of the cylinders in order to emulate the concave lens; a perspective is shown (a). Since all measurements are done in the microwave region the dimensions of the lens have to be selected accordingly (b).

TE polarization

The first frequency interval, $\frac{a}{\lambda} \in [0.5; 0.66]$, can be considered as long range wavelengths since the shortest wavelength is almost a factor 2 longer than the lattice constant of the lens. One expects that all irregularities related to the cylinders shape and their position are not very critical. Indeed, measurements in this frequency interval showed a very good focusing features of the lens. Figure 7.4 shows the dependence of the Intensity Gain (IG) versus the radiation frequency.

The IG behavior resembles a Gaussian like distribution. There is a clearly defined maxima at $\frac{a}{\lambda} = 0.58$ with a value for the IG = 5.4 followed by a less pronounced one at $\frac{a}{\lambda} = 0.62$ with a corresponding IG = 4.2. The IG distribution on the focal spot, for the first maxima, is clearly defined. For the IG distribution at $\frac{a}{\lambda} = 0.62$ one could observe formation of further maxima (another four). The IG distribution is somewhat spoiled. Due to the perfect symmetry of the measured element, it is obvious that the modes (clearly) seen in the picture on the left of the focal spot are as intense and have the same form on its right. This was confirmed by the simulations [166, 167]. The formation of more "focal spots" is of some potential practical interest since it offers the possibility to split the radiation beam. This feature will be analyzed in more details further in the text. In Fig. 7.4 are intentionally included two IG distributions corresponding to some other frequencies in this interval. They show a typical distribution of the IG for the frequencies where focusing is weak. Although the focal spot is very well defined for e.g. $\frac{a}{\lambda} = 0.63$, the IG on the focal spot hardly reaches 1.5.

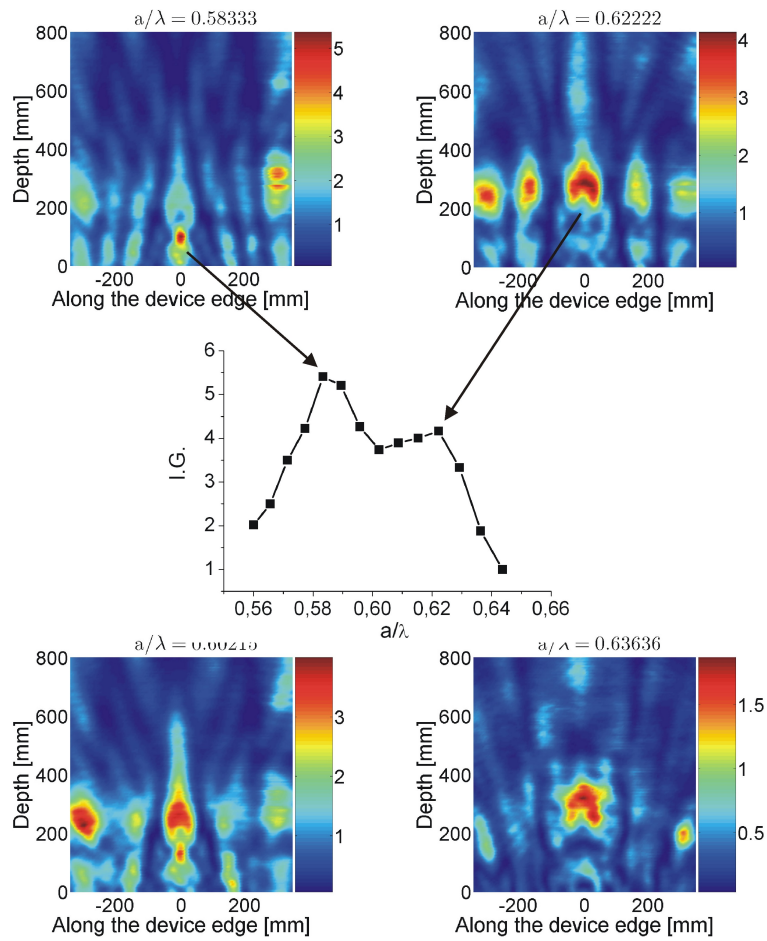


Figure 7.4: The IG on the focal spot for the TE polarization over the first frequency interval from the Table 7.1. The shown graph is accompanied by several pictures of the IG distribution. The best focusing for the TE polarization is shown.

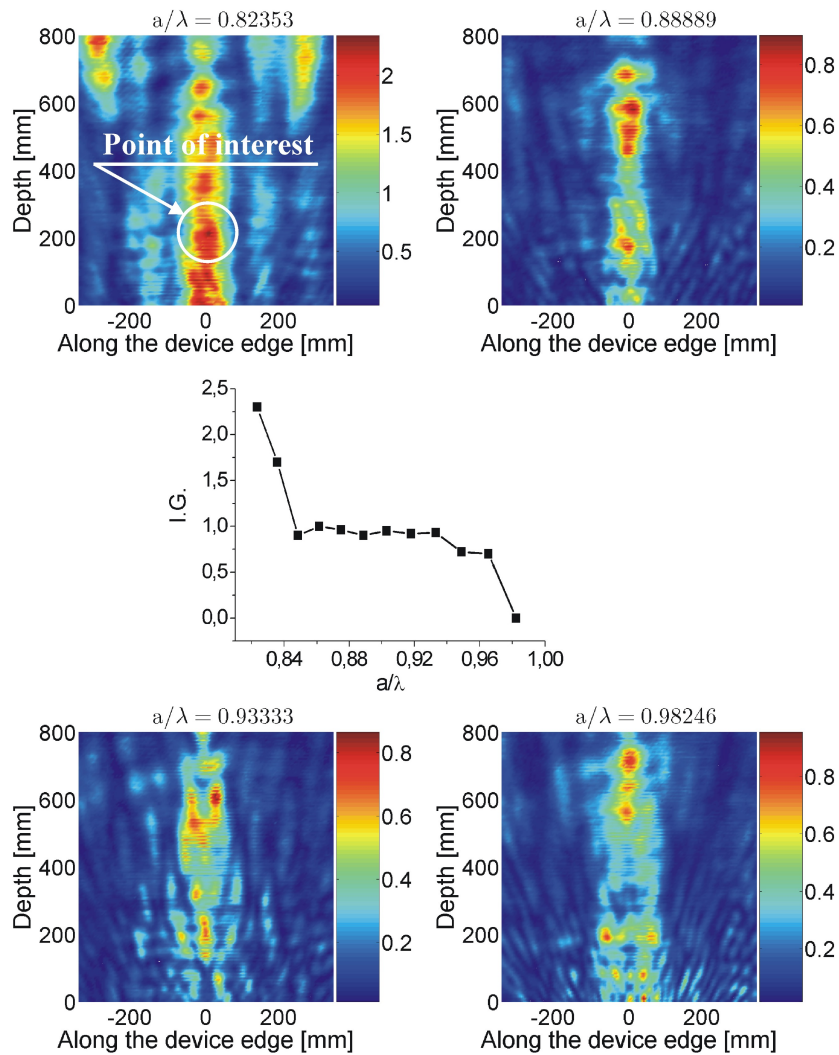


Figure 7.5: The IG distribution for the second frequency interval in Table 7.1; TE polarization. The IG distribution shows a weak focusing for longer wavelengths, but which will disappear very fast as the wavelength increases.

In the next frequency interval the focusing effect is less pronounced and it disappears very fast with increasing wavelength. The IG values start with 2.5 and decreases linearly to a magnitude that fluctuates near 1. The IG shown in Fig. 7.5 is taken from a focal point marked with a white circle in the IG distribution map for $\frac{a}{\lambda} = 0.82$. Even at this frequency, where the highest IG is attested, the focal point is not very well defined. It resembles a leaky mode that is very strong transversally confined. On the IG maps for other frequencies the focal point is completely missing. Still one could see a tendency to concentrate the radiation along the center of the lens, but nothing similar to a focal spot could be identified.

Similarly to the previous interval, for the range $\frac{a}{\lambda} \in (1, 1.1)$, no focusing was observed, see Fig. 7.6 although the absolute values for the IGs are somewhat bigger than 1. For this frequency interval no IG is shown because for all measured frequencies no clearly defined focal spot is obtained.

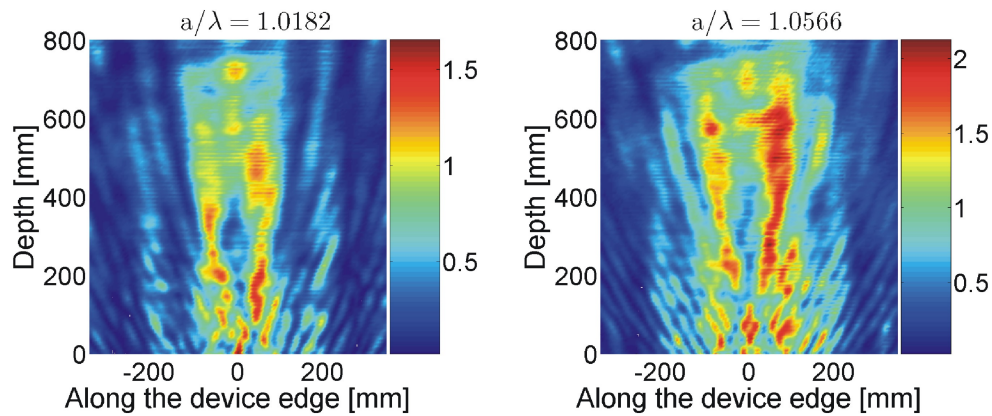


Figure 7.6: *The IG distribution for two selected cases in the last interval for the TE polarization. For the rest of the cases in the investigated frequency range the IG distribution looked very similar with slight variations in the IG absolute values. Normalization done with the smoothed free space.*

As shown in Fig. 7.4, for some frequencies, the focal spot is flanked by additional maxima. This effect is called beam splitting. A closer analysis of the splitting effect reveals the fact that it occurs at two positions and the IG is strongly dependent on the radiation wavelength. The two positions for the splitting are: (i) at about 350mm (called 1st - splitting) and (ii) at about 180mm (called 2nd - splitting) from the centre of the device taken along its edge. As to what the depth is concerned both 1st and 2nd - splitting are positioned at the same depth, i.e. about 250mm.

The maximum IG magnitude is recorded on the 1st and 2nd - splitting as well as on the focal spot and plotted as a function of the wavelength, Fig. 7.7a. The green (squares) curve shows the 1st - splitting; the blue (circles) curve shows the 2nd - splitting; the black (triangles) curve shows the IG on the focal spot (it is identical to the one in Fig. 7.4 shown here again only

for comparisons reasons). Figure 7.7b shows a typical case for the IG distribution when the 1st - splitting is very well pronounced; Fig. 7.7c shows the same for the 2nd - splitting. The small asymmetry in the IG distribution maps, presumably, arises from some distortions while measuring, otherwise there is no single reason why an asymmetry should occur.

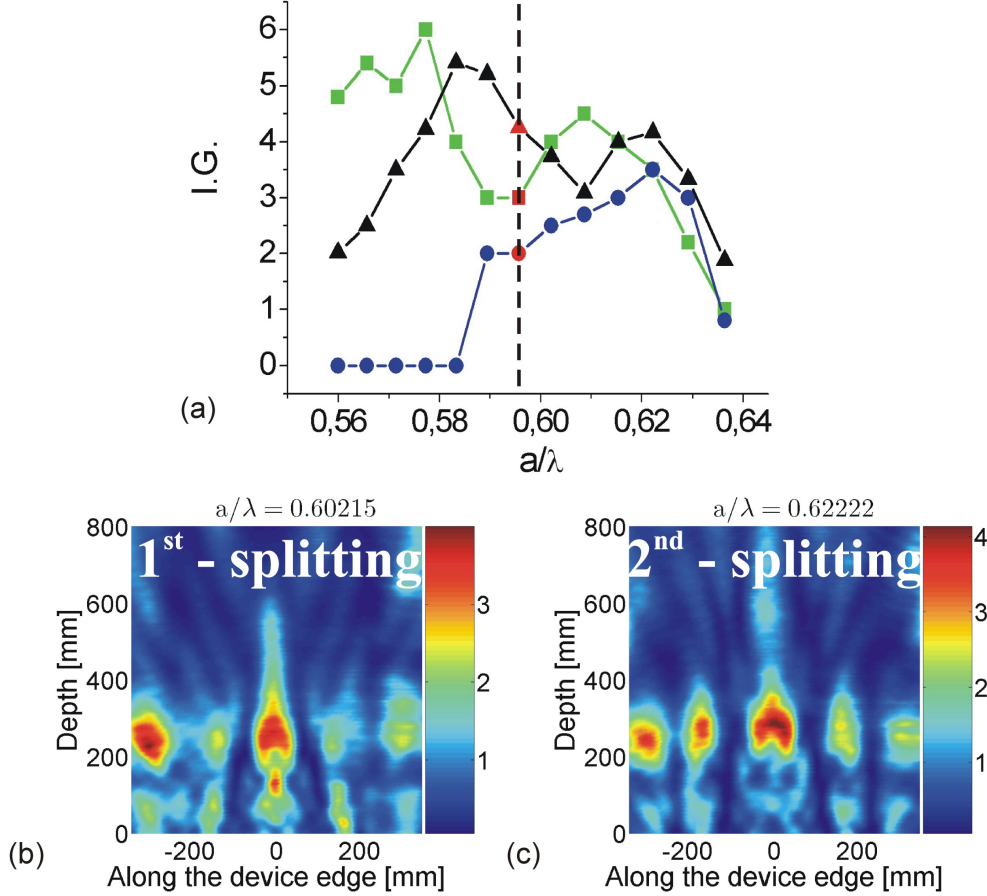


Figure 7.7: The beam splitting effect in the first frequency interval in Table 7.1. The green (squares) curve shows the IG magnitude for the 1st - splitting; the blue (circles) curve for the 2nd - splitting; the black (triangles) curve shows the IG on the focal spot similar to the one in Fig. 7.4 (a). Two IG distributions maps are included to represent the 1st - splitting (b) and the 2nd - splitting (c) respectively.

The graphs in Fig. 7.7a show that for very low wavelengths only the focusing and the 1st - splitting occurs, see Fig. 7.7b. The IG on the 2nd - splitting is almost 0. For $\frac{a}{\lambda} = 0.589$ there is the first appearance of the 2nd - splitting. At this wavelength the IGs for the 1st, 2nd - splittings and focusing are clearly distinct from each other. They become comparable for higher wavelengths, marked by a red point on the graph in Fig. 7.7a. One can clearly see that the focal point is singularly defined only in a very narrow interval. Starting with $\frac{a}{\lambda} = 0.596$ (marked as a red point on the graph) the IG values start to be comparable and this persists

until the end of the focusing interval. The IG maps, beginning with this wavelength, look similar as to the one in Fig. 7.7c. Note that ignoring the permanent presence of the focal spot, there is no situation when solely the 2nd - splitting occurs as is the case of the 1st - splitting for the long wavelengths. Similarly there is no situation where only the focal spot alone exists, without being flanked at least by the 1st - splitting.

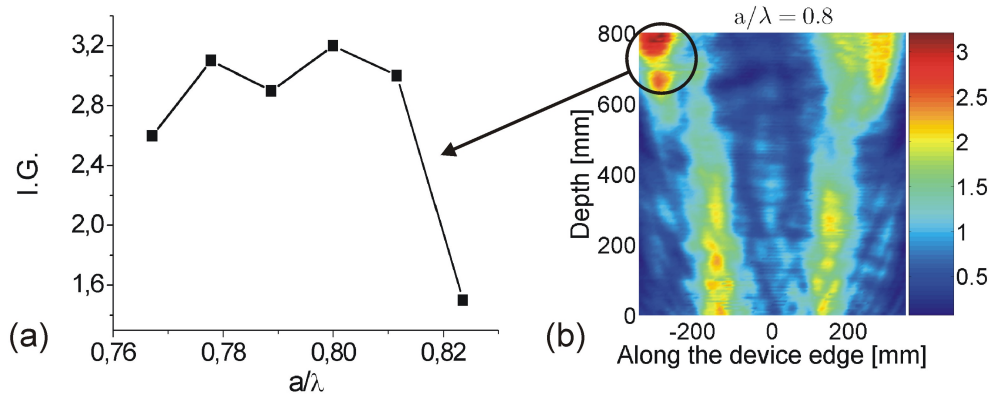


Figure 7.8: The IG distribution on the splitting spot (a). A typical IG distribution showing a beam splitting occurring somewhat distant from the lens edge (b).

Figure 7.8a represents the IG on the splitting spot for the wavelengths interval $\frac{a}{\lambda} \in (0.767, 0.824)$. While originally not predicted by the theory as being of some interest, the next wavelength interval shows interesting functionality. On the IG distribution in Fig. 7.8b two possible spots for the splitting can be seen: one in the next proximity of the lens edge, at about 180mm and the second one somewhat deeper, at about 800mm. The analysis is focused on the deeper one since it is better pronounced. As it can be seen on the graph in Fig. 7.8a the IGs are not very big, i.e. distributed around 3. As the wavelength increases the IG will decrease drastically, until reaching values smaller than 1 on that position.

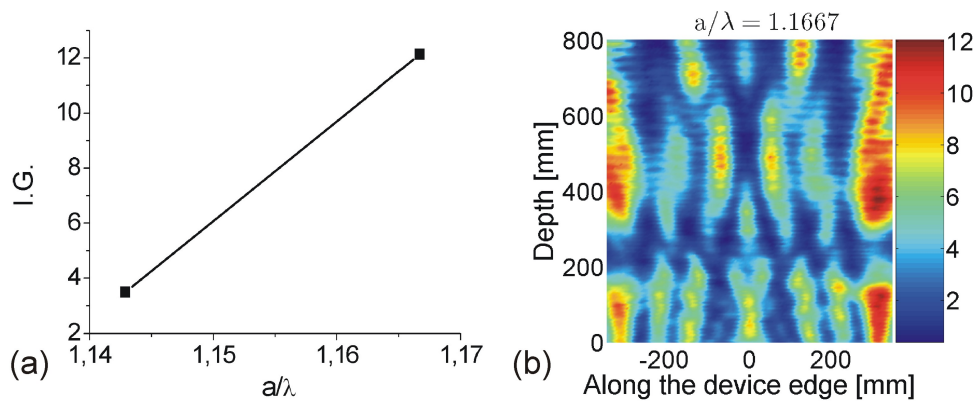


Figure 7.9: The IG distribution on the splitting spot for last interval (a). A typical IG distribution showing a beam splitting occurring at the edges of the scanned field (b).

The final type of the splitting treated here was observed at the end of the third interval in Table 7.1 where the PC has an $n_{eff} < 1$. Unfortunately the measuring setup did not allow further increase of the radiation wavelength, this being the reason why the graph in Fig. 7.9a consists of only two points.

The splitting for these, comparably short wavelengths, occurs at the edges of the scanned field at a depth of almost 400mm and somewhat near to the lens edge, about 100mm in the depth. Both types are however equally intense independent on the radiation wavelength. The IG distribution in Fig. 7.9b shows that some "rests" of focusing are also present. Very probable this interval belongs to the one where the PC has an unusual index of refraction. Presumably, some further increase of the wavelength would increase the focusing effect and perhaps similar effects would be observed as in the case from Fig. 7.7. The IG on the splitting spot shows a very high value, not met for other splittings discussed here, i.e. $IG = 12$. It is, however, hard to speculate if this is a general tendency for the shorter wavelengths.

TM polarization

For the TM polarization only two wavelengths intervals are predicted where the PC behaves as a homogeneous material with $n_{eff} < 1$ and thus is supposed to focus the radiation. For the long wavelengths range, i.e. $\frac{a}{\lambda} \in [0.59; 0.93]$ was found the best focusing. This is shown in Fig. 7.10. The presented curve shows the dependence of the IG upon the wavelength. Similarly to the TE polarization, a Gaussian like behavior could be observed. There is a clearly defined optimum at $\frac{a}{\lambda} = 0.71$ where the IG is found to be as high as $IG = 6.4$. The included IG distribution map shows a very clear defined focal spot.

Figure 7.10 shows typical IG maps for the TM polarization at $\frac{a}{\lambda} = 0.62$. Although the IG on the spot is relatively small, it is often observed that the focal spot is sort of split into two. This feature will however disappear very fast as soon as the wavelength is increased. For shorter wavelengths the focal spot is somewhat spoiled. It is always flanked by another maxima indicating toward the splitting features discussed for the TE polarization. While being an interesting feature *per se*, it might be of little importance for some practical applications due to low IG on both the focal spot as well as the split spots.

The second (and last) interval of interest is predicted to limit at $\frac{a}{\lambda} = 1.15$, however, looking at the PBS in Fig. 7.2, it is rather difficult to distinguish the exact (top) limit of the corresponding interval. Some results that are outside the assumed range will be also presented.

The curve in Fig. 7.11 shows relatively small values for the IG. There are clearly defined two maxima at $\frac{a}{\lambda} = 1.052$, $\frac{a}{\lambda} = 1.098$ and a weaker one at around $\frac{a}{\lambda} = 1.16$. The figure includes also IG maps for all three maxima. For shorter wavelengths a very good defined focal spot can be seen containing the maximum IG for this interval, i.e. $IG = 3$. At least, insofar as it could be measured, the focal spot looks very clean. However, the picture shows only a good

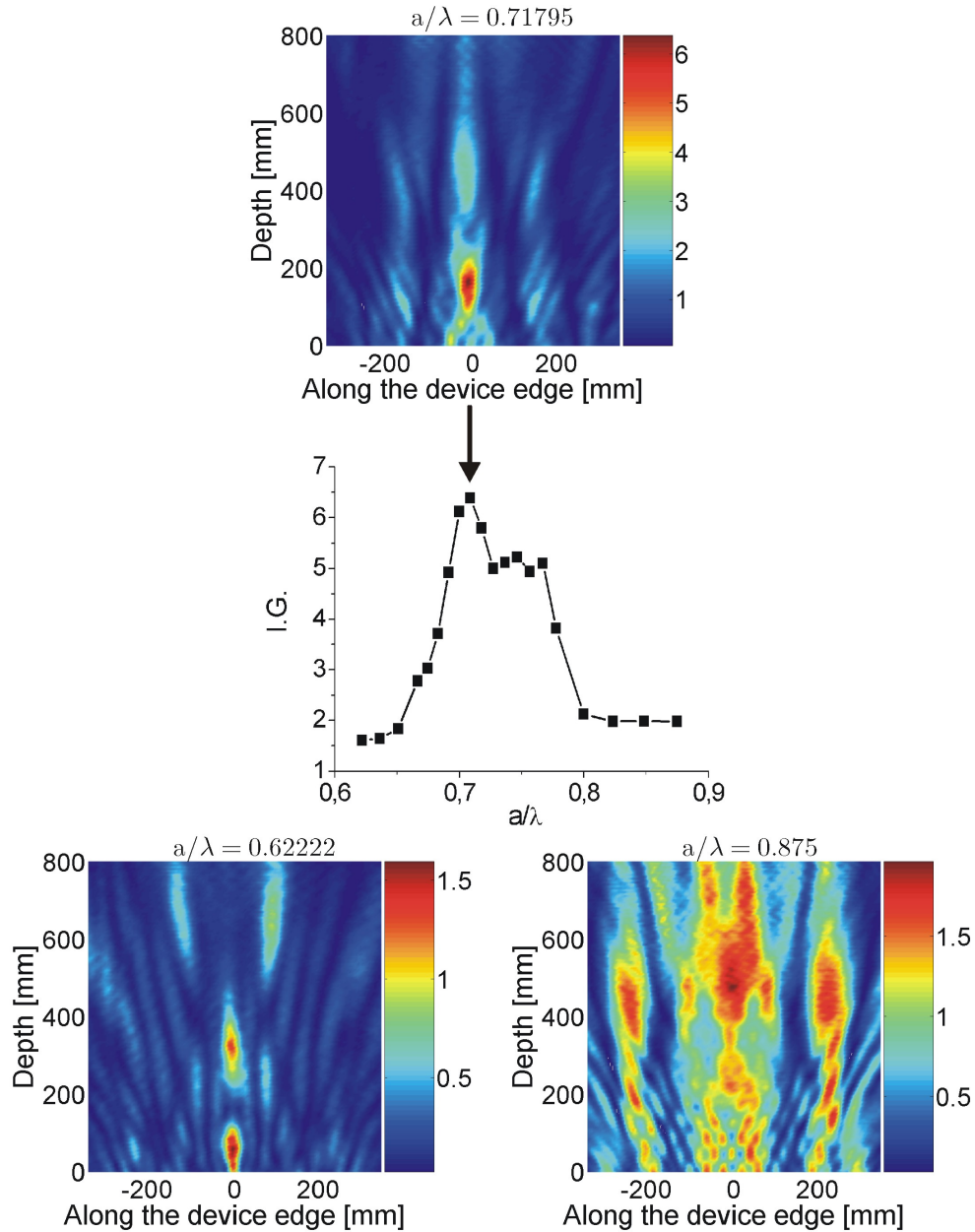


Figure 7.10: The IG as a function of radiation wavelength for the TM polarization. Here it is treated the first interval of interest from the Table 7.1 The curve is accompanied by typical IG distributions representing the best focusing and some peculiar cases where the focusing is not very strong, but which merits discussion.

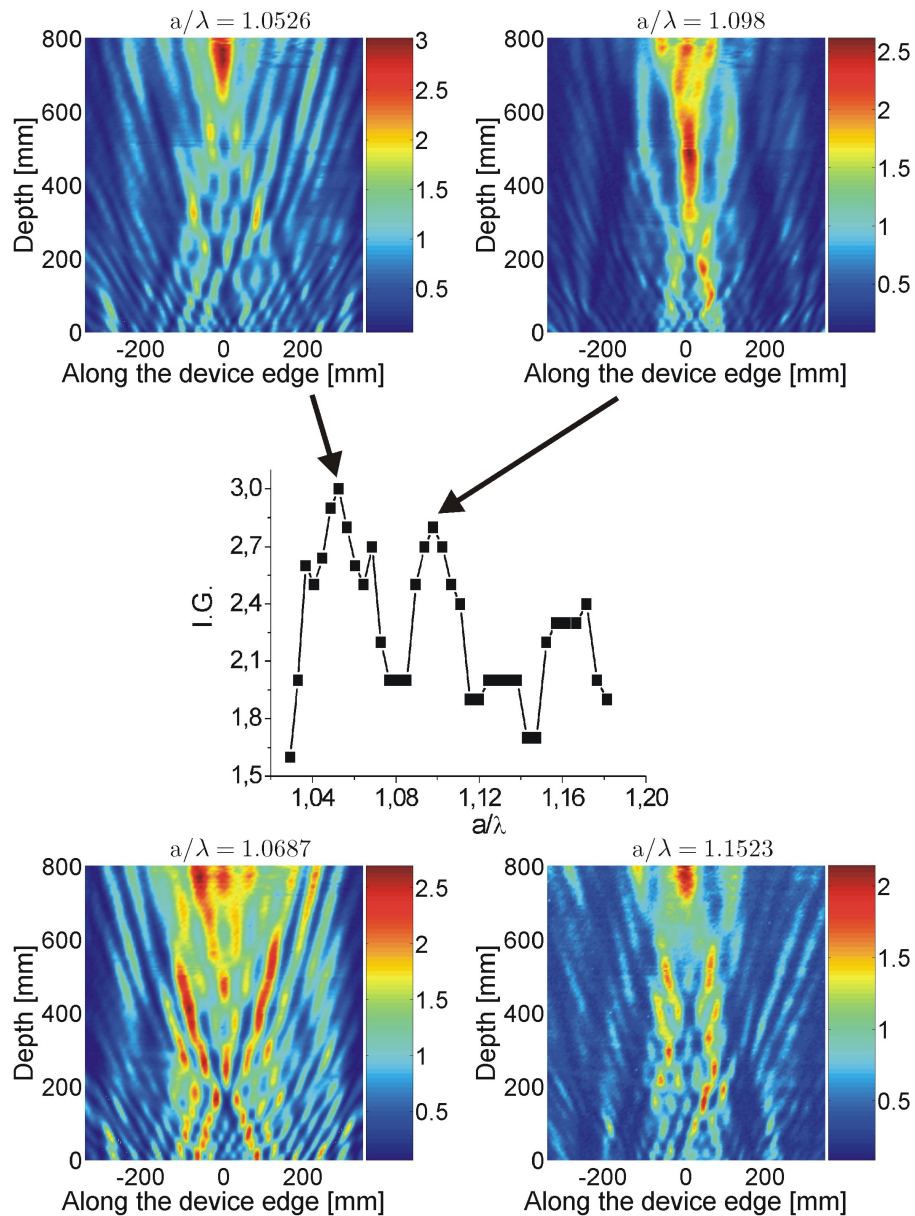


Figure 7.11: The IG as a function of radiation wavelength representing the second interval from the Table 7.1. Besides the curve there are included three additional IG distributions for all maxima on the curve. Also an IG distribution is shown that resembles a typical beam splitting functionality inherent to the TE polarization.

half of the spot and one can only speculate that it remains as clean further into the depth.

The next focal spot is slightly scattered in the depth and weaker than to the previous one. It occurs at $\frac{a}{\lambda} = 1.098$ where the IG = 2.8. The last maxima is relatively bad defined. The IG distribution at $\frac{a}{\lambda} = 1.152$ shows a focal spot similar to the one at $\frac{a}{\lambda} = 1.052$ where only a part of it could be seen.

7.2.2 Triangular lattice lens

This section treats a lens made from a PC with the cylinders arranged in a triangular lattice. For this particular geometry a full PB is observed in the wavelength interval $\frac{a}{\lambda} \in (0.5; 0.53)$. At shorter wavelengths also PBGs are present, but no full PB.

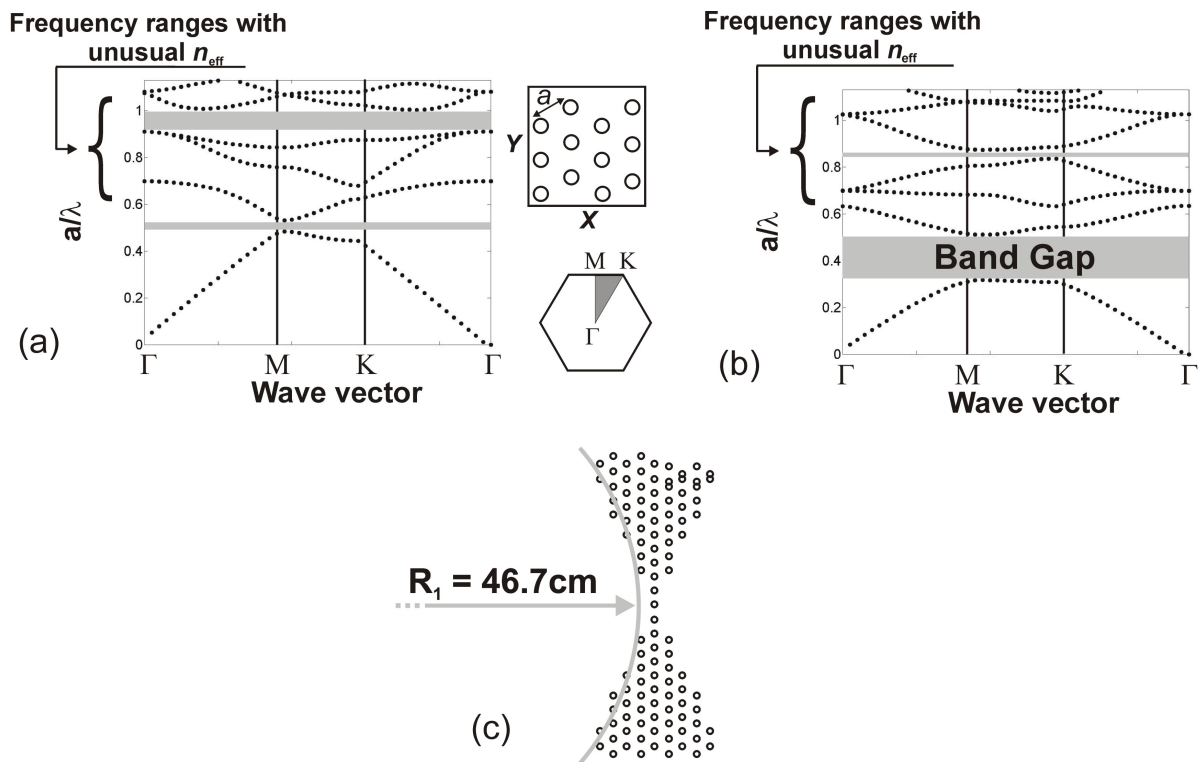


Figure 7.12: The PBS for the PCs consisting of alumina cylinders arranged in a triangular lattice. The calculations are done for the TE polarization (a) and for the TM polarization (b). On both diagrams are indicated the frequency intervals where the PCs can be ascribed an unusual index of refraction. The measured concave lens is shown in (c); the lattice constant $a = 2.8 \text{ cm}$.

The calculated PBS of the triangular lattice PC are shown in Fig. 7.12a for the TE polarization and in Fig. 7.12b for the TM polarization, respectively. The structural parameters are similar to those for the square lattice, i.e. $a = 2.8 \text{ cm}$ and the cylinders radius $r = 0.18a$.

Table 7.2 contains the wavelengths (intervals) where the unusual index effects are expected. The case of triangular lattice PC becomes very enticing since some of the indicated magnitudes are in the proximity of the band gap and, as it will be shown, will lead to very interesting functionality.

Table 7.2: Frequency intervals with unusual index for the PC with a triangular lattice type.

TE polarization	TM polarization
around $\frac{a}{\lambda} \approx 0.7$	$\frac{a}{\lambda} \in [0.6; 0.8]$
around $\frac{a}{\lambda} \approx 0.9$	around $\frac{a}{\lambda} \approx 1$

Moreover, the shape of the triangular lattice concave lens, represented in Fig.7.12c, is peculiar. First, being very compact, it becomes even more attractive for applications due to the reduced size. Second, on the margins of the lens there are sufficient cylinders "shells" to ensure that the PC effect is fulfilled². Third, there is only one row in the middle of the lens, which contrarywise indicates that there is no PC effect in the middle of the lens.

TE polarization

The first point of interest for the TE polarization is at $\frac{a}{\lambda} \approx 0.7$. This is the first opening of the band and the single one for the large wavelengths. The focusing could be found here in two very narrow intervals $\frac{a}{\lambda} \in (0.63; 0.66)$ and $\frac{a}{\lambda} \in [0.67; 0.73)$. The IG dependence on the wavelength, for the first interval, is shown in Fig. 7.13a. The IG is not very high and falls well below 1 already for $\frac{a}{\lambda} \approx 0.65$. Figure 7.13b shows typical IG maps selected for the best focusing. The focal spot is very well defined. By contrast, in $\frac{a}{\lambda} \in (0.66; 0.67)$ no clear focusing could be detected.

The IG analysis for the next interval is shown in Fig.7.13c. The magnitudes are not too high: slightly higher than 1.5. After a linear increase, a maximum around $\frac{a}{\lambda} \approx 0.719$ is reached followed by a decay. The last point on the graph is where a focal spot could be still distinguished. For smaller wavelengths a focal spot can be observed too, but flanked by some other maxima which makes it uninteresting from the application point of view. Figure 7.13d shows a typical focusing for this interval. Compared with the previous case the focal spot has a smaller area and is placed much closer to the edge of the lens. Its position remains fixed as a function of wavelength as well as its area does not change considerably. It is located at about 152 mm from the lens "vertex".

For the second point of interest in the Table 7.2, i.e. $\frac{a}{\lambda} \approx 0.9$ no functionality of the optical element could be observed. According to the PBS in Fig. 7.12a this is very close to a large band gap for the TE polarization. For some wavelengths around this point only minor

²The PC concept involves an infinitively large structure.

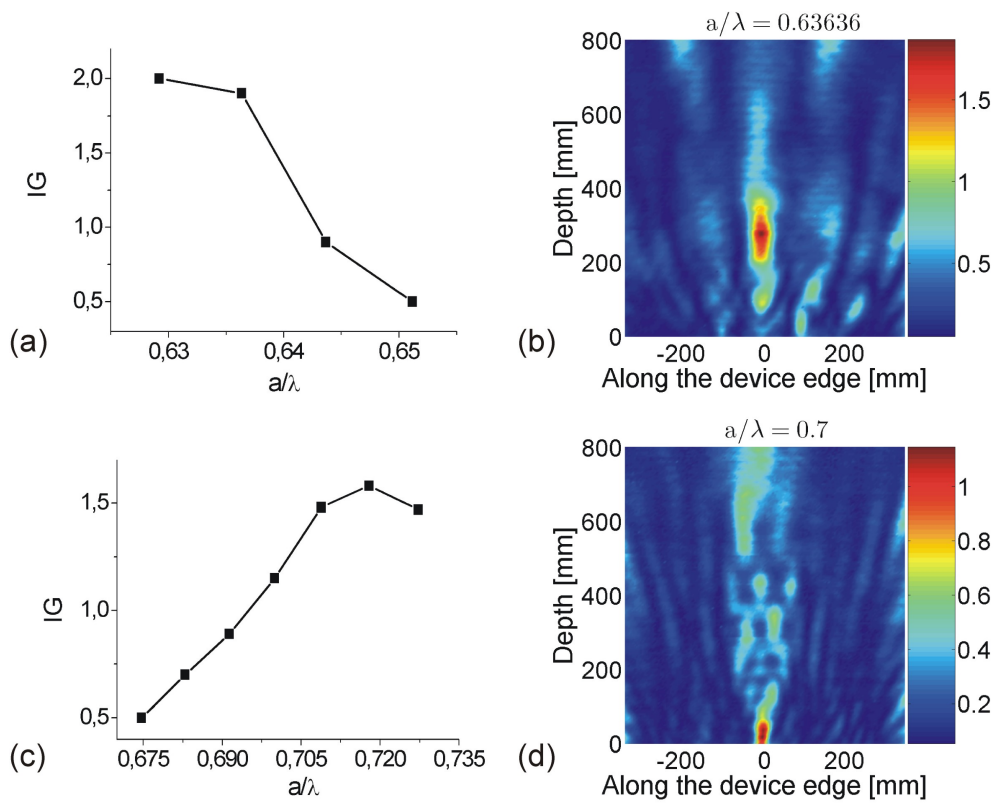


Figure 7.13: Analysis of the lens focusing performance for the TE polarization done in the proximity of $\frac{a}{\lambda} \approx 0.7$. Focusing is observed for two half intervals; see the text for details. First half (a); typical distribution showing the focusing effect (b). Second half (c); peculiar focusing showing maxima very close to the lens edge.

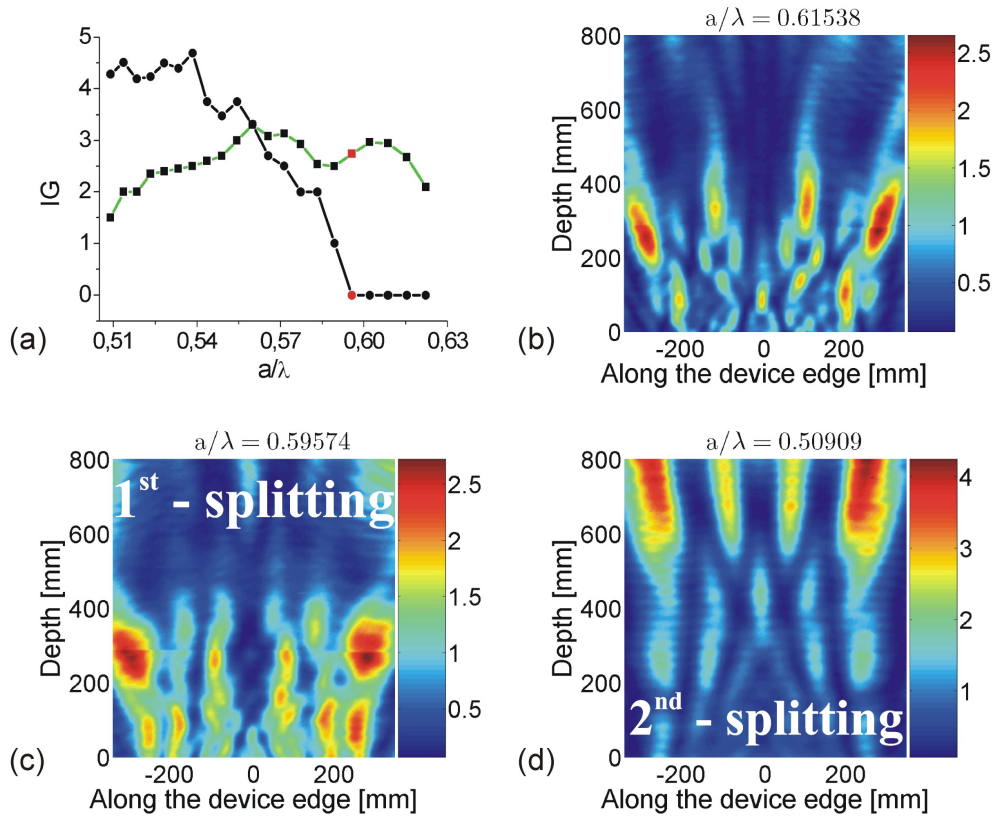


Figure 7.14: Beam splitting for the TE polarization. IG analysis over the wavelengths interval where the effect is observed (a). The green squares curve indicate the IG on the 1st splitting and the black circles curve indicate the IG on the 2nd splitting. The 1st-splitting for long (b) and short (c) wavelengths. The 2nd-splitting far off from the lens edge (d).

amounts of radiation could be detected in the scanning area, most probably originating from the middle part of the lens, however, no defined IG pattern could be observed. Even for those wavelengths where some pattern could be observed the net IG was well below 1 and hence did not present any interest.

Similar to the square lens, the beam splitting is also observed at long wavelengths. This is illustrated in Fig. 7.14a where a detailed IG analysis is performed over the wavelengths interval for which this functionality can be found. The splitting is found in two distinct locations. One is closer to the lens edge (from now on called 1st-splitting) and another somewhat far off (from now on 2nd-splitting). In the Fig. 7.14a the green squares curve indicates the IG for the 1st-splitting and the black circles curve indicates the 2nd-splitting. The 1st-splitting has two distinct shapes: first occurring at short wavelengths until $\frac{a}{\lambda} \approx 0.59$ characterized by a smaller area of the focal spot than the one occurring for longer wavelengths which has a larger area of the focal spot, c.f. Fig. 7.14b and c. The transition from one form to the other is indicated as a red dot on the graph in Fig. 7.14a. Finally the splitting occurring far off the lens edge is shown in Fig. 7.14d.

Figure 7.14a shows explicitly the concomitant variation of the IG on both types of the splitting as a function of wavelength. One can see that for short wavelengths only the 1st-splitting is appearing with a maximum at $\frac{a}{\lambda} \approx 0.60$ and $IG \approx 3$. For wavelengths longer than $\frac{a}{\lambda} \approx 0.59$ (red point on the curves) the 2nd-splitting shows up and also the 1st-splitting changes its shape. Starting with this point both types of the splitting exist simultaneously. The IG on the 1st-splitting is, however, stronger as on the 2nd-splitting. In a very narrow wavelengths interval, i.e. $\frac{a}{\lambda} \approx 0.56$ the both types of beam splitting are of comparable intensity. For shorter wavelengths the 2nd-splitting becomes predominant in the IG and the 1st-splitting is also present. One could consider that instead of the trivial beam splitting it is some sort of beam quadrupling.

TM polarization

For the square lens, good focusing is observed rather for the TM polarization. Figure 7.15a presents the IG dependence on the wavelength for the first interval indicated in Table 7.2. Focusing could be observed for short wavelengths, however with a relatively low IG. The typical IG distribution is shown in Fig. 7.15b. There can be seen a clearly defined focal spot situated at about 274 mm from the lens "vertex". In the wavelength range $\frac{a}{\lambda} \in (0.62; 0.65)$ no focusing could be detected. Generally, no pattern was observed behind the lens. Apart from a few weak spots the IG is well below 1. After this "functionality gap" the focusing is further present until $\frac{a}{\lambda} \approx 0.7$.

For longer wavelengths the focal spot is located very close to the lens edge, as is the one imaged in Fig. 7.15d. The focal spot is situated only 30 mm off the lens edge and has a very

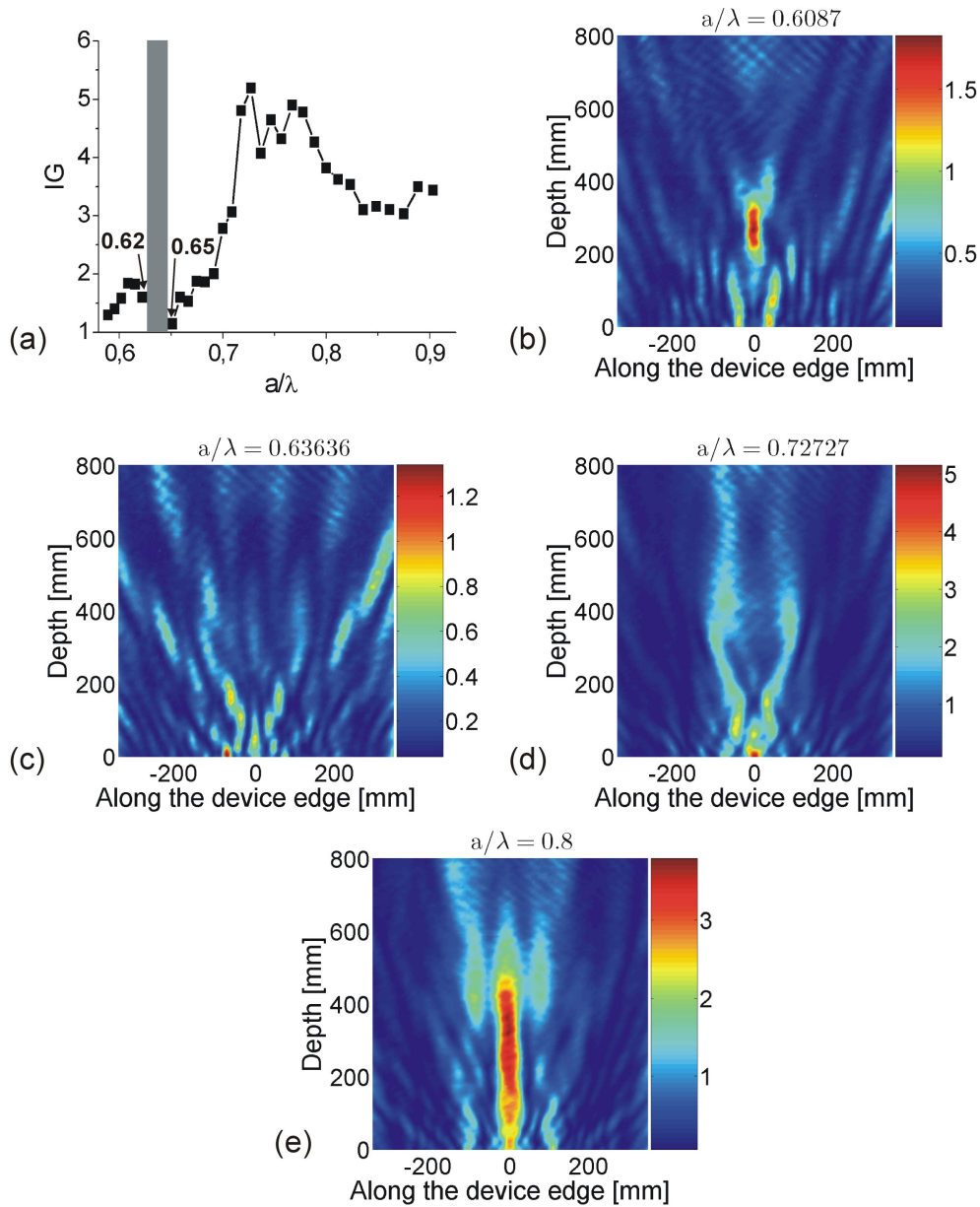


Figure 7.15: *The analysis of the focusing performance for the TM polarization: IG variation as a function of wavelength (a). IG distribution showing focusing for long wavelengths (b). IG distribution for a wavelength where no pattern formation and no significant radiation transmission could be detected behind the lens (d). Very peculiar focusing occurring very close to the lens edge (d). Focusing confined laterally (e).*

small area. It is present there also for shorter wavelengths, however only until $\frac{a}{\lambda} \approx 0.73$. For even longer wavelengths it degenerates into a larger focal spot. Its area increases with the wavelength. However, it remains confined into the depth of the measured field. An example of such a focusing is shown in Fig. 7.15e. The IG analysis of the whole focusing interval reveals a clearly defined maximum which is found at $\frac{a}{\lambda} = 0.727$ with $IG \approx 5.2$. The focusing efficiency drops starting with $\frac{a}{\lambda} \approx 0.78$ until $IG \approx 3$ and it remains further constant at this magnitude until the focusing will completely disappears for $\frac{a}{\lambda} > 0.9$.

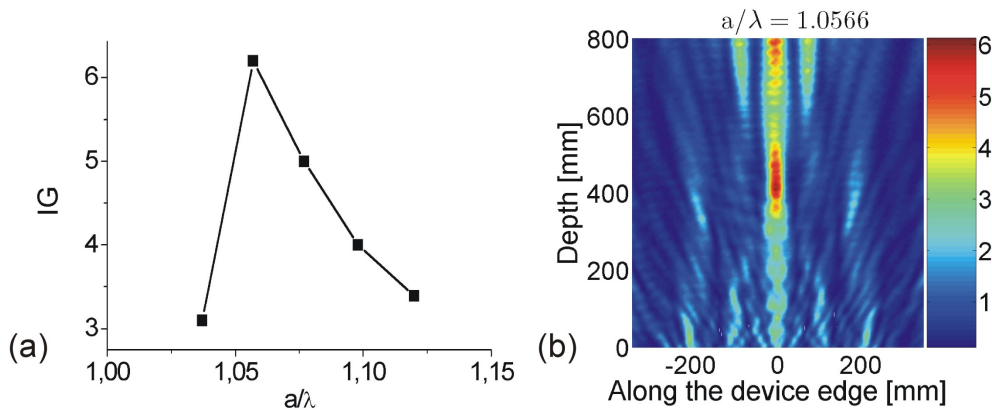


Figure 7.16: *IG analysis for the focusing found in the vicinity of $\frac{a}{\lambda} \approx 1$ (a). The IG distribution for the strongest focusing (b).*

The next point of interest, according to the PBS in Fig. 7.12b, is at $\frac{a}{\lambda} \approx 1$ where two bands open at the Γ point. The IG analysis over the focusing interval is shown in Fig. 7.16a. One can see a very well defined maximum at $\frac{a}{\lambda} \approx 1.06$ with $IG = 6.2$. The efficiency drops very fast for both shorter as well as longer wavelengths. Figure 7.16b shows the IG distribution for the wavelength with the best focusing. An interesting feature is shown in the curve in Fig. 7.16a. It falls much faster for longer wavelengths. Note that beyond the interval shown no focusing pattern could be measured.

Apart from the focusing feature a very interesting type of beam splitting is found for the long wavelengths interval $\frac{a}{\lambda} \in (0.52; 0.57)$. The IG analysis of this interval is shown in Fig. 7.17a. The IG magnitudes are moderately high reaching a plateau at about $IG = 2.6$. The beam splitting, shown in Fig. 7.17b occurs very close to the lens edge on a similar position as the focusing in Fig. 7.15d, i.e. at about 30 mm. The area of the focal spot on the split beam is also smaller than the radiation wavelength. Note also that the distance between the maxima in Fig. 7.17b is ≈ 224 mm which is close to $8a$. Counting $8a$ along the lens from its center leads to the conclusion that the maxima occur opposite to the edges of the full hexagons which follow when the row of singular cylinders ends. No dependence of the distance between the maxima upon the radiation wavelength was observed.

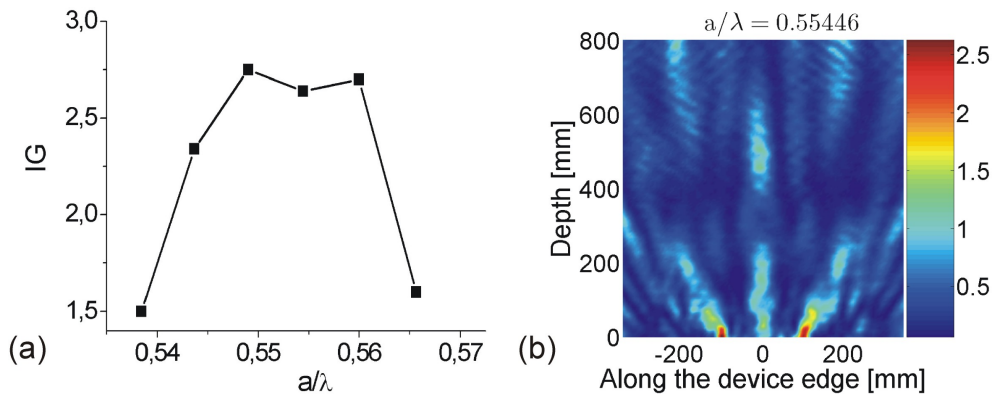


Figure 7.17: *IG analysis for the beam splitting effect (a). The IG distribution for the best beam splitting in this interval (b).*

7.2.3 Discussion

The design of the lenses started with the assumption that PCs have wavelengths regions where they do behave as optically homogeneous materials. The primary characteristic of an "optically homogeneous" material is its refractive index. For the lenses known from geometrical optics, the n can be calculated from the so called thin lens formula (or Gaussian formula) which is defined as follows:

$$\frac{1}{f} = (n - 1) \left(\frac{1}{R_1} - \frac{1}{R_2} \right) \quad (7.7)$$

where f is the focal length of the lens and R_1 and R_2 are the radii of the circumferences that approximate the external faces of the lens. Extracting n from the Eq. 7.7 must deliver some sort of n_{eff}^{lens} which generally has to match (or at least be comparable with) the n_{eff}^{PC} of the "parent" PCs.

For both lenses studied, such circumferences were traced with the indicated approximative radii, see Fig. 7.3 for the square lens and Fig. 7.12 for the triangular lattice. One has to mention that for the concave form $R_1 = -R_2$ and $R_1 < 0$. The focal length could be estimated from the measured data.

It is well known, and also quite obvious from the Eqn. 7.7, that for the regular lenses there is a slight dependence of the focal length upon the wavelength, also known as *Lateral Chromatic Aberration* (LCA). More precise, for a focusing lens, LCA increases with the radiation wavelength.

Figure 7.18 shows the variation of the effective refractive index of the PC n_{eff}^{PC} estimated from the analysis of the EFS [73]. Fig. 7.18a shows it for the TE and Fig. 7.18b for the TM polarizations (the filled circles curves). The values increase with decreasing wavelengths which indicate a clear similitude with the generic materials far from the resonance. Back to the Eqn. 7.7 and considering the good match with homogeneous materials, the focal length

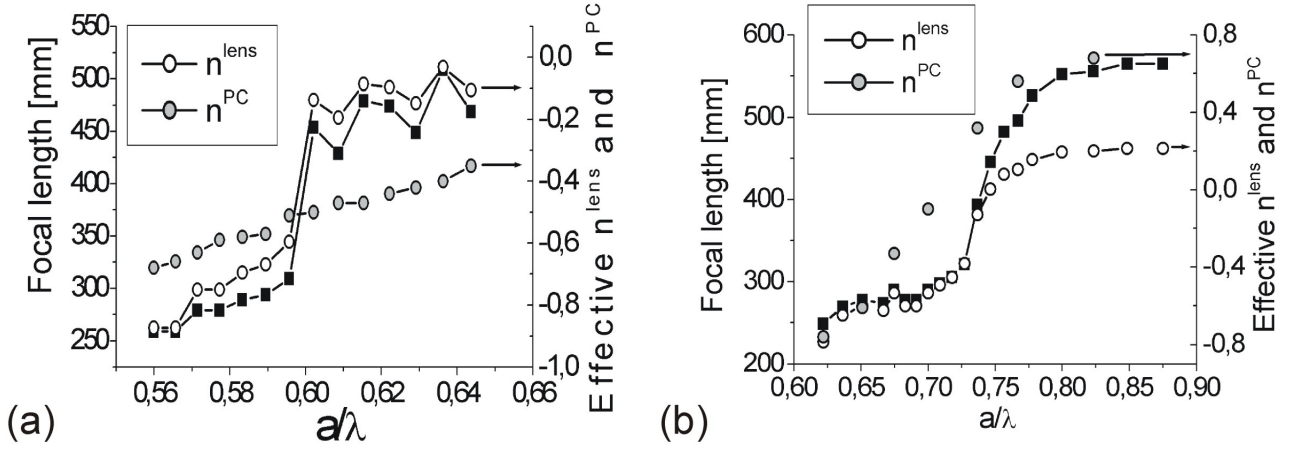


Figure 7.18: Focal length and n_{eff}^{lens} , calculated with the thin lens formula, for TE (a) and TM (b) polarizations; experiments done with the square lattice lens. On both curves the theoretically calculated n_{eff}^{PC} according to Ref. [73] is also included; the curve is represented with filled circles in both graphs.

of the lenses measured here has to increase with decreasing wavelength (due to its concave form). This is exactly what was obtained experimentally and shown in Figs. 7.18a and -b. Compared to regular lenses, however, this variation of the focal length is considerably stronger. In both cases it changes with almost 100% at the end of the focusing intervals compared to its beginning.

Knowing the focal length of the lens one can plug it back into Eqn. 7.7 and calculate the n_{eff}^{lens} . The respective curves are shown in Fig. 7.18 with empty circles. It is indeed remarkably that the curves for both refractive indexes, i.e. n_{eff}^{lens} and n_{eff}^{PC} , follow the same trend. Although calculated completely separately it is important to note that both of the curves will show inflection at similar (or very close) magnitudes of the wavelengths.

The small deviation of the two types of the n_{eff} can be explained as follows. The n_{eff}^{PC} is calculated from analyzing EFS, see the Section 3.1.2. PBS in turn is a characteristic of a PC which is a theoretical concept always involving an untruncated structure (infinitely large). Since the lenses treated here represent only drastically reduced versions of the initial PC it is unlikely that the two n_{eff} will perfectly match. Indeed, in no case two rows of cylinders, being in the center of the studied lens, can be treated as a PC and moreover described by a PBS.

An interesting feature is the negative value of n_{eff} (obtained through both methods) for some wavelengths. When the $n_{eff}^{PC} < 0$ a plane plate lens would also focus the radiation. This topic is extensively treated in the literature experimentally, [168, 169, 170, 171, 172, 173, 174, 175, 176], as well as analytically, [171, 177, 178, 179, 180, 181, 182]. There is no report in the literature,

however, treating the performance of the *Negative Index Materials* (NIMs) as host materials for any other optical devices, e.g. similar to concave lenses treated here. It becomes interesting if for those wavelengths intervals where $n_{eff}^{lens} < 0$ and $n_{eff}^{PC} < 0$ some features inherent to plane plate lenses from NIM are observable. First, this applies to the superresolution effect, i.e. focusing beyond the diffraction limit known from the geometrical optics. To answer this question, for the ranges where the lens focused, the focal spot is fitted by a 2D Gaussian function from which the *Full Width at Half Maximum* (FWHM) is calculated and further on used for the estimation of the area of the focal spot.

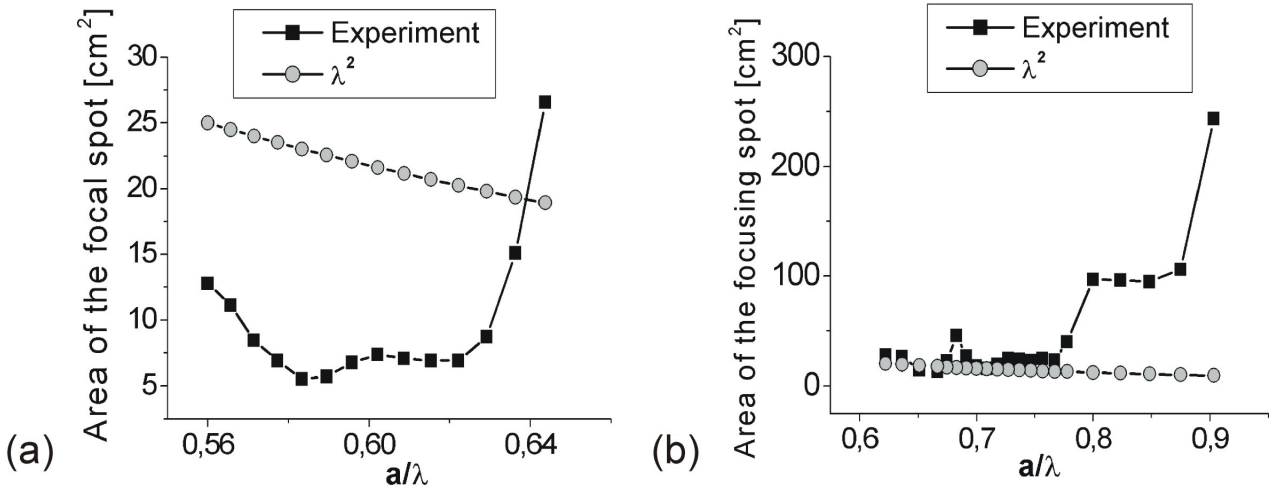


Figure 7.19: *The area of the focal spot for the TE (a) and TM (b) polarizations; experiments done with the square lattice lens. For comparison, the corresponding λ^2 is shown on both graphs; the curve is represented with filled circles.*

In Figs. 7.19a (TE polarization) and -b (TM polarization) can be seen the area of the focal spot as a function of the radiation wavelength drawn together with the corresponding λ^2 . One can see that for the TE polarization, for most of the wavelengths, the spot area is much smaller than the λ^2 . By contrast, for the TM polarization, minimum of the focal spot area is comparable to the λ^2 , all other values lying much beyond this limit. In Ref. [177] is shown that negative refraction, and especially superresolution effect, is expected to occur also for the first band in the PBS even though $n < 0$ is not generally expected to be found for those frequencies (although theoretically not excluded). For the case shown here this is true for the TE polarization where the wavelengths, for which the lens focuses, belong rather to the first band in the PBS. Remarkably, the results are in full agreement with the theoretical considerations of Luo et al. [177].

By contrast to the square lattice lens, for the triangular lens the wavelength interval where the lens focuses is found only for the TM polarization. There is some focusing for the TE polarization too, but it is rather weak and occurs in a very narrow wavelength interval. The

last can be indeed as particular feature interpreted since such a behavior can be used for filtering purposes.

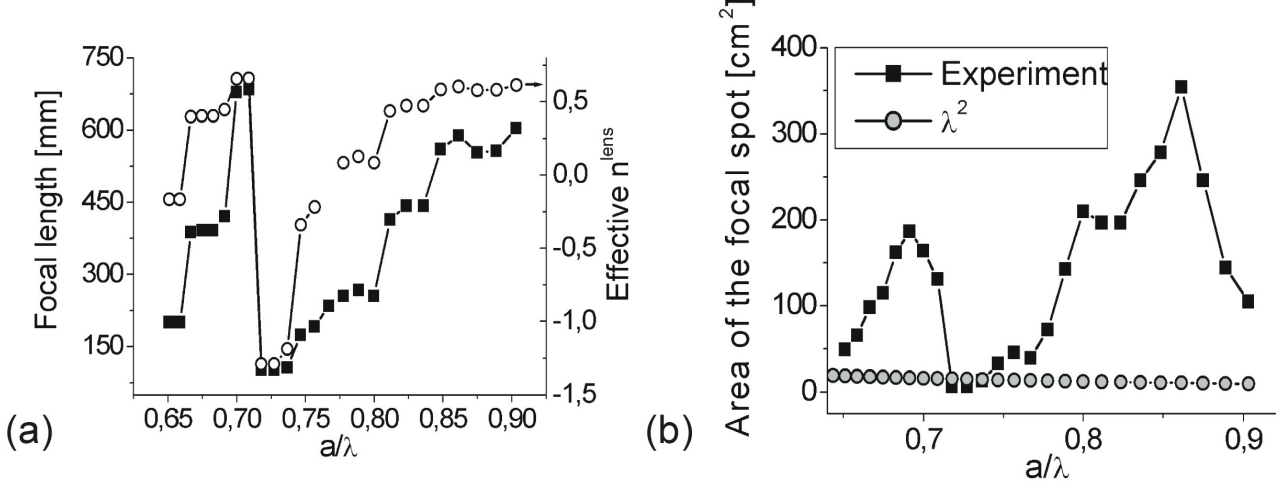


Figure 7.20: Focal length and calculated n_{eff}^{lens} with the thin lens formula (a). The area of the focus spot for the TM polarization; for comparison, the corresponding λ^2 is shown (b). Experiments done for the triangular lattice lens.

The analysis for the triangular lattice lens is focused only on the TM polarization, for the wavelength interval presented in Fig. 7.15. An interesting behavior is revealed by the focal length, see Fig. 7.20a. As in the case of the square lattice lens, the shape of the curve repeats that of the IG, i.e. the wavelengths for which the IG is maximum, the focal spot is placed far off from the lens edge and vice versa. The n_{eff}^{lens} is calculated according to the Eq. 7.7. For this case, however, only for a few wavelengths n_{eff}^{lens} is smaller than 0. For short wavelengths the index is always positive. One has to mention here that the n_{eff}^{PC} was not calculated for this type of the lens. As it was mentioned, the concept of EFS becomes critical for small structures and particularly for this case, when only a row of cylinders forms the middle of the lens. Comparing an eventual magnitude for n_{eff}^{PC} with n_{eff}^{lens} would rise many questions as to its validity and correctness. However, as it will be emphasized later, the advantage of this particular lens is that due to the very close packed structure, the upper and lower flanks of the lens do behave, in a much better approximation by contrast to the square lattice lens, as PC and the effects of the PBG are also seen in the operation of the device.

As it can be seen from Fig. 7.20b the area of the focal spot is considerable above the λ^2 . An exception is the wavelength interval $\frac{a}{\lambda} \in [0.72; 0.74]$ where the focal spot area is comparable with the λ^2 . For higher wavelengths the focal spot area increases because of the typical confinement of the focal spot, as shown in Fig. 7.15e.

At the wavelengths intervals where the PC behaved as homogeneous material with $n_{eff}^{PC} < 0$,

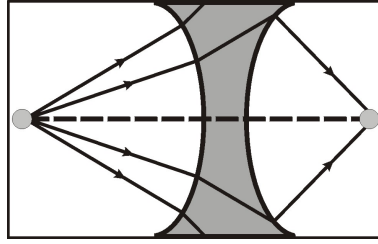


Figure 7.21: Schematic ray tracing according to the Snell's law for a concave lens manufactured of NIM.

for both types of the lenses the area of the focal spot is smaller than or comparable with the diffraction limit. A very good correlation between the magnitudes of the n_{eff}^{PC} and the area of the focal spot can be observed. For instance, the magnitudes of the n_{eff}^{PC} belonging to the TE polarization are much smaller as those belonging to the TM polarization. It correlates well with areas found for the focal spots which are much smaller for the TE polarization than for the TM polarization. For both cases when $n_{eff}^{lens} > 0$, the area of the focal spots increases drastically.

In Fig. 7.21 a concave lens from a NIM is schematically drawn. One can see that the negative index has the feature of collecting mostly rays from a small angle. Also peculiar is the formation of the image point, i.e. the focal length, closer to the lens edge, by contrast to focusing concave lenses with positive index materials. These feature might be very useful for integrated optics and could be eventually further exploited. One drawback of the concave lens based on NIM is the existence of the optical axis. One has to mention here, however, that although there is an abundance of reports in the literature concerning the plane plate lenses based on NIM, there is no report normalizing the measured EM field with the free space, thus making impossible to compare the efficiency of the lenses treated here with other in the published works.

One of the remarkable feature for both lenses, not expected from the theory (at least not as a straightforward conclusion), is the beam splitting. For both types of the lenses it occurs mainly for the TE polarization and in the low band of the PBS. In both cases the effect is obtained at wavelengths that are either close to the edges of the PBG or at the large openings of the bands. Both lenses have some big amount of cylinders building their upper and lower parts (i.e. building blocks). By contrast to their centers these already could act as PCs that "feel" the PBG and thus do not allow the propagation of the EM radiation. Most probable the radiation is squashed to the centers of the lenses, i.e. thin parts, where no information of the PBS is preserved. Thus further propagation of the waves is allowed. It is important to mention that the triangular lens is a better example of such a contrast in the functionality. Being a closed packed structure, the building blocks will mimic even better the behavior of

a PC while having only a single row of cylinders in the middle allows any wave to propagate through the device. This supposition is also supported by the fact that the distance between the maxima on the beam splitting remain insensitive to the radiation wavelength. In Fig. 7.17b, for instance, the distance between the maxima is exactly the length of the singular rods row for the triangular lattice.

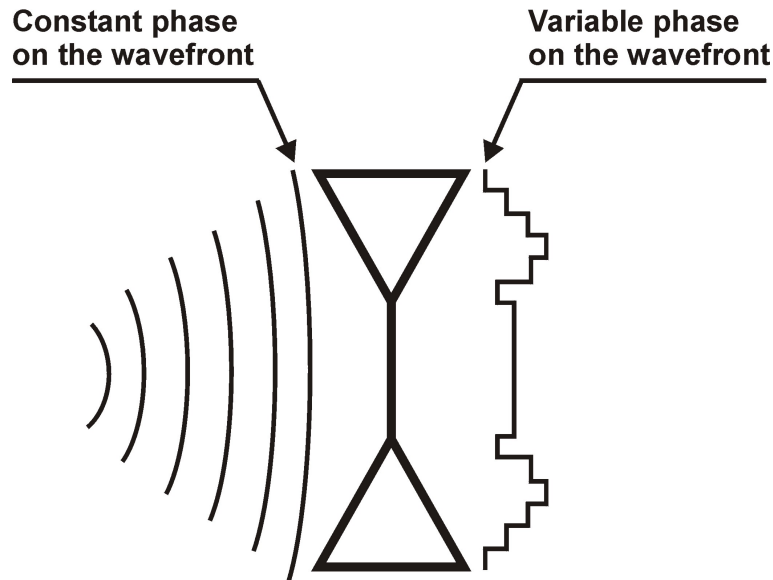


Figure 7.22: Possible scenario describing the functionality of the optical elements treated here. The hypotheses assumes the distortion of the phase on outgoing wavefront.

Beam splitting occurs also in the regions where the bands are quite dense, c.f. Fig. 7.9 and 7.8. In this case, the reasoning might not necessary coincide with the one above. The effect can also result due to the peculiar deformation of the wavefront at the exit of the device, see Fig. 7.22. That is, the wavefront will no longer be characterized by a constant phase, but can be discretized in regions of different phase depending on the thickness of the element in each particular region. This is similar to what is called Zernike aberration of the wavefront. This principle is also extensively used by the microwave community for designing "optical" components [183]. While this approach sounds plausible, its major drawback is calculating the exact change in the phase for any portion of the wavefront becomes very difficult, if not even impossible. This is because the phase shift depends on the exact refractive index of the structure in the corresponding region, i.e. one has to discretize the n_{eff}^{lens} too, which is somewhat imprecise. One has to mention however that many of the experimental result could be simulated by using this method and by approximating the distribution of the n_{eff}^{lens} . The qualitative match is very good, however, there exists a consistent deviation between the quantitatively measured and simulated results.

The lenses studied here, although obviously far from being perfect PCs, emulate their prop-

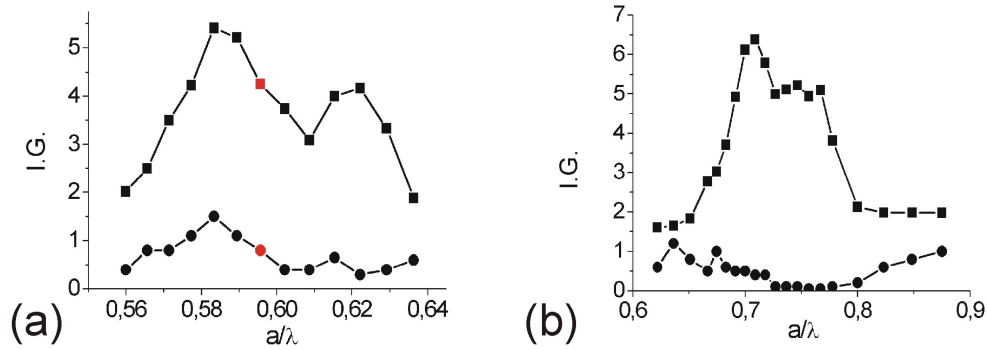


Figure 7.23: The IG of the square lattice lens (squares curve) plotted together with the IG obtained purely from diffraction of two rows of cylinders (circles curves). The data is shown for the TE (a) and for the TM (b) polarizations.

erties very well. Indeed the focusing features are mostly found only in intervals predicted by theory, i.e. where the PCs behave as homogeneous materials $n_{eff} < 1$. Moreover, there is a clear absence of the focusing effects outside those intervals. One can consider that the functionality of the lenses arises mainly from the PCs features. For additional confirmation, measurements were done using, instead of the lens, only two rows of cylinders (two rows each consisting of 26 cylinders, i.e. the total number of cylinders from one end to the other of the lens). In this way one can examine the contribution to the IG originating purely from the diffraction in the middle part of the lens. The results (circle curves) are plotted together with the IG magnitudes inherent to the focusing intervals (square curves) for the square lattice lens: TE (Fig. 7.23a) and TM (Fig. 7.23b) polarizations. It can be seen that the diffraction does not bring any significant contribution to the focusing. Maximum IG magnitude is around 1.5 corresponding to a focusing IG of 5.5 for the TE polarization.

Using a PC with $n_{eff}^{PC} < 1$ brings additional advantages for designing optical elements due to very peculiar beam propagation inside the crystal. Combined with some additional effects this lead to the construction of devices that can act as lenses, beam splitters, filters, beam quadruples, etc. The literature reports, however, a very high degree of reflections for PCs with $n_{eff} < 1$ [184]. That is, working on the band edges, most of the coupled radiation will be effectively reflected by the PC. This limits the maximum obtainable IG for different devices. Further engineering on this issue would imply better impedance match between the PC and the environment. This implies, however, that besides knowing the ϵ_{eff}^{PC} one has to also assess the μ_{eff}^{PC} (effective magnetic permeability) of the PC. Unfortunately, there are many good theories proposed how to calculate the first, but there is no consistent theory that might give some quantities concerning the second parameter. Finally, increasing the IG involves knowing the $\epsilon_{eff}''^{PC}$ too or to know how to manipulate on the losses inside the PCs. As is the case for the magnetic permeability this parameter is also not known how to be calculated for such

composites materials, thus limiting the activity in this sense. Nevertheless all these issues are very important and also interesting from the theoretical point of view. Progress in this direction would have a great impact for the entire field of optical design.

7.3 Derivate of the concave lens

7.3.1 Refractive index and lattice constant gradient lenses

As it was shown for both concave lenses, although based on their geometrical structure they only represent some traces of PCs, their properties, predicted by the PC theory, match observations surprisingly well. Being far from an ultimate understanding of their functionality makes it rather difficult to formulate a robust algorithm for the optimization of their characteristics. That is to answer the question: what has to be done in order to increase the IG while e.g. keeping constant the cylinders number, material type, etc? In this respect some additional knowledge can be gained if other forms of the concave lenses are tested. First, a lens is measured which has a supposed gradient in the refractive index: the center of the lens has a $n_{eff} = 1$ which decays toward the margins of the lens to values < 1 .

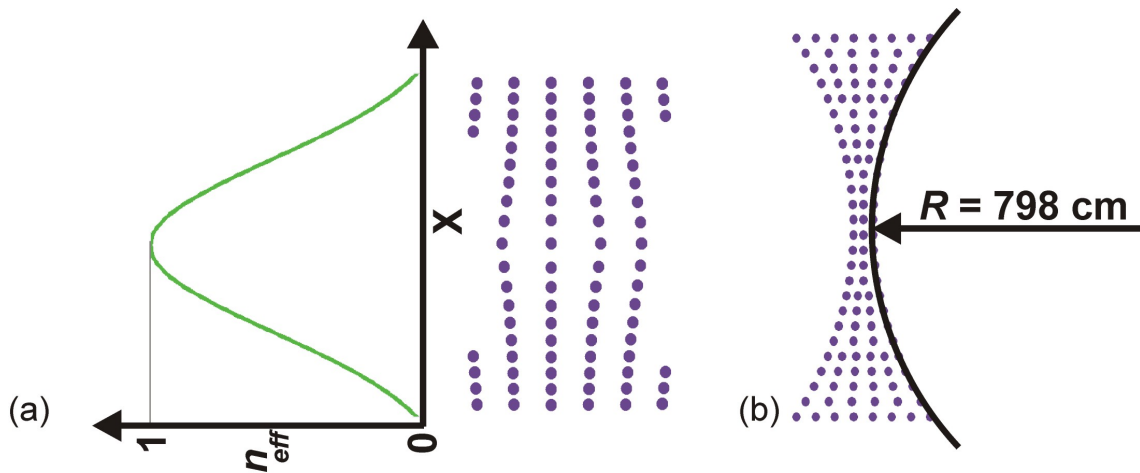


Figure 7.24: *The structure of the lenses with a gradient in the refractive index (a) and a gradient in the lattice (b).*

The form of the measured lens with the gradient in the n_{eff} is shown in Fig. 7.24a. The lattice constant for modeling each n_{eff} is the one which a PC would have in order to exhibit a corresponding n_{eff} . Since using only a few cylinders for representing the portion with a specified refractive index, this is again only an approximation of a real PC.

The next lens to be tested is shown in Fig. 7.24b. In this case the idea is to have a lens surface that resembles as much as possible a real concave lens, i.e. which is smooth and not abrupt as was the case for the square and triangular lenses. The lattice inside the lens is then destroyed by adjusting an equidistant position of the cylinders along one line. In this case, there is no trace of any PC crystal and no PBS can be ascribed to such a PC since it is not periodic.

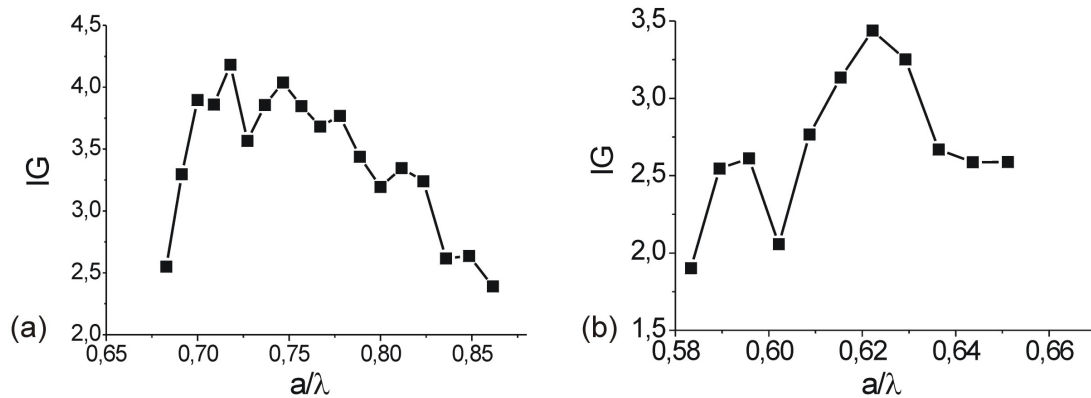


Figure 7.25: *The measured IG for the refractive index gradient lens (a) and the lattice constant gradient lens (b).*

The results of the measured IGs are shown in Fig. 7.25. For both types of the lenses focusing could be found only for the TM polarization. By contrast to the regular lenses no pronounced Gaussian like distribution of the IGs could be observed and hence the filtering effect is weakly pronounced. Additionally, there could not be found any beam multiplication. The maximum IG for the refractive index gradient lens is $IG = 4.25$ however the focal spot is not as well defined as was the case of the regular lenses. For the lattice constant gradient lens the maximum IG is even lower, $IG = 3.5$.

These two cases show that having the lattice is a prerequisite in order to achieve good focusing. Yet the fact that the index gradient lens could exhibit, however poor, focusing is very interesting since this supports the hypothesis that it is n_{eff} that determines the functionality of the device. The lattice gradient lens is rather difficult to understand since there is no theory which will describe the features of such an arrangement of cylinders. The small focusing that could be found is an indication that such a structure also modifies the wave front in a way leading to focusing. However, having no mechanism to determine, for each front portion, the n it is rather impossible to reconstruct the focusing from rearranging the phases on the outgoing wave front.

7.3.2 Holographic lenses

In any actual technological field there is a strong effort to reduce the sizes of the components. If it is about the lenses discussed here a reduced form might be achieved by either using a smaller number of the cylinders or by decreasing their size. While the last is directly coupled to the operational frequency of the device, i.e. the PBS of the PC is strictly dependent on the cylinders geometry and lattice constant; using a smaller number of cylinders by ensuring the same functionality of the devices sounds interesting and deserves a separate treatment. The main question is: starting with a functional device with a certain characteristic could one find a method for reducing its size while preserving its functionality? This topic is rarely addressed in the literature and no ultimate optimization technique is known.

Hakanson et al. proposed the use of genetic algorithms for optimizing the architecture of optical devices based on 2D PCs [185, 186, 187]. The essence of their approach is starting with a certain (usually periodic) arrangement of alumina cylinders and find such a combination of cylinders locations which is optimal with respect to certain functionality of a device. That leads to some very fancy arrangements of the cylinders that indeed, for some specific frequencies, focused the radiation very well or worked as a wavelength de-multiplexer [188]. In their cases they indeed obtained optical elements by using less cylinders than needed if applying the common known theories of the optical elements design. The big disadvantage of their method is the huge computational power needed. Essentially they have to traverse all possible combination of the cylinders positions and see whether it influences the result in the positive or negative direction and decide upon further going at each step.

In this work another approach is chosen. It is based on commonly accepted axiom in physics - *time-reversal invariance*. It says that if a process occurs, the reverse process can also occur. Translated in optics this can be interpreted as: a ray following a path from the source to the detector will follow exactly the same path if send back from the position of the detector toward the source. This principle is further used for reducing the number of the cylinders in the optical elements:

1. It starts with a certain, predefined, arrangement of the cylinders which focuses the radiation, e.g. the concave lenses [189] treated in previous sections.
2. A special algorithm analyzes the scattering cross-section of each cylinder in the tested structure while a forward wave is send through the structure.
3. A source of radiation of the same frequency is placed in the image point of the focusing structure which radiates a backward wave.

4. The scattering cross-section of each cylinder is analyzed again, in this case obtained as a result of the forward and backward waves.
5. Assuming the principle of *time-reversal invariance* one considers that the backward wave started from the image point will follow exactly the same path as those parts of the forward wave contributing to the formation of the focal point.
6. As a result of the supposition of the waves those cylinders having a constructive contribution to the image formation will exhibit a considerably higher scattering cross section as compared to the cylinders that "deviate" parts of the forward wave from traveling to the image point, i.e. redundant cylinders with respect to the specific functionality.
7. The redundant cylinders are removed from the lattice and the algorithm might start again.

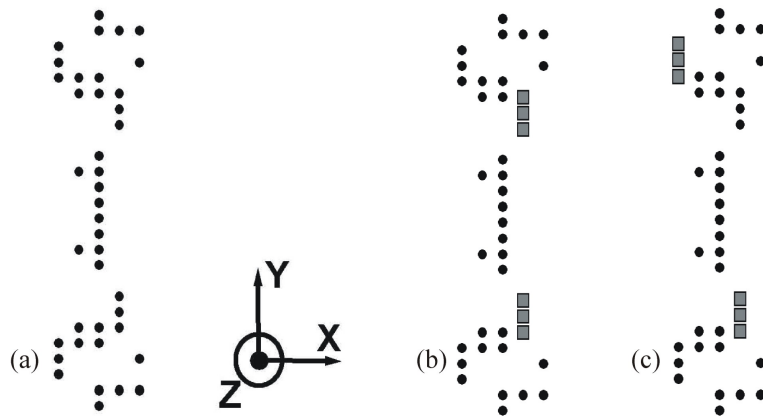


Figure 7.26: *The top view of the measured devices: the regular lens (a); the symmetric defect lens (b) and the asymmetric defect lens (c). The gray squares indicate which cylinders are removed from the arrangement.*

The optical element, shown in Fig. 1a, is essentially an optimized successor (by using the above mentioned algorithm) of the square lattice concave lens presented earlier, see also Ref. [189]. The data shown in this section represent the result of the optimization of the focusing effect for the TM polarization. Since the optimization methods resembles to some extent the holography, such lenses are further on called "holo-lenses".

Additionally it is shown that various (quasi) periodic arrangements of such cylinders lead to the formation of interesting optical elements that might be used for future integrated optics. This new generation of optical devices can exhibit actually much more enticing properties as only focusing the radiation. Besides all, it is always interesting to know: if, a simple algorithm decides that certain cylinders from the arrangement are redundant, what should be done next

- remove them from the existing structure or place them on some different positions? Such questions as: what determines a periodic arrangement of cylinders to focus the radiation - their number or their positioning are not yet fully understood. This being the reason why in this work, starting with a certain optimized focusing device we introduced some defects, meaning that some cylinders are removed. We show how this influenced the behavior of the initial structure and also exhibited some interesting functionality that might trigger enticing applications.

Besides testing the lens in Fig. 7.26a a series of defect structures were investigated: starting with the original construction, some cylinders are removed from their original positions. We discuss two types of defects introduced in the holo-lens. A symmetric defect, i.e. six cylinders from symmetrical locations according to the "optical axis" are removed. The element structure is shown in Fig. 7.26b. Also an asymmetric defect is created leading to a structure as in Fig. 7.26c, i.e. there are removed three cylinders from both sides of the "optical axis", however not from symmetrical positions. For both defect structures the missing rods are marked by gray squares in Figs. 7.26b and 7.26c.

A typical focusing for the holo-lens is shown in Fig. 7.27a. The region where the radiation is concentrated is clearly visible. As it was mentioned we do not deal here with a real lens so that common parameters known from the geometrical optics, e.g. focal length, are hardly applicable. Nevertheless, some features of the lens could be assessed and we analyzed the dependence of the distance from the device edge to the focal spot as a function of the wavelength. A clear linear behavior can be observed, as shown in Fig. 7.27b. Some deviation of the points in Fig. 7.27b from a perfect linear comportment are due to the methodology used for extracting the data from the measurements. The distance was always measured between the lens edge and the brightest point on the focal spot. Its position, however, could be also influenced by some side effects as formation of the standing waves or perhaps some parasitic reflections. The increase is also clearly pronounced since it varies between 700mm for the $a/\lambda = 0.51$ to more than 1000mm whilst $a/\lambda = 0.59$.

It is found that for the TE polarization the best focusing frequency interval lies between 0.5 and 0.6 of the inverse of the wavelength. The corresponding IG is shown in Fig. 7.27c. The maximum IG = 5.6 is achieved for $a/\lambda = 0.51$. The IG on the focal spot remains nearly constant for the interval $a/\lambda \in [0.5; 0.56]$. The IG will slightly decrease with increasing wavelength and already for $a/\lambda > 0.6$ no focusing is observed. This holds for both the low value for IG as well as for its distribution where no focal spot is detected. Note that the same efficiency was earlier reported by our group for a concave lens based on 2D PCs consisting of 112 cylinders, i.e. almost a factor of 3 more as for the device presented here.

Focusing is found for the TM polarization as well. A typical IG distribution is shown in Fig.

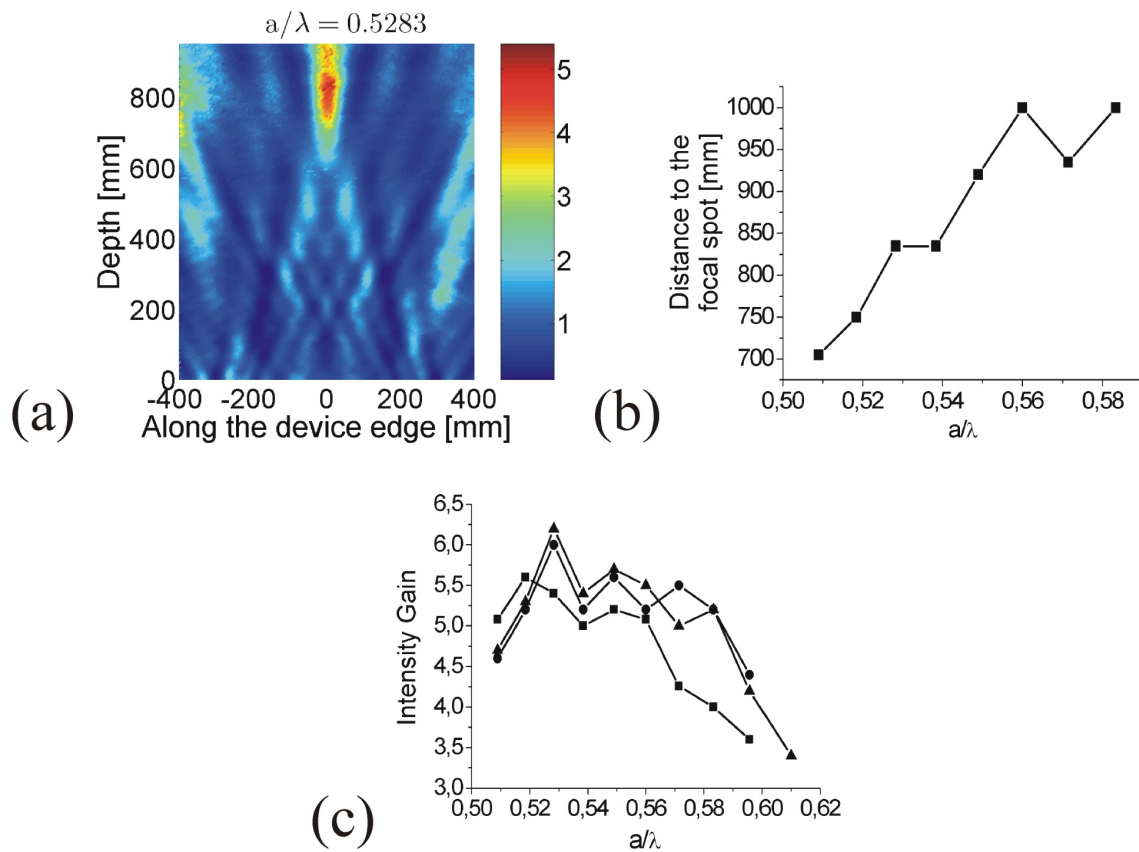


Figure 7.27: Data for the TE polarization. The spatial distribution of the IG for a typical focusing for the TE polarization (a). The distance between the edge of the lens and the most brightest point on the focal spot is plotted versus the wavelength (b). Selected frequency intervals plotting the focusing efficiency of the optical device (c).

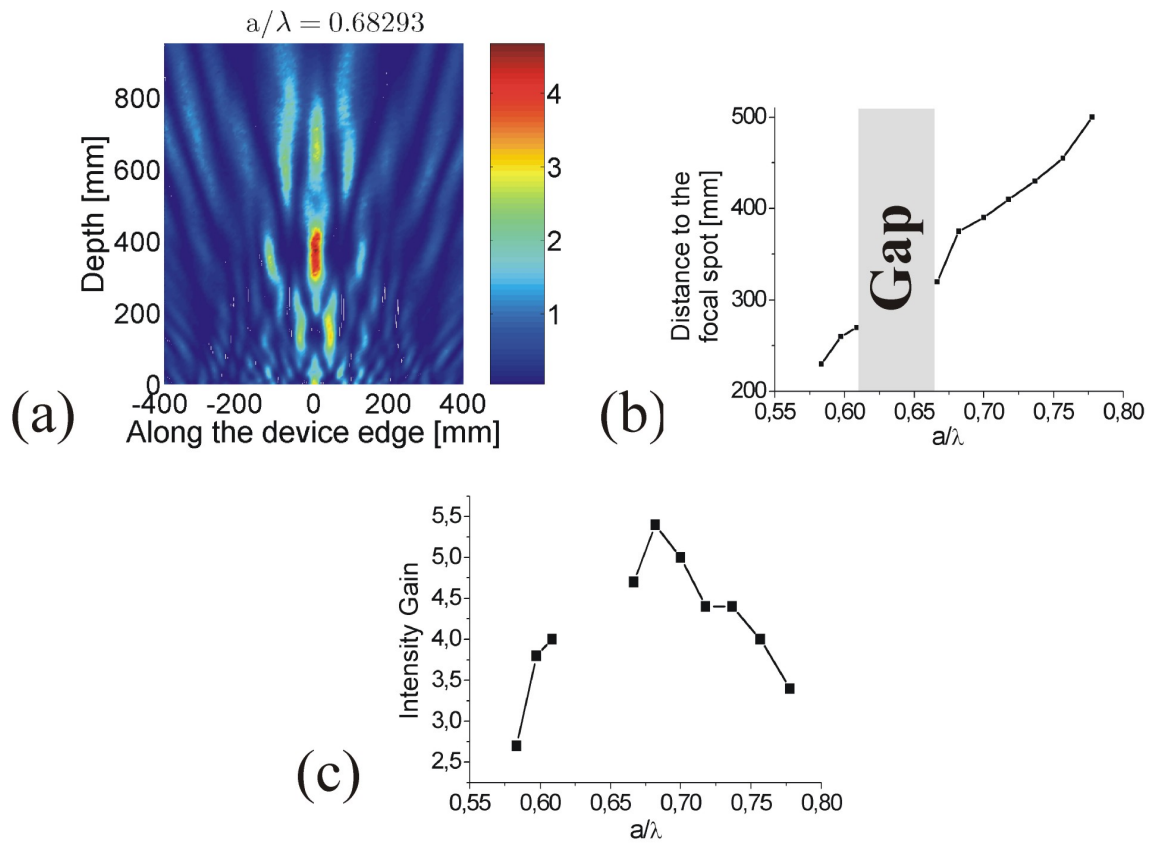


Figure 7.28: Measured data for the *TM* polarization. *IG* distribution which shows a very good focusing of the device (a). The distance between the edge of the lens and the most brightest point on the focal spot is plotted versus the wavelength (b). Selected frequency intervals plotting the focusing efficiency of the optical device (c).

7.28a. A clearly defined focal spot is visible at about 400mm from the edge of the lens. The active wavelengths range, i.e. where the lens focuses, lies between 0.58 and 0.78, yet with a small wavelengths interval, $a/\lambda \in (0.61; 0.66)$, where there is no focusing effect at all. In Fig. 7.28b the distance to the focal spot versus the radiation wavelength is plotted. By contrast to the TE polarization, clearer linear behavior of the corresponding magnitude could be observed although it does not vary as strong with the wavelength.

In Fig. 7.28c the best focusing, $IG = 5.4$ is found for $a/\lambda = 0.68$. By contrast to the TE polarization the IG vary much stronger with the radiation wavelength. There is also a clearly defined optimum for the focusing efficiency.

Common for both polarizations is that the focusing will disappear (i.e. $IG < 2$) completely outside the mentioned frequency space. Peculiar for the TM polarization is the existence of a sort of gap where the lens doesn't focus the radiation at all. All this leads to the conclusion that the proposed element could be used as a filter, but better suitable for the TM polarization.

Comparing the behavior of the distance to the focal spot one can see a clear difference between the both polarization and namely that TM polarization focuses the radiation much closer to the lens edge as the TE polarization does. Apart from this fact variation of the distance for the TM polarization is more sensitive to the change of the wavelength. It will vary in the range of almost 50% from the maximum distance whereas for the TE polarization this is only by up to 30% from the maximum distance. Thus having a device with strong polarization dependence of the focusing characteristics might be exploited as some kind of polarizator.

The defect structures are tested only in the intervals where the holo-lens focuses. Experiments are performed for both polarizations. The IG for the defect lens is plotted together with the original one for the TE polarization in Fig. 7.27c; triangles for the structure with a symmetric defect. Although somewhat counterintuitive, for the structure in Fig. 7.26b a very good focusing is found. For the $a/\lambda = 0.53$ an $IG = 6$ could be achieved. Generally, one can observe that the defect structure focuses with a higher efficiency over the whole interval. Another feature is the formation of an optimum in the IG, although generally less sensitivity to the radiation wavelength is observed. The IG remains quite constant over the investigated wavelength interval.

The introduction of the defect doesn't have any influence on the distance to the focal spot. For both cases it shows the same behavior of this magnitude as a function of the wavelength. The maps for the IG distribution for the defect lens are identical to the ones for the regular lens.

The influence of the defect for the TM polarization showed more interesting effects. Although the focusing effect is still preserved, the addition of the defect changed the position of

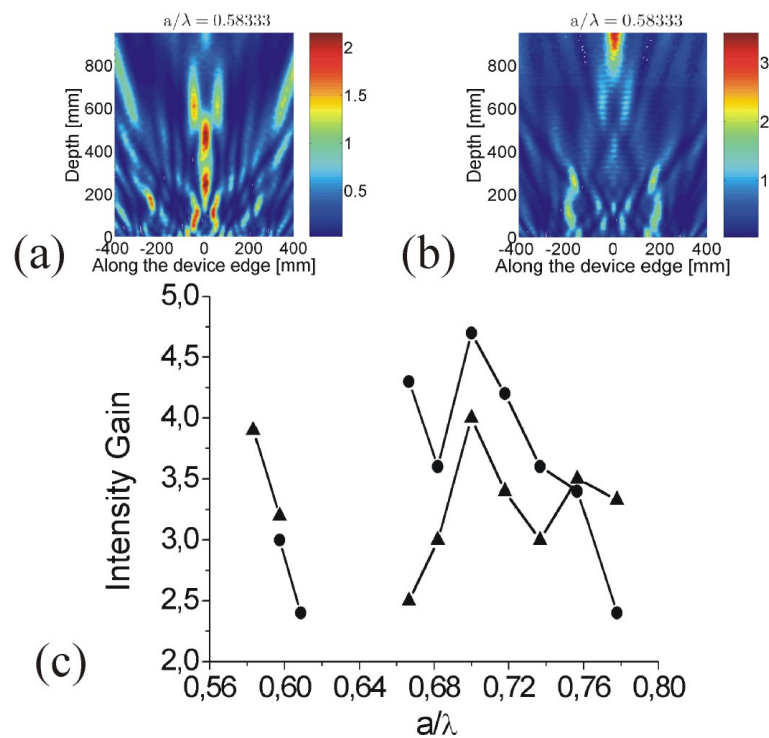


Figure 7.29: The data for the TM polarization. The IG distribution for the original lens (a). Once the symmetrical defect is induced the lens completely change its functionality (b). The IG magnitude on the brightest point of the focal spot is plotted as a function of wavelength (c).

the focal spot as compared to the regular lens. This is clearly seen by comparing Figs. 7.29a and 7.29b. In Fig. 7.29a is shown a typical focusing of the lens as in Fig. 7.26a. It can be seen also that there are actually two main points where the radiation is concentrated: one at about 250mm and another at 450mm from the edge of the lens. Also the IG magnitude is not very high being at about 2.5 for both spots. The ulterior introduction of the defect, see Fig. 7.29b, suppressed the radiation concentration at the mentioned positions and shifted the focusing spot at about 1000mm from the lens edge. Although one can see only part of the focusing spot (for measurements could not be further continued) simulations showed that it is indeed a single focal spot.

Comparing the curves in Fig. 7.29c and Fig. 7.28c it can be seen that the IG values for the defect structures are indeed lower (triangles curve on the Fig. 7.29c). Although the position of the focal spot is changed for the defect structure the IG distribution remains basically unchanged. Notice that even the wavelength gap for non focusing feature coincides for both type of the devices. It was observed that the defect influence can be also the opposite. Thus for frequencies where the regular lens did focus the radiation very well, ulterior remove of the cylinders caused the complete spoiling of the focusing effect.

As it was mentioned in the introductory part, the lens presented here is actually an optimized form of an earlier device where the redundant cylinders were removed from the construction. Naturally one can ask what is optimal form of such a device and how many cylinders could be removed until the highest performance of the device is achieved.

The increase in IG magnitude, for the TE polarization, should not appear contradictory. By removing the cylinders, more or less by accident, we come to a new device which destination is only to focus the radiation in the mentioned interval. That is, if some other (also not necessarily six) cylinders would have been removed, the device functionality might be completely changed and focusing being observed for a completely different frequency interval. This is partially the case of the TM polarization where the removed cylinders lead to a new device that maybe focuses better in some other frequency intervals (not tested here), but which however lead to a worst efficiency with respect to this particular functionality.

It is of some particular interest to see how the operation of the mentioned device changes when an asymmetric defect is introduced, see the arrangement in Fig. 7.26c. This type of the experiments should also shed more light on the contribution of specific cylinders to the formation of the electromagnetic field behind the lens.

In Fig. 7.30a a clear bending of the beam can be seen, i.e. where the rays trajectory is changed. A black dashed line is drawn, which crosses the center of the scanned field, in order to guide the eyes. For some lower wavelengths, the distribution of the IG looks differently. Figure 7.30b shows a bending of the beam that rather arises from the stronger excitement of

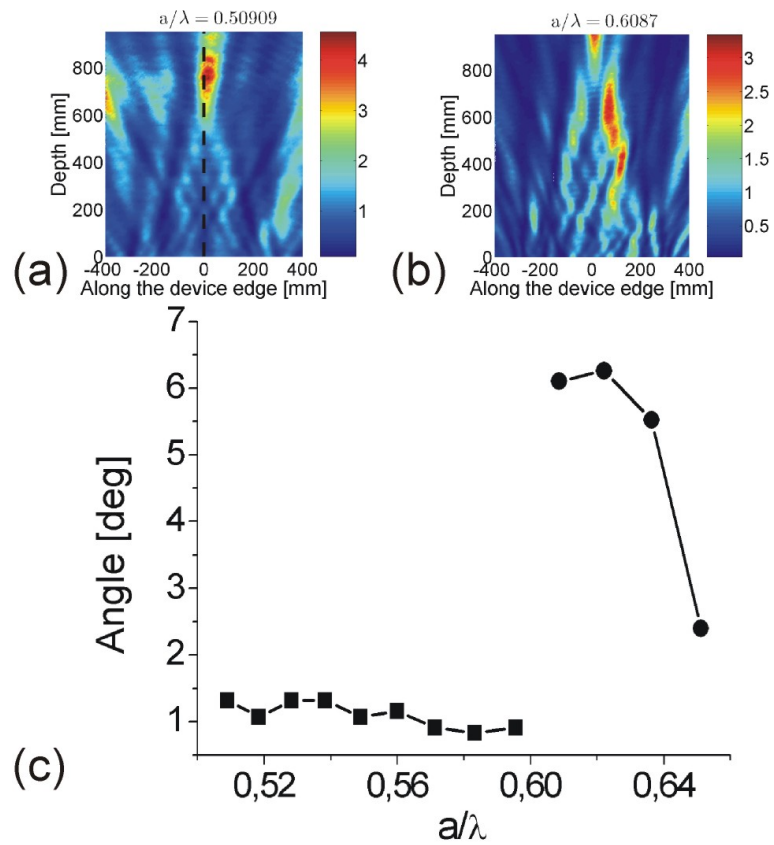


Figure 7.30: The data for the TE polarization. Two mechanisms of bending the beam: changing the trajectory of the rays (a) or exciting stronger already existing modes (b). The strength of bending plotted as a function of the wavelength (c).

some lateral modes which are not as strong in the case of the regular lens, cf. Fig. 7.30b and Fig. 7.27a.

In Fig. 7.30c is analyzed the strength of the bending as a function of the radiation wavelength. Plotted is the angle formed between the line traced through the middle of the scanned field, i.e. black line in Fig. 7.30a, and a line traced through the 0 point and the brightest point on the focal spot. In Fig. 7.30c the estimated angle is plotted. The squares plot the angle formed while bending the beam by changing the rays trajectory. Only a slight variation can be seen, which lies in the range of 1° - 2° , with no clear dependence on the wavelength. The circle line plots the bending angle for the distributions similar to those in Fig. 7.30b. An optimum in the bending strength can be seen, which is at $a/\lambda = 0.62$ corresponding to about 6° , drastically dropping as the wavelength will further decrease.

The circle line in Fig. 7.27c shows the IG dependence on the focal spot for the bent beam versus the change in the wavelength. It can be seen that also with the asymmetric defect the IG magnitudes are well above the IG for the holo-lens. To some extent, the IG for the asymmetric lens repeats the one for the symmetric defect lens.

Figure 7.31a shows the IG distribution behind the regular lens for the TM polarization and how the distribution is changed when the asymmetric defect is introduced, Fig. 7.31b. The inverse of the radiation wavelength is $a/\lambda = 0.72$. Comparing Figs. 7.31a and 7.31b it is possible to conclude that the bending occurs according to the same schemata as for the TE polarization when the trajectory of the beam is changed. This idea is also supported by the fact that the excited mode in Fig. 6b is generally not seen in Fig. 7.31a (or its IG is well below 1).

The dependence of the bending angle versus the inverse of the wavelength is plotted in Fig. 7.31c. There is also represented a polynomial fit of the 5th degree for guiding the eyes. Comparing the results with the TE polarization remarkable is a stronger variation of the bending angle. Apart from that, one can also see a maximum in the angle at $a/\lambda = 0.66$, yet not very clearly pronounced. Figure 7.29c represents the IG variation on the focal spot as a function of the wavelength. The behavior is almost the same as for the case of the symmetric defect, thus being completely different from the IG distribution for the defect free lens, cf. Fig. 7.28c.

Concerning the beam bending for both polarizations one can be assumes, with a strong degree of confidence, that the opposite effect will be achieved if changing the symmetry of the defect in Fig. 7.26c.

The primary intention of the device shown in Fig. 7.26a is to focus the radiation, i.e. act as a lens. While a regular lens implies also the possibility of imaging an object, at this phase, this is not expected for the devices in Fig. 7.26. This feature is also not probed in our

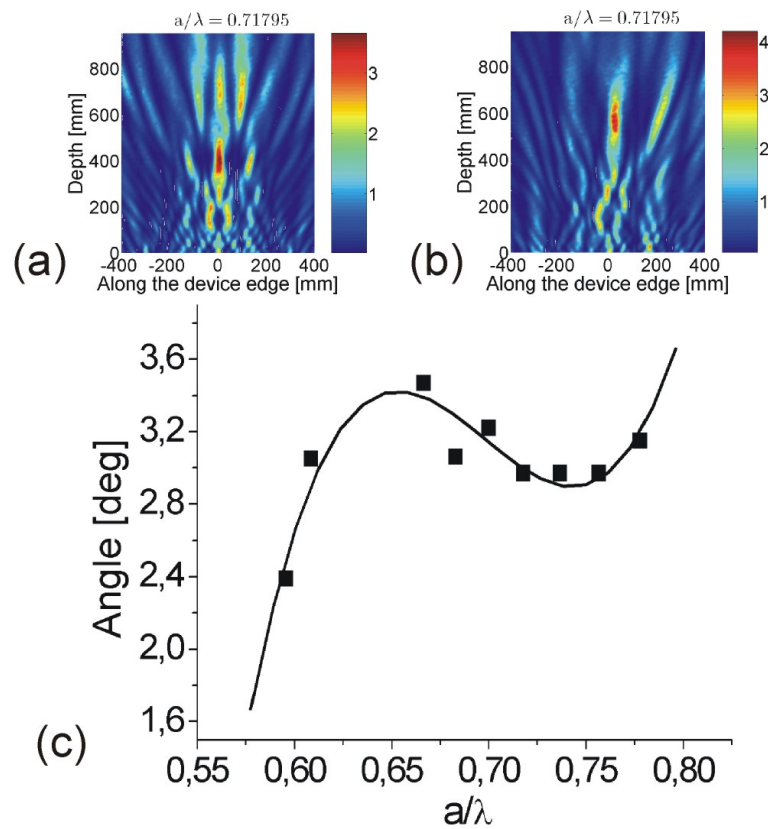


Figure 7.31: *The data for the TM polarization. The distribution of the IG for the regular lens (a). The introduction of the asymmetric defect excites the focusing of the radiation in a new location (b). Dependence of the bending angle plotted as a function of the wavelength (c).*

experiments. Besides the IG value, another important characteristic would be the resolution of such devices. One has to mention, however, that the focal spot itself, in some cases, is kind of spoiled, often drastically exceeding the size of the dipole used as a point source. Since the size of the focal spot is strongly wavelength dependent, so is the resolution of the lenses. In most of the cases, however, this is not very high. That is also the main reason why while designing such elements it is important to understand and assess the contribution of any cylinder to the electromagnetic field distribution behind the lens. Later this information will allow to optimize the devices such that only desired distributions could be obtained.

Intuitively, any focusing device would have to resemble in its form a lens, as known from the geometrical optics. If it is about the photonic crystals based lenses then at least its elements (e.g. dielectric cylinders in our case) would have to be arranged in a manner appearing like a lens which is the case of devices presented in [169, 189, 190]. In our case, we achieved with a very rudimentary arrangement of the cylinders the formation of a fairly sophisticated device (at least to what its functionality is concerned). In particular its operation is proved to be very selective both to the radiation polarization as well as its wavelength.

7.4 Negative index materials with inhomogeneous rods

The concept of left-handed electromagnetic media, which are also known as negative-index materials (NIMs), was introduced by Veselago [191] as a theoretical curiosity. Interest in these metamaterials was rejuvenated by Pendry [192] and Smith et al. [193], who noted that the growth of evanescent fields within a NIM provides the opportunity for building a "perfect lens" that can focus electromagnetic waves to a spot size much smaller than a wavelength. Although various aspects of Pendry's treatment of NIMs have been questioned [194, 195], negative refraction has nonetheless been confirmed in recent experiments [168, 196, 197], and its theoretical background has been further explored [198, 199, 200]. Negative-index materials have recently been designed on the basis of composite wire and split ring resonator structures [193, 197, 201], backward-wave transmission lines [202], and PCs [73, 199, 177].

Very often, NIMs based on dielectrics are designed from periodically arranged homogeneous materials, which would usually mimic also properties inherent to PCs. In such a case, for instance, thick slabs consisting of a large number of rods are required for realizing good focusing. In this work, it is proposed to design the NIM lens from dielectric rods with a specific dielectric constant profile. This design leads to comparable or even improved focusing from much thinner slabs thus containing a much smaller number of rods.

The proposed approach is based on using dielectric rods which themselves possess a negative refractive index at definite wavelengths. The approach consists of the following steps:

- the design of elementary units (rods) exhibiting properties of NIM;
- different periodic or quasi-periodic structures assembled from these elementary units are considered, and their properties are calculated numerically with the goal of producing negative refraction and optimizing the focusing effect.

A highly efficient and accurate multiple-scattering approach [165] is used to calculate propagation of electromagnetic waves through these structures.

The elementary building blocks of the design are dielectric rods with a changeable refractive index. According to Sergentu et al. [203] its gradient must resemble a "fish-eye" profile [204] given by:

$$n(r) = \frac{n_0}{1 + \left(\frac{r}{r_0}\right)^2} \quad (7.8)$$

where r is the distance from the center of the rod and n_0 , r_0 are some constants. In such a material light propagates in circular (or spiral) trajectories with a radius comparable to the quantity r_0 , i.e. a medium with the "fish-eye" dielectric constant profile behaves like a NIM from the point of view of light scattering. The illustration of this effect is shown in Fig. 7.32.

The idea for making a rod with a fish-eye profile in the dielectric constant originates from

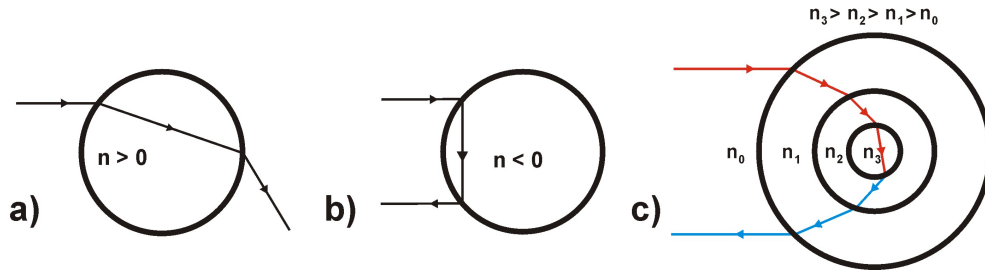


Figure 7.32: *The schematic representation of the origins fish-eye concept. It shows the ray bending in a cylinder with $n > 0$ (a) and the beam bending similitude between the homogeneous NIM cylinder (b) and the fish-eye cylinder (c).*

analyzing the beam bending in cylinders with $n > 0$ and $n < 0$. By applying the Snell's law, for a cylinder with $n > 0$ the beam is bent as shown in Fig. 7.32a. The same Snell's law, valid also for NIM [192], if applied for a cylinder consisting of homogeneous material with $n < 0$, predicts that the beam is bent back out from the cylinder, as shown in Fig. 7.32b. One can then think of building a special cylinder consisting of materials with $n > 0$ (i.e. found in nature), but which will bend the beam the same way a NIM cylinder does. Figure 7.32c illustrates the beam propagation through a cylinder with a fish-eye profile for the dielectric constant. It is clearly seen that from the radiation scattering point of view Figs. 7.32b and -c are similar, thus the fish-eye cylinder acts as a NIM material. Such a cylinder can be treated as build from an effective material to which an effective ϵ_{eff} will be ascribed. Further in the text it is discussed the exact method for assessing the ϵ_{eff} . One has to mention here, however, that in Fig. 7.32b and -c shown approach is valid only for this special angle of incidence.

An ideal emulation of the fish-eye behavior would be a Gaussian distribution of the refractive index from the cylinder's center to its edges. However, technologically this is rather impossible to be implemented and this is the reason why using a step function, c.g. Fig. 7.33, would approximate, to some extent, the fish-eye profile. The approximation can be done by making the cylinder consisting of only three shells, which is the case treated in Fig. 7.32c or it can be even finer resolved if using more shells which must lead to better emulation of the fish-eye profile. Quite obvious, there exist infinitely possible variants for the cylinders configuration. Finding the optimum construction, in terms of the cylinder's structural parameters, necessities relatively high computational power. Without mentioning that there is no clearly defined search algorithm that would guarantee a final solution for this optimization problem.

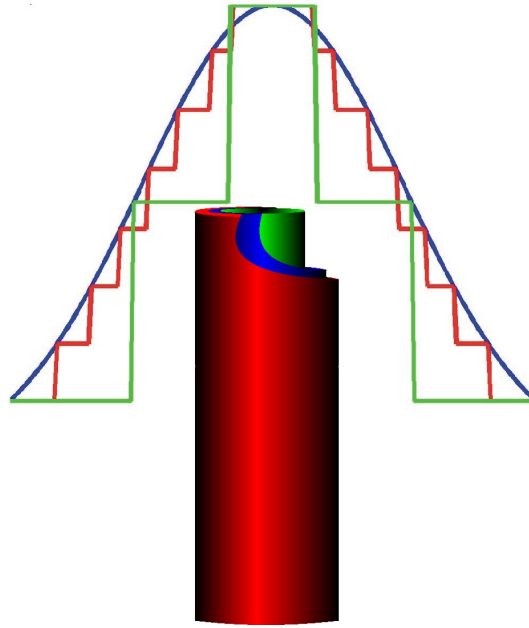


Figure 7.33: *The design of the fish-eye cylinder used in this work. It consists of three layers which intends to emulate the refractive index distribution given by Eq. 7.8*

7.4.1 Results of simulations

In this work the approach consisting of only three shells is selected. This is both due to the good results the configuration exhibited, but also because of the ease with which the experiment could be conducted.

Obviously the situation with the beam bending shown in Fig. 7.32c is generally valid only for short wavelengths, i.e. $\lambda \lg d_{cylinder}$, otherwise Snell's law cannot be directly applied. The first question that arises is: will the same effect be present for the wavelengths larger than the cylinder diameter? If so what would n_{eff} be? For this a modified version of the *Probe Medium Approach* (PMA) presented in [167] is used allowing to assess the n_{eff}^{rod} in a very good approximation.

In the PMA the scattering cross section of the rod is calculated as a function of the refractive index of the background medium. It is obvious that the scattering cross section should exhibit a minimum when the refractive index of the background medium approaches that of the rod under investigation. The scattering cross section for a fish-eye rod was analyzed, which consists of three layers with the radii $r_1 = 0.5a$, $r_2 = 0.25a$, and $r_3 = 0.1a$, having a total diameter d and refractive indices $n_1 = 1.5$, $n_2 = 3$, and $n_3 = 4$.

The calculations were performed for the wavelength $a/\lambda = 0.67$. As one can see from Fig. 7.34a, a decrease of the scattering cross section occurs around the refractive index value of -0.85. It means that for this wavelength the rod behaves as a NIM with the refractive

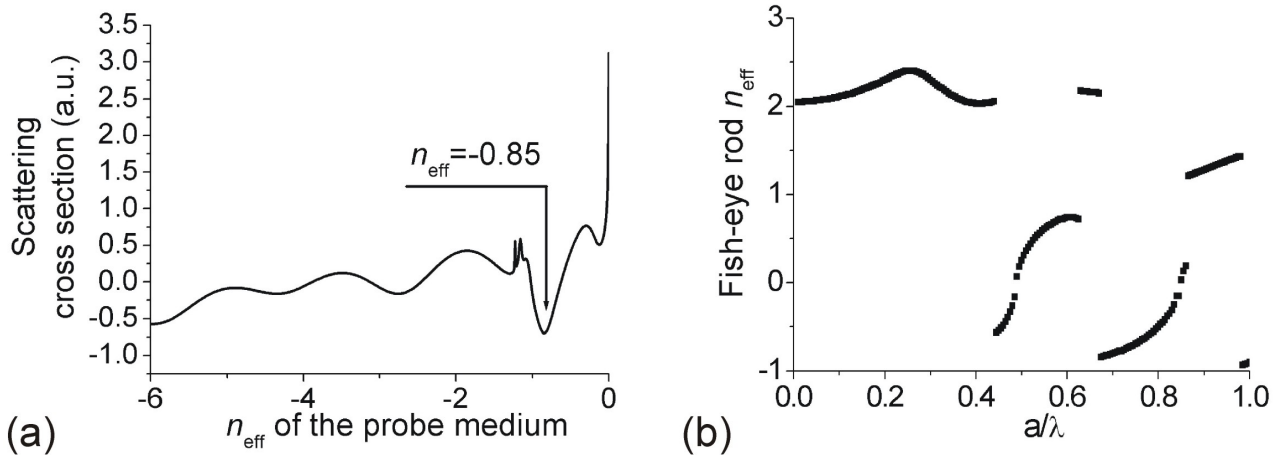


Figure 7.34: The scattering cross section estimated via PMA for the fish-eye cylinder (a). The variation of the fish-eye cylinder n_{eff} as a function of a/λ (b).

index equal to -0.85 . Nevertheless, one should note for completeness that the calculations performed for a homogeneous rod with the refractive index of -1 exhibit a more sharp decrease of the scattering cross section. Analogous calculations are performed for a specific wavelength interval. The effective refractive index of the rod as a function of the radiation wavelength is illustrated in Fig. 7.34b. One can see that within the wavelength ranges given by $0.67 < d/\lambda < 0.83$ and $0.44 < d/\lambda < 0.49$ the rod involved behaves like a NIM from the point of view of light scattering, exhibiting the best properties at wavelengths around $d/\lambda = 0.67$. The calculations performed for the wavelength $d/\lambda = 0.67$ showed a pronounced minimum of the scattering cross section around the refractive index value of -0.85 , meaning that at this wavelength the rod behaves as a NIM with the refractive index equal to -0.85 .

The calculations presented show that the fish-eye rod indeed behaves as a NIM for wavelengths even longer than its diameter. One could assume, with a high degree of confidence (see the *Discussion* part of this section for more details), that if being able to fill a volume with such cylinders, it would behave as a NIM material too. Actually, having cylinders as building blocks makes it impossible to fill a volume, for instance a cube or a parallelepiped, up to 100%. That is why the best approximation, in this sense, would be a closed packed lattice consisting of fish-eye cylinders, i.e. arranged in a triangular lattice provided that all cylinders have the same diameter d . If such an arrangement, e.g. a filled parallelepiped, with a point source in front of it, should it indeed behave as a NIM, then a focusing effect must be observed. The construction and the effect is similar to what is treated in the literature under the name of "plane plate lens" [192].

For testing this concept a triangular lattice is considered with the lattice constant $a = d$. Figure 7.35 shows the imaging of a point source placed at the distance $3a$ in front of the

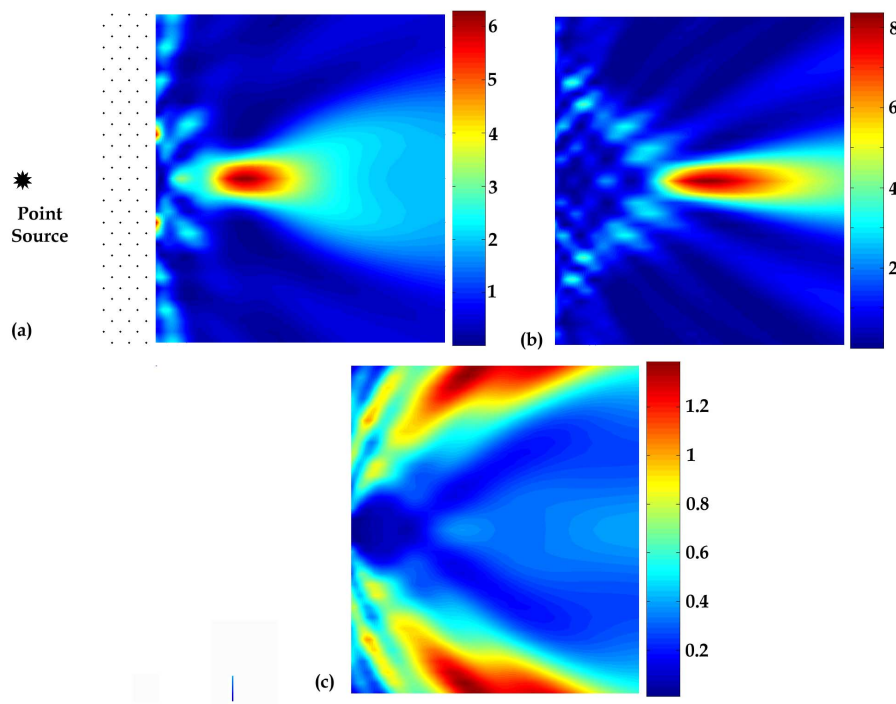


Figure 7.35: *Electric field intensity map of a cross-sectional view of the 2D source-image system when imaging by a triangular lattice photonic crystal slab consisting of "fish-eye" rods at the radiation wavelength $a/\lambda = 0.45$ (a), $a/\lambda = 0.67$ (b), and $a/\lambda = 0.55$ (c).*

considered slab at different radiation wavelengths. The slab has the dimensions of $4.3a \times 20.5a$ consisting of 126 fish-eye cylinders. The patterns represent the distribution of the IG. The calculations are performed for a polarization with the electric field vector E parallel to the axis of the cylindrical rods. One can see, as predicted by the analysis of the fish-eye rod properties (Fig. 7.34), that good focusing occurs at the wavelength $a/\lambda = 0.45$, Fig. 7.35(a), and $a/\lambda = 0.67$, Fig. 7.35(b). No focusing is observed at $a/\lambda = 0.55$, Fig. 7.34(c). Further investigations of imaging properties of the slab demonstrated its inability to focus radiation at frequencies $a/\lambda < 0.44$ and $a/\lambda > 0.85$.

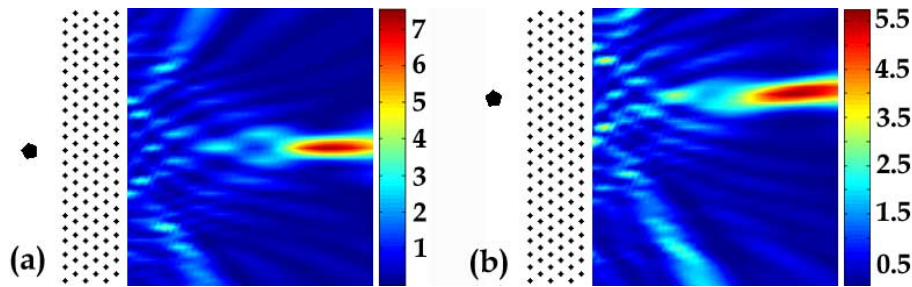


Figure 7.36: *IG map for the behavior of the NIM slab when: the source is shifted closer to the slab; at the distance $2a$ (a); the source is moved by the $4a$ toward one of the edges of the slab (b).*

After showing that the slab indeed focuses the radiation, some other features of the plane plate lens could be tested. First, the shift of the source toward the lens has to be seen in the corresponding outward movement of the image point. Figure 7.36a shows the simulation of this effect, and it can be seen that the image point indeed shifts with shifting the point source. Second, the source could be shifted toward one of the lens edges. Due to the absence of the optical axes for the plane plate lenses this should lead in the concomitant displacement of the imaging point. This situation is simulated in Fig. 7.36b where the point source is shifted up along the lens edges and it can be seen that the image point follows perfectly the source. Hence it is worthwhile to mention that the slab consisting of the fish-eye cylinders indeed behaves as a bulk material with $n < 0$.

7.4.2 Experimental results

In the next step the fish-eye concept is experimentally tested. This is done for the microwave range of the spectrum. In order to realize the desired profile in the dielectric constant for the microwaves one needs some special materials that are either very expensive or very difficult to be manufactured. For instance, it is relatively difficult to find easy handling materials for the microwaves that have a $n_3 = 4$ and at the same time very low absorptions. That is why the following materials are considered: (1) for the inner cylinder, with the highest n_3 , Al_2O_3

rods are used which have an $\epsilon = 9$, the diameter of the rods is selected to be $d = 4$ mm; (2) the alumina cylinder was inserted into a hollow glass tube, and in order to avoid mechanical damage of the components, arising from the imperfect diameter of the alumina rod and the inner diameter of the hollow tube, a small air gap between them is left with the thickness $s_A = 1$ mm; (3) the glass acts as the second layer with $n_2 \approx 4$ with the wall thickness $s_G = 2$ mm; (4) for the next and final layer air is used, i.e. the cylinders are packed in a triangular lattice such that between the margins of the glass tubes of neighboring rods an air gap is left corresponding to an air shell with the thickness of 1 mm for each cylinder. Taken all together, this results in a lattice constant for the NIM slab of $a = 12$ mm. The scheme of the fish-eye slab is shown in Fig. 7.37 where all the structural parameters can be seen.

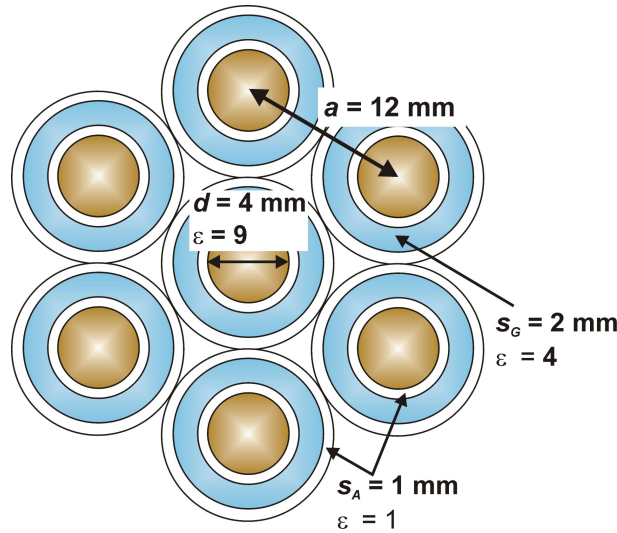


Figure 7.37: The structural parameters of the measured slab consisting of the fish-eye cylinders.

The slab constructed for the microwave measurements has an important difference to the theoretically studied lens. First, as can be seen in Fig. 7.37, there exists an air gap between the alumina cylinder and the glass tube. This is not considered in the theory and this small gap might influence, to some extent, the measurements. However, due to its reduced size a strong influence on the measurements is generally not expected. Also the imperfection in the diameters of both the alumina cylinder as well as the glass tube will perfectly compensate for the existence of this gap. Moreover, since the measurements performed here serve as a model system, which can be further scaled down to smaller frequencies, it is important to assess the effect of the imperfections arising during the fabrication process of the size reduced structures. This is well emulated by the air gap. In this case the air gap becomes a necessary component.

Figure 7.38a shows the calculated scattering cross section for the fish-eye cylinder used in the

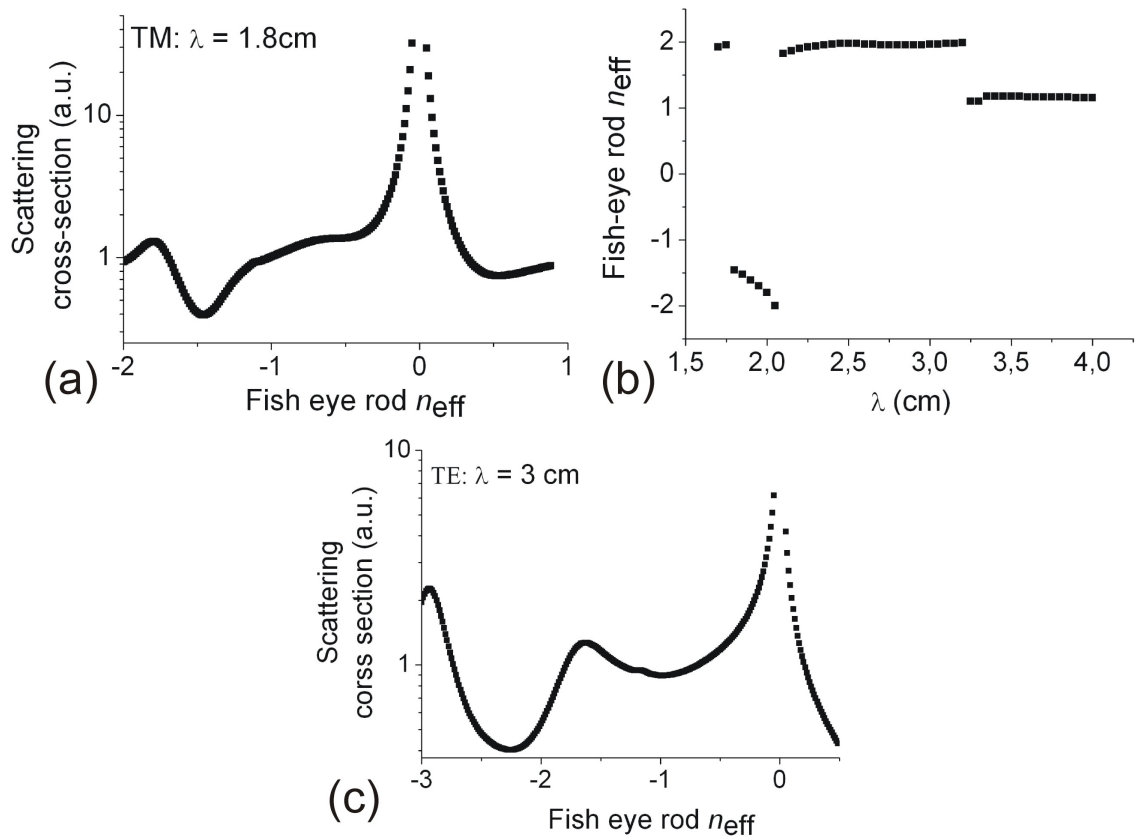


Figure 7.38: Calculations for the fish-eye cylinder used in the experiments. An example of the scattering cross section as a function of the fish-eye rod n_{eff} ; the radiation wavelength is considered to be $\lambda = 1.8\text{ cm}$ (a). The variation of the fish-eye rod n_{eff} as a function of the wavelengths interval used in the experiment (b). TM is the considered polarization. The scattering cross section calculated for $\lambda = 3\text{ cm}$ and TE polarization (c).

measurements with the TM polarized radiation. The calculations are done for a wavelength $\lambda = 1.8$ cm and serve only as an example in order to show how one can estimate if the fish-eye rod behaves as a NIM. One can see that indeed there is a strong decay in the scattering cross section at the $n_{eff} = -1.46$. A complete analysis over a wavelength interval is shown in Fig. 7.38b. It can be seen that all n_{eff} are predominantly positive except for the interval $\lambda \in (1.8; 2.1)$ where $n_{eff} < 0$. That is the interval where the slab consisting of the fish-eye cylinders is expected to focus the radiation. Similarly, the scattering cross section is calculated for the TE polarization, shown in Fig. 7.38c. It can be seen that by contrast to the TM polarization the minimum is less well defined. This makes the assessment of the exact rod's n_{eff} relatively difficult. As it is further shown, also the focusing effect is much weaker defined for this polarization.

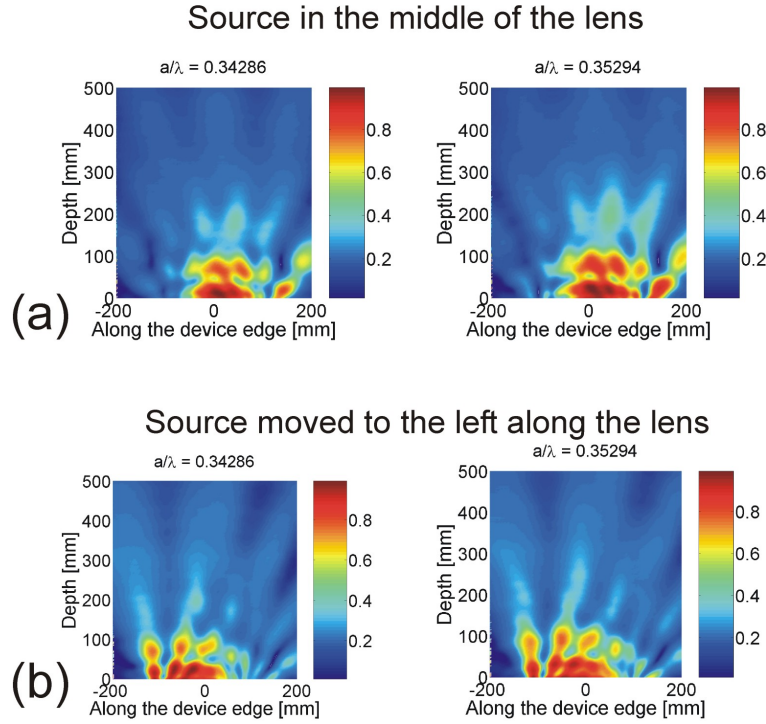


Figure 7.39: *The focusing effect for the TE polarization. The EM field scanned behind the lens for the case when the source is placed in the middle of the lens (a) and when the source is shifted to the left with 50mm (b).*

Figure 7.39 shows the focusing effect for the TE polarization; only the wavelengths (two of them) where this is best observed are shown. One can see the somewhat smashed focusing spot which is followed by the characteristic concentric rings, Fig. 7.39a. The estimated width of the focal spots is $W_{TE}^{a/\lambda=0.34} \approx 7\text{cm} \approx 2\lambda$ and $W_{TE}^{a/\lambda=0.35} \approx 8\text{cm} \approx 2.35\lambda$. In both cases the area of the focal spot is much bigger than the λ^2 which indicates that the fish-eye lens does not possess the feature of superresolution focusing for the TE polarization. Nevertheless the

focusing due to the negative refraction is clearly seen. Indeed, also after moving the radiation source the imaging point will follow it perfectly, Fig. 7.39b. The source in this case is moved with 5 cm from the middle of the lens which is mirrored in the shift of the image point. Hence, the lens as expected, misses the optical axis and is able to perform imaging. One can see that after being moved, the image point becomes even less defined. This is clearly an effect arising from the lens boundary.

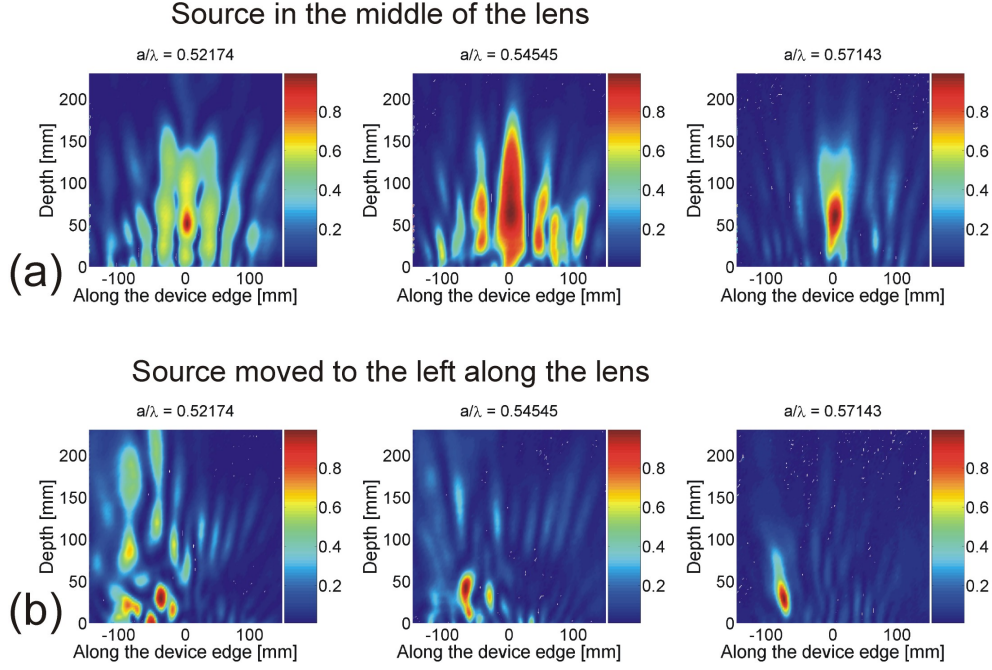


Figure 7.40: *The focusing effect for the TM polarization. The EM field scanned behind the lens for the case when the source is placed in the middle of the lens (a) and when the source is shifted to the left with 70mm (b).*

The focusing effect is tested for the TM polarization as well. From Fig. 7.38b the expected interval where a *single fish-eye rod* behaves as a NIM can be seen. The corresponding wavelength interval translated into the inverse of the wavelength (normalized through the lattice constant of the cylinders assembly will be: $\frac{a}{\lambda} \in (0.57; 0.67)$). Figure 7.40a shows the focusing for the TM polarization. Those wavelengths are selected where the effect is best observed. One can see that for $\frac{a}{\lambda} = 0.57$ there is a very good defined focal spot. As the wavelength increases the focal spot becomes very large, $\frac{a}{\lambda} = 0.55$, but will reach again a better defined shape for shorter wavelengths, $\frac{a}{\lambda} = 0.52$. From the experimental results (not all shown here) the wavelength interval where the slab focuses is $\frac{a}{\lambda} \in (0.52; 0.63)$ which shows a systematic deviation, with $\frac{a}{\lambda} \approx 0.05$ cm, from the theoretically predicted one.

From the measurements in Fig. 7.40a one can estimate the width of the focal spot. The following magnitudes are found: $W_{TM}^{a/\lambda=0.52} \approx 0.6\text{cm} \approx 0.23\lambda$, $W_{TM}^{a/\lambda=0.55} \approx 1.7\text{cm} \approx 0.8\lambda$ and

$W_{TM}^{a/\lambda=0.57} \approx 1.3\text{cm} \approx 0.6\lambda$. As the numbers show there is a clearly defined superresolution effect for the TM polarization. Figure 7.40b shows the results for the case when the radiation source is shifted to the left by 7.5 cm. As one can see, the image point is also shifted by the same magnitude. For the case of $\frac{a}{\lambda} = 0.52$, however, the focus becomes distorted. Since this point belongs to the longer wavelengths the most probable reasons for that are the effects related to the boundaries of the lens. For shorter wavelengths, the image perfectly follows the source. Hence, the slab based on the fish-eye rods can do imaging for the TM polarization as well. Even with the naked eye, one can observe that the superresolution effect is further preserved. For all three cases shown here, by shifting the source, the lateral width of the focus becomes smaller as compared to the case with the source in the middle.

7.4.3 Discussion

Besides the heuristic concept of the fish-eye cylinder shown in Fig. 7.32, the next, not so straightforward step, in the construction of the NIM slab was considering that if having a NIM cylinder as a building block then filling some volume with such cylinders will behave as a NIM too. In what follows it is shown that, in some restrictive sense, this approach is generally valid and that an assembly of such cylinders could indeed be considered as NIM.

Assume the existence of a certain mixture of materials with $n = 1$ (i.e. $\epsilon = 1$ and $\mu = 1$) and $n = -1$ (i.e. $\epsilon = -1$ and $\mu = -1$). Maxwell equations, Eq. 3.2, will describe the propagation of a wave with a frequency ω through such a medium. If the magnetic component from Eqs. 3.2 is excluded then they can be condensed in:

$$\omega^2 \epsilon(r) E(r) + \text{rot} \left(\frac{\text{rot}(E(r))}{\mu(r)} \right) = 0 \quad (7.9)$$

Rearranging the second term in the above equation it follows:

$$\omega^2 \epsilon(r) \mu(r) E(r) - \nabla \left(\frac{1}{\mu(r)} \right) \times \text{rot}(E(r)) + \text{rot} \left(\frac{\text{rot}(E(r))}{\mu(r)} \right) = 0 \quad (7.10)$$

This equation can be transformed such that instead of containing $\epsilon(r)$ and $\mu(r)$ it will contain only $\epsilon(r) \mu(r)$ or $\mu(r)^2$:

$$\omega^2 \epsilon(r) \mu(r) E(r) - \nabla (\mu(r)^2) \times \frac{\text{rot}(E(r))}{2\mu(r)^2} + \text{rot}(\text{rot}(E(r))) = 0 \quad (7.11)$$

It can be expressed in a more convenient form by multiplying with $\mu(r)^2$:

$$\omega^2 \epsilon(r) \mu(r)^3 E(r) - \nabla (\mu(r)^2) \times \frac{\text{rot}(E(r))}{2} + \mu(r)^2 \text{rot}(\text{rot}(E(r))) = 0 \quad (7.12)$$

The same can be done for the magnetic field:

$$\omega^2 \epsilon(r)^3 \mu(r) H(r) - \nabla (\epsilon(r)^2) \times \frac{\text{rot}(H(r))}{2} + \epsilon(r)^2 \text{rot}(\text{rot}(H(r))) = 0 \quad (7.13)$$

Since $\epsilon(r)^3 \mu(r) = \mu(r)^2 = \epsilon(r)^2 = 1$ the dispersion spectra is given by:

$$\begin{aligned} \omega^2 E(r) + \text{rot}(\text{rot}(E(r))) &= 0 \\ \omega^2 H(r) + \text{rot}(\text{rot}(H(r))) &= 0 \end{aligned} \quad (7.14)$$

As it follows from the Eqs. 7.14 the PBS will be similar for a medium with $n = 1$ or $n = -1$. As to what a mixture of materials with $n = 1$ and $n = -1$ is concerned, according to the Eqs. 7.14, it will indeed behave as a homogeneous material with either of the indexes. Further in order to decide upon the exact sign of n one needs some deeper analysis. It is however obvious from these theoretical considerations that this type of "homogenisation" works, but strictly only for mixtures of materials with $n = 1$ and $n = -1$. This validates the initial approach assuming that once a cylinder has a $n_{eff} = -1$ then filling a volume with such cylinders will generate a new homogeneous material with $n = \pm 1$. For the fish-eye NIM experimentally studied here this is valid only for the wavelengths close to 1.8 cm where the fish-eye cylinder has a $n_{eff} \approx -1$.

In Fig. 7.38b can be seen that the n_{eff} of the rod reaches values even smaller than -1. For the considerations discussed above this clearly restricts their applicability. It remains thus unclear what are the effects leading to the NIM behavior. In order to answer this question more generally, the analysis continues with treating the cylinder assembly as a PC and applying the whole know-how related with this theoretical concept. Indeed, this is a reasonable step since the cylinders are arranged in a perfectly triangular lattice for which the PBS can be easily calculated. The inherent spectra calculated for the TM polarization (TE polarization is not further considered due to poor functionality of the fish-eye lens) is shown in Fig. 7.41a

The red lines indicate the light lines for $n = -1$ and their intersection with the PBS show the frequencies where the NIM effect of the PC is expected to occur [73, 205]. The intersection points serve only as a reference since a full answer whether the PC behaves as a homogeneous NIM can be given only after analyzing the EFS too. This will not be done here since the measurements indicate clearly those wavelengths where the NIM effect is present.

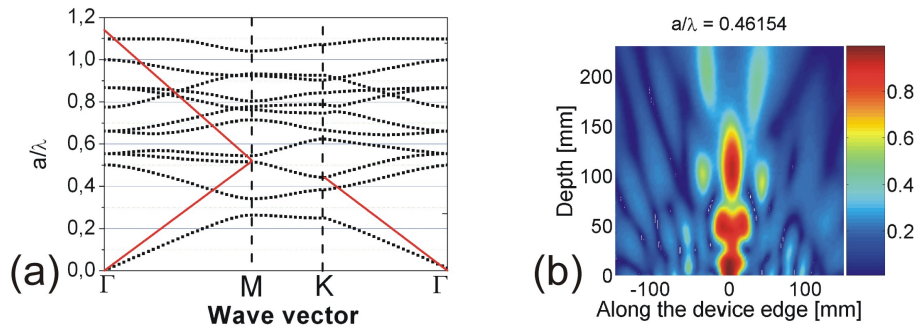


Figure 7.41: The PBS for the PC consisting of fish eye rods for the geometry shown in Fig. 7.37. Calculations are done for the TM polarization (a). The EM distribution for the fish-eye slab for $\frac{a}{\lambda} = 0.46$ (b).

From the PBS follows that the NIM effect can be observed at such wavelengths as e.g. $\frac{a}{\lambda} = 0.52$. This is the wavelength for which according to the calculations, the n_{eff} for a single rod is ≈ -1 . Thus it shows that the NIM effect in this case may be defined by the rod nature as well as by the PC effect. Another wavelength obtained at the intersection of the light line with the PBS is $\frac{a}{\lambda} = 0.46$. Note that exactly for this wavelength the fish-eye cylinder has a $n_{eff} \approx 2$, i.e. positive and no focusing would be expected. Figure 7.41b shows, however, a clear focusing effect. In this case the phenomena is already a result of the cylinders collective interaction rather than the nature of each separate rod [168]. Note that this is a very interesting and somewhat counterintuitive since the wavelength is rather long and at the first glance the n_{eff} of the filled volume would rather be determined by the n_{eff} of the single rods which is, however, not the case. For this wavelength the PC features become predominant even for longer wavelengths.

The both cases are enough to conclude that the NIM nature of the slab with fish-eye cylinders is a mixed effect of the individual cylinders features as well as the PC they do form. Obviously a clear separation between these two effects is a complex task and needs very elevated calculations involving complicated and not yet enough consistent physical models. The NIM effect is not observed for all intersection points of the light line with the PBS. From the Fig. 7.38b the fish-eye rod would exhibit $n_{eff} \approx -1$ in a very narrow wavelength interval. As far as the long range wavelengths are concerned, this might be a plausible explanation why at these wavelengths no clear focusing feature is observed. However, for some shorter wavelengths, due to the PC effects, further NIM effects may be observed, unfortunately not measured here due to the hardware limitations.

Finally, one has two methods to assess the wavelengths interval where the slab behaves as a NIM: the PBS and the n_{eff} for each individual rod. The first seems to be more consistent however its predictive power becomes very weak if no EFS are constructed. Furthermore, the

reference wavelengths on the PBS are given either by the be light lines which, for the sake of completeness, have to be constructed for other negative indexes too. In order to assess those additional indexes, which for the long wavelengths are mainly determined by the fish-eye rod, the calculations in Fig. 7.38b serve as a very helpful tool. However, for more precise statements, such calculations still miss the effects originating from the interaction among the cylinders. This could be the reason for a constant offset of $\frac{a}{\lambda} = 0.05$ cm between the predicated wavelengths interval in Fig. 7.38b and the one experimentally found. That is why a combination between both of them serve as a good hint where the wavelengths of interest are located and the experimental results shown here perfectly prove this approach.

One can also see that the NIM effect is mainly dominating for the TM polarization, i.e. where the \vec{E} field is parallel to the cylinders axes. This is generally expected since for the TM polarization, according to the Maxwell equations boundary conditions, the perpendicular \vec{E} field component at the cylinder's interface has to be conserved and hence its intensity is not decaying. Since the fish-eye rods are not magnetically active materials, the \vec{H} field suffers no change too. This is however not the case for the TE polarization, where the \vec{E} field is strongly decaying inside the cylinders which leads to an overall much weaker transmission and interaction with and among the cylinders and hence less impregnated effects. Nevertheless, theoretically NIM features are allowed for the TE polarization as well [177] and in the experiments shown here the focusing effect could be also observed.

One has to mention that the NIM shown here presents a big advantage due to a high degree of freedom in its optimization. Besides the other common parameters as the lattice geometry, the fish-eye NIM features are strongly influenced by additional characteristics of the cylinders as e.g. number of shells, their refractive index (and profile) and thickness. All these strongly influence the n_{eff} of the cylinders and hence of the NIM too. Also note that the structures studied here can be scaled to higher frequencies and the technology for their preparation is generally enough developed. Suffice is to mention that the most straightforward fabrication method is the etching of macropores in Si, discussed in more details in this thesis, with ulterior deposition of different materials on the pores walls. It can be done with the atomic layer deposition, which allows depositing almost any material and of any thickness [206], but also employing the electroplating of metals [207] and polymers [208] in the porous templates.

7.5 Conclusions

Different optical components could be developed based on PCs with unusual index of refraction. The unusual propagation of the Bloch modes inside the PC allowed for the design of

optical devices with a very enticing and diverse functionality. In particular very efficient lenses could be created that exhibited good focusing. Note also, that the IGs shown here are among the best reported in the literature for the optical devices based on the PC.

The unusual index character of the PC enlarged the functionality of the tested lenses. In particular besides the very well defined filtering features of the lenses, such operations as beam splitting could be obtained as well. Note also that the operation of the devices is strongly dependent on the polarization of the incident wave thus even more increasing their selectivity.

For both lenses the best focusing could be observed for the TM polarization, for the TE polarization mainly beam splitting occurred (occasionally focusing could be measured as well, see the square lattice lens). Distortions introduced to the lens lattice, with the aim of their optimization, lead to malfunction of the devices. This is a clear indication that the lattice is needed in order to ensure the good function of the devices and hence the PC effect is the governing one.

An efficient algorithm was proposed allowing to drastically reduce the size of the lenses while keeping their functionality. In particular, for the TM polarization it was achieved to preserve the focusing at almost the same wavelength, with a minor deviation from the regular lens, having a system that consists of only 40 cylinders by contrast to 112 used for the original lens. Note that the size of the proposed lens is in the range of 20 radiation wavelengths. The algorithm still has its limitations. For instance optimizing the focusing might lead to structures that very efficiently focus the radiation, but then do not split the beam any longer. This makes the algorithm suitable only for some class of problems in optical design however there is room for its improvement.

The devices presented here could be described as optically passive elements. It was shown that by changing the structure, i.e. in particular the arrangement of the cylinders, different enticing functionality can be achieved. One could also imagine that instead of alumina, some other optical active materials could be used as constituent materials for the cylinders, which refractive index or absorption properties could be changed as a function of some external parameters, i.e. applied voltage. In this case, the results presented here with the defect type of the lens, could be also practically implemented when some particular cylinders are "changed" in the structure either by reducing their refractive index or making them more absorbing.

The fish-eye approach proposed here helped to design a new generation of NIM. The plane plate lens based on the fish-eye cylinders allows very good focusing and for the TM polarization the imaging features of the device could be well demonstrated. Note also that in the virtue of the fish-eye rod peculiarities the NIM proposed here exhibits the advantage of many degrees of freedom for its design. The number of shells, type of the materials, index profiles are only

a few to mention. Note that a profile for the refractive index inverse to the one proposed here ensures the same functionality of the device. This opens the possibility to design the fish-eye concept by using macoporous Si with subsequent coating of the pores with different materials.

Yet the theory of the PCs used for the design of these devices need more development. Simulations showed that the main reason for the functionality of the devices is the "correct" deformation of the outgoing wave front. The main deficit of this field of optics remains however the ineptitude of solving the bottom-up problem: design of optical devices according to a desired functionality. More research in the direction and understanding of the exact way of wave front deformation might add considerable knowledge to this field and hence generate more applications.

The aim of this chapter is to make the proof of principle for the devices shown here. The results shown in the chapter combined with the formation of the porous Si represent some preliminary work done toward the realization of the optical components shown here through the use of porous semiconductors and composite materials. Since the devices proposed here are some model systems that can be scaled to any frequency range, these type of structures could be implemented as miniature and multifunctional optical devices for higher frequencies. Their fabrication using the Si technology makes them extremely attractive for the next stage of the integrated optics.

8 Summary and Outlook

Modeling and simulations of the Si-HF interface

The work presents a deep and detailed analysis of the electrochemical current and potential oscillations at the Si-HF interface. Calculations and simulations are based on the current burst model (CBM), which allows to calculate all local electrode features, e.g., current, potential, oxide thickness, interface roughness or capacitance as a function of time. The CBM was extended to the simulation of various oscillatory phenomena at the Si-HF interface, observed by others and taken from the literature.

Different kinds of current oscillations could be simulated: damped and stable; forced; and externally synchronized. Apart from a detailed analysis of current oscillations in various modes, potential oscillations could be simulated for the first time, too. Profiting from faster computers and a new implementation mode of the CBM simulation program, each class of oscillations could be modeled for different anodization currents or potentials. As a result one could obtain such characteristics as the oscillation frequency, its decay constant, or the oscillation envelope as a function of the anodization parameters. The results fit very well with the experimentally found data and give additional insight into the dynamics of oscillating electrodes.

A completely new parameter was extracted from the simulations: the correlation length of the growing and dissolving areas on the oxide thickness maps. This means that this work includes for the first time a quantification of this parameter. Additionally, the new simulation results and the possibility to simulate larger electrodes areas changed considerably the concept of a domain and lead to the introduction of new entities.

Despite many results there is still room for improvements of the CBM and suitable implementations in the simulation program. This was extensively discussed in the fifth chapter and here only the key ideas will be summarized:

1. The pH variation on the electrode surface and its impact on the oxide dissolution dynamics;
2. "Introduce" more chemistry, apart from existing SiO_2 dissolution rate and indirectly the oxide quality, in the CB dynamics;

3. The aging effect, i.e. the hydrogen passivation of the bare Si surface. This would allow simulating the Si-HF behavior outside the oscillation regime;
4. Change from the simulation in 2D to 3D, i.e. consider different crystallographic planes;
5. Reduce the computational complexities in order to allow the simulation of much larger areas. A realistic target would be $5 \times 5 \mu\text{m}^2$ (currently the program is limited to $0.3 \times 0.3 \mu\text{m}^2$);
6. When the previous points are implemented, extend the CBM simulation program to the simulation of pore growth.

The last item in the above list, ideally allowing to quantify pore growth, is actually the dream of the engineers dealing with porous semiconductors, but a mighty challenge for the theoreticians. As it was shown in chapter six, where the experimental results on the macropore growth in Si are presented, a lot of unanswered questions still exist. In spite of that, using the input from the CBM and results from a newly introduced *in-situ* characterization technique, i.e. the FFT impedance spectroscopy, much progress has been made toward a better understanding of the macropore growth phenomenology.

Macropore growth in n-Si

While current-voltage impedance spectroscopy is a standard technique in electrochemistry, it was used for the first time *in-situ* during the macropore formation in this work. A completely new mode was introduced with the (backside) photo impedance. Both modes deliver valuable information about the macropore growth process. In particular, the pore quality could be quantified for the first time *in-situ*, especially by extracting the valence of the ongoing process; a valence of 3 was found to describe stable and homogeneous macropore growth. The so-called "inductive" loop (known for long time to be present in the measurements of porous electrodes) was used for the first time for calculating the dissolution valence at the pore tip.

While the general fact that macropore growth in alcohol containing electrolytes is always considerably improved was known in the literature, there was no systematic study on the alcohol type influence on the macropore size and quality. This work provides preliminary studies on the macropores features as a function of alcohol type; this was done for three most common alcohols.

An additional macropore feature intensively investigated in this work is the pore wall roughness. A good understanding of the processes causing the roughness of the pore walls was achieved by testing different electrolytes, covering a large spectrum of possible chemistries variations: pH, oxidation power, etching rate, surface tension. In effect, the pore wall roughness could be reduced from 60 nm down to 8 nm on a $2 \mu\text{m}$ scale. In particular, a new

type of electrolyte showed a high performance, its working details, however, are not yet fully understood.

The next topics that would bear a closer investigation are:

1. Further experiments to check the behavior of the valence dependence on different parameters. This involves direct etching parameters as, e.g.: potential, electrolyte concentration, temperature as well as different pore types, in particular p-macro(org) pores and mesopores;
2. Improve the model for the photo impedance;
3. Apply FFT-IS for a deeper understanding of the roles of alcohols. It is also very interesting to see how the alcohol chain length influences the macropore quality. This is interesting from the application point of view as well as from a purely scientific interest;
4. Apply FFT-IS for a deeper understanding of the role of viscosity;
5. Establish a knowledge database and use FFT-IS for controlling pore etching in-situ (either model-based or by "fuzzy logic").

Fabrication of composite materials

The possibility to fabricate composite materials by electroplating metals into porous templates was tested. The metal investigated was Cu. It was possible to fill macropores with a depth of up to 150 μm . At the first glance the electroplating technology seemed to be easily translated to different pore morphologies, but filling of crystallographically oriented pores in GaAs failed at the beginning. based on this, a model was developed that enabled a better understanding of the filling process. Using the guidelines of the model, fractal-like domains in GaAs could be filled with Cu.

For follow-up topics meriting further investigation one could be mention:

1. Use FFT-IS during the deposition process. Of particular interest is the deposition of metals into p-Si under BSI conditions. Photo impedance data obtained during this process would most likely help to achieve a better understanding of these "nano-galvanics";
2. Deposition of different metals, e.g. Ni, Ag, etc., and use of different semiconductors substrates and pore morphologies.

PCs and applications

As already mentioned in the introductory part, the research related to the fabrication of macroporous n-Si was primary guided by the necessity to etch structures like PCs designated

for spectroscopic gas sensors. Besides work for this concrete application, the topic of PCs was addressed in this thesis from another perspective, too. The unusual index PCs, i.e. $n_{eff} < 1$, were investigated, and optical components with a wide range of functionality based on this class of PCs were designed and tested. Envisioned uses included lenses, filters, beam splitters, antennas, etc.

The performance of the lenses reported here is among the best in comparison to structures of a similar class as reported in the literature. The interesting behavior of the components shown here could only be achieved by addressing PCs with $n_{eff} < 1$, which allow unusual beam propagations inside the structures. A sketch of an optimization algorithm was proposed, too; it might serve as a base for further improvements.

A new type of NIM was proposed and tested. Very good focusing properties of plane plate lenses, based on this material, could be obtained. Besides a good functionality of the lens, the results obtained present also a challenge as theoretical problem. The advantage of the NIM lens proposed here is the large number of degrees of freedom for their fabrication; the number of shells, their refractive index, their seize, are only a few to mention. Finally, the NIM lens as well as all other optical components investigated represent model systems that can be always scaled to higher frequencies.

As potential new research steps for this topic one could mention:

1. Further investigation on the optimization methods for the optical devices. This has to be done with respect to their performance and size;
2. Explore the possibility of using optically active materials for the PCs constituents, i.e. materials that can change their n as a function of some external parameters;
3. Extend the existing theory in order to consider such additional effects as absorption and reflection from the structures;
4. For the NIM materials, different geometries should be tested;
5. All structures shown here are based on 2D PCs design. Their performance has to increase considerably if 3D design would be used. This is also an interesting option to be investigated;
6. Scale down the measured structures and work in the direction of their integration in concrete applications.

Bibliography

- [1] B. Atalay, *Math and the Mona Lisa. The Art and Science of Leonardo da Vinci.*, Smithsonian Books. Collins., 2006.
- [2] M. Faraday, *Phil. Trans. Roy. Soc., Ser. A*, 1834, **124**, 77.
- [3] O. Teschke, F. Galambeck, and M. Tenan, *J. Electrochem. Soc.*, 1985, **132**(6), 1284.
- [4] P. Russell and J. Newman, *J. Electrochem. Soc.*, 1986, **133**(1), 59–69.
- [5] P. Russel and J. Newman, *J. Electrochem. Soc.*, 1987, **134**(5), 1051.
- [6] Z. Fei, R. Kelly, and J. Hudson, *J. Phys. Chem.*, 1996, **100**(49), 18986.
- [7] A. J. Pearlstein, H. Lee, and K. Nobe, *J. Electrochem. Soc.*, 1985, **132**(9), 2159.
- [8] M. Bassett and J. Hudson, *J. Electrochem. Soc.*, 1993, **137**(3), 922.
- [9] M. Bassett and J. Hudson, *J. Electrochem. Soc.*, 1990, **137**(6), 1815.
- [10] W. Li, X. Wang, and K. Nobe, *J. Electrochem. Soc.*, 1990, **137**(4), 1184.
- [11] U. Franck, *Angewandte Chemie*, 1978, **1**, 1.
- [12] W. Jessen, *Naturwissenschaften*, 1978, **65**(9), 449–455.
- [13] U. Franck, *Ber. Bunsenges. Phys. Chem.*, 1980, **84**, 334–341.
- [14] S. Langa, J. Carstensen, I. Tiginyanu, M. Christophersen, and H. Föll, *Electrochem. and Solid State Lett.*, 2001, **4**, 50.
- [15] M. Christophersen, S. Langa, J. Carstensen, P. Fauchet, and H. Föll In *MRS Proceedings Spring Meeting: Invited Paper*, Vol. , 2003.
- [16] C. Fang, H. Föll, and J. Carstensen, *J. Electroanal. Chem.*, 2006, **589**, 259.

- [17] S. Langa, J. Carstensen, M. Christophersen, I. Tiginyanu, and H. Föll, *Phys. Stat. Sol. (a)*, 2003, **197**(1/2).
- [18] J. Carstensen, R. Prange, G. Popkirov, and H. Föll, *Appl. Phys. A*, 1998, **67**, 459.
- [19] A. Uhler, *Bell System Tech. J.*, 1956, **35**, 333.
- [20] V. Lehmann, *Electrochemistry of Silicon*, Wiley-VCH, Weinheim, 2002.
- [21] L. Canham, A. Nassiopoulou, and V. P. (Eds.), *Phys. Stat. Sol. (a)*, 2005, **202**(8).
- [22] K. Busch, S. Lölkes, R. Wehrspohn, and H. F. (Eds.), in *Photonic Crystals: Advances in Design, Fabrication, and Characterization*, Wiley-VCH Verlag GmbH & Co. KGaA, Weinheim, 2004.
- [23] J. Knight, T. Birks, P. Russell, and D. Atkin, *Opt. Lett.*, 1997, **21**, 1547.
- [24] T. Geppert, S. Schweizer, J. Schilling, C. Jamois, R. Wehrspohn, A. v. Rhein, D. Pergande, S. Schweizer, R. Wehrspohn, R. Glatthaar, P. Hahn, A. Feisst, and A. Lambrecht In *Proc. of the SPIE 5511*, p. 61, 2004.
- [25] O. Painter, R. Lee, A. Scherer, A. Yariv, J. O'Brien, P. Dapkus, and I. Kim, *Science*, **284**(5421).
- [26] V. Lehmann and H. Föll, *J. Electrochem. Soc.*, 1990, **137**, 653.
- [27] A. Bard and L. Faulkner, *Electrochemical Methods*, John Wiley & Sons, New York, 1980.
- [28] S. Frey *Novel formation regimes and mechanisms for macropores and porous anodic oxides in silicon* Phd thesis, University of Kiel, 2005.
- [29] K. Kolasinski, *Phys. Chem. Chem. Phys.*, 2003, **5**, 1270–1278.
- [30] J. Chazalviel and F. Ozanam, *J. Appl. Phys.*, 1997, **81**, 7684–7686.
- [31] E. Probst and P. Kohl, *J. Electrochem. Soc.*, 1994, **141**, 1006–1013.
- [32] V. Lehmann, *J. Electrochem. Soc.*, 1993, **140**, 2836.
- [33] V. Lehmann and S. Rönnebeck, *J. Electrochem. Soc.*, 1999, **146**, 2968.
- [34] D. Turner, *J. Electrochem. Soc.*, 1958, **105**, 402.
- [35] H. Gerischer and M. Lübke, *Ber. Bunsenges. Phys. Chem.*, 1988, **92**, 573.

- [36] J.-N. Chazalviel and F. Ozanam, *J. Electrochem. Soc.*, 1992, **139**, 2501.
- [37] A. Zhabotinsky, *Biofizika*, 1964, **9**, 306.
- [38] H. Föll, *Appl. Phys. A*, 1991, **53**, 8.
- [39] M. Eddowes, *J. Electroanal. Chem.*, 1990, **280**(2), 297.
- [40] R. Smith and S. Collins, *J. Appl. Phys.*, 1992, **71**.
- [41] J.-N. Chazalviel and F. Ozanam, *Ber. Bunsenges. Phys. Chem.*, 1992, **96**(12), 1809.
- [42] F. Ozanam, J.-N. Chazalviel, A. Radi, and M. Etman, *J. Electrochem. Soc.*, 1992, **139**, 2491.
- [43] F. Ozanam, J.-N. Chazalviel, A. Radi, and M. Etman, *Ber. Bunsenges. Phys. Chem.*, 1991, **95**, 98.
- [44] F. Ozanam, N. Blanchard, and J.-N. Chazalviel, *Electrochem. Acta*, 1993, **38**, 1627.
- [45] H.-J. Lewerenz and M. Aggour, *J. Electroanal. Chem.*, 1993, **351**, 159.
- [46] J. Grzanna, H. Jungblut, and H. Lewerenz, *J. Electroanal. Chem.*, 2000, **486**, 181.
- [47] J. Grzanna, H. Jungblut, and H. Lewerenz, *J. Electroanal. Chem.*, 2000, **486**, 190.
- [48] J. Grzanna, H. Jungblut, and H. Lewerenz, *Phys. Stat. Sol.*, 2006, p. in press.
- [49] V. Lehmann, *J. Electrochem. Soc.*, 1996, **143**(4), 1313.
- [50] V. Parkhutik and E. Matveeva, *Electrochem. Sol. State Lett.*, 1999, **2**, 371.
- [51] V. Parkhutik, *Mat. Sc. Eng.*, 2002, pp. 269–276.
- [52] H. Föll, J. Carstensen, M. Christophersen, and G. Hasse, *Phys. Stat. Sol. (a)*, 2000, **182**(1), 7.
- [53] S. Langa, I. Tiginyanu, J. Carstensen, M. Christophersen, and H. Föll, *Appl. Phys. Lett.*, 2003, **82**(2), 278.
- [54] J. Wloka, K. Müller, and P. Schmuki, *Electrochem. Sol. State Lett.*, 2006, **8**(12).
- [55] J. Carstensen, R. Prange, and H. Föll, *J. Electrochem. Soc.*, 1999, **146**, 1134.
- [56] S. Frey, B. Grésillion, F. Ozanam, J.-N. Chazalviel, J. Carstensen, H. Föll, and R. Wehrspohn, *Electrochem. Sol. State Lett.*, 2005, **8**, B25.

- [57] D. Dumin, *J. Electrochem. Soc.*, 1995, **142**(4), 1272.
- [58] W. Weibull In *Swedish Royal Institute Engineering Research Proceedings: A statistical theory of the strength of materials.*, pp. Stockholm, Sweden, 1939.
- [59] K. Krischer and H. Varela, in: *Handbook of Fuel Cells*, ed. by W. Vielstich, A. Lamm and H. Gasteiger, John Wiley & Sons, Ltd, 2003, **2**(6), 679.
- [60] O. Nast, S. Rauscher, H. Jungblut, and H.-J. Lewerenz, *J. Electroanal. Chem.*, 1998, **442**, 169.
- [61] S. Böhm, L. Peter, G. Schlichthörl, and R. Greef, *J. Electroanal. Chem.*, 2001, **500**, 178.
- [62] J. Carstensen, R. Prange, and H. Föll In *Proc. ECS 193rd Meeting, San Diego*, number 10, p. 148, 1998.
- [63] A. Birner, R. Wehrspohn, F. Müller, U. Gösele, and K. Busch, *Adv. Mat.*, 2001, **13**, 377.
- [64] V. Kochergin, *Omnidirectional Optical Filters*, Kluwer Academic Publishers, Boston, 2003.
- [65] V. Lehmann, *Nat. Mat.*, 2002, **1**, 12.
- [66] E. Ponomarev and C. Lévy-Clément, *J. Electrochem. Soc. Lett.*, 1998, **1**, 1002.
- [67] R. Wehrspohn, J.-N. Chazalviel, and F. Ozanam, *J. Electrochem. Soc.*, 1998, **145**, 2958.
- [68] M. H. A. Rifai, M. Christophersen, S. Ottow, J. Carstensen, and H. Föll, *J. of Porous Materials*, 2000, **7** (1/2/3), 33.
- [69] X. Zhang, *Electrochemistry of silicon and its oxide*, Kluwer Academic - Plenum Publishers, New York, 2001.
- [70] C. Jäger, C. Dieker, W. Jäger, M. Christophersen, J. Carstensen, and H. Föll Vol. **164**, p. 507, 1999.
- [71] J. Carstensen, M. Christophersen, G. Hasse, and H. Föll, *Phys. Stat. Sol. (a)*, 2000, **182**(1), 63.
- [72] P. Belov, C. Simovski, and S. Tretyakov, *Phys. Rev. E*, 2002, **66**, 036610.
- [73] M. Notomi, *Phys. Rev. B*, 2000, **62**, 10696.
- [74] P. Halevi, A. Krokhin, and J. Arriaga, *Phys. Rev. Lett.*, 1999, **82**(4), 719.

- [75] E. Hecht, *Optics*, Addison Wesley Longman, Reading, 1998.
- [76] J. Joannopoulos, R. Meade, and J. Winn, *Photonic Crystals: Molding the Flow of Light*, Princeton University Press, Princeton, 1995.
- [77] U. Grüning, V. Lehmann, and C. Engelhardt, *Appl. Phys. Lett.*, 1995, **66**(24), 3254.
- [78] P. Atkins and J. Paula, *Physical chemistry, 7th*, Oxford University Press, New York, 2002.
- [79] D. Miller, J. Rard, L. Eppstein, and R. Robinson, *J. Solution Chem.*, 1980, **9**(7), 467.
- [80] H. Okorn-Schmidt, *IBM J. Res. Develop.*, 1999, **43**(3), 351.
- [81] J. MacDonald, *Impedance spectroscopy*, John Wiley & Sons, 1987.
- [82] E. Foca, J. Carstensen, and H. Föll, *Phys. Stat. Sol. (a)*, 2005, **74**(8), 1524.
- [83] C. Serre, S. Barret, and R. Herino, *J. Electrochem. Soc.*, 1994, **141**, 8.
- [84] G. Hasse *Untersuchungen der kinetischen Prozesse an Silizium-Elektroden mit Stromtransienten- und Impedanzmessungen* Dissertation, Universität Kiel, 2005.
- [85] J.-N. Chazalviel, F. Ozanam, M. Etman, F. Paolucci, L. Peter, and J. Stumper, *J. Electroanal. Chem.*, 1992, **327**, 343.
- [86] M. Christophersen, J. Carstensen, A. Feuerhake, and H. Föll, *Mater. Sci. Eng. B*, 2000, **69-70**, 194.
- [87] K. Krischer, in *Modern Aspects of Electrochemistry*, ed. by B.E. Conway, J.o'M. Bockris and R.E. White. New York: Plenum Press, 1999, **32**, 1.
- [88] H. Föll, M. Christophersen, J. Carstensen, and G. Hasse, *Mat. Sci. Eng. R*, 2002, **39**(4), 93.
- [89] V. Parkhutik, *Electrochimica Acta*, 1991, **36**(10), 1611.
- [90] R. Prange *Elektrochemische Charakterisierung und Modellierung langsamer Strom- und Spannungszillationen am Silizium-Flüssäure-System* Dissertation, Universität Kiel, 1998.
- [91] H. Föll, J. Carstensen, and E. Foca, *Int. J. Mat. Res.*, 2006, **2006**(7).

- [92] S. Frey, S. Keipert, J.-N. Chazalviel, F. Ozanam, J. Carstensen, and H. Föll, *Phys. Stat. Sol. (c)*, 2006, p. in press.
- [93] S. Langa, M. Christophersen, J. Carstensen, I. Tiginyanu, and H. Föll, *Phys. Stat. Sol. (a)*, 2003, **197**(1/2), 77.
- [94] J. Wloka, D. Lockwood, and P. Schmuki, *Chem. Phys. Lett.*, 2005, **414**, 47.
- [95] E. Foca, J. Carstensen, and H. Föll, *Phys. Stat. Sol. (c)*, 2006.
- [96] D. AG, I. AG, and BMBF, *Photonic Crystals for gas sensing applications (PHOKISS Research Project)*, 2003.
- [97] T. Geppert *Towards Photonic Crystals-Based Spectroscopic Gas Sensors* Phd thesis, Martin-Luther-Universitaet Halle-Wittenberg, 2006.
- [98] E. Foca, J. Carstensen, G. Popkirov, and H. Föll, *Phys. Stat. Sol. (a)*, 2007, **204**(5), 1378–1382.
- [99] M. Keddam, O. Mattos, and H. Takenouti, *J. Electrochem. Soc.*, 1981, **128**(2), 257–266.
- [100] M. Keddam, O. Mattos, and H. Takenouti, *J. Electrochem. Soc.*, 1981, **128**(2), 266–274.
- [101] O. Barcia, O. Mattos, N. Pebere, and B. Tribollet, *J. Electrochem. Soc.*, 1993, **140**(10), 2825–2832.
- [102] J. Diard, J. L. Canut, B. L. Gorrec, and C. Montella, *Electrochim. Acta*, 1998, **43**(16-17), 2485–2501.
- [103] P. Searson and X. Zhang, *J. Electrochem. Soc.*, 1990, **137**, 2539.
- [104] P. Searson and X. Zhang, *Electrochim. Acta*, 1991, **36**(3/4), 499.
- [105] I. Raistrick, *Electrochim. Acta*, 1990, **35**(10), 1579.
- [106] J. Fleig and J. Maier, *Solid State Ionics*, 1997, **94**, 199.
- [107] H.-K. Song, Y.-H. Jung, K.-H. Lee, and L. Dao, *Electrochim. Acta*, 1999, **44**, 3513.
- [108] O. Barcia, E. D’Elia, I. Frateur, O. Mattos, N. Pebere, and B. Tribollet, *Electrochim. Acta*, 2002, **47**, 2109.
- [109] H.-K. Song, J.-H. Sung, Y.-H. Jung, K.-H. Lee, L. Dao, M.-H. Kim, and H.-N. Kim, *J. Electrochem. Soc.*, 2004, **151**.

- [110] A. Lasia, *J. Electroanal. Chem.*, 1997, **428**, 155.
- [111] A. Lasia, *J. Electroanal. Chem.*, 2001, **500**, 30.
- [112] D. Vanmaekelbergh and P. Searson, *J. Electrochem. Soc.*, 1994, **141**, 697.
- [113] H. Lewerenz, J. Stumper, and L. Peter, *Phys. Rev. Lett.*, 1988, **61**(17), 1989–1992.
- [114] S. Rönnebeck, J. Carstensen, S. Ottow, and H. Föll, *Electrochem. Sol. State Lett.*, 1999, **2**, 126.
- [115] S. Rönnebeck, S. Ottow, J. Carstensen, and H. Föll, *Journal of Porous Materials*, 2000, **7**, 353.
- [116] X. Zhang, S. Collins, and R. Smith, *J. Electrochem. Soc.*, 1989, **136**, 1561.
- [117] X. Zhang, *J. Electrochem. Soc.*, 1991, **138**, 3750.
- [118] V. Lehmann and U. Gösele, *Mat. Res. Soc. Symp. Proc.*, 1993, **283**, 27.
- [119] J.-N. Chazalviel, *Electrochim. Acta*, 1990, **35**, 1545–1552.
- [120] S. Schweizer, R. Wehrspohn, and J. Schilling, *203rd meeting of the Electrochem. Soc., Paris*, 2003, p. Abstract 2747.
- [121] S. Cattarin and M. Musiani, *J. Phys. Chem. B*, 2006, **110**, 2451–2457.
- [122] C. Lee, J. Baek, H. Yoo, and S. Woo, *J. Electrochem. Soc.*, **143**.
- [123] M. Leisner, J. Carstensen, and H. Föll, *J. Electroanal. Chem.*, 2007.
- [124] D.-H. Eom, K.-S. Kim, and J.-G. Park, *Jap. J. Appl. Phys: Part 1*, 2002, **41**, 5881–5886.
- [125] H. Katayama and K. Kitagawa, *J. Chem. Eng. Data*, 2006, **51**, 2103.
- [126] M. Christophersen, J. Carstensen, S. Rönnebeck, C. Jäger, W. Jäger, and H. Föll, *J. Electrochem. Soc.*, 2001, **148**.
- [127] S. Frey, M. Kemell, J. Carstensen, S. Langa, and H. Föll, *Phys. Stat. Sol. (a)*, 2005, **202**, 1369.
- [128] R. Beranek, H. Hildebrand, and P. Schmuki, *Electrochem. Sol. State Lett.*, 2003, **6**.
- [129] H. Tsuchiya, J. Macak, L. Taveira, and P. Schmuki, *Chem. Phys. Lett.*, 2005, **410**, 188.

- [130] J. Macak, H. Tsuchiya, L. Taveira, S. Aldabergerova, and P. Schmuki, *Angew. Chem.*, 2005, **44**, 7463–7465.
- [131] P. Bandaru and E. Yablonovitch, *J. Electrochem. Soc.*, 2002, **149**, 599.
- [132] F. Farid, K. Kamada, T. Kobayashi, T. Sakka, and Y. Ogata, *J. Electrochem. Soc.*, 2005, **152**(4).
- [133] K. Rajeshwar, N. Tacconi, and C. Chenthamarakshan, *Chem. Mater.*, 2001, **13**, 2765.
- [134] R. Sherman-Jr. and W. Ford, *Langmuir*, 2005, **21**, 5218.
- [135] R. Sinnenfeld and B. Schardt, *Appl. Phys. Lett.*, 1986, **49**(18), 1172.
- [136] O. Magnussen, J. Hotlos, R. Nichols, D. Kolb, and R. Behm, *Phys. Rev. Lett.*, 1990, **64**(24), 2929.
- [137] X. Gao, A. Hamelin, and M. Weaver, *Phys. Rev. Lett.*, 1991, **67**(5), 618.
- [138] O. Chyan, J.-J. Chen, H. Chien, J. Sees, and L. Hall, *J. Electrochem. Soc.*, 1996, **143**(1), 92.
- [139] G. Oskam, J. Long, A. Natarajan, and P. Searson, *J. Phys. D: Appl. Phys.*, 1998, **31**, 1927.
- [140] G. Oskam, P. Vereecken, and P. Searson, *J. Electrochem. Soc.*, 1999, **146**(4), 1436.
- [141] P. Hoffmann, A. Radisic, and P. Searson, *J. Electrochem. Soc.*, 2000, **147**(7), 2576.
- [142] D. Edelstein, J. Heidenreich, R. Goldblatt, W. Cote, C. Uzoh, N. Lustig, P. Roper, T. McDevitt, W. Motsiff, A. Simon, J. Dukovic, R. Wachnik, H. Rathore, R. Schulz, L. Su, S. Luce, and J. Slattery, *Technical Digest, IEEE International Electron Devices Meeting*, 1997, p. 773.
- [143] A. West, *J. Electrochem. Soc.*, 2000, **147**(1), 227.
- [144] T. Pricer, M. Kushner, and R. Alkire, *J. Electrochem. Soc.*, 2002, **149**(8).
- [145] A. Frank and A. Bard, *J. Electrochem. Soc.*, 2003, **150**(4).
- [146] D. Hamm, T. Sakka, and Y. Ogata, *Phys. Stat. Sol. (c)*, 2005, **2**(9), 3334.
- [147] P. Vereecken, R. Binstead, H. Deligianni, and P. Andricacos, *IBM J. Res. Dev.*, 2005, **49**(1), 3.

- [148] S. Kim and J. Kim, *Electrochem. and Sol. State Lett.*, 2004, **7**(9).
- [149] A. Dikumar, P. Globa, O. Redcozubova, S. Sidelnikova, L. Sirbu, V. Vieru, and I. Tiginyanu, *Electrochem. Sol. State Lett.*, 2005, **8**(3).
- [150] Y. Harada, X. Li, P. Bohn, and R. Nuzzo, *J. Am. Chem. Soc.*, 2001, **123**, 8709.
- [151] P. Gorostiza, P. Allongue, R. Diaz, J. Morante, and F. Sanz, *J. Phys. Chem. B*, 2003, **107**, 6454.
- [152] L. Porter, Jr., H. Choi, A. Ribbe, and J. Buriak, *Nano. Lett.*, 2002, **2**(10), 1067.
- [153] F. Farid, K. Kamada, J. Sasano, S. Izuo, T. Sakka, and Y. Ogata, *Phys. Stat. Sol. (a)*, 2005, **202**(8), 1683.
- [154] K. Kobayashi, F. Harraz, S. Izuo, T. Sakka, and Y. Ogata, *J. Electrochem. Soc.*, 2006, **153**(4).
- [155] S. Matthias, J. Schilling, K. Nielsch, F. Müller, R. Wehrspohn, and U. Gösele, *Adv. Mater.*, 2002, **14**(22), 1618.
- [156] H. Sato, T. Homma, K. Mori, T. Osaka, and S. Shoji, *Electrochemistry*, 2005, **73**(4), 275–278.
- [157] S. Nicewarner-Pena, R. Freeman, B. Reiss, L. He, D. Pena, I. Walton, R. Cromer, C. Keating, and M. Natan, *Science*, 2001, **294**, 137.
- [158] M.-L. Tian, J.-G. Wang, J. Kurtz, T. Mallouk, and M. Chan, *Nano. Lett.*, 2003, **3**(7), 919.
- [159] M. Molares, V. Buschmann, D. Dobrev, R. Neumann, R. Scholz, I. Schuchert, and J. Vetter, *Adv. Mater.*, 2001, **13**(1), 62.
- [160] S. Langa, J. Carstensen, M. Christophersen, H. Föll, and I. Tiginyanu, *Appl. Phys. Lett.*, 2001, **78**, 1074.
- [161] G. Sauer, G. Brehm, S. Schneider, K. Nielsch, R. Wehrspohn, J. Choi, H. Hofmeister, and U. Goesele, *J. Appl. Phys.*, 2002, **91**(5), 3243–3247.
- [162] C. Fang, E. Foca, L. Sirbu, J. Carstensen, I. Tiginyanu, and H. Föll, *Phys. Stat. Sol. (a)*, 2007, **204**(5), 1388–1393.
- [163] M. Zach, K. Ng, and R. Penner, *Science*, 2000, **290**, 2120.

- [164] F. Harraz, K. Kamada, J. Sasano, S. Izuo, T. Sakka, and Y. Ogata, *Phys. Stat. Sol. (a)*, 2005, **202**(8), 1683.
- [165] L.-M. Li and Z.-Q. Zhang, *Phys. Rev. B*, 1998, **58**, 9587.
- [166] E. Foca, H. Föll, F. Daschner, V. Sergentu, J. Carstensen, S. Frey, R. Knöchel, and I. Tiginyanu, *Phys. Stat. Sol. (a)*, 2005, **202**(4), R 35.
- [167] E. Foca, H. Föll, F. Daschner, V. Sergentu, J. Carstensen, R. Knöchel, and I. Tiginyanu In ed. J. Theil, M. Böhm, D. Gardner, and T. Blalock, *Materials, Integration and Technology for Monolithic Instruments*, p. D4.4, Warrendale, PA, 2005. Mater. Res. Soc. Symp. Proc. 869.
- [168] P. Parimi, W. Lu, P. Vodo, and S. Sridhar, *Nature*, 2003, **426**, 404.
- [169] B. C. Gupta and Z. Ye, *Phys. Rev. B*, 2003, **67**, 153109.
- [170] E. Cucukcu, K. Aydin, E. Özbay, S. Foteinopoulou, and C. Soukoulis, *Nature*, 2003, **426**, 604.
- [171] X. Hu and C. Chan, *Appl. Phys. Lett.*, 2004, **85**(9), 1520.
- [172] A. Martinez, H. Miguez, A. Griol, and J. Marti, *Phys. Rev. B*, 2004, **69**, 165119.
- [173] P. Parimi, W. Lu, P. Vodo, J. Sokoloff, J. Derov, and S. Sridhar, *Phys. Rev. Lett.*, 2004, **92**(12), 127401-1.
- [174] P. Vodo, P. Parimi, W. Lu, S. Sridhar, and R. Wing, *Appl. Phys. Lett.*, 2004, **85**(10), 1858.
- [175] P. Vodo, P. Parimi, W. Lu, and S. Sridhar, *Appl. Phys. Lett.*, 2005, **86**, 201108-1.
- [176] Z. Lu, C. Chen, C. A. S. amd Shouyua Shi, J. A. Murakowski, G. J. Schneider, and D. W. Prather, *Applied Physics Letters*, 2005, **87**, 091907.
- [177] C. Luo, S. Johnson, J. Joannopoulos, and J. Pendry, *Phys. Rev. B*, 2002, **65**, 201104(R).
- [178] C. Luo, S. G. Johnson, J. Joannopoulos, and J. Pendry, *Phys. Rev. B*, 2003, **68**, 045115-1.
- [179] Z.-Y. Li and L.-L. Lin, *Phys. Rev. B*, 2003, **68**, 245110-1.
- [180] H.-T. Chien, H.-T. Tang, C.-H. Kuo, C.-C. Chen, and Z. Ye, *Physical Review B*, 2004, **70**, 113101.

- [181] X. Wang, Z. Ren, and K. Kempa, *Appl. Phys. Lett.*, 2005, **86**, 061105–1.
- [182] S. Feng, Z.-Y. Li, Z.-F. Feng, B.-Y. Cheng, and D.-Z. Zhang, *Applied Physics Letters*, 2006, **88**, 031104.
- [183] R. York and Z. P. Eds., *Active and quasi-optical arrays for solid-state power combining*, Wiley-VCH, Weinheim, 1997.
- [184] B. Schwartz and R. Piestun, *Appl. Phys. Lett.*, 2004, **85**(1), 1.
- [185] A. Hakanson and J. Sanchez-Dehesa, *Phys. Rev. B*, 2004, **70**, 214302.
- [186] L. Sanchis, A. Hakansson, D. Lopez-Zanon, J. Bravo-Abad, and J. Sanchez-Dehesa, *Appl. Phys. Lett.*, 2004, **84**(22), 4460.
- [187] A. Hakanson, F. Cervera, and J. Sanchez-Dehesa, *Appl. Phys. Lett.*, 2005, **86**, 054102.
- [188] A. Hakanson and J. Sanchez-Dehesa, *Appl. Phys. Lett.*, 2005, **87**, 193506.
- [189] E. Foca, H. Föll, J. Carstensen, V. Sergentu, I. Tiginyanu, F. Daschner, and R. Knöchel, *Appl. Phys. Lett.*, 2006, **86**, 011102.
- [190] Y. Saado, M. Golosovsky, D. Davidov, and A. Frenkel, *J. Appl. Phys.*, 2005, **98**, 063105.
- [191] V. Veselago, *Sov. Phys. Usp.*, 1968, **10**(4), 509.
- [192] J. Pendry, *Phys. Rev. Lett.*, 2000, **85**(18), 3966.
- [193] D. Smith, W. Padilla, D. Vier, S. Nemat-Nasser, and S. Schultz, *Phys. Rev. Lett.*, 2000, **84**, 4184.
- [194] P. Valanju, R. Walser, and A. Valanju, *Phys. Rev. Lett.*, 2002, **88**, 187401.
- [195] N. Garcia and M. Nieto-Vesperinas, *Phys. Rev. Lett.*, 2002, **88**(20), 207403.
- [196] C. Parazzoli, R. Gregor, K. Li, B. Koltenbah, and M. Tanielian, *Phys. Rev. Lett.*, 2003, **90**(10), 107401–1.
- [197] A. Houck, J. Brock, and I. Chuang, *Phys. Rev. Lett.*, 2003, **90**(13), 137401–1.
- [198] J. J. Pachenco, T. Grzegorzczuk, B. Wu, Y. Zhang, and J. Kong, *Phys. Rev. Lett.*, 2002, **89**, 257401.
- [199] S. Foteinopoulou, E. Economou, and C. Soukoulis, *Phys. Rev. Lett.*, 2003, **90**, 107402.

- [200] D. Smith, D. Schurig, and J. Pendry, *Appl. Phys. Lett.*, 2002, **81**, 2713.
- [201] R. Shelby, D. Smith, and S. Schultz, *Science*, 2001, **292**, 77–79.
- [202] A. Iyer and G. Eleftheriades In *IEEE MIT-S International Microwave Symposium Digest 2002*, Vol. 2, p. 1067, 2002.
- [203] V. Sergentu, V. Ursaki, I. Tiginyanu, E. Foca, H. Föll, and R. Boyd, *Appl. Phys. Lett.*, 2007, p. accepted for publication.
- [204] C. Tai, *Nature*, 1958, **182**, 1600.
- [205] T. Decoopman, G. Tayeb, S. Enoch, D. Maystre, and B. Gralak, *Phys. Rev. Lett.*, 2006, **97**, 073905.
- [206] M. Ritala and M. Leskela, *Nanotechnology*, 1999, **10**(1), 19–24.
- [207] C. Fang, E. Foca, S.-F. Xu, J. Carstensen, and H. Foell, *J. Electrochem. Soc.*, 2007, **154**(1).
- [208] M. Steinhart, J. Wendorff, A. Greiner, R. Wehrspohn, K. Nielsch, J. Schilling, J. Choi, and U. Goesele, *Science*, 2002, **296**, 1997.

Partial publications

List of publications

- [1] E. Foca, J. Carstensen, G. Popkirov, H. Föll, "Controlling macropores etching in n-Si by means of FFT in-situ voltage and photo impedance spectroscopy", ECS Transactions 6 (2), 345 (2007).
- [2] E. Foca, E. Ossei-Wusu, J. Carstensen, O. Riemenschneider, H. Föll, "Smoothing the pore walls in macroporous n-Si", ECS Transactions 6 (2), 367 (2007).
- [3] E. Foca, J. Carstensen, O. Riemenschneider, M. Leisner, H. Föll, "Impact of the alcohols containing electrolytes on the macropores etching in n-Si ", ECS Transactions 6 (2), 395 (2007).
- [4] E. Foca, V.V. Sergentu, J. Carstensen, I.M. Tiginyanu, and H. Föll, "Polarization dependent functionality of optical elements based on (quasi) periodic two-dimensional structures", J. Appl. Phys., submitted (2007).
- [5] E. Foca, J. Carstensen, and H. Föll, "Modeling electrochemical current and potential oscillations at the Si electrode", J. Electroanal. Chem. 603, 175 (2007).
- [6] C. Fang, E. Foca, S. Xu, J. Carstensen, and H. Foell, "Deep Si macropores filled with copper by electrodeposition", J. Electrochem. Soc. 154(1), D45-D49 (2007).
- [7] J. Carstensen, H. Föll, E. Foca, and C. Fang, "A stochastic model for current and voltage oscillations of the Si electrode", Solid State Phenomena, 1115 (2007).
- [8] E. Foca, H. Föll, J. Carstensen, V.V. Sergentu, I.M. Tiginyanu, F. Daschner, and R. Knöchel, "Strongly frequency dependent focusing efficiency of a concave lens based on two-dimensional photonic crystals", Appl. Phys. Lett. 86, 011102 (2006).
- [9] E. Foca, J. Carstensen, G. Popkirov, and H. Föll, "Pore growth control by *in-situ* FFT impedance spectroscopy", Phys. Stat. Sol. (a) 204 (5), 1378-1382 (2007).
- [10] E. Foca, J. Carstensen, and H. Föll, "Quantitative modeling of voltage oscillations and other oscillatory phenomena with the Current Burst Model", Phys. Stat. Sol. (c) 4 (6), 1883-1887 (2007).

- [11] V.V. Sergentu, V.V. Ursaki, I.M. Tiginyanu, E. Foca, H. Föll, and R.W. Boyd, "Design of negative refractive index materials on the basis of rods with a gradient of the dielectric constant", *Appl. Phys. Lett.*, accepted for publication (2007).
- [12] I.M. Tiginyanu, V.V. Ursaki, E. Monaico, E. Foca, and H. Föll, "Pore Etching in III-V and II-VI Semiconductor Compounds in Neutral Electrolyte", *Electrochem. Solid-State Lett.*, accepted for publication (2007).
- [13] V.V. Sergentu, V.V. Ursaki, I.M. Tiginyanu, E. Foca, H. Föll, and R.W. Boyd, "Focusing slabs made of negative index materials based on inhomogeneous dielectric rods", *Phys. Stat. Sol. (a)* 203(6), R48-R50 (2006).
- [14] H. Föll, J. Carstensen, and E. Foca, "Self-induced oscillations in Si and other semiconductors", *Int. J. Mat. Res.* 2006(7) (2006).
- [15] C. Fang, E. Foca, L. Sirbu, J. Carstensen, I.M. Tiginyanu, and H. Föll, "Formation of metal wire arrays via electrodeposition in pores of Si, Ge and III-V semiconductors", *Phys. Stat. Sol. (a)* 204 (5), 1388-1393 (2007).
- [16] F. Daschner, R. Knöchel, E. Foca, J. Carstensen, V.V. Sergentu, H. Föll, and I.M. Tiginyanu, "Photonic crystals as host material for a new generation of microwave components", *Adv. Radio Sci.* 4, 1 (2006).
- [17] E. Foca, J. Carstensen, and H. Föll, "Monte Carlo simulation of electrochemical oscillations in the electropolishing regime", *Phys. Stat. Sol. (a)* 74(8), 1524 (2005).
- [18] E. Foca, H. Föll, F. Daschner, V.V. Sergentu, J. Carstensen, S. Frey, R. Knöchel, and I.M. Tiginyanu, "Efficient focusing with a concave lens based on a photonic crystal with an unusual effective index of refraction", *Phys. Stat. Sol. (a)* 202(4), R 35 (2005).
- [19] E. Foca, H. Föll, F. Daschner, V.V. Sergentu, J. Carstensen, R. Knöchel, and I.M. Tiginyanu, in *Materials, Integration and Technology for Monolithic Instruments*, eds. J.A. Theil, M. Böhm, D.S. Gardner, and T. Blalock, D4.4, *Mater. Res. Soc. Symp. Proc.* 869, Warrendale, PA (2005).
- [20] V.V. Sergentu, E. Foca, S. Langa, J. Carstensen, H. Föll, and I.M. Tiginyanu, "Focusing effect of photonic crystal concave lenses made from porous dielectrics", *Phys. Stat. Sol. (a)* A 201, R31 (2004).
- [21] E. Foca, H. Föll, F. Daschner, V.V. Sergentu, J. Carstensen, S. Frey, R. Knöchel, and I.M. Tiginyanu, "Efficient focusing with a concave lens based on a photonic crystal with an unusual effective index of refraction", *Phys. Stat. Sol.(b)* 235, 1 (2003).
- [22] I.M. Tiginyanu, S. Langa, M. Christophersen, J. Carstensen, V. Sergentu, E. Foca, and H. Föll, "Properties of 2D and 3D Dielectric Structures Fabricated by Electrochemical Dissolution of III-V Compounds", *MRS Proceedings Fall Meeting: Progress in Semiconductor Materials for Optoelectronic Applications* 692, K2.7 (2001).

International Conferences

Oral presentations

[1] E. Foca, J. Carstensen, G. Popkirov, H. Föll, "Controlling macropores etching in n-Si by means of FFT in-situ voltage and photo impedance spectroscopy", The Electrochemical Society Meeting, Chicago, USA (Mai, 2007)

[2] E. Foca, J. Carstensen, O. Riemenschneider, M. Leisner, H. Föll, "Impact of the alcohols containing electrolytes on the macropores etching in n-Si ", The Electrochemical Society Meeting, Chicago, USA (Mai, 2007)

[3] E. Foca, J. Carstensen, H. Föll, "Describing the Si-HF contact with the Current Burst Model: from oscillatory behavior to pore formation", The Electrochemical Society Meeting, Chicago, USA (Mai, 2007)

[4] E. Foca, V.V. Sergentu, H. Föll, J. Carstensen, F. Daschner, R. Knöchel, I.M. Tiginyanu, "Efficient Focusing with an Ultra-Low Effective-Index Lens Based on Photonic Crystals", Materials Research Society, San Francisco, USA (2005)

[5] E. Foca, J. Carstensen, H. Föll, "A stochastic model for electrochemical oscillations at the Si/HF interface", The Electrochemical Society of America, Quebec, Canada (2005)

[6] E. Foca, H. Föll, V.V. Sergentu, I.M. Tiginyanu, F. Daschner, R. Knöchel, "Optical components based on 2D photonic crystals with unusual index of refraction", International Conference on Microelectronics and Computer Science, Chisinau, Moldova (2005)

[7] E. Foca, V.V. Sergentu, H. Föll, J. Carstensen, F. Daschner, R. Knöchel, I.M. Tiginyanu, "Microwave components based on 2D Photonic Crystals with Unusual Index of Refraction", Vortrag an der Technischen Universität Darmstadt auf Einladung von Prof. Dr. Hartnagel, Darmstadt, Germany

[8] E. Foca, J. Carstensen, G. Popkirov, H. Föll, "Pore growth control by in-situ FFT impedance spectroscopy", International Conference on Porous Semiconductors: Science and Technology, Barcelona, Spain (2006)

[9] E. Foca, C. Fang, L. Sirbu, J. Carstensen, I.M. Tiginyanu, and H. Föll, "Formation of Metal Wire Arrays via Electrodeposition in Pores of Si, Ge and III-V Semiconductors", International Conference on Porous Semiconductors: Science and Technology, Barcelona, Spain (2006)

Poster

[1] E. Foca, E. Ossei-Wusu, J. Carstensen, O. Riemenschneider, H. Föll, "Smoothing the pore walls in macroporous silicon", The Electrochemical Society Meeting, Chicago, USA (Mai,

2007)

[2] E. Foca, J. Carstensen, H. Föll, "Monte Carlo simulation of electrochemical oscillations in the electropolishing regime", International Conference on Porous Semiconductors: Science and Technology, Valencia, Spain (2004)

[3] E. Foca, J. Carstensen, H. Föll, F. Daschner, R. Knöchel, V.V. Sergentu, I.M. Tiginyanu, "Unusual Index Photonic Crystals as Metamaterials for an efficient Concave Lens", IPRA/NPIS, Optical Society of America, San Diego, USA (2005)

[4] E. Foca, J. Carstensen, H. Föll, F. Daschner, R. Knöchel, V.V. Sergentu, I.M. Tiginyanu, "Optical Elements Based on Unusual Index Photonic Crystals", Photonic and Electronic Crystals Structures, Agia Pelagea, Crete, Greece (2005)

[5] E. Foca, J. Carstensen, H. Föll, "Voltage oscillations and many other experimental results confirmed by the current burst model", International Conference on Porous Semiconductors: Science and Technology, Barcelona, Spain (2006)

[6] E. Foca, J. Carstensen, H. Föll, F. Daschner, R. Knöchel, V.V. Sergentu, I.M. Tiginyanu, "Polarization dependent functionality of optical elements based on (quasi) periodic two-dimensional structures", Metamaterials: from Random to Periodic, Optical Society of America, Bahamas Grand Island, The Bahamas.

Curriculum Vitae

Personal Data

Name	Eugen Foca
Date of birth	the 19 th of March, 1979
Place of birth	Chisinau, Moldova
Citizenship	Moldova
Parents	Nina and Valeriu Foca

Education

1985 - 1993	Primary School, Chisinau, Moldova
1993 - 1996	Academical Romanian-English High School "Mircea Eliade", Chisinau, Moldova
1996 - 2001	Studies at the Faculty of Computers, Informatics and Microelectronics, Technical University of Moldova, Chisinau, Moldova
February-June, 2001	State examination and diploma thesis at the Chair for Computer Science, Technical University of Moldova (Prof. Dr. Ion M. Tiginyanu)
2001 - 2003	Master Program at the Faculty of Engineering, Christian-Albrechts-University of Kiel, Kiel, Germany
May-October, 2003	Master thesis at the Chair for General Materials Science, Faculty of Engineering, Christian-Albrechts-University of Kiel (Prof. Dr. Helmut Föll)
April, 2004 - May, 2007	PhD work at the Chair for General Materials Science, Faculty of Engineering, Christian-Albrechts-University of Kiel (Prof. Dr. Helmut Föll)

Acknowledgments

I want to thank Prof. Dr. Helmut Föll for the opportunity to join his research group. I especially appreciate the freedom he gave me in designing my experiments as well as his precious contribution for the interpretation of my scientific results. But most of all I like to thank him for being my *Professor* and showing me the *Science* section in the Borders Library on Union Square in San Francisco. He made me love science!

I want to thank Prof. Dr. Ion M. Tiginyanu for giving me the first flavor of what science is, but most of all for convincing me doing science. It is him who brought me in contact with such topics as *Photonic Crystals*, *Semiconductors electrochemistry* and many others. All kind of support and motivation I obtained from him, during the last years, is invaluable. He made me feel always confident!

A great person without the help of whom many things would not have been possible is Dr. J. Carstensen. I thank you, Jürgen, for helping me make order in my thoughts and ideas. It is so important to work together with a competent person and it is so seldom you can meet such people!

I want to thank Dr. Vladimir V. Sergentu and Dr. Frank Daschner for their contribution to the chapter of *Photonic Crystals*. I thank Dr. Sergentu for his patience in teaching me how the story with light works and I thank Frank for his optimism and big contribution on setting up the experiments.

Prof. Dr. Georgi Popkirov is acknowledged for his moral and scientific support. I thank him for introducing me to the theory of electrochemistry and impedance spectroscopy. I will never forget the weekends we spent together in the lab - he gave them always life and motivated me to pursue further.

My great friend and a very good chemist, Dr. Oliver Riemenschneider, is acknowledged here as well. I thank him for all his help with the chemistry, supply of new and valuable ideas as well as for his great help with everything else. He was a big support for me during my stay here.

Another equally great friend and a very clever engineer Jörg Bahr is also acknowledged. It

Acknowledgments

is important to mention that without his ideas my experiments would never work as I wanted them. During our discussions it turned out often that he guessed much better than me what I actually need. I also thank Jörg for valuable discussions about family, children and life in general.

I want to thank Katrin Brandenburg simply for being all these years with us. It is so important to have somebody you can fully rely on and who misses in his vocabulary "I can not". I thank for her care which allowed us all concentrate on doing only science.

My friend Emmanuel Ossei-Wusu is acknowledged here as well. I thank him for helping me to find staff in the lab and for his commitment to helping me with my experiments while I was exceeding all possible deadlines.

I thank Dr. Cheng Fang for the nice discussions we had about everything in the world. Especially I acknowledge his major contribution to the experimental part with composite materials.

Prof. Dr. R. Wehrspohn, Dr. S. Schweizer, Dr. T. Geppert, Dr. A. von Reihn formerly from the University of Paderborn and Dr. A. Lamprecht from Dräger AG, Prof. Dr. V.V. Ursaki, S. Albu from the Technical University of Moldova are acknowledged for the enjoyable teamwork.

My colleagues Dr. Stefan Frey, Dr. Gunther Hasse, Stefan Mathijssen are acknowledged for the nice times we had together and always very exciting discussions. I thank Stefan Frey for his advises and help since I started as a student here. I thank Gunther for finding always time to listen to me. I thank Stefan Mathijssen for giving me the feeling there is always somebody who can help.

Sinje Keipert, Andreas Schütt, Robert Bock, Sufan Xu, Enno Lage, Alireza Abdollahinia are acknowledged for being good colleagues and establishing an agreeable atmosphere at our Chair. I thank Sinje for being always cute; Sufan and Enno for joining me in the lab.

A lot of friends from Romania and Moldova made me feel a piece of home, here in Germany. Adriana and Dr. Ciprian Zafiu, Dr. Simona Gheorghe, Eszter and Zalan Kramer, Alina and Dr. Iulian Teliban, I thank them for the wonderful times we had all together. I wish you know how much I miss them. Ghenadie Ulinici, Viorica and Dr. Eugen Balaur I thank for their calls and not forgetting me.

My valuable friends Dr. Ala Cojocar and Malte Leisner I thank for everything they did for me in the last year. I am pretty bad at saying nice words, but you deserve the nicest for all your help. I would really had hard times without you, guys.

I thank Angela and Dr. Sergiu Langa, Valentina and Gabriel Bradu for their moral support. The calls we had, the visits we payed to each other and simply the fact that you were always there gave me power and courage to advance.

Acknowledgments

I want to thank Cornelia Horoiu and Dr. Adrian Neagu as well as Sandel and Maura Horoiu for taking care of me and my wife and for being "the older" brothers and sisters.

I thank our "nasi" Ina and Andreas Metzen. I really appreciate their care great hearts.

I thank my parents in law Ion and Adriana Horoiu for their love and care. Their warm words and attitude gave strength and made feel protected.

I want to thank my brother and his wife Adrian and Silvia Foca for being always with me and for bringing peace in my soul. Since I left home in Moldova they had to replace the void I left in the souls of my parents and they did it so well.

Finally I want to thank my marvelous wife Dr. Magdalena Foca and my lovely son Matei Horatiu for being. I never thought you will have so much understanding for the missing vacations and weekends in family during the last three years. I thank you so much for supporting me and encouraging me. I thank you for showing me the light at the end of the tunnel every time I was losing it.

Last I want to thank my parents Nina and Valeriu Foca for the huge support and encouragements during the last years. I thank them for guiding me all this time and for bringing me back on the right road any time I was skidding. I thank them for giving me the confidence that anything I do is what I have to do. I thank them for understanding me.

Hiermit erkläre ich an Eides Statt, dass die vorliegende Abhandlung - abgesehen von Beratung durch meine Betreuer Herren Prof. Dr. H. Föll, Prof. Dr. I.M. Tiginyanu, Dr. J. Carstensen, Dr. V.V. Sergentu und Dr. F. Daschner - nach Inhalt und Form meine eigene Arbeit ist. Ich habe bisher keinen Promotionsversuch unternommen.

Eugen Foca

Kiel, den 02. Juli, 2007